THE UNIVERSITY OF QUEENSLAND
AUSTRALIA

Synthesis of Nanoporous Silica Membrane and Their Gas Transport Mechanism

Xuechao Gao
Master of Chemical Engineering

A thesis submitted for the degree of Doctor of Philosophy at
The University of Queensland in 2014

School of Chemical Engineering

Abstract

A fundamental understanding of the processes affecting fluid transport in the voids of porous materials constitutes a key step in numerous emerging applications in nanotechnology, materials design, membrane science and biology. By a purely hard sphere treatment of the diffusant, for over a century the Knudsen-based method has been the primary technique in our craft for investigating the transport of fluids in confined space, particularly in narrow disordered nanoporous adsorbents, catalysts and membranes. However, recent theoretical results and simulations, as well as experimental data on transport in well characterised narrow nanoporous materials indicate that the apparent success of the correlation is not necessarily a vindication of the Knudsen theory. Instead, these simulations, and the unrealistically high tortuosities obtained on application of the correlation, demonstrate the Knudsen model to substantially overestimate the diffusivity due to significant dispersive fluid-solid interaction. Besides affecting the molecular trajectories, which are no longer linear, the presence of the fluid-solid interaction leads to strong density profiles and adsorbate inhomogeneity in the direction normal to the pore walls. In this work, contributions are made involving such fundamental understanding of fluid transport in nanopores, and novel approaches are developed to facilitate the comprehensive analysis of transport in supported silica membranes.

Firstly, an analysis of the transport of single gases in macroporous α-alumina substrates having a mean pore size of around 500 nm was conducted, and the results indicate that the tortuosity is dependent on the gas, and varies with operating conditions in the slip flow regime. A new effective medium theory (EMT) approach for modelling the transport in the substrate was developed to include the entire pore size distribution and the pore aspect ratio effect due to finite pore length. Theoretical results of the EMT provide an improvement on existing models that are based on empirical correlations using a representative pore size. The dependence of tortuosities on operating conditions in macroporous networks in slip flow regime is caused by the difference in dependence of Knudsen and viscous flow-based permeability on pore size, temperature and pressure; these yield different tortuosity limits for the pure Knudsen and viscous flow, respectively, in the presence of pore size distribution. Besides these, the importance of the choice of representative pore radius in determining the apparent tortuosity trends with temperature is also extensively provided in different nanoporous network.

Moreover, a mesoporous γ-alumina membrane having a mean pore size around of 10.4 nm was synthesized on the surface of the macroporous α-alumina substrate by dip-coating. The transport mechanism of single gases in the mesoporous γ-alumina layer was investigated by the EMT approach to predict the macroscopic flow rate, using the classical slip flow model and a version corrected for finite molecular size, as well as the recent-developed Oscillator model in this laboratory. The analysis results indicate that all the three diffusion models describe the experimental data accurately and the interfacial pressure is correctly resolved in the approach, without the artifacts observed with the methodology using a single pore size.

In addition, using literature data on the diffusion of N_2, Xe and i-C_4H_{10} in mesoporous Shell silica spheres (mean pore size 14.2 nm), the transport of gases was also analyzed to predict the pore coordination number for various diffusion models. It has found that both the Knudsen model and the Oscillator model adequately interpret the data in conjunction with EMT approach due to this large pore size. A mesoporous amorphous silica layer having mean pore size of around 3.7 nm was further synthesized on the asymmetric support comprising a macroporous substrate and mesoporous interlayer. The transport mechanism of single gases in the mesoporous silica layer was investigated to predict the membrane thickness. The most satisfactory results were obtained with the Oscillator model, in which the fitting error was significantly reduced using an acceptable membrane thickness, indicating that the Knudsen model fails to represent the transport for the mesopores in silica.

Finally, a microporous amorphous silica layer was also synthesized on the asymmetric support, having a mean pore size around 1.5 nm. The adsorption and transport mechanism of single gases in the microporous silica membrane was examined, with the pore resistance represented by a combination of pore mouth and internal pore diffusion resistances. It has found that the pore mouth barrier dominates the overall transport resistance; and the internal diffusion resistance in the relatively smaller pores is significant, especially for weakly adsorbed gases at higher temperature.

Overall, this thesis explored gas transport in different porous materials under low pressure limits, using modification of established diffusion models. The results provide fundamental understanding about how the adsorptive and diffusive behaviour of adsorbate is affected by the adsorbent structure at the nanoscales. These results are accompanied by detailed investigations to explain fluid-dependence of tortuosity under different transport mechanisms. While this work has predominantly focused on silica membranes, the results and models developed are generally applicable to transport in other nanoporous materials.

Declaration by author

This thesis is composed of my original work, and contains no material previously published or written by another person except where due reference has been made in the text. I have clearly stated the contribution by others to jointly-authored works that I have included in my thesis.

I have clearly stated the contribution of others to my thesis as a whole, including statistical assistance, survey design, data analysis, significant technical procedures, professional editorial advice, and any other original research work used or reported in my thesis. The content of my thesis is the result of work I have carried out since the commencement of my research higher degree candidature and does not include a substantial part of work that has been submitted to qualify for the award of any other degree or diploma in any university or other tertiary institution. I have clearly stated which parts of my thesis, if any, have been submitted to qualify for another award.

I acknowledge that an electronic copy of my thesis must be lodged with the University Library and, subject to the General Award Rules of The University of Queensland, immediately made available for research and study in accordance with the *Copyright Act 1968*.

I acknowledge that copyright of all material contained in my thesis resides with the copyright holder(s) of that material. Where appropriate I have obtained copyright permission from the copyright holder to reproduce material in this thesis.

Publications during candidature

X. Gao, M.R. Bonilla, J.C. Diniz da Costa, S.K. Bhatia, The transport of gases in macroporous α-alumina supports*, J. Membr. Sci.*, 409-410 (2012) 24-33.

X. Gao, M.R. Bonilla, J.C. Diniz da Costa, S.K. Bhatia, The transport of gases in a mesoporous γ-alumina supported membrane, *J. Membr. Sci.,* 428 (2013) 357-370.

X. Gao, J.C. Diniz da Costa, S.K. Bhatia, The transport of gases in a supported mesoporous silica membrane, *J. Membr. Sci.,* 438 (2013) 90-104.

X. Gao, J.C. Diniz da Costa, S.K. Bhatia, Understanding the diffusional tortuosity of porous materials: An effective medium theory perspective, *Chem. Eng. Sci.* 110 (2014) 55–71.

X. Gao, J.C. Diniz da Costa, S.K. Bhatia, Adsorption and transport of gases in a supported microporous silica membrane, *J. Membr. Sci.*, 460 (2014) 46-61.

S.K. Bhatia, X. Gao, Effective medium theory-based modelling of transport in disordered nanoporous membranes, *AICHE 2013 Annual Meeting, San Francisco,* November 2013

X. Gao, S.K. Bhatia, Gas transport in a supported mesoporous silica membrane: mechanisms and modelling, *Engineering Postgraduate Research Conference, Brisbane,* June 2013

Publications included in this thesis

X. Gao, M.R. Bonilla, J.C. Diniz da Costa, S.K. Bhatia, The transport of gases in macroporous α-alumina supports, *J. Membr. Sci.*, 409-410 (2012) 24-33 – incorporated as Chapter 3.

Contributor	Statement of contribution
Author Xuechao Gao (Candidate)	Designed and conducted experiments (90%) Analysis and interpretation of data (50%) Paper drafting and writing (70%) Wrote computer code (40%)
Author Mauricio Rincon Bonilla	Paper drafting and writing (30%) Wrote computer code (60%)
Author Joao C. Diniz da Costa	Designed experiments (10%)
Author Suresh K. Bhatia	Analysis and interpretation of data (50%)

X. Gao, M.R. Bonilla, J.C. Diniz da Costa, S.K. Bhatia, The transport of gases in a mesoporous γ-alumina supported membrane, *J. Membr. Sci.*, 428 (2013) 357-370 – incorporated as Chapter 4.

Contributor	Statement of contribution
Author Xuechao Gao (Candidate)	Designed and conducted experiments (90%) Analysis and interpretation of data (50%) Paper drafting and writing (70%) Wrote computer code (100%)
Author Mauricio Rincon Bonilla	Paper drafting and writing (30%)
Author Joao C. Diniz da Costa	Designed experiments (10%)
Author Suresh K. Bhatia	Analysis and interpretation of data (50%)

X. Gao, J.C. Diniz da Costa, S.K. Bhatia, The transport of gases in a supported mesoporous silica membrane, *J. Membr. Sci.*, 438 (2013) 90-104 – incorporated as Chapter 5.

Contributor	Statement of contribution
Author Xuechao Gao (Candidate)	Designed and conducted experiments (80%) Analysis and interpretation of data (50%) Paper drafting and writing (60%) Wrote computer code (100%)
Author Joao C. Diniz da Costa	Designed experiments (10%) Paper drafting and writing (10%)
Author Suresh K. Bhatia	Designed experiments (10%) Analysis and interpretation of data (50%) Paper drafting and writing (30%)

X. Gao, J.C. Diniz da Costa, S.K. Bhatia, Understanding the diffusional tortuosity of porous materials: an effective medium theory perspective, *Chem. Eng. Sci.*, 110 (2014) 55-71 – incorporated as Chapter 6.

Contributor	Statement of contribution
Author Xuechao Gao (Candidate)	Designed and conducted experiments (70%) Analysis and interpretation of data (50%) Paper drafting and writing (60%) Wrote computer code (100%)
Author Joao C. Diniz da Costa	Designed experiments (10%) Paper drafting and writing (10%)
Author Suresh K. Bhatia	Designed experiments (20%) Analysis and interpretation of data (50%) Paper drafting and writing (30%)

X. Gao, J.C. Diniz da Costa, S.K. Bhatia, Adsorption and transport of gases in a supported microporous silica membrane, *J. Membr. Sci.*, 110 (2014) 55-71 – incorporated as Chapter 7.

Contributor	Statement of contribution
Author Xuechao Gao (Candidate)	Designed and conducted experiments (70%) Analysis and interpretation of data (50%) Paper drafting and writing (60%) Wrote computer code (100%)
Author Joao C. Diniz da Costa	Designed experiments (10%) Paper drafting and writing (10%)
Author Suresh K. Bhatia	Designed experiments (20%) Analysis and interpretation of data (50%) Paper drafting and writing (30%)

Contributions by others to the thesis

Contributions were made by Prof. Bhatia and Prof. Joe da Costa in experiment design, concept, analysis, interpretation, drafting, and writing in the advisory capacity.

Statement of parts of the thesis submitted to qualify for the award of another degree

None

Acknowledgements

I have been the most fortunate to meet and work with the world-class researchers in adsorption and diffusion area on which I started to peruse my doctorate degree. In this thesis, I would like to take the opportunity to thank them for their useful contributions and recommendations to my PhD project.

Foremost, I would like to express my sincere gratitude to my principal supervisor Prof. Bhatia for his continuous patience, guidance and immense knowledge during my research. I am greatly indebted in his effort to bring me into research and his concern in the development of my future career. I would never have been able to finish my work and dissertation without his brilliant theory.

Besides my principal advisor, my deep gratitude also goes to my co-supervisor Prof. Joe da Costa, who helps me with the experimental work, including the membrane synthesis and characterization. The useful discussion and arguments in his group meetings and seminars really helped me to understand the principle and artifacts of the current membrane research.

I also wish to thank my committee members (Prof. John Zhu and Prof. David Nicholson), who were more than generous with their expertise and precious time.

I would like to thank Dr. Simon for preparing the membrane module and training the instruments as well as the ordering of the related instruments parts, such as tubes and chemicals.

I would like to thank all members in the Bhatia's group: Dr. Thanh Xuan Nguyen, Dr. Sandeep Sarathy, Dr. Pradeep Shukla, Dr. Mauricio Rincon Bonilla, Dr. Kimia Alizadeh, Mr. Ali Shahtalebi, Mr. Guozhao Ji, Mr. Benjamin Ballinger, Mr. Amir Hajiahmadi Farmahini and Mr. Lang Liu, for the their useful discussions on the gas diffusion and adsorption in porous materials.

Last but not the least, I would like to thank my family, including my parents (Youzeng Gao and Shenglan Shen), my wife (Peng Zhang) and my two brothers (Xingmin Gao and Xingjun Gao) for spiritual and continuous support throughout my life.

Keywords

transport mechanism, supported silica membrane, nanoporous materials, disordered porous media, effective medium theory, oscillator model, transition-state theory, knudsen model, tortuosity, dispersive interaction

Australian and New Zealand Standard Research Classifications (ANZSRC)

ANZSRC code: 090404, Membrane and Separation Technologies, 60%
ANZSRC code: 090402, Catalytic Process Engineering, 30%
ANZSRC code: 091201, Composite and Hybrid Materials, 10%

Fields of Research (FoR) Classification

FoR code: 0904, Chemical Engineering, 90%
FoR code: 0912, Material Engineering, 10%

Tables of Contents

List of Figures

List of Tables

Chapter 1: Introduction

1.1 Background

Modeling fluid transport and adsorption in narrow pores has been an object of interest for over one century due to its significance of industrial applications, e.g. heterogeneous catalysis and adsorptive separation [1]. Among these, models based on viscous and Knudsen flow are most commonly used to represent the effect of fluid-fluid and fluid-wall interaction in the disordered porous materials [2]. Recently, with rapid development of novel nanomaterials [3-8], the topic has gained renewed attention. However, the century-old Knudsen-based model is still used as a routine to explain experimental data even for the narrow microporous materials by conducting empirical fittings. Unrealistically high tortuosities are generally obtained in the correlation, especially for silica materials [9], indicating the diffusivity is significantly over predicted in the narrow pores. As in such narrow pores, the dispersive interaction between fluid molecule and pore walls is expected to produce new types of phase transition and diffusive reflection that are not observed in the large pores in which the classic Knudsen model is frequently applied. Therefore, a fundamental understanding of confinement on diffusion and adsorption is central to the design and application of the novel nanomaterials to fulfill the newly-emerged technology, such as membrane separation, gas storage and drug delivery [5].

In recent years, the rapid development of computing technology has enable scientists and engineers to develop and apply molecular modeling and theory to investigate the fluid behaviors in the new porous materials to provide fundamental mechanism of the diffusion and adsorption in the narrow pores. Molecular dynamics (MD) simulation has become a new recourse for predicting gas diffusivity and shown that the Knudsen approach has significantly overpredicted the diffusivity for 2 and 3 nm pores of silica membrane [10, 11], suggesting the importance of fluid-solid interaction on the transport efficiency. The main advantage of MD simulation is that once the pore structure and the fluid-pore interaction are determined, the fluid adsorption and transport behaviour can be extensively examined For instance, the MD approach has successfully predicted the extreme fast diffusivity in carbon nanotube due to the smooth surface texture of the carbon wall [12]. Another significant artifact of the Knudsen model in predicting the transport of fluid in the narrow pore is the assumption of uniform fluid density across the pore radius, which is always identical to the bulk density in the Knudsen model, regardless of the temperature and gas species. However, extensive simulation results have indicated that the local density in the pore is dependent on the interaction between the fluid and pore wall, which is expected to substantially differ from the bulk density and varies with temperature [13, 14]. More details about the comparison between MD simulation and

Knudsen model are available in the literature [1, 10, 15-17]. On the other hand, due to the time-consuming nature of MD, new tractable theories are still highly desirable. In the line of the Knudsen model, activated diffusion model is proposed by incorporating an empirical activated energy to reduce the diffusivity, with using a stronger temperature dependence as a generalization of the Knudsen model [18-22]. However, such treatment still significantly over-predicts the diffusivity when the pore diameter is above 1 nm in comparison with the MD result [16].

Contrary to the above suggestions of modification of the Knudsen model in mesopores and micropores, some tractable theories are proposed based on the consideration of the nonuniform density profile in the pore. However, these models involve approximations, and have not been validated against molecular simulations [23-25]. Other models have neglected dispersive fluid-fluid interactions [26].

Aided by the finding from MD simulations that the nonuniform equilibrium density profile of the fluid is essentially preserved during the transport [27], significant success is achieved in Bhatia's laboratory through consideration of dispersive interaction and equilibrium density profile to simplify the transport mechanical model for low density region (low Knudsen number). The new developed model is termed as "Oscillator model", which is extremely efficient from a computational standpoint, and the model has been extensively validated by the MD simulation [22]. By including the fluid-fluid interaction in a way of frictional approach, the "Oscillator model" can be extended to higher density regions (high Knudsen number) [2]. Although the Oscillator model has been extensively validated against the MD results and some experimental data, the theory needs further validation based on experimental data, and this constitutes one of the aims of this subject.

In this project, the supported silica membrane is employed to investigate the transport mechanism of light gases and validate the applicability of the Oscillator model in the narrow nanopores. For such materials, the whole system generally consists of different layers for the convenience of industrial purpose. For instance, a typical supported silica membrane is constructed in an asymmetric fashion, comprising a thin membrane layer with narrower pores, in which the gas separation occurs, coated on a relatively thick porous asymmetric support. A thick porous α-alumina substrate coated with a thin γ-alumina interlayer is usually selected as the asymmetric support [28-30]. The substrate is made of unconsolidated micron sized (~3 μm) crystal particles, to provide good mechanical strength for the whole membrane; the main pores of the substrate are macroporous. The γ-alumina crystal particles in the interlayer are significantly smaller (~0.05 μm) and deposited on the surface of the substrate to obtain a smooth, defect-free surface over which the active silica layer is coated; the main pores of the interlayer are mesoporous.

In addition, the main challenge attending the application of any theory to experimental transport data in the supported membrane is the complicacy of the pore network, including the pore connectivity and shape as well as the presence of nonuniformity of the size. The 'traditional' method to model the transport in the supported membrane is based on empirical correlation in the spirit of dusty gas model (DGM), by choosing a representative pore for each layer. However, the interfacial pressures between layers are not directly measurable, and the analysis of diffusion through each layer is often based on arbitrary assumptions, regardless of the variation of controlling mechanism with operating conditions, including temperature and gas species [31]. Furthermore, the typical correlation of the DGM rely on the assumption that the tortuosity is exclusively determined by the topology of the porous medium; however, some work has extensively shown that the apparent tortuosity can be significantly influenced by the diffusion mechanism in the pores due to the pore size distribution [16, 32].

Effective medium theory (EMT) provides the necessary machinery to resolve the above issues, and in this method, a nonuniform network with a distribution of conductance is replaced by a uniform one in which each conductance is assigned an effective value [33-35]. The effective medium theory has been extensively used to investigate the tortuosity for microporous silica membrane by assuming infinite long capillaries, discovering the dependence of gas species and temperature [16, 17]. However, the symmetric support made of Al_2O_3 crystal particles by sintering at high temperature is different from the silica media as the pore dimension in the substrate and the interlayer is comparable to the pore length, leading axial divergence of the local transport direction in the pore. Thus, it is very interesting to extend EMT to model the transport mechanism of unconsolidated alumina support by considering the aspect ratio effect, to determine the pressure profile in the whole membrane system. The advantage of effective medium method over the 'traditional' approach is that the entire pore size distribution of each layer is taken into account, rather than using an arbitrary representative pore size as shown by DGM. By utilizing the relationship between pore structure and macroscopic flow rate, the diffusion model can be directly validated.

1.2 Objectives

The main target of this PhD thesis is to investigate the transport mechanism of gases through nanoporous silica membrane and validate the applicability of the Knudsen model and the Oscillator model at the single pore level. The core work of this project is to apply the well-known effective medium theory based methodology in the typical mesoporous/microporous supported silica membrane system layer by layer, to test the corresponding diffusion model step by step, so as to provide a general approach at different levels and demonstrate the connection between molecular modeling and its application to practical supported silica membranes. In particular, the following objectives are achieved:

1. Investigating the transport mechanism in the macroporous alumina substrates at low pressure regime and exploring the relationship between the apparent tortuosity and pore network structure by effective medium theory with considering the aspect ratio effect.

2. Synthesizing a mesoporous γ-alumina interlayer on the substrate by crystal particle packing method by dip-coating process, and investigating the transport mechanism of the mesoporous interlayer to validate the applicability of the Knudsen model and the Oscillator model by effective medium theory.

3. Synthesizing a mesoporous supported silica membrane by controllable surfactant template by sol-gel process, and investigating the diffusion mechanism of the mesoporous silica membrane to validate the applicability of the Knudsen model and the Oscillator model by effective medium theory.

4. Synthesizing a microporous supported silica membrane by acid hydrolysis of TEOS and MTES, and investigating the adsorption and transport in the microporous silica membrane by effective medium theory, with decomposing the pore resistance into internal pore body resistance and pore body resistance based on the combination of the Oscillator model and transition-state theory.

1.3 Summary of the thesis

The thesis comprises of eight chapters of which five chapters covers all the works finished in the time frame of the PhD project, in particular, chapters 3, 4, 5, 6 and 7 are comprised of the author's relevant journal manuscripts. A short description of the chapters is briefly provided as follows:

Chapter 1 addresses an overview of significance of adsorption and transport phenomena of nanomaterial to practical industrial applications and understanding the transport of confined fluid in the supported silica membrane as well as problems needed to be solved. Accordingly, concrete objectives of this thesis are given.

Chapter 2 provides a comprehensive description of the synthesis of supported membranes and a summary of the existing important transport models and theories for the supported silica membranes made by sol-gel process in which the Knudsen model, the Oscillator model and effective medium theory are emphasized.

Chapter 3 presents the transport mechanism of single gases in macroporous α-alumina substrates (mean pore size 500 nm) with considering the pore aspect ratio effect, based on the modelling results of effective medium theory, showing that the tortuosity is dependent on operating condition in the slip flow regime.

Chapter 4 presents the transport mechanism of single gases in a mesoporous γ-alumina interlayer with a mean pore size 10.4 nm by predicting the macroscopic permeation results based on effect medium theory.

Chapter 5 presents the transport mechanism of single gases in a mesoporous supported silica membrane with a mean pore size 3.7 nm by effect medium theory approach to validate the Oscillator model, showing that the Oscillator model provides more accurate apparent diffusivity than the Knudsen model.

Chapter 6 presents the transport mechanism in a mesoporous silica spheres with a mean pore size 14.5 nm based on the new N_2 adsorption isotherm by effect medium theory approach and Dusty Gas Model to investigate the diffusion mechanism. Furthermore, the relationship between the tortuosity and the representative pore radius is also addressed.

Chapter 7 presents the adsorption and transport mechanism of single gases in a microporous supported silica membrane with a mean pore size 1.5 nm by effective medium theory approach based on the combination of the transition state theory and the Oscillator model.

Chapter 8 summaries conclusions based on all the works conducted in this thesis. Further, recommendations for extension of the current research project are also addressed in the end.

1.4 References

[1] S.K. Bhatia, M.R. Bonilla, D. Nicholson, Molecular transport in nanopores: a theoretical perspective, Phys. Chem. Chem. Phys., 13 (2011) 15350-15383.

[2] S.K. Bhatia, D. Nicholson, Friction based modeling of multicomponent transport at the nanoscale, J. Chem. Phys., 129 (2008) 164709.

[3] P.F. Lito, C.F. Zhou, A.S. Santiago, A.E. Rodrigues, J. Rocha, Z. Lin, C.M. Silva, Modelling gas permeation through new microporous titanosilicate AM-3 membranes, Chem. Eng. J., 165 (2010) 395-404.

[4] C.J. Brinker, G.W. Scherer, Sol-Gel Science: The Physics and Chemistry of Sol-Gel Processing, Academic Pr., San Diego, CA, 1990.

[5] Y. Wan, D. Zhao, On the controllable soft-templating approach to mesoporous silicates, Chem. Rev., 107 (2007) 2821-2860.

[6] Y. Lu, G. Cao, R.P. Kale, S. Prabakar, G.P. López, C.J. Brinker, Microporous silica prepared by organic templating: relationship between the molecular template and pore structure, Chem. Mater., 11 (1999) 1223-1229.

[7] C.J. Brinker, T.L. Ward, R. Sehgal, N.K. Raman, S.L. Hietala, D.M. Smith, D.W. Hua, T.J. Headley, Ultramicroporous silica-based supported inorganic membranes, J. Membr. Sci., 77 (1993) 165–179.

[8] C.T. Kresge, M.E. Leonowicz, W.J. Roth, J.C. Vartuli, J.S. Beck, Ordered mesoporous molecular sieves synthesized by a liquid-crystal template mechanism, Nature, 359 (1992) 710-712.

[9] X. Gao, J.C. Diniz da Costa, S.K. Bhatia, The transport of gases in a supported mesoporous silica membrane, J. Membr. Sci., 438 (2013) 90-104.

[10] R. Krishna, J.M. van Baten, An investigation of the characteristics of Maxwell-Stefan diffusivities of binary mixtures in silica nanopores, Chem. Eng. Sci., 64 (2009) 870-882.

[11] R. Krishna, J.M. van Baten, Unified Maxwell-Stefan description of binary mixture diffusion in micro-and meso-porous materials, Chem. Eng. Sci., 64 (2009) 3159-3178.

[12] A.I. Skoulidas, D.M. Ackerman, J.K. Johnson, D.S. Sholl, Rapid transport of gases in carbon nanotubes, Phys. Rev. Lett., 89 (2002) 185901.

[13] O.G. Jepps, S.K. Bhatia, D.J. Searles, Modeling molecular transport in slit pores, J. Chem. Phys., 120 (2004) 5396-5406.

[14] S.K. Bhatia, D. Nicholson, Transport of simple fluids in nanopores: Theory and simulation, AIChE J., 52 (2006) 29-38.

[15] R. Krishna, J.M. van Baten, Influence of segregated adsorption on mixture diffusion in DDR zeolite, Chem. Phys. Lett., 446 (2007) 344-349.

[16] S.K. Bhatia, Modeling pure gas permeation in nanoporous materials and membranes, Langmuir, 26 (2010) 8373-8385.

[17] S.K. Bhatia, D. Nicholson, Some pitfalls in the use of the Knudsen equation in modelling diffusion in nanoporous materials, Chem. Eng. Sci., 66 (2010) 284-293.

[18] J. Xiao, J. Wei, Diffusion mechanism of hydrocarbons in zeolites-I. Theory, Chem. Eng. Sci., 47 (1992) 1123-1141.

[19] M.B. Rao, S. Sircar, Nanoporous carbon membranes for separation of gas mixtures by selective surface flow, J. Membr. Sci., 85 (1993) 253-264.

[20] A.J. Burggraaf, Single gas permeation of thin zeolite (MFI) membranes: theory and analysis of experimental observations, J. Membr. Sci., 155 (1999) 45-65.

[21] H.M. Alsyouri, J.Y.S. Lin, Gas diffusion and microstructural properties of ordered mesoporous silica fibers, J. Phys. Chem. B, 109 (2005) 13623-13629.

[22] O.G. Jepps, S.K. Bhatia, D.J. Searles, Wall mediated transport in confined spaces: exact theory for low density, Phys. Rev. Lett., 91 (2003) 126102.

[23] T.K. Vanderlick, H.T. Davis, Self-diffusion in fluids in microporous solids, J. Chem. Phys., 87 (1987) 1791-1795.

[24] Z. Guo, T. Zhao, Y. Shi, Simple kinetic model for fluid flows in the nanometer scale, Phys. Rev. E, 71 (2005) 035301.

[25] A.W. Thornton, T. Hilder, A.J. Hill, J.M. Hill, Predicting gas diffusion regime within pores of different size, shape and composition, J. Membr. Sci., 336 (2009) 101-108.

[26] G. Arya, H.C. Chang, E.J. Maginn, Knudsen diffusivity of a hard sphere in a rough slit pore, Phys. Rev. Lett., 91 (2003) 26102.

[27] S.K. Bhatia, D. Nicholson, Hydrodynamic origin of diffusion in nanopores, Phys. Rev. Lett., 90 (2003) 016105.

[28] D. Uhlmann, S. Liu, B.P. Ladewig, J.C. Diniz da Costa, Cobalt-doped silica membranes for gas separation, J. Membr. Sci., 326 (2009) 316-321.

[29] S. Battersby, T. Tasaki, S. Smart, B. Ladewig, S. Liu, M.C. Duke, V. Rudolph, J.C. Diniz da Costa, Performance of cobalt silica membranes in gas mixture separation, J. Membr. Sci., 329 (2009) 91-98.

[30] H.L. Castricum, R. Kreiter, H.M. van Veen, D.H.A. Blank, J.F. Vente, J.E. ten Elshof, High-performance hybrid pervaporation membranes with superior hydrothermal and acid stability, J. Membr. Sci., 324 (2008) 111-118.

[31] D.M. Ruthven, W. DeSisto, S. Higgins, Diffusion in a mesoporous silica membrane: validity of the Knudsen diffusion model, Chem. Eng. Sci., 64 (2009) 3201-3203.

[32] X. Gao, M.R. Bonilla, J.C. Diniz da Costa, S.K. Bhatia, The transport of gases in macroporous α-alumina supports, J. Membr. Sci., 409-410 (2012) 24-33.

[33] V.N. Burganos, S.V. Sotirchos, Diffusion in pore networks: effective medium theory and smooth field approximation, AIChE J., 33 (1987) 1678-1689.

[34] P.D. Deepak, S.K. Bhatia, Transport in capillary network models of porous media: theory and simulation, Chem. Eng. Sci., 49 (1994) 245-257.

[35] S. Kirkpatrick, Classical transport in disordered media: Scaling and effective-medium theories, Phys. Rev. Lett., 27 (1971) 1722-1725.

Chapter 2: Literature review

This chapter reviews the existing literature on silica supported membranes for gas separation application. It begins with an introduction to the membrane (synthesizing methods and pore network structure and characterization) in section 2.1, with focusing on sol-gel process by molecular imprinting method. Then the existing problem in modelling of gas transport for the disordered nanoporous materials and the evolutions of transport models of gases in the pore are addressed in section 2.2, with emphasis on the classic Knudsen model, Activated Diffusion model, Transition-state theory (TST), “Oscillator model”, Dusty Gas model (DGM), Maxwell-Stefan model (MSM) and “Friction model”. Finally, the fundamental principles of effective medium theory (EMT) for modelling the transport of gases in the disordered materials are discussed in section 2.3.

2.1 Overview of silica membranes

Fluid diffusion and adsorption in confined space is an important unit operation in industry, ranging from the traditional applications such as industrial gas separation and purification, carbon capture and storage, catalysis reaction, and removal of volatile organic liquid from air exhaust stream, to a host of new applications such as drug delivery, fuel cell, desalination, clean energy and lab-on-chip technology [1-3]. Among these, a large amount of work has been done on membrane-based devices in the last two decades [4-10]. The membrane separation process is believed to be more energy efficient and holds a promise to be an alternative way to replace the well-established and energy intensive methods such as cryogenic distillation and adsorptive process. A key advantage of inorganic membranes over polymeric membranes for gas separation is the thermal stability under harsh conditions where organic membranes undergo degradation [11]. Different methods have been developed to synthesize silica membranes for several decades, and some important approaches are briefly introduced in the following

2.1.1 Membrane synthesis approaches

Not only should an ideal membrane have an excellent stability under a wide range of operation conditions, but also produce high selectivity and permeance for chemicals of interest. Therefore, the development of high performance membranes for industrial application with low cost attracts increasing attention from both researchers and industry. In 1980s, porous Vycor glasses were employed to obtain silica amorphous membrane by heat treatment and acid etching of alkaliorosilicate glasses to separate H_2 from H_2S, and the pore size was in the range of 3-5 nm, yielding low gas selectivities < 5 [12]. In 1989, Chemical vapour deposition (CVD) methodology is successfully employed to prepare thin silica membrane on porous substrate in the work of Gavalas and Megiris et al.[13] by SiH_4 oxidation within the walls of porous Vycor tubes, demonstrating the potential of gas separation by size exclusion by creating ultramicropores. In 1993, the hydrothermal seed method was proposed to synthesis zeolite membrane on the α-Al_2O_3 substrate [14]. The use of seed crystals facilitates the fabrication of zeolite membranes as a seeded substrate grows to a pure-phase zeolite membrane more easily even when the crystallization conditions (pH and temperature) and the chemical batch composition are not optimum.

Although the silica membrane synthesised by CVD and hydrothermal method demonstrated very high selectivity, it is rather difficult to control for the cases of micropores larger than the size of nitrogen [15, 16]. Finally sol-gel silica [17], although studied as a material since 1980s, was employed as gas separation membranes by dip-coating process in the work of de Lange in 1990s [18-20], and generally produces higher permeance and lower selectivities than CVD silica membranes. Although, the obtained porous silica is hydrophilic [14-16] and to be easily susceptible to hydrolytic cleavage by adsorbed water vapour, the sol-gel derived membrane offers a simple and cost-effective route in microporous silica membranes.

Since this time, extensive research on silica membranes has been mainly concentrated on the improvement of permeance and ideal selectivities, and the improvement of membrane stability [21]. After the first synthesis of the mesoporous silicate molecular sieves such as M41S by molecular imprinting method [22], the formation of the mesoporous phases was later discovered by Huo et al. through a cooperative self-organization of charged surfactant micelles and inorganic species [23], and an intense research has been devoted to make molecular sieve membranes (MSS) for various purpose. Since the main pore size of the membrane can be tailored by changing surfactants and templates [24-28] in this approach, the sol-gel process are discussed in details.

2.1.2 Sol-gel silica process

A silica sol-gel process can be described as colloidal suspension of polymerised silica formed by the hydrolysis and polycondensation of monomeric silicon alkoxide precursors ($Si(OR)_4$) with water, using mineral acid or base as catalyst [17]. The reactions involved in the process are summarized in eqs. (2.1)-(2.3). In the hydrolysis reaction, the organic alkoxy group (-OR) of the silica precursor is hydrolysed with water to form silanol (Si-OH) bonds and alcohol (R-OH) as the by-product. The silanol (Si-OH) precursor can further either react with alkoxy group to produce siloxane (Si-O-Si) bonds and alcohol, or with another silanol group to form siloxane and water. As indicated by the reserve of eqs. (2.2) and (2.3), it can participate in esterification or alcoholysis reactions.

$$\equiv \text{Si-OR} + \text{H}_2\text{O} \underset{esterification}{\overset{hydrolysis}{\rightleftharpoons}} \equiv \text{Si-OH} + \text{R-OH} \tag{2.1}$$

$$\equiv \text{Si-OR+HO-Si} \equiv \underset{alcoholysis}{\overset{condensation}{\rightleftharpoons}} \equiv \text{Si-O-Si} \equiv +\text{R-OH} \tag{2.2}$$

$$\equiv \text{Si-OH+HO-Si} \equiv \underset{alcoholysis}{\overset{condensation}{\rightleftharpoons}} \equiv \text{Si-O-Si} \equiv +\text{H}_2\text{O} \tag{2.3}$$

The obtained silica sol solution can greatly vary with the composition of the three main components: the silica precursor, water and alcohol, which is also used in excess as a solvent to promote hydrolysis reaction. Because water is produced as a by-product of the condensation reaction, a value of 2 is theoretically sufficient to completely hydrolyse and polymerize the silica precursor to yield anhydrous, as shown by the net reaction:

$$n\text{Si(OR)}_4 + 2n\text{H}_2\text{O} \rightarrow \text{SiO}_2 + 4n\text{ROH} \tag{2.4}$$

However, numerous experiments have shown that the hydrolysis reaction does not go to the completion even in excess water (r>>2, r is the molar ratio between two reactants), instead, a spectrum of intermediate species ($[\text{SiO}_x(\text{OH})_y(\text{OR})_z]_n$; where $2x+y+z=4$ and y is the number of hydroxyl group) are produced [17].

Although silica-sol formation can be described into the three base equations, the idealised number of unique, individual silica species is 15, giving 165 unique reactions in theory [29]. In practice, as the sol-gel reaction proceeds, macromolecule of silica polymer are formed, leading to an exponential increase in the number of unique molecular species and unique reactions, and ultimately a polymeric silica matrix is obtained. To characterize the network of the amorphous polymeric silica gel, Kay and Assink suggested 15 distinct silica species based on the number of each of the four relevant bonds (Si-O-R; Si-O-H; Si-O-Si) around an individual silicon atom to show how the silica skeletal structure is influenced by the hydrolysis and condensation reactions [29].

Figure 2.1 depicts 4 basic polymeric silica units according to the Si-O bonds arbitrarily labelled as Q^0-Q^4 to represent partially and fully condensed silica species, where the Q number refers to the number of siloxane bonds (O-Si-O) for each silicon atom. In addition, ^{29}Si-NMR spectroscopy has the ability to characterize the silicon-oxygen bonds of Q^0-Q^4 and is routinely used to determine condensation degree of the silica gel based on the deconvolution of the Nuclear Magnetic Resonance spectroscopy (NMR) spectrum.

Based on fractal theory [17], high concentration of silanol (Q^2 and Q^3) is a good indication of high fraction of weakly branched structure and favours the formation of micropores after calcination. As depicted in Figure 2.2, the ^{29}Si-NMR spectrum can be mathematically deconvoluted, and Diniz da Costa et al. [3] has employed this technique to analysis the composition of the molecular sieve silica (MSS) to conclude that two-step sol–gel process produces films with smaller pore size than the single-step sol–gel process as the two-step xerogels consistently had higher Q^3 and Q^2 species compared with single-step xerogels.

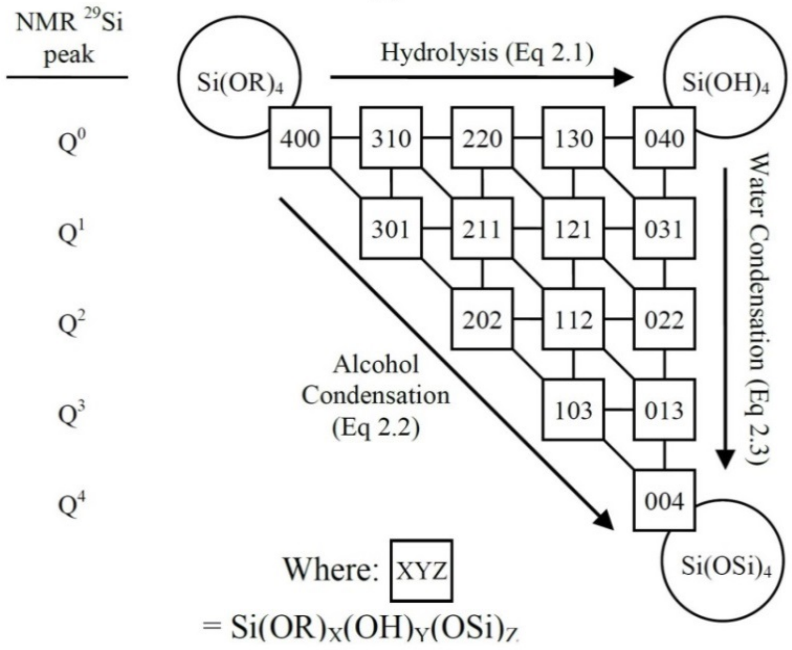

Figure 2.1 Reactions and Si species in sol gel synthesis (adapted from [29]).

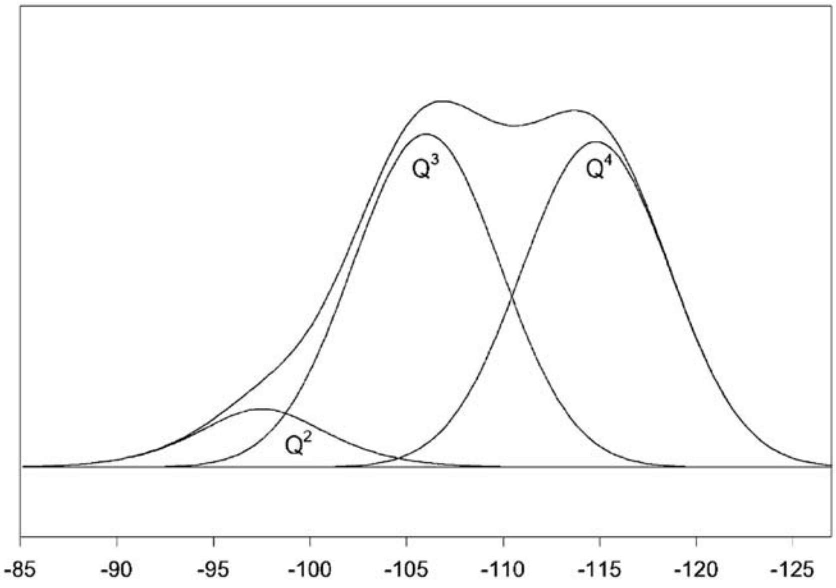

Figure 2.2 De-convoluted ^{29}Si-NMR spectrum (adapted from [3]).

Either mineral acids or bases can be used to catalyse the hydrolysis and condensation reaction. As illustrated in Figure 2.3, it is evident that acid condition favours the formation of long-chained and weakly-branched silica monomers, and the preferred reaction sites for condensation are the least acidic (most likely protonated) silanol bonds at the ends of silica chain [17]. In this way an acid catalysed sol produces long chains of siloxane bonds (Q^4) and weakly branched silica (Q^1, Q^2 and Q^3) polymer. After drying and calcination, the silica sol is densified into a mesh like structure and the connected interchain apertures form pores of 2-4 Å, which has been confirmed in several nitrogen adsorption studies that an increase in sol acidity gives higher microporous volume [30].

Conversely, base catalysis favours the formation of highly-branched silica as in this case the preferred reaction sites for condensation are the most acidic (most likely deprotonated) silanol bonds of the Q^3 Si atoms, allowing the structure to settle to its most thermodynamically favoured configuration with as many siloxane bonds (Q^4) as possible and creating a highly branched silica network. After calcination, the highly branched base catalysed sol is densified into small clusters containing larger (>2 nm) intercluster pores. The acid-catalysis based sol-gel process is extensively used to explore molecular sieve membranes for gas separation [4, 7, 10, 31-35], and the selectivity can go up to thousands [3, 36].

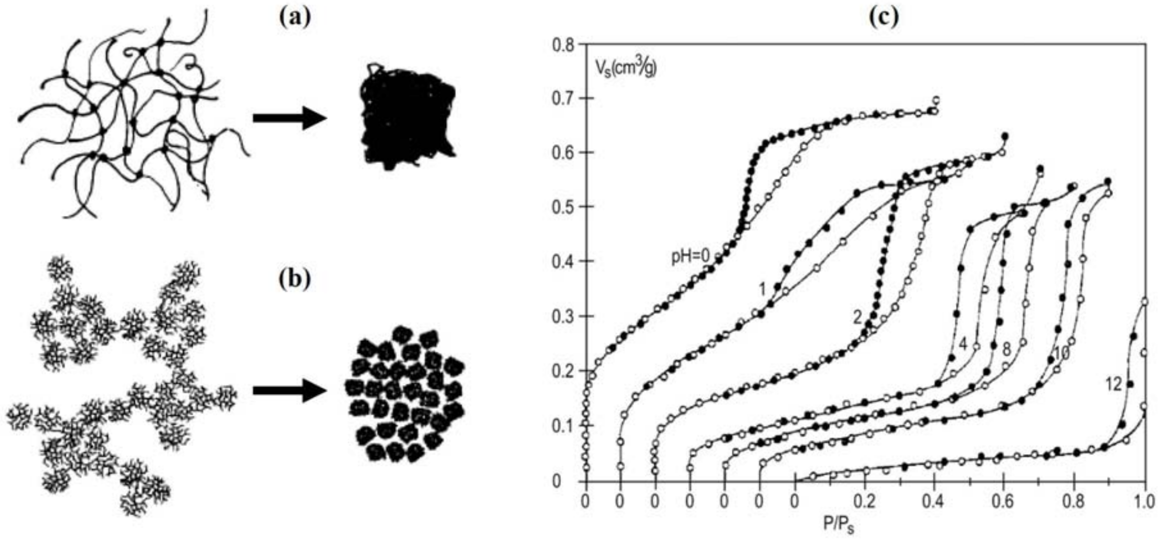

Figure 2.3 Comparison of (a) acid and (b) base catalysed sol-gel structure evolution during calcinations [37], and (c) N$_2$ adsorption isotherms of pH controlled xerogels [30].

2.1.3 Molecular imprinting method

Although polymeric condensation of silica precursor in sol-gel process can produce very narrow pores for the molecular sieves membrane and adsorbents [7], most of microporous and mesoporous silica materials are largely synthesized by molecular imprinting method [2, 6, 8, 22-24, 26, 28, 38, 39] to fulfil various applications, such as catalytic support, pervaporation, desalination and drug delivery nanocarriers [40-43]. In chemistry, molecular imprinting is a technique to create template-shaped confined spaces in polymeric materials with memory of the template molecules (surfactant or ligand) to be used in the molecular recognition.

The first experiment of molecular imprinting on a solid was attempted by Russian scientist, Poljakov, in 1930s [44], in which a silica gel was prepared in the presence of aromatic hydrocarbon and a relatively high adsorption capacity was observed for smaller adsorbate molecule as the template after drying. Because the nanopore analysis techniques (such as pressure swing adsorption process) were not invented yet, the significance of this research was not realised. However, the modern molecular template imprinting in pore synthesis occurred in 1970s by Lussier et al. [45] through the preparation of pillared clay or silicates to create large internal surfaces and cavities that enhance catalytic activity and adsorptive capacity [39, 45-47].

Figure 2.4 depicts the synthesis mechanism of the pillared clay. It is evident that the fundamental principle of pillared clay is based on the ion exchange of cationic hydroxy transition complexes with alkali metallic ion, and the pores are formed by intercalation of layered aluminosilicates, thus changing the types of the cationic complexes, the pore size is controllable. However, not only are the pores in these materials generally irregularly spaced and broadly distributed, but also the final products retains, in part, the layered nature of the precursor material [39]. Despite these efforts, mesostructured molecular sieves with regular, ordered channel systems have remained ambiguous, and the significance of "template" was not fully explored [2], thus the technique is not widely used in the synthesis of nanoporous materials.

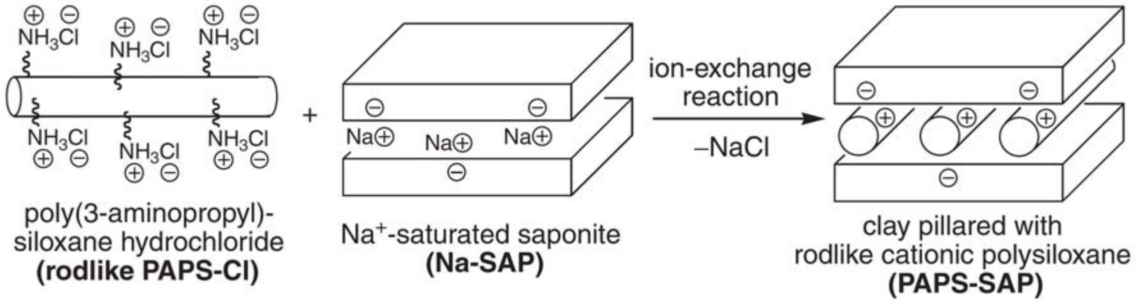

Figure 2.4 Schematic drawing of pillared clay mechanism [46].

Considerable success was achieved in 1990s in the work of Mobil scientists [22] and Japanese scientists [48], through the discovery of mesostructured silicates, which incorporates surfactant molecules in the sol-gel process. The cationic surfactant molecule is comprised of hydrophobic and hydrophilic functional groups and cooperatively assembled as micelle in the inorganic precursor species solvent [24]. After hydrolysis and condensation, the polymeric structure is densified around the surfactant assembles, which is vaporized at high temperature, creating well-defined and regular open pore network. A liquid crystal templating mechanism (LCT) has been proposed for the formation of these materials, in which surfactant liquid crystal structures serve as organic templates [2, 22]. More importantly, the concept of molecular imprinting was first postulated and explored in the synthesis of mesoporous silicate materials [49-51]. The key advantage of this method over the pillared clays process is that pores are directly designed, with high hydrothermal stability and regularity, and the pore dimension can be tailored through the choice of templates [2, 39].

2.1.4 Membrane synthesis by dip-coating

A sol-gel silica membrane can be described as a membrane formed from a silica sol-gel solution, and this is generally achieved through the deposition of a sol-gel onto a porous substrate through a dip-coating process. In gas separation area, the microporous membrane thickness should be as small as possible in order to get high permeability and selectivity of gases for industrial application [3, 31, 32, 52]. The preparation of mesoporous silica thin film by surfactant self-assembly took its origin from the pioneer work by Ozin's and Brinker's group [53-55]. Figure 2.5 depicts the scheme of mesostructured thin film deposition in dip-coating process by evaporation induced self-assembly (EISA) and its various successive steps. It is evident that EISA can thus be described by competitive processes related to the kinetics of condensation versus the kinetics of organization.

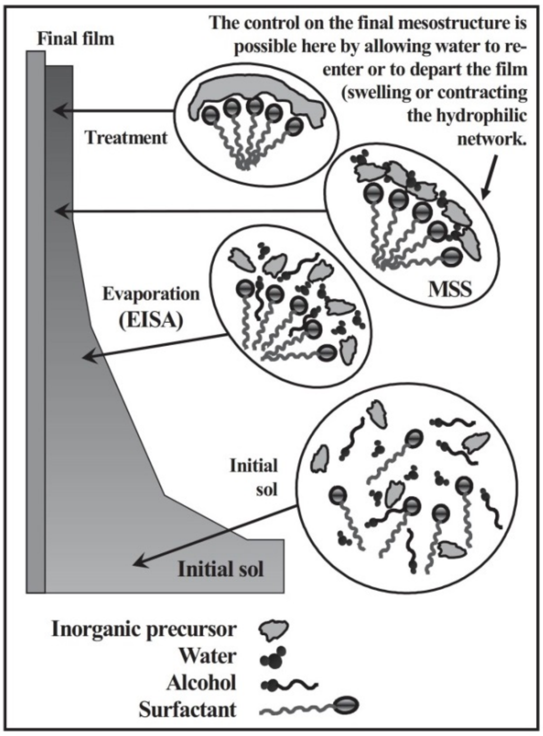

Figure 2.5 Mesostructured thin-film formation by dip-coating [25].

A typical structure of silica membrane coated on the asymmetric alumina support is depicted in Figure 2.6 [56]. It evident that a complete supported silica membrane system is comprised by a thin selective top layer with narrow pores, in which the separation occurs, and a relative thick macroporous support to provide main mechanical stability and robustness required for effective operation. A thick porous α-alumina substrate coated with a thin γ-alumina interlayer is usually selected as the asymmetric support [21, 56, 57]. The α-alumina substrate is made of unconsolidated micron sized crystal particles, to obtain a macroporous structure with good mechanical resistance and low flow resistance, and the γ-alumina crystal particles in the interlayer are much smaller and deposited on the surface of the α-alumina substrate to create a smooth, defect-free surface over which the active silica layer is coated. An intermediate layer may greatly lower the roughness of a surface by means of the preferential deposition of more material into the greatest defects.

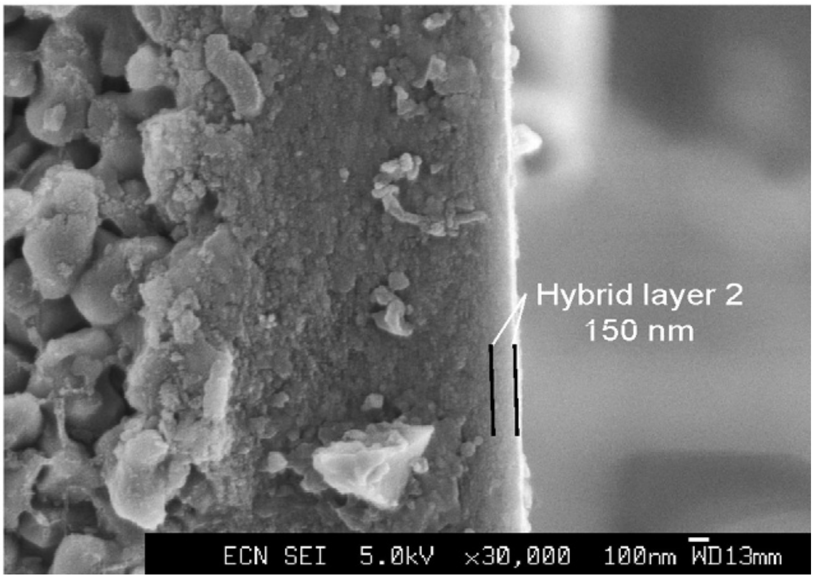

Figure 2.6 A typical structure of membrane synthesized by dip-coating [56].

When mass transfer takes place through a supported silica membrane system, the penetrant molecule must migrate through not only the membrane layer itself but also all of the other layers surrounding the membrane, such as the boundary layers, which produces additional resistances to the mass transport process. For porous membrane, the transport process through the membrane itself depends on the fluid-solid and fluid-fluid interaction, and the corresponding flow mechanism and theories that may occurs in the pores of the supported silica membrane is largely determined by pores size and fluid species [58]. To understand the transport mechanism in the supported membrane, the pore network of each layer must be explicitly provided, including the pore size distribution, shape, structure and porosity and tortuosity coefficient [59], thus a variety of different of diffusion models such as the classic Knudsen and viscous model, surface diffusion and activated diffusion as well as the recent-developed Oscillator model, will be extensively addressed in the next section.

2.2 Theories of fluid transport in narrow pores

The transport of fluids in narrow pores has long been of interest to engineers and scientists due to its importance in several well-established industrial applications such as catalytic and noncatalytic fluid-solid reactions as well as in adsorptive separations and electrochemical processes, and the optimization of their performance heavily relies on a deeper understanding of how the fluid flow is affected by the topology of the pore space. Recent advances in templating methods and techniques of nanomaterials synthesis have led to a rapid growth of a vast array of novel nanoporous materials such as carbon nanotubes (CNT) [60], MCM-41 silicas [22] and metalorganic frameworks (MOF) [61], which have catalyzed the emergence of new applications such as gas storage, lithium battery, and supercapacitor as well as drug delivery.

On the other hand, complement to these inventions in the nanopores materials synthesis [62], the interest of molecular diffusion in these porous solids has been significantly enhanced since the movement of fluids into the narrow pore spaces of such materials is common to all above applications. In addition to the diffusion, the understanding of structural characterization and adsorption equilibrium is also crucial to the modeling and process design of such applications as the adsorption effect is significant even in the mesopores at room temperature [1, 63, 64]. Based on the principles of nonequilibrium thermodynamics [65], the diffusional properties of the single components and the binary/ternary mixtures related to the application of silicas are generalized in the following.

2.2.1 Pure component transport

In this subsection, we review some of the most influential theories of mass transfer in small pores and confined spaces, which is the foremost information that you must have to gain an understanding of the transport mechanism in a porous system. Considering a simpler medium, a straight and structureless cylindrical capillary, several types of flow can be more readily identified, which can be used as basis to represent the transport for the pore structure of a real solid through mathematical idealisation. Starting from the classic viscous flow, century old Knudsen diffusion, activation diffusion and the recent-developed Oscillator model which share a common point of departure in the Maxwell–Stefan diffusion equations are addressed. In particular, the conceptual basis of the models and the validity of the assumptions and simplifications necessary to obtain their final expression are displayed to cover a wide pore size range and operation conditions.

2.2.1.1 The viscous model

When the flow of gas is stimulated by a driving force of total pressure gradient due to the Newtonian viscosity, the flow is called the viscous or laminar flow. As given in Figure 2.7, in the flow a continuum regime and molecular chaos prevail and the equation of continuity holds, so all species move at the same speed and pass through the tube without any separation. In addition, since the flow inside the pore is assumed laminar and no slip at the surface of the wall, the velocity profile is parabolic in shape [47].

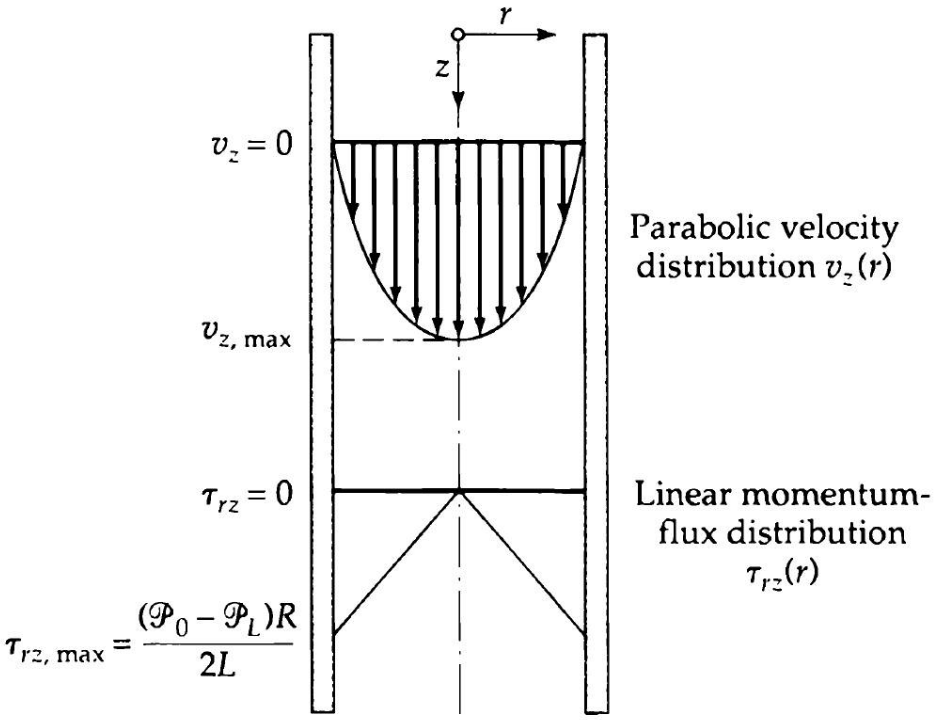

Figure 2.7 The momentum-flux distribution and velocity profile in the axial direction for a downward flow in a circular tube [62].

In such a flow, a majority of the gas molecules undergo intermolecular collisions rather than wall collisions, thus the flux equation in a narrow pore with radius, r_p, can be derived based on the Newton's law of viscosity as:

$$j_v = \frac{(P_i + P_o) r_p^2}{16 \eta R_g T} \nabla P \tag{2.5}$$

where j_v is flux; P_i is feed pressure; P_o is outlet pressure; η is the dynamic viscosity; R_g is the gas constant coefficient; T is Kelvin temperature; ∇P is pressure gradient. Eqn. (2.5) is the well-known

Hagen-Poiseuille equation, which is independently discovered by Hagen and Poiseuille in 1839 and 1840, respectively, by investigating the linear flow in pipe [47]. This mode of viscous flow is only validated for low Reynolds number (less than 2100) when the mean free path, λ, as estimated by eqn. (2.6), is much smaller to the pore diameter (high Knudsen number region, Kn = λ/d >>1).

$$\lambda = \frac{k_B T}{\sqrt{2}\pi\sigma_{ff}^2 P} \tag{2.6}$$

where k_B is Boltzmann constant; σ_{ff} is the collision diameter of gas molecules.

2.2.1.2 The Knudsen model

In small pore size, as the pressure reduces, the viscous continuum mechanism will break down, the mean free path, λ, of a molecule increases, hence the collisions of molecule-wall becomes more and more significant as the gas diffusing through the pore. A low density gas condition will set in when the fluid-wall collision become dominated over the intermolecular collisions, and the flow is termed as Knudsen flow due to the proposition by Knudsen by conducting the experiments with relative large glass tubes of 33-145 μm under vacuum conditions [1, 66, 67]. Knudsen's initial analysis was proposed based on the argument of momentum conservation, and it was later improved by Smoluchowski [58] through a detailed argument of molecular trajectories to provide the now classic equation for diffusivity

$$D_{Kn} = 97 r_p \sqrt{\frac{T}{M}} \tag{2.7}$$

where, D_{Kn} is Knudsen diffusivity in m^2/s and M is molecular molar mass in g/mol. Based on the phenomenological model, the Knudsen diffusivity permits the estimation of flux for the fluid molecule diffusing in a pore of r_p (m) under the bulk pressure gradient, ∇P.

$$j_{Kn} = -\frac{D_{Kn}}{R_g T}\nabla P \tag{2.8}$$

Figure 2.8 depicts the schematic drawing of molecular trajectory and potential field profile in pore for the Knudsen diffusion. It is evident that the gas molecules are assumed to be "hard spheres" which travels axially in the chemical potential field, and there is no solid-fluid interaction until collision, thus the adsorption effect of gases exerted by the wall is neglected and the radial density gradient of a pore cross section is uniform and constant [68, 69]. In the model, the hard sphere particle was reflected diffusely during the collision and lost all memory of their original tangential momentum [58].

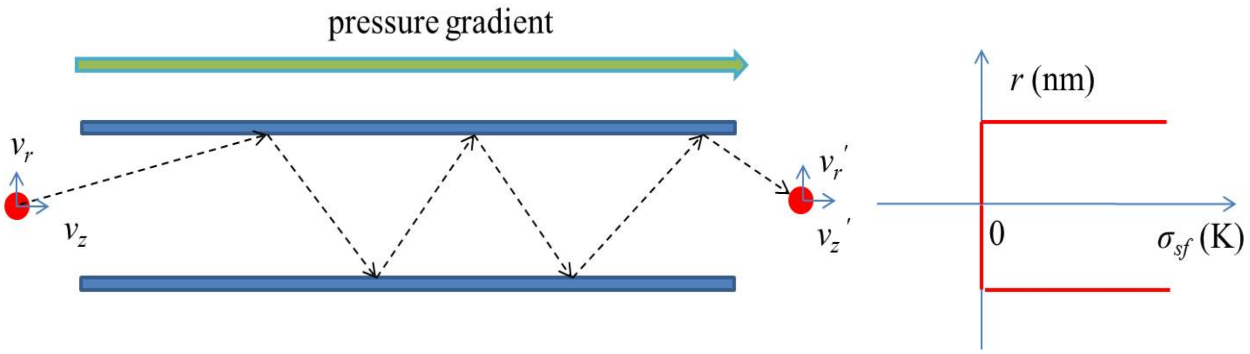

Figure 2.8 Schematic drawing of Knudsen diffusion mechanism.

As shown in eqn. (2.7), it is evident that the Knudsen diffusivity depends on the molecular weight of the diffusant and molecules with smaller weight travel faster than the heavier ones under the same operating conditions. Thus, separation of mixtures is possible with this mechanism, and the selectivity factor coefficient of the two gases, S_{AB}, can be estimated by

$$S_{AB} = \sqrt{\frac{M_B}{M_A}} \tag{2.9}$$

It is important to note that the linear correlation of diffusivity with $\sqrt{T/M}$ and the selectivity coefficient between two gases, as established by the Knudsen model, are often used as a criterion to validate assumptions regarding transport mechanisms in nanoporous materials [6, 70]. Further, if the size exclusion effect of fluid molecules is included since the molecules cannot completely reach the pore wall because of repulsive forces, the Knudsen diffusivity is corrected as

$$D'_{Kn} = 97(r_p - 0.5\sigma_{ff})\sqrt{\frac{T}{M}} \tag{2.10}$$

where σ_{ff} is the Lennard-Jones (LJ) fluid-fluid collision diameter in metre.

The Knudsen model normally occurs at very low pressure and channels of small sizes in the range between 10 nm and 100 nm [71], while the viscous flow is more dominant in large pores at high pressures. At intermediate pressures and pore size, the mean free path is comparable to pore size, and both viscous and Knudsen flow are important, thus the two fundamentals of diffusion mechanisms are expected to control the transport. In such a case, a combined flow is proposed as slip flow to predict the pore flux ($j = j_v + j_{Kn}$).

Diffuse reflection for molecule-wall collisions is a key assumption in the development of the Knudsen model. Such an assumption has shown to be reasonable for the oxide surfaces, such as zeolites and silicates [58], at which gas-solid interactions are governed by the surface oxygen atoms. However, the diffusion of fluids through CNTs has been shown to be significantly higher than the Knudsen diffusivity. This is due to molecular specular reflections in wall collisions as the carbon surfaces are extraordinary ordered and smooth, leading to a very low momentum accommodation (fraction of tangential momentum lost to the wall) and rapid mass transfer. Therefore, the diffuse reflection held by the Knudsen model is no longer applicable for the transport of gases in ordered and smooth surface.

Another important assumption used in the development of the Knudsen model is the disregard of the dispersive solid-fluid interaction arising from the presence of walls between two concessive reflections, so fluid density in the pore is uniform and identical to the bulk gas. This assumption has shown to be reasonable when the molecular/channel is very small, and good agreement with experiments has been observed in relatively wide cylinders of a few micrometers diameter [58]. Nevertheless, for mesopores (in the size range of 2 to 50 nm) below a certain temperature which increases with decrease in pore size, the molecules will not have enough velocity to escape from the wall attraction field in the vicinity of the pore wall, thus adsorption is expected and the pore density begins to vary with radial position and differs from the bulk, especially for gases with a strong affinity to the solid, at low temperatures and under stringent confinement. Further, gas-solid interaction can alters not only pore density, but also increase the collision frequency by reducing the mean time of the trajectory, so the pore diffusivity is significantly overestimated by the Knudsen-based model [72]. The failure of the Knudsen model in the presence of fluid-solid interaction has been shown in extensive available experimental and theoretical results [42, 73-77] .

2.2.1.3 Surface diffusion model

When the pore size is comparable to the fluid molecular dimensions but still larger than the effective range of the external potential field of the solid wall, the interaction between the gas molecules and the pore walls cannot be neglected because of large internal area. In such as case, the Knudsen model fails and gas mobility through the narrow pore channels, such as zeolites or bulk solid oxides, require adsorption of molecules on the pore surface first before the subsequent diffusion process, and this phenomenon, referred as ‘surface diffusion’, is frequently used to represent the gas permeation through the microporous materials. Although the transport mechanism of surface diffusion is the very complicated process, and extensive research has been devoted to better understand this type of diffusion [78].

Figure 2.9 depicts the schematic drawing of molecular hopping mechanism to describe the surface transport. It is evident that the pore surface is comprised of specific adsorption sites, at which adsorbed molecules are anchored. Assuming the energy intensity of these sites to be higher than the thermal energy of a molecule ($k_B T$, where k_B is the Boltzmann constant), molecules at each site must gain enough energy to jump from one site to the next vacancy [47].

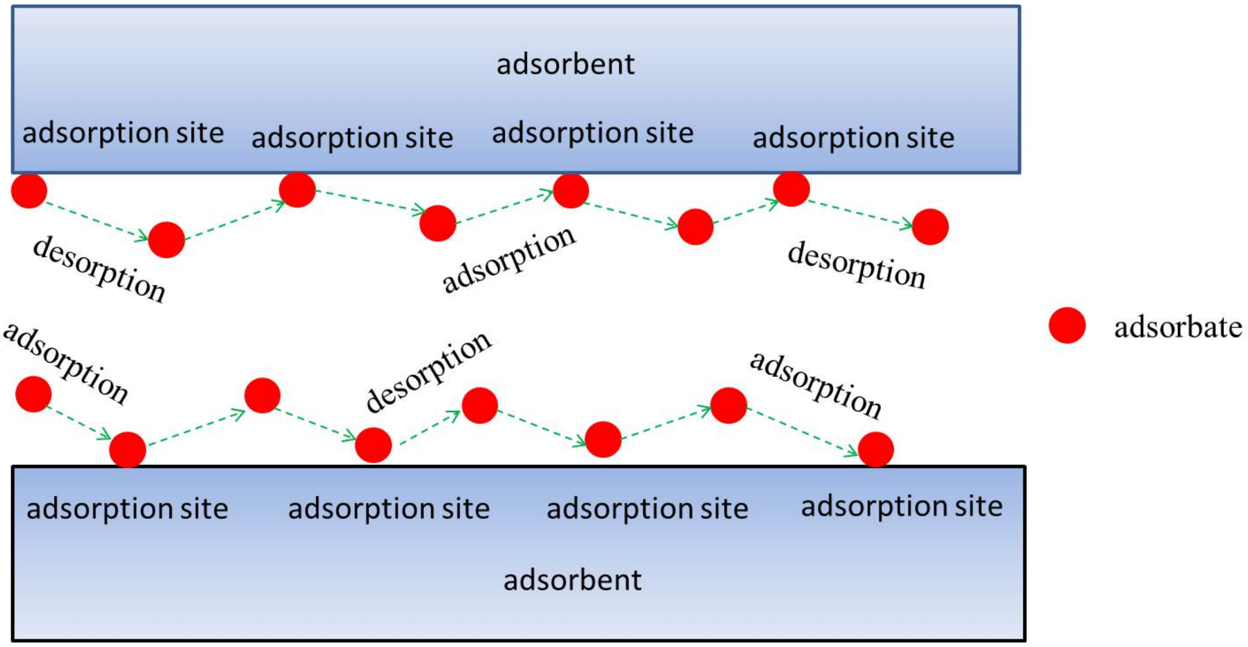

Figure 2.9 Schematic drawing of surface diffusion mechanism.

Based on Fick law and local equilibrium theory, the adsorbed gas molecules on the pore surface can migrate through the pores driven by the surface concentration gradients, and the surface diffusion flux, j_s, is estimated as [79-81] .

$$j_s = -D_s \frac{dC_s}{dz} \tag{2.11}$$

Here D_s is the surface diffusivity C_s (mol/m^3) represents the surface concentrations under a certain pressure.

In contrast to the Knudsen diffusion, the surface diffusivity of adsorbed molecules varies with the loading and normally increases sharply with loading, thus the contribution of surface diffusion increases with increase in molecular size (σ_{ff}) and weight (M) since these molecules are the most easily condensed and adsorbed species, having higher loading density [47]. Based upon the statistical mechanical theory, the surface concentration can be treated as functions of the temperature and pressure in gas bulk phase [82], and the diffusivity can be estimated from the surface coverage of the adsorption isotherm. The surface diffusion model is frequently used to combine with bulk flow in parallel to interpret the observed permeation data (c.f. Figure 2.10), with dispersive adsorption and inhomogeneity of adsorbate density [58] empirically considered in the surface diffusivity.

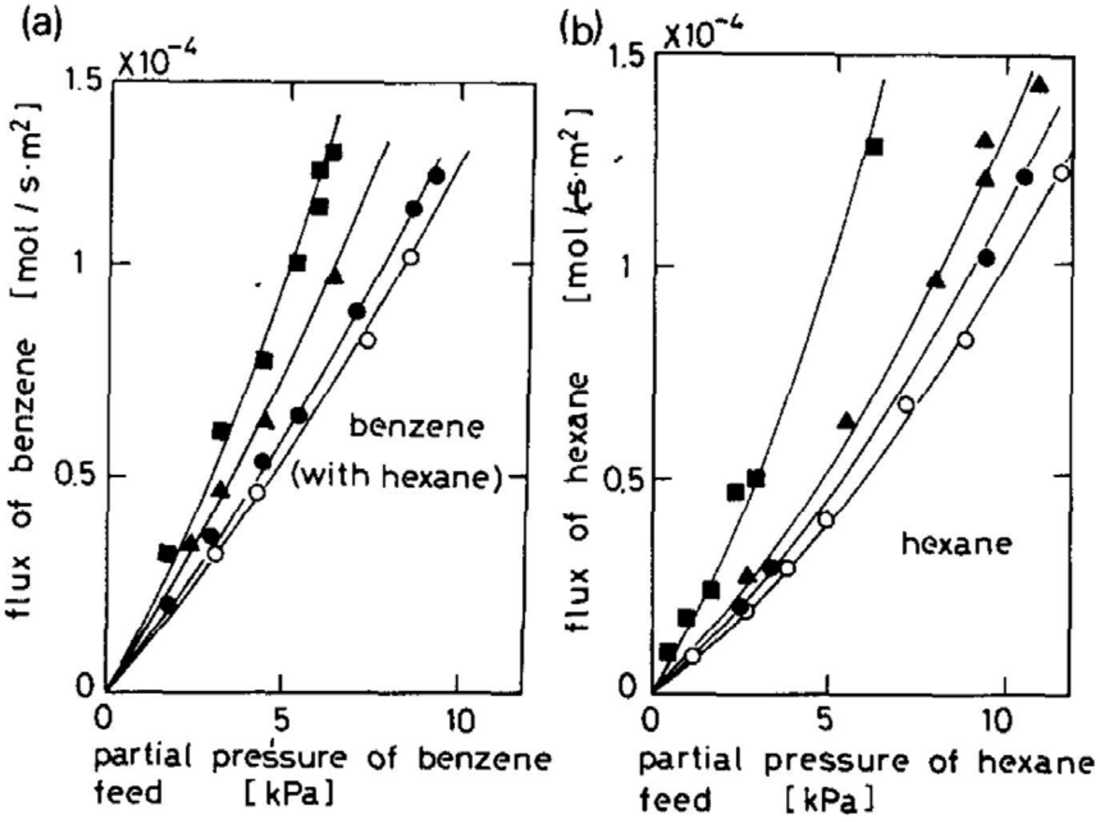

Figure 2.10 Permeation flux of benzene (a) and hexane (b) on porous glass membrane with a mean pore diameter of 4 nm by experiments (symbols) and surface diffusion model (solid lines) [81].

2.2.1.4 Activated diffusion model

When the pore size further decreases and approaches molecular dimension, the potential intensity is so amplified and the adsorbates are strongly constrained by the surroundings. In such a case, the ordinary methods of determining surface diffusion encounter a difficulty as the gas molecules need to acquire sufficient energy to overcome large potential barriers before passing through the narrow and long passages. This phenomenon, termed as activated diffusion', is widely employed to represent the gas permeation through ultramicroporous silica-based materials [3].

Figure 2.11 depicts the schematic drawing of molecular hopping mechanism to describe the surface transport. It is evident that the hopping rate of a penetrant depends greatly upon the concentration of 'gates' that are large enough to accommodate the penetrant molecule. This concept of acquiring a "sufficient amount of energy" is justified by by incorporating an Arrhenius form activation energy that has been observed experimentally [3, 27, 63], and given as

$$D = D_o\left(\frac{-E_m}{R_g T}\right) \tag{2.12}$$

where D_o is a temperature independent proportionality constant, E_m is the mobility energy for (J mol^{-1}). The activated flux is treated much same as the surface diffusion based on Fick law as given in eqn. (2.11).

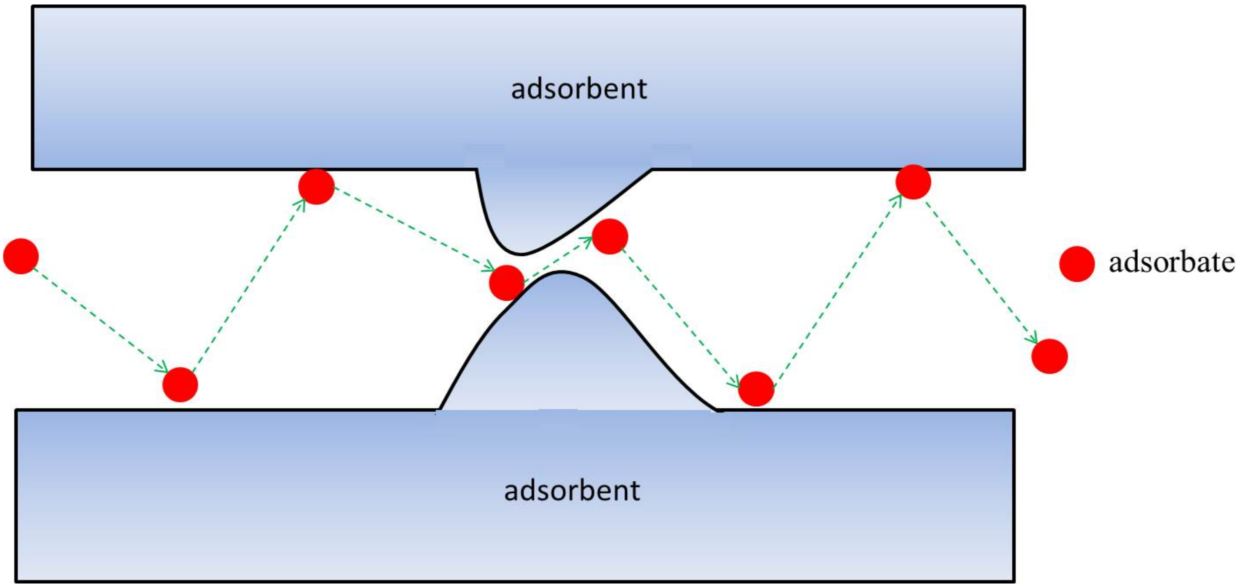

Figure 2.11 Schematic drawing of activated diffusion mechanism.

Assuming the adsorption occurs in the Henry law region, the surface molar concentration, C, is evaluated as

$$C = KP \tag{2.13}$$

where P is the pressure (Pa) and K is the Henry's coefficient, which can be estimated from a van't Hoff equation:

$$K = K_o e^{\frac{Q_{st}}{RT}} \tag{2.14}$$

where Q_{st} is the isosteric of adsorption heat, (J mol^{-1}).

Substituting eqs. (2.12)–(2.14) into eqn. (2.11), a temperature dependency flux in the Henry regime, is obtained

$$j = -D_o K_o e^{E_a / R_g T} \frac{dP}{dz} \tag{2.15}$$

where E_a ($E_a = Q_{st} - E_m$) is the apparent activation energy which is required to passing through the pore barrier.

The activated diffusion is treated much same as the surface diffusion, based on the assertion that the pore spaces are so narrow and the distinction between the gas phase and the adsorbed phase disappear under the overlap of interaction potentials from the pore walls. This will create a much stronger potential to trap the gas molecules, however, an activation energy barrier may need to be overcome to travel through the pore passage or the pore entry. Thus, the interaction potential field is included in the activation energy and adsorption coefficient. Although the activated model could fit the permeation data and predict temperature dependence of flux [34, 83-85], the diffusion models discussed so far, lack the ability to accurately predict the activated process in terms of size, shape, and chemical nature of the penetrant, empirical correlation is still necessary to obtain the activation energy (E_a) and diffusivity constant ($D_o K_o$) .

2.2.1.5 Transition-state theory

In microporous silicas and zeolites, the pore network is often fabricated in a regular pattern of narrow cages and channels, and the gas molecules are tightly confined by the effects of the walls throughout the whole host region through which the guest travels, so molecular walls interaction must be adequately modeled. In such cases, guests often imply activated diffusion that enables passage through an aperture of the same size as the kinetic diameter of the guest [86].

Figure 2.12 describes the schematic drawing of molecular hopping trajectory and its potential energy changes. As shown in the diagram, a hypersurface assumed in phase space has two properties: (1) it divides space into a reactant region (S_i) and a product region (S_j), and (2) similar to reversible reaction, the trajectory migrating through this "dividing surface (DS)" in the products direction originated at reactants and will not recross the surface until being thermalized and attained in a product state [87]. In transition-state theory (TST), the dividing surface is conventionally placed at the saddle point of potential fields and diffusivity coefficient can be estimated by equating the net rate coefficient to the one way flux.

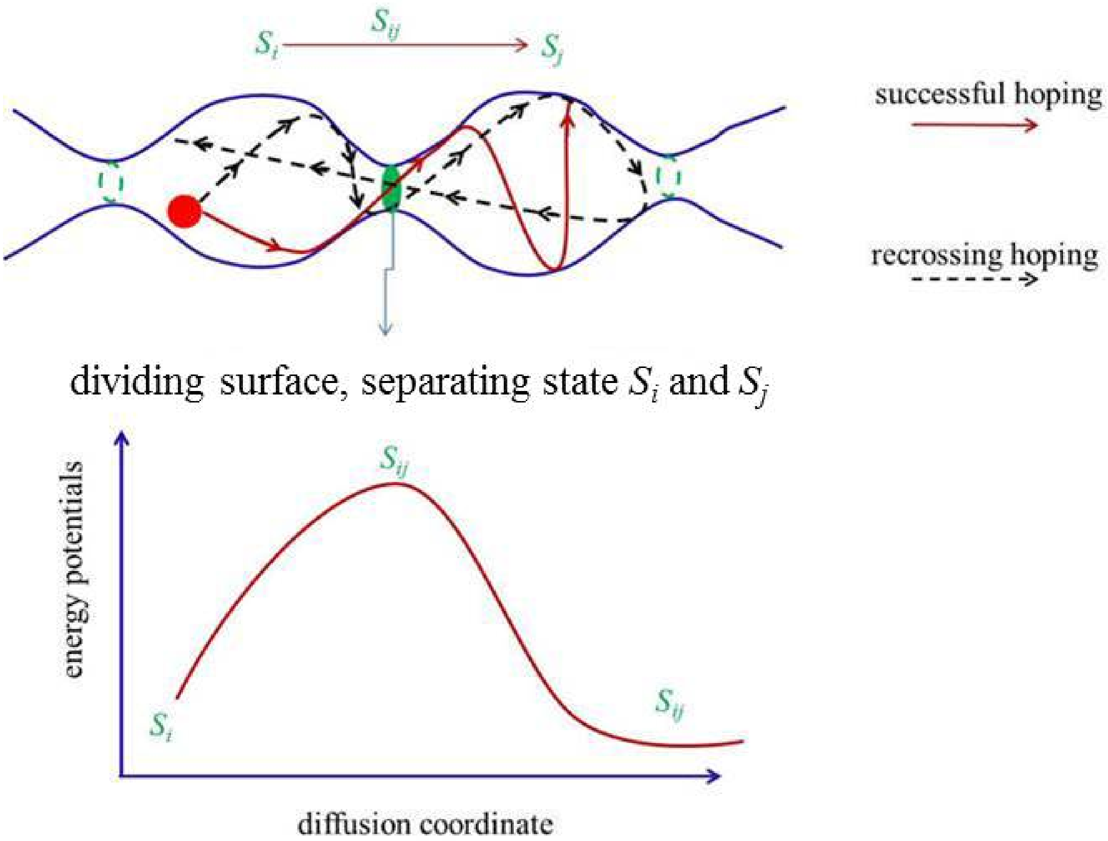

Figure 2.12 Schematic drawing of transition state theory mechanism for a system with three-dimensional configuration space, and an assumed potential energy changes during one successful trajectory from state S_i to state S_j through the bottle neck.

In a successfully migration, the hopping time, τ, from a pore body i to a neighboring pore body j is generally given as [72]

$$\tau_{A\to B} = \frac{1}{k_{A\to B}} \tag{2.16}$$

Here the crossing frequency $k_{A\to B}$ constant is essentially a ratio of two configurational integrals and are readily estimated by potential filed integration over the dividing surface and cage volume once the states and dividing surface have been determined, which follows [88]

$$k_{A\to B} = \sqrt{\frac{k_B T}{2\pi m}} \frac{\int_{DS} e^{-\beta\varphi(\mathbf{r})} d^2\mathbf{r}}{\int_{\substack{state\ i\\ volume}} e^{-\beta\varphi(\mathbf{r})} d^3\mathbf{r}} \tag{2.17}$$

Here m is the molecular mass and $\varphi(\mathbf{r})$ is the potential energy of the guest molecule. It is evident that not all trajectories that migrates the dividing surface in the direction from i to accomplish ultimate thermalized state of the system in the destination state j. For instance, like reversible reaction, recrossing may occurs as given in Figure 2.13, wherein the guest gas 'jump; back through the dividing surface and thermalizes in the origin state. Thus a dynamical correction factor, or transmission coefficient, κ, is defined as [88]

$$\kappa = \frac{sucessful\ trajectories\ through\ DS}{attempted\ trajectories\ through\ DS} \tag{2.18}$$

The value of κ, varies with guest and is general obtained from the average over a large number of MD trajectories initialized at the transition state, using the truncated implementation. The detailed procedure to determine at an arbitrary loading is described in the literature [89-91], which have shown a strong variation of gases and pore system. However, the transmission probability is generally close to unity for light gases [88, 92, 93].

Finally, the diffusivity in transition state theory is readily obtained [91]:

$$D_{TST} = \kappa k_{A \to B} \zeta^2 / 6 \tag{2.19}$$

where ζ is the centre-to-centre distance between neighbouring pores (i and j).

Following the arguments of Nguyen and Bhatia [88, 92] and Nguyen et al. [94], eqn. (2.19) can be approximated to be an Arrhenius form.

$$D_{TST} = A_o \sqrt{\frac{T}{M}} e^{-E_a/RT} \tag{2.20}$$

Here E_a is the activation energy, given by the enthalpy barrier and is affected by the interaction between the fluid and pore walls. A_o is a constant related to the pore length, fluid molecular size and pore shape.

2.2.1.6 The Oscillator model

As discussed above, fluid particles in the century-old Knudsen formulation are treated as 'hard sphere', and the dispersive fluid-solid interaction is neglected between the diffuse collisions, so the Knudsen model can be applied to predict the transport coefficients in sufficiently large pores where the adsorption effects are negligible. However, as pores reduce in size, the fluid-solid interaction becomes more and more important where the adsorption effect in the pore is substantially important. In such a case, the Knudsen diffusivity fails, and the statistical mechanical 'Oscillator model', developed in this laboratory provides an analytical result for the diffusivity in low-density limit for a LJ fluid oscillates between diffuse reflections with pore walls under the interaction of a conservative one-dimensional potential field exerted by the wall [95-97].

In the Oscillator model, fluid particles are treated as ‘soft spheres’, and the dispersive fluid-solid interaction is explicitly considered between the concessive collisions. The Oscillator model can be used to predict the adsorption effect and transport diffusivity for a wide pore size, ranging from micropores to macropores, without requiring any empirical activation energy amendments and any assumptions concerning about the fluid-solid interaction intensity. This represents a significant advantage over the earlier Knudsen model and other approaches, and the pore fluid is treated as a whole, without any flow segregation between bulk and surface contributions, avoiding the empiricism associated with this partitioning [58].

In the Oscillator model, the diffusivity of a LJ particle under conditions of diffuse reflection in a cylindrical pore, D_{osc}, is estimated as [95]

$$D_o = \frac{k_B T}{2m} < \tau > \tag{2.21}$$

τ is the reflecting time between two concessive wall collisions, which is estimated by

$$\tau(r, p_r, p_\theta) = 2m \int_{r_{cl}(r,p_r,p_\theta)}^{r_{co}(r,p_r,p_\theta)} \frac{dr'}{p_r(r', r, p_r, p_\theta)} \tag{2.22}$$

where p_r and p_θ are the radial and angular components of the molecular momentum, and r_{cl} and r_{co} represent the radial bounds of a fluid molecule trajectory between consecutive diffuse reflections (c.f. Figure 2.13), determined through the solution of $p_r(r',r,p_r,p_\theta)=0$. Here $p_r(r', r, p_r, p_\theta)$ is the radial momentum at position r' for a molecule having radial momentum p_r at position r. The hoping time, τ, is dependent on the motion energy in radial direction and the profile of radial momentum $p_r(r', r, p_r, p_\theta)$ can be obtained by solving the motion equations of a particle in the force field produced by the wall as

$$p_r(r?\, r,\, p_r,\, p_\theta) = \left(2m\left[\varphi(r) - \varphi(r')\right] + \frac{p_\theta^2}{r^2}\left[1 - \left(\frac{r}{r'}\right)^2\right] + p_r^2(r) \right)^{1/2} \tag{2.23}$$

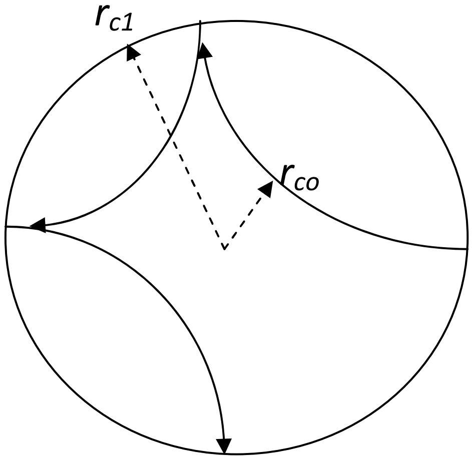

Figure 2.13 Schematic of trajectories of an oscillating molecule projected onto the pore cross section [97].

Assuming a canonical distribution of energies, the average hoping time, $< \tau >$ can be obtained and the final formulation of D_{osc}, is given by [98]

$$D_o = \frac{2}{m\pi Q}\int_0^{\infty} e^{-\beta\varphi(r)}dr\int_0^{\infty} e^{-\frac{\beta p_r^2}{2m}}dp_r\int_0^{\infty} e^{-\frac{\beta p_\theta^2}{2mr^2}}dp_\theta\int_{r_-}^{r_+}\frac{dr'}{p_r(r',r,p_r,r_\theta)} \tag{2.24}$$

where $\varphi(r)$ is the solid-fluid potential, m is fluid particle mass, $\beta = 1/k_BT$ and $Q = \int_0^\infty re^{-\beta\varphi(r)}dr$.

In low density limit, the adsorption effect is represented by the equilibrium constant, K, and it is evaluated by

$$K = \frac{2}{r_p^2 T}\int_0^{r_p} e^{-\varphi(r)/k_BT}rdr \tag{2.25}$$

It is evident that the dispersive interaction has significant influence on the diffusivity and adsorption effect. The value of the fluid-wall interaction potential, $\varphi(r)$, strongly depends on the pore wall composition and structure. If the pore is composed of infinitely thick walls, the interaction potential profile, $\varphi(r)$, is given by [99]

$$\varphi(r) = \pi^2\varepsilon_{sf}\rho_v\sigma_{sf}^3\left\{\frac{7F_h(-4.5,-3.5,1;(r/r_{osc})^2)}{32(r_{osc}/\sigma_{sf})^9\left[1-(r/r_{osc})^2\right]^9} - \frac{F_h(-1.5,-0.5,1;(r/r_{osc})^2)}{(r_{osc}/\sigma_{sf})^3\left[1-(r/r_{osc})^2\right]^3}\right\} \tag{2.26}$$

Here σ_{sf} is the LJ solid-fluid collision diameter, ε_{sf} is the LJ potential well depth, ρ_v is the atoms density in the wall (atoms per unit volume) and $F_h(x,y,z;w)$ is the Hypergeometric function.

If the pore is composed of a single layer wall, the interaction potential profile, $\varphi(r)$, is readily obtained by [100]

$$\varphi(r) = 4\pi^2\varepsilon_{sf}\rho_s\sigma_{sf}^2\left\{\frac{63F_h(-4.5,-4.5,1;(r/r_{osc})^2)}{128(r_{osc}/\sigma_{sf})^{10}\left[1-(r/r_{osc})^2\right]^{10}}-\frac{3F_h(-1.5,-1.5,1;(r/r_{osc})^2)}{4(r_{osc}/\sigma_{sf})^4\left[1-(r/r_{osc})^2\right]^4}\right\} \tag{2.27}$$

where ρ_s is the pore wall surface density (atoms per unit area).

Figure 2.14 depicts the diffusivity comparison of the Oscillator model with Knudsen model and molecular dynamic simulation (MD) for methane in cylindrical silica pores at 450K [95]. It is evident that the agreements between oscillator model with the MD results at all pore sizes, in both the micro and the mesopore region, and the Knudsen diffusivity represents an upper limit that can only be reached when $\varphi(r) = 0$.

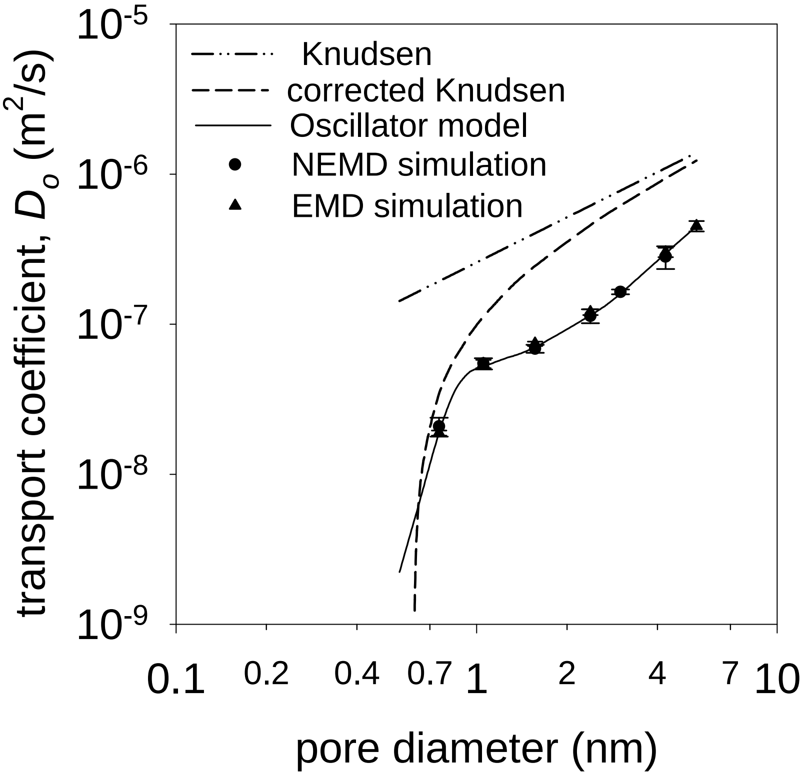

Figure 2.14 Variation with pore diameter of the low density transport coefficient calculated by MD and theoretical method for methane at 450K in cylindrical silica pores. Taken from Bhatia et al [95].

The Oscillator model has been extensively validated by the molecular simulation and experimental work. It has been shown that, in the high temperature and large pore size limit, Oscillator diffusivity converges to the Knudsen diffusion coefficient demonstrating the consistency of this approach.

2.2.2 Multicomponent transport

The above diffusion models are generally derived from the single component experiments or molecular ‘statistic mechanics’ without considering any momentum interspecies exchanges, so these models can be straightforwardly used to predict the transport phenomena for the gas mixtures when only gas-solid interactions are important in low density limits. However, adaptations of the single fluid theories are only useful for a limited type of systems. In narrow mesoporous and microporous materials at low temperature, the fluid density in the vicinity of pore wall significantly differs from the low pressure density in the bulk arising from strong fluid-solid interaction, leading strong interspecies friction force, thus the development of a more generally applicable tractable model for multicomponent is still necessary. In this subsection, several important empirical and rigorous diffusion theories of multicomponent that may be applied in the nanoporous materials are extensively discussed [101].

2.2.2.1 Dusty Gas Model

Based on the arbitrary combination of wall-mediated and fluid-fluid diffusion of gases in porous glass membranes, the dusty gas model (DGM) developed by Evans and co-workers has become the most popular strategy to model multicomponent transport in porous media [102-105]. The fundamentals of this model initially originates from the concept of the Lorentz gas for isobaric system where the membrane solid is treated as motionless dusts due to the extreme large molecular mass and uniformly distributed with other gas species [106]. Following this idea, ‘dust’ molecules are secured in space by assigning an external ‘clamping’ force to balance the dragging force exerted by the other fluids. It is evident that the membrane solid is automatically selected as the reference framework of the whole system in the binary gas diffusion [58].

The theory is later refined by unified framework for a combined the wall-mediated and bulk diffusion when a pressure gradient is applied in the membrane. By incorporating the ‘dust’ species in the Maxwell-Stefan diffusion equations, the relationship between the fluxes and transport driving forces are obtained. The general equation form of an ideal gas mixture of *n* species, without any external forces, is given as

$$\sum_{\substack{j=1\\ i\neq j}}^{n}\frac{x_j j_i - x_i j_j}{\rho_t Đ_{ij}^{e}}+\frac{j_i}{\rho_t D_{i0}^{e}}=-\frac{1}{P}\frac{dP_i}{dz}-\frac{x_i B_0}{\eta D_{i0}^{e}}\frac{dP}{dz}\qquad i=1,\dots,n \tag{2.28}$$

where P_i is the partial pressure of species, i, ρ_t is the total molar density, B_0 is a constant characteristic of the medium alone, $Đ_{ij}^e$ represent the effective binary pair diffusion coefficients in the porous medium which are inversely proportional to the pressure and independent of pore size, $Đ_{i0}^e$ is the effective diffusivity from the dragging force exerted by the porous medium. x_i and x_j are the molar fraction for i and j, respectively. The second term on the right-hand side is called the permeation flux and is applied to take into account the effect of total pressure gradient on mass transport (viscous permeation flux). The wall-affected diffusivity is often estimated based on the Knudsen model, which is supplemented by a surface diffusion contribution when adsorption occurs, without any contribution in regards of the hydrodynamic flow in the bulk [107].

It is evident that the DGM lacks of a firm molecular basis in its derivation, and its validity in multicomponent systems has been criticized by Kerhof and Geboers [101] and Bhatia et al [58] on the grounds that the internal reference frames for the wall-mediated and interspecies diffusion in its original development are inconsistent with each other, with one is located on the motionless pore wall and the other is chosen as the mass center, respectively. Not only does the model inherit the shortcomings from assumption of the Knudsen diffusion for wall mediated transport, but also from the inhomogenously dispersed “dusty gas molecules”. Thus the model can only empirically correlate the experimental flux when the assumption fails under conditions of practical importance [73], and its apparent success in application is largely due to the presence of structure-related fitting parameters such as tortuosity, which mask model errors [1].

In addition, use of a single representative pore size is another key deficiency of this approach, as the pore size distribution (PSD) has significant influence for nanoscale porous materials [1]. For instance, the recent study in our laboratory has demonstrated that the variation of tortuosity with operating conditions such as pressure, temperature and gas species, is expected for the disordered nanoporous materials in the presence of pore size distribution, and this conclusion is completely in contradiction to the assumption of DGM in the derivation, in which the tortuosity is exclusively determined by the pore network [73, 108-111].

2.2.2.2 Generalized Maxwell-Stefan Model

The Maxwell-Stefan Model (MSM) is a theory that is independently proposed by Maxwell and Stefan, and it is employed to describe the gas diffusion in multicomponent systems under steady state [112]. The basic concept of the model is that a difference between the molecular friction and thermodynamic interactions leads to the diffusion flux, and the molecular friction between two components is proportional to their speed difference and mole fractions. The Maxwell–Stefan equation is given as

$$-\nabla x_i = \sum_{\substack{j=1 \\ j \neq i}}^{n} \frac{x_j j_i - x_i j_j}{C_t Đ_{ij}} \tag{2.29}$$

where $Đ_{ij}$ is Maxwell-Stefan binary diffusivity, C_t is total molar concentration of fluid mixtures, and there is no *i* - *i* interaction diffusivity in the theory as the intermolecular interaction of the same species (*i-i*) won't cause any net changes to average momentum for the whole '*i*' species. In the derivation of MSM, $Đ_{ij}$ is defined as $Đ_{ij} = P/f_{ij}$, where f_{ij} is the drag coefficient for the drag that the molecule "*i*" feels as a result of interactions with the molecule of type "*j*.

The MSM can be simplified to be Fick law. However, the MS diffusivity has the physical significance of an inverse drag coefficient and is more easily interpretable and predictable than Fickian diffusivity (D_{ij}). For instance, $Đ_{ij}$ depends on the characteristics of species *i* and *j* (molecule shapes, etc.) as well as the system temperature and pressure, but largely independent on their relative compositions, and D_{ij} is complicated functions of composition. In addition, the Fickian diffusion coefficients (D_{ij}) may be negative and defined based on a molar-averaged velocity reference frame, while $Đ_{ij} \geq 0$ and is independent of reference frame; the binary diffusivity matrix is symmetric ($Đ_{ij} = Đ_{ji}$) but the Fickian diffusivity matrix is not symmetric ($D_{ij} \neq D_{ji}$). However, it is important to note that the GMS approach does not explicitly incorporate pore adsorption field, but implicitly considered through the MS pure component diffusivity, which may be obtained from experiment or MD simulation.

The 'traditional' Maxwell-Stefan formulation is later extended by Krishna and co-workers in a spirit of DGM to account for the adsorption effect in narrow nanoporous thin membrane by introducing a surface diffusion contribution when adsorption is prevalent [107], which is termed as Generalized Maxwell-Stefan (GMS) theory, and it has become the most-common used model to describe the multicomponent mass transport in a zeolite and molecular sieve membrane [35, 64, 69, 113]. According to the theory, the driving force at isotherm conditions is the chemical potentials ($\nabla_T \mu_i$), which is balanced by the friction due to the velocity of molecule (*j*) and the diffusivity ($Đ_{ij}$).

In their derivation, molecules are assumed to jump from one adsorption site to the other one driven by the adsorbate concentration gradient, and the adsorption site to which a molecule jumps may be vacant or inhabited by another adsorbate. When a molecule of *i* jump to a vacant site, a momentum exchange between the "vacant" site and the molecule is occurred and characterized by a surface diffusion coefficient, $Đ_i^s$. Further, when a molecule of *i* jumps to a site which is already inhabited by a molecule of *j* and replaces the latter, a net momentum change of *i* in this process is referred by a Maxwell-Stefan binary surface diffusion coefficient, $Đ^{s}_{ij}$. It is evident that no net change on the average momentum for species *i* will occur when the molecule is displaced by another molecule of *i* [58].

Based on above discussion, the MSM could be developed to investigate adsorbate-adsorbent system as an alternative way to describe surface diffusion by rewriting the chemical potential gradients in terms of mole fraction gradient by introducing thermodynamic factor Γ_{ij} and assuming the adsorbed site as (n+1)th component

$$-\frac{\theta_i}{R_g T}\nabla_T \mu_i = \sum_{\substack{j=1\\ j\neq i}}^{n} \frac{\theta_j j_i^s - \theta_i j_j^s}{\rho_p \varepsilon_p q_{sat} \;\; {}^{s}_{ij}} + \frac{j_i^s}{\rho_p \varepsilon_p \;\; {}_{sat} \;\; {}^{s}_{i}}; \qquad i, j = 1, \ldots, n \tag{2.30}$$

θ_i is the fractional coverage of *i* and given by

$$\theta_i = \frac{q_i}{q_{sat}} \tag{2.31}$$

where q_i is the adsorption amount of *i* in the adsorbent in mmol/g and q_{sat} is the saturation adsorption amount. ρ_p is particle density, ε_p is particle porosity. Analogous to Fick's law, the surface chemical potential gradient can be rewritten in terms of the gradient of fractional occupancy by introducing a matrix of thermodynamic factors (Γ_{ij})

$$\frac{\nabla_T \mu_i}{R_g T} = \sum_{j=1}^{n} \Gamma_{ij} \nabla \theta_j \qquad \Gamma_{ij} = \frac{\partial \ln f_i}{\partial \theta_j} \tag{2.32}$$

where f_i is the fugacity of *i* in the bulk fluid mixture. Introducing an n-dimensional square matrix $[B^s]$ having elements,

$$B^s_{ii} = \frac{1}{\text{行}^{s}_{i}} + \sum_{\substack{j=1\\ j\neq i}}^{n} \frac{\theta_j}{{}^{s}_{ij}}; \; B^s_{ij} = -\frac{\theta_i}{Đ_{ij}}; i, j = 1, 2, \ldots n \tag{2.33}$$

eqn. (2.30) can be recast into n-dimensional matrix notation, after some manipulation.

$$(\mathbf{J}^s) = -\rho_p \varepsilon_p [\mathbf{q}_{sat}][B^s]^{-1}[\Gamma]\nabla(\theta) \tag{2.34}$$

Where Γ_{ij} could be computed from the adsorption isotherm and *f* is the fugacity. For low pressure, Γ_{ij} is easily obtained from classical adsorption isotherms, e.g. Langmuir equation.

$$\theta_i = \frac{b_i P_i}{1+\sum_{j=1}^{n} b_j P_j} \qquad (2.35)$$

$$\Gamma_{ij} = \delta_{ij} + \frac{\theta_i}{1-\sum_{j=1}^{j=n}\theta_j} \qquad \delta_{ij} = \begin{cases} 1 & \text{if } i = j \\ 0 & \text{if } i \neq j \end{cases} \qquad (2.36)$$

The countersoprtion diffusivity ($Đ_{ij}^s$) can be empirically evaluated based only on information of pure component diffusivities ($Đ_i^s$) by Vignes equation [35].

$$Đ_{ij}^s = [Đ_i^s]^{\theta_i/(\theta_i+\theta_j)} \times [Đ_j^s]^{\theta_j/(\theta_i+\theta_j)} \qquad (2.\ 37)$$

The coefficient $Đ_i^s$ must in general be estimated experimentally or through molecular simulation. The GMS theory could be described as a surface diffusion due to equilibrium adsorption for the mass transport at high occupancies, which is supplemented by an activated gaseous process for mass transport at low occupancies.

2.2.2.3 The relevant site model

Because the GMS theory only caters for the correlation effects that causes slowing down of the more mobile species and does not cater for the additional hindrance effect due to the steric expelling, so it could not explain the concentration dependency of the diffusivity in the cage-like zeolite. The Relevant Sit Model (RSM) [114-117] is based on Maxwell-Stefan framework with one extra parameter that describes the adsorption properties of the relevant site to solve this issue. The model is formulated around the idea of segregated adsorption in cage-like zeolite, where the molecules are located either in the cage or its window site, and only the molecules located at the windows site are able to hop to another cage, therefore the surface MS diffusivity in the model depends on the concentration, which is observed in some work. In RSM, the concentration dependency of the MS diffusivity is given by [117]

$$Đ_i = Đ_i^*(0)(1-\theta_i) \qquad (2.38)$$

Where $Đ_i^*(0)$ is diffusivity constant, q_i is the loading of guest molecules in zeolite, q_i^* is the loading of molecules at the relevant site, θ_i is the total occupancy ($\theta_i = q_i / q_i^{stat}$, q_i^{stat} being the saturation loading).

By incorporating the MS diffusivity in the expression of flux in terms of relevant site properties ($j_i = -\rho \text{Đ}_i^* q_i^* \nabla \ln f_i$), the final model formulation is given as

$$j_i = -\rho \text{Đ}_i^*(0)(1-\theta_i) q_i^* \nabla \ln f_i \tag{2.39}$$

The relevant loading is evaluated by Langmuir type isotherm.

$$q_i^* = \frac{q_i^{stat*} K^*_i f}{1+K^*_i f} \tag{2.40}$$

where the q^{sat*} and K^* are the Langmuir constant of the relevant site and f is the fugacity corresponding to the total loading of q. The adsorption constant K^* is normally assumed a Van't Hoff dependency and related to the activation energy.

The above equations plus the adsorption isotherm are sufficient to describe the loading dependency of the MS diffusivity. The model could depict the simulation data very well for single components by optimizing the parameters empirically (c.f. Figure 2.15), and derive constant activation energy and extend to the binary mixtures compared to the Reed-Ehrlich approach [77]. Although all mentioned parameters have particular physical meaning, all of them can be only empirically obtained by regression, so some parameters are not predictive and could not be separated, such as the lump diffusivity, $q_i^{sat*} D_i^*$.

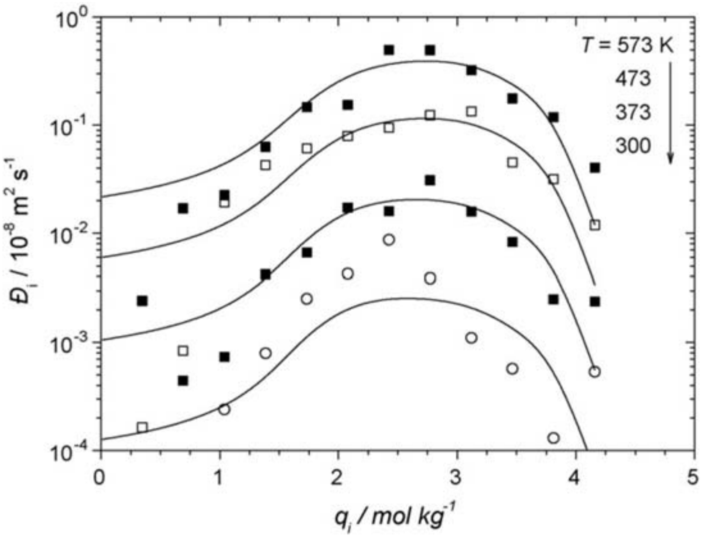

Figure 2.15 MS diffusivity of CH_4 in DDR at 300, 373, 473, 573 K calculated from MD simulation (symbols). Lines represent model results with the RSM except the data at 300 K, where the line represents a model prediction based on the parameters obtained from the data for 373, 473 and 573 K [116].

2.2.2.4 Friction based model

Since the Knudsen model and the DGM-based model have their own problems in describing the density inhomogeneity of narrow pores for mixtures, a friction based model is proposed to validate the finite density by directly considering fluid-wall potentials without arbitrarily flow segregations [74]. In the theory, the diffusion driving force of specie, *i*, is balanced by Newtonian internal shear stress tensor and dragging force of other species when fluid-fluid interaction is of importance such as in the bulk of the pore, and a wall friction force is added when the molecules enter into the repulsive region of the fluid-solid interaction potential as gas density falls into low density limit. Figure 2.16 depicts the molecules under friction effect nearby the potential minimum region from the walls.

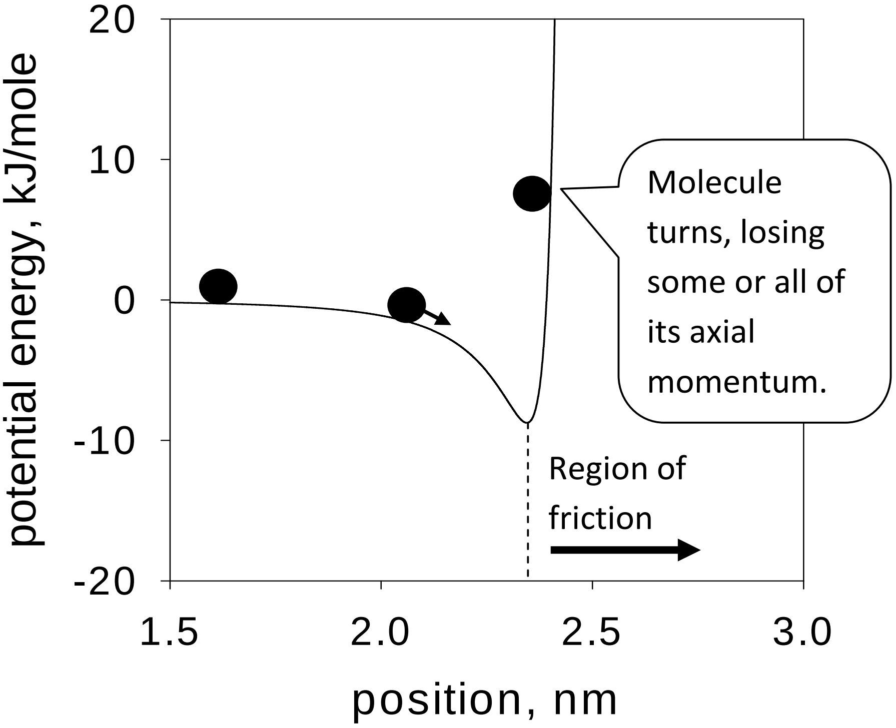

Figure 2.16 Illustration of potential energy profile and region of friction corresponding to the repulsive part of the potential energy curve [118].

For one-dimensional axial flow of a fluid mixture in a cylindrical pore of radius, *R*, the equation of motion for species, *i*, reads [74]

$$\frac{1}{r}\frac{d}{dr}(r\eta_i\frac{d\bar{v}_i}{dr})=\rho_i(r)\frac{d\mu_i}{dz}+\rho_t(r)k_BT\sum_{j=1}^{n}\frac{x_ix_j(\bar{v}_i-\bar{v}_j)}{Đ_{ij}}+\xi_i\rho_i(r)\bar{v}_ia(r-r_{oi}) \qquad i=1,2,...n \qquad (2.41)$$

in which the chemical potential, μ_i/dz, is the chemical potential in axial direction, ρ_i and ρ_t are the local molar density of specie *i* and total local molar density for all the species, respectively, $\bar{v}_i$ is the local mean axial velocity, $Đ_{ij}$ represents the MS mutual diffusivity, ξ_i is a uniformly distributed wall friction coefficient for species *i* and is independent of fluid density and position. Beside, $a(r - r_{oi})$ is the Heaviside function whose value is unity for $r > r_{oi}$ and zero otherwise. It is evident that the last term on the right hand side of eqn. (2.41) stands for the rate of momentum loss due to wall collisions in the vicinity of the wall, $r_{oi} < r < r_p$, where r_{oi} represents the position of the minimum of the fluid-solid potential for species *i*.

The velocity profile is derived by integration as:

$$\begin{aligned}\bar{v}_i(r) = \bar{v}_{io}(r) + \frac{d\mu_i}{dz}\int_0^r \frac{dr'}{r'\eta_i(r')}\int_0^{r'} r''\rho_i(r'')dr'' + k_B T\sum_{j=1}^{n}\int_0^r \frac{dr'}{r'\eta_i(r')}\int_0^{r'} \frac{r''(\bar{v}_i - \bar{v}_j)\rho_i(r'')\rho_j(r'')}{\rho_t(r'')Đ_{ij}(r'')}dr'' \\ + a(r - r_{oi})\xi_i\int_{r_{oi}}^{r}\frac{dr'}{r'\eta_i(r')}\int_{r_{oi}}^{r'} r''\rho_i(r'')\bar{v}_i(r'')dr'' \qquad i = 1,2,...n\end{aligned} \tag{2.42}$$

ξ_i is determined in the low density limit by the Oscillator model as

$$\xi_i = \frac{k_B T\int_0^R re^{-\frac{\phi(r)}{k_B T}}dr}{D_{oi}^{LD}\int_{r_{oi}}^{R} re^{-\frac{\phi(r)}{k_B T}}dr} \tag{2.43}$$

In addition, the density and viscosity profile must be provided. Aided by the finding from MD that the density inhomogeneity is essentially preserved during the transport [58], the density profile across the pore, $\rho_i(r)$, can be estimated by density functional theory, Monte Carlo simulation (MC), and locally averaged density model (LADM) with a suitable correlation theories, and the mixture viscosity in the pore can be predicted based on the approach developed by Galliero et al [119].

Upon expressing the velocity in terms of chemical potential gradients, eqs. (2.42) and (2.43) may be iteratively solved for the centerline velocities $\bar{v}_{io}(r)$ and the velocity profile $\bar{v}_{io}(r)$ which are respectively described as

$$\bar{v}_{io}(r) = -\sum\nolimits_{j=1}^{n} A_{ij}\frac{d\mu_i}{dz} \tag{2.44}$$

$$\bar{v}_i(r) = -\sum\nolimits_{j=1}^{n} X_{ij}\frac{d\mu_i}{dz} \tag{2.45}$$

Then the Onsager coefficient of irreversible thermodynamics [120-122] can be readily estimated as

$$\Omega_{ij} = \frac{2}{R^2}\int_0^R r\rho_i(r)X_{ij}dr \tag{2.46}$$

This permits evaluation of flux based on friction coefficients from intermolecular interaction parameters. The friction-based model of binary transport has been validated by the molecular simulation, showing significant success for the mesopores [74].

2.3 EMT theory

All of the above diffusion models are developed for a single cylindrical pore. However, as discussed in section 2.1, a critical issue of testing the validity of any transport theory in the recent-developed nanoporous materials is that the common mesoporous solids such as silicas and aluminas are highly disordered and possess a complex multi-scalar pore network [58]. This is clearly demonstrated in the typical supported silica membrane (c.f. Figure 2.6), which includes a macroporous α-alumina substrate, a mesoporous γ-alumina interlayer and amorphous silica layer. In the substrate and interlayer, the pores are synthesized by the cavities confined by the consolidated large crystal particles, thus not only must the pore size distribution and connectivity be considered, but also the pore aspect ratio and shape distribution assumes importance [108]. However, in most experimental studies [6], it is common to ignore the above complexities in nanoporous materials, and the corresponding diffusion models are arbitrarily applied to investigate the transport in the pores based on a mean pore radius by introducing pore network related parameters, such as porosity and tortuosity, which usually masks the failure of the diffusion model [76].

Effective medium theory (EMT) provides a necessary machinery to consider all these complexities of the pore network of each layer by replacing the nonuniform pore network with an effective one having pores of uniform conductance, and the diffusion model which is dependent on the pore size, can be directly used in the single pore level [123]. Bhatia et al [1, 111] has recently used this technique to predict the variation of apparent tortuosity with adsorbate, temperature and pore size distribution for silica microporous membranes, showing the tortuosity is not exclusively determined by solid morphology but is also affected by fluid species and operating conditions.

Figure 2.17 depicts the schematic drawing for the fundamental principle behind EMT. It is evident that the actual network of disordered pores with randomly distributed conductance is replaced by an ordered, uniform one providing the same overall resistance of flow as the original one. For two-phase medium, the equation is given as

$$\left\langle \frac{(\lambda-\lambda_e)}{(\lambda+(N/2-1)\lambda_e)} \right\rangle = 0 \tag{2.47}$$

where λ is the conductance and λ_e is the effective conductance; N is the coordination number or pore connectivity, i.e., the number of pores meeting at the intersection. It is noted that the effective conductance is derived based on the pore number distribution, which can be obtained from the experimental pore volume distribution, $f_v(r_p)$, by

$$f_N(r_p)=\frac{f_v(r_p)}{r_p^2\int_0^{\infty}\frac{f_v(r_p)}{r_p^2}dr_p} \tag{2.48}$$

For a pore of radius of r_p, the conductance, λ, is defined as the ratio of the molecular current to the chemical potential gradient, following:

$$\lambda=\frac{\pi r_p^2 D_o(r_p)K(r_p)}{l} \tag{2.49}$$

where $D_\mathrm{o}(r_\mathrm{p})K(r_\mathrm{p})$ is the apparent diffusivity, including both the diffusivity and equilibrium constant (K) based on the relevant diffusion models and pore size as provided above, and l is the pore length.

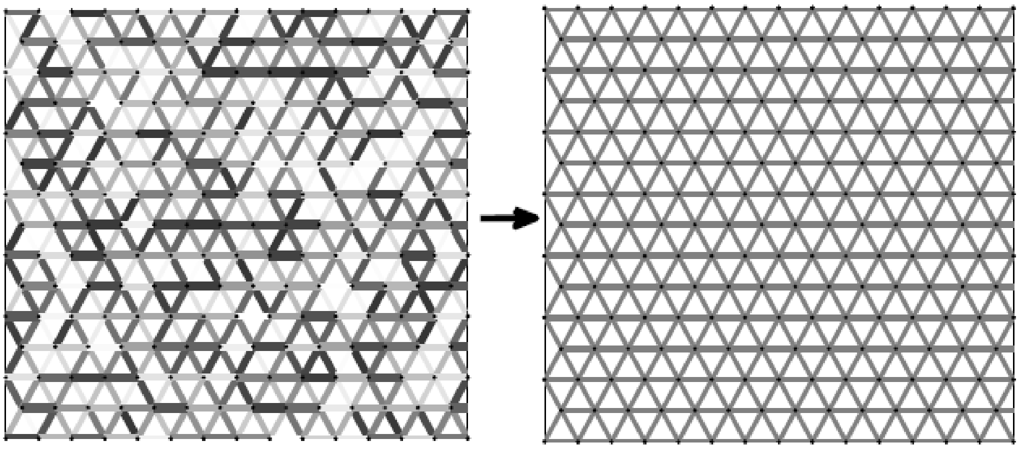

Figure 2.17 Illustration of the EMT approach. The network on the left represents the original system illustrated by the disordered of the width and the grey level of a bond. The right panel represents the EMT with a regular, non-disordered structure [124].

The flux in a pore of radius, r_p, is estimated by

$$j(r_p)=\frac{\lambda_e l}{\pi r_p^2 R_g T}\left(\frac{N-1}{N+1}\right)\overline{\cos^2(\theta)}\left(-\frac{dP}{dz}\right) \tag{2.50}$$

where z represents the coordinate along the macroscopic diffusion direction, $(N\text{-}1)/(N\text{+}1)$ is a correlation effect factor due to the finite possibility that a diffusant returns to a pore that it has just passed through, and $\overline{\cos^2(\theta)}$ stands for the local diffusion direction effect in a single pore level, which is not necessarily axial when the pore length is comparable to the pore diameter, and the aspect ratio effect (defined as $x=r_p/l$) must be taken into account [126-128]. By assuming the local transport direction to be that closest to the macroscopic flux direction, the expression for $\overline{\cos^2(\theta)}$ can be rewritten as [127, 128]

$$\overline{\cos^2(\theta)} = g(x) = 1 + \frac{4x}{3(1+4x^2)} - \frac{2}{3(1+4x^2)^{1/2}} \tag{2.51}$$

where $g(x)$ is the reciprocal coefficient of random orientation under the restriction

$$g(x)_{x=0} = 1/3 \tag{2.52}$$

where the local diffusion will become axial for vanishing aspect ratio, and the pores could then be safely treated as infinite long channels.

Assuming the pseudo pressure to be locally uniform in the network, the net flux in the equivalent uniform network is obtained by the integration of eqn. (2.50) over the pore volume distribution, to provide

$$J = \frac{\varepsilon\lambda_e < l^2 g(x) >}{\pi < r_p^2 l > R_g T}\left(\frac{N-1}{N+1}\right)\left(-\frac{dP}{dz}\right) \tag{2.53}$$

As mentioned above, in practice, experimental data is commonly interpreted phenomenologically based on a mean pore radius, $\overline{r}_p$, by introducing pore network related parameters such as tortuosity and porosity, following

$$J = \frac{\varepsilon D_o(\overline{r}_p)K(\overline{r}_p)}{\tau_{app} R_g T}\left(-\frac{dP}{dz}\right) \tag{2.54}$$

where τ_{app} is an apparent tortuosity that is generally obtained by fitting the experimental flux. Comparing Eqs. (2.53) and (2.54), the theoretical prediction of apparent tortuosity is given by

$$\tau_{app} = \frac{\pi < r_p^2 l > D_o(\overline{r}_p)K(\overline{r}_p)}{< l^2 g(x) > \lambda_e}\left(\frac{N+1}{N-1}\right) \tag{2.55}$$

This permits evaluation of flux and apparent tortuosity for the nanoporous materials with a pore size distribution, which can be directly used to compare with macroscopic experimental data [73, 109].

2.4 Summary

From above discussion, it is clear that the flow mechanism is highly determined by the pore size, thus different transport models may be combined with effective medium theory to describe the experimental results for the different types and layers of supported silica membranes. However, in general, the Knudsen and viscous diffusion may be applied for macropores above 50 nm without consideration of fluid-solid dispersive interaction; while the Oscillator model and Knudsen model will be attempted in the mesoporous and microporous silica membranes in low density limits.

2.5 References

[1] S.K. Bhatia, Modeling pure gas permeation in nanoporous materials and membranes, Langmuir, 26 (2010) 8373-8385.

[2] Y. Wan, D. Zhao, On the controllable soft-templating approach to mesoporous silicates, Chem. Rev., 107 (2007) 2821-2860.

[3] J.C. Diniz da Costa, G.Q. Lu, V. Rudolph, Y.S. Lin, Novel molecular sieve silica (MSS) membranes: characterisation and permeation of single-step and two-step sol-gel membranes, J. Membr. Sci., 198 (2002) 9-21.

[4] B. Ballinger, J. Motuzas, S. Smart, J.C. Diniz da Costa, Palladium cobalt binary doping of molecular sieving silica membranes, J. Membr. Sci., 451 (2014) 185-191.

[5] M.C. Duke, J.C. Diniz da Costa, G.Q. Lu, M. Petch, P. Gray, Carbonised template molecular sieve silica membranes in fuel processing systems: permeation, hydrostability and regeneration, J. Membr. Sci., 241 (2004) 325-333.

[6] D.M. Ruthven, W. DeSisto, S. Higgins, Diffusion in a mesoporous silica membrane: validity of the Knudsen diffusion model, Chem. Eng. Sci., 64 (2009) 3201-3203.

[7] C.J. Brinker, T.L. Ward, R. Sehgal, N.K. Raman, S.L. Hietala, D.M. Smith, D.W. Hua, T.J. Headley, Ultramicroporous silica-based supported inorganic membranes, J. Membr. Sci, 77 (1993) 165–179.

[8] Y. Lu, G. Cao, R.P. Kale, S. Prabakar, G.P. López, C.J. Brinker, Microporous silica prepared by organic templating: relationship between the molecular template and pore structure, Chem. Mater., 11 (1999) 1223-1229.

[9] D.K. Wang, J.C. Diniz da Costa, S. Smart, Development of Rapid Thermal Processing of Tubular Cobalt Oxide Silica Membranes for Gas Separations, J. Membr. Sci, 456 (2014) 192–201.

[10] D.K. Wang, J. Motuzas, J.C. Diniz da Costa, S. Smart, Rapid thermal processing of tubular cobalt oxide silica membranes, Int. J. Hydrogen, 38 (2013) 7394-7399.

[11] K. Kusakabe, S. Sakamoto, T. Saie, S. Morooka, Pore structure of silica membranes formed by a sol-gel technique using tetraethoxysilane and alkyltriethoxysilanes, Sep. Purif. Technol., 16 (1999) 139-146.

[12] T. Kameyama, M. Dokiya, M. Fujishige, H. Yokokawa, K. Fukuda, Production of hydrogen from hydrogen sulfide by means of selective diffusion membranes, Int. J. Hydrogen Energ., 8 (1983) 5-13.

[13] G.R. Gavalas, C.E. Megiris, S.W. Nam, Deposition of H_2-permselective SiO_2 films, Chem. Eng. Sci., 44 (1989) 1829-1835.

[14] S. Ernst, Advances in nanoporous materials, Elsevier, 2009.

[15] B. Herreros, J. Klinowski, Hydrothermal synthesis of zeolites from 5-coordinate silicon compounds, J. Phys. Chem., 99 (1995) 1025-1029.

[16] M. Niwa, Y. Murakami, CVD zeolites with controlled pore-opening size, J. Phys. Chem. Solids, 50 (1989) 487-496.

[17] C.J. Brinker, G.W. Scherer, Sol-Gel Science: The Physics and Chemistry of Sol-Gel Processing, Academic Pr., San Diego, CA, 1990.

[18] R.S.A. De Lange, J.H.A. Hekkink, K. Keizer, A.J. Burggraaf, Permeation and separation studies on microporous sol-gel modified ceramic membranes, Microporous Mater. , 4 (1995) 169-186.

[19] R.S.A. De Lange, J.H.A. Hekkink, K. Keizer, A.J. Burggraaf, Formation and characterization of supported microporous ceramic membranes prepared by sol-gel modification techniques, J. Membr. Sci., 99 (1995) 57-75.

[20] R.S.A. De Lange, K. Keizer, A.J. Burggraaf, Analysis and theory of gas transport in microporous sol-gel derived ceramic membranes, J. Membr. Sci, 104 (1995) 81-100.

[21] D. Uhlmann, S. Liu, B.P. Ladewig, J.C. Diniz da Costa, Cobalt-doped silica membranes for gas separation, J. Membr. Sci., 326 (2009) 316-321.

[22] C.T. Kresge, M.E. Leonowicz, W.J. Roth, J.C. Vartuli, J.S. Beck, Ordered mesoporous molecular sieves synthesized by a liquid-crystal template mechanism, Nature, 359 (1992) 710-712.

[23] Q. Huo, D.I. Margolese, U. Ciesla, D.G. Demuth, P. Feng, T.E. Gier, P. Sieger, A. Firouzi, B.F. Chmelka, F. Schuth, G.D. Stucky, Organization of organic molecules with inorganic molecular species into nanocomposite biphase arrays, Chem. Mater., 6 (1994) 1176-1191.

[24] P.C.A. Alberius, K.L. Frindell, R.C. Hayward, E.J. Kramer, G.D. Stucky, B.F. Chmelka, General predictive syntheses of cubic, hexagonal, and lamellar silica and titania mesostructured thin films, Chem. Mater., 14 (2002) 3284-3294.

[25] D. Grosso, F. Cagnol, G.J.A.A. Soler-Illia, E.L. Crepaldi, H. Amenitsch, A. Brunet-Bruneau, A. Bourgeois, C. Sanchez, Fundamentals of mesostructuring through evaporation induced self assembly, Adv. Funct. Mater., 14 (2004) 309-322.

[26] N.K. Raman, C.J. Brinker, Organic "template" approach to molecular sieving silica membranes, J. Membr. Sci., 105 (1995) 273-279.

[27] J. Xiao, J. Wei, Diffusion mechanism of hydrocarbons in zeolites-II. Analysis of experimental observations, Chem. Eng. Sci., 47 (1992) 1143-1159.

[28] D. Zhao, J. Feng, Q. Huo, N. Melosh, G.H. Fredrickson, B.F. Chmelka, G.D. Stucky, Triblock copolymer syntheses of mesoporous silica with periodic 50 to 300 angstrom pores, Science, 279 (1998) 548-552.

[29] B.D. Kay, R.A. Assink, Sol-gel kinetics: II. Chemical speciation modeling, J. Non-Cryst. Solids, 104 (1988) 112-122.

[30] R. Leboda, E. Mendyk, V.A. Tertykh, Effect of medium pH on hydrothermal treatment of silica gels (xerogels) in an autoclave, Mater. Chem. Phys., 43 (1996) 53-58.

[31] T. Yoshioka, E. Nakanishi, T. Tsuru, M. Asaeda, Experimental studies of gas permeation through microporous silica membranes, AIChE J., 47 (2004) 2052-2063.

[32] T. Yoshioka, M. Kanezashi, T. Tsuru, Micropore size estimation on gas separation membranes: a study in experimental and molecular dynamics, AIChE J., 59 (2012) 2179-2194.

[33] A. Marković, D. Stoltenberg, D. Enke, E.-U. Schlünder, A. Seidel-Morgenstern, Gas permeation through porous glass membranes: Part II: transition regime between Knudsen and configurational diffusion, J. Membr. Sci., 336 (2009) 32-41.

[34] C. Yacou, S. Smart, J.C. Diniz da Costa, Long term performance cobalt oxide silica membrane module for high temperature H2 separation, Energ. Environ. Sci., 5 (2012) 5820-5832.

[35] G. Ji, G. Wang, K. Hooman, S.K. Bhatia, J.C. Diniz da Costa, The fluid dynamic effect on the driving force for a cobalt oxide silica membrane module at high temperatures, Chem. Eng. Sci., 111 (2014) 142-152.

[36] G. Ji, G. Wang, K. Hooman, S.K. Bhatia, J.C. Diniz da Costa, Computational fluid dynamics applied to high temperature hydrogen separation membranes, Front. Chem. Sci. Eng., 6 (2012) 3-12.

[37] C.J. Brinker, K.D. Keefer, D.W. Schaefer, R.A. Assink, B.D. Kay, C.S. Ashley, Sol-gel transition in simple silicates II, J. Non-Cryst. Solids, 63 (1984) 45-59.

[38] S. Higgins, W. DeSisto, D.M. Ruthven, Diffusive transport through mesoporous silica membranes, Micropor. Mesopor. Mat., 117 (2009) 268-277.

[39] J.S. Beck, J.C. Vartuli, W.J. Roth, M.E. Leonowicz, C.T. Kresge, K.D. Schmitt, C.T.W. Chu, D.H. Olson, E.W. Sheppard, A new family of mesoporous molecular sieves prepared with liquid crystal templates, J. Am. Chem. Soc., 114 (1992) 10834-10843.

[40] S. Cao, Y. Zhu, J. Wu, K. Wang, Q. Tang, Preparation and sustained-release property of triblock copolymer/calcium phosphate nanocomposite as nanocarrier for hydrophobic drug, Nanoscale Res. Lett., 5 (2010) 781-785.

[41] F. Ye, H. Guo, H. Zhang, X. He, Polymeric micelle-templated synthesis of hydroxyapatite hollow nanoparticles for a drug delivery system, Acta. Biomater., 6 (2010) 2212-2218.

[42] H. Preising, D. Enke, Relations between texture and transport properties in the primary pore system of catalyst supports, Colloids Surf. A, 300 (2007) 21-29.

[43] E. Iglesia, S.L. Soled, J.E. Baumgartner, S.C. Reyes, Synthesis and catalytic properties of eggshell cobalt catalysts for the Fischer-Tropsch synthesis, J. Catal., 153 (1995) 108-122.

[44] S. Piletsky, A. Turner, Molecular Imprinting of Polymers, Biotechnology Intelligence Unit, Landes Bioscience, Georgetown,Texas, USA., 2006.

[45] R.J. Lussier, J.S. Magee Jr, D.E.W. Vaughan, Pillared Interlayered Clay Materials Useful as Catalysts and Adsorbents, in, W. R. Grace & Co., USA, 1979.

[46] Y. Kaneko, N. Iyi, T. Matsumoto, K. Kitamura, Preparation of a clay pillared with rodlike cationic polysiloxane, Chem. Lett. , 33 (2004) 1486-1487.

[47] D. Duong, Absorption Analysis: Equilibria and Kinetics, Imperial College Pr., London, 1998.

[48] T. Yanagisawa, T. Shimizu, K. Kuroda, C. Kato, The preparation of alkyltrimethylammonium-kanemite complexes and their conversion to microporous materials, Bull. Chem. Soc. Jpn, 63 (1990) 988-992.

[49] A. Imhof, D.J. Pine, Ordered macroporous materials by emulsion templating, Nature, 389 (1997) 948-950.

[50] W. Li, D. Zhao, Extension of the Stöber Method to Construct Mesoporous SiO2 and TiO2 Shells for Uniform Multifunctional Core–Shell Structures, Adv. Mater., 25 (2013) 142-149.

[51] Z. Xie, L. Bai, S. Huang, C. Zhu, Y. Zhao, Z. Gu, New Strategy for Surface Functionalization of Periodic Mesoporous Silica Based on meso-HSiO1. 5, J. Am. Chem. Soc., 136 (2014) 1178–1181.

[52] R.M. De Vos, H. Verweij, Improved performance of silica membranes for gas separation, J. Membr. Sci., 143 (1998) 37-51.

[53] H. Yang, N. Coombs, I. Sokolov, G.A. Ozin, Free-standing and oriented mesoporous silica films grown at the air–water interface, Nature, 386 (1996) 589-592.

[54] H. Yang, A. Kuperman, N. Coombs, S. Mamiche-Afara, G.A. Ozin, Synthesis of oriented films of mesoporous silica on mica, Nature, 379 (1996) 703-705.

[55] Y. Lu, H. Fan, A. Stump, T.L. Ward, T. Rieker, C.J. Brinker, Aerosol-assisted self-assembly of mesostructured spherical nanoparticles, Nature, 398 (1999) 223-226.

[56] H.L. Castricum, R. Kreiter, H.M. van Veen, D.H.A. Blank, J.F. Vente, J.E. ten Elshof, High-performance hybrid pervaporation membranes with superior hydrothermal and acid stability, J. Membr. Sci, 324 (2008) 111-118.

[57] S. Battersby, T. Tasaki, S. Smart, B. Ladewig, S. Liu, M.C. Duke, V. Rudolph, J.C. Diniz da Costa, Performance of cobalt silica membranes in gas mixture separation, J. Membr. Sci., 329 (2009) 91-98.

[58] S.K. Bhatia, M.R. Bonilla, D. Nicholson, Molecular transport in nanopores: a theoretical perspective, Phys. Chem. Chem. Phys., 13 (2011) 15350-15383.

[59] R. Aris, The mathematical theory of diffusion and reaction in permeable catalysts. Vol. I: The theory of the steady state, Clarendon Press, London, 1975.

[60] S. Lijima, Helical microtubules of graphitic carbon, Nature, 354 (1991) 56-58.

[61] A.K. Cheetham, G. Férey, T. Loiseau, Open framework inorganic materials, Angew. Chem. Int. Edit, 38 (1999) 3268-3292.

[62] R.B. Bird, W.E. Stewart, E.N. Lightfoot, Transport Phenomena, John Wiley & Sons, New York-Chichester-Weinheim-Brisbane-Singapore-Toronto, 2006.

[63] J. Xiao, J. Wei, Diffusion mechanism of hydrocarbons in zeolites-I. Theory, Chem. Eng. Sci., 47 (1992) 1123-1141.

[64] G. Ji, G. Wang, K. Hooman, S.K. Bhatia, J.C. Diniz da Costa, Simulation of binary gas separation through multi-tube molecular sieving membranes at high temperatures, Chem. Eng. J., 218 (2013) 394–404.

[65] S. Hwang, Fundamentals of membrane transport, Korean J. Chem. Eng., 28 (2011) 1-15.

[66] H. Rhim, S. Hwang, Knudsen flow under an external potential field, Phys. Fluids, 19 (1976) 1319-1323.

[67] M. Knudsen, W.J. Fisher, The molecular and the frictional flow of gases in tubes, Phys. Rev., 31 (1910) 586-588.

[68] M.R. Bonilla, S.K. Bhatia, The low-density diffusion coefficient of soft-sphere fluids in nanopores: accurate correlations from exact theory and criteria for applicability of the Knudsen model, J. Membr. Sci., 382 (2011) 339-349.

[69] M.R. Bonilla, S.K. Bhatia, Multicomponent effective medium-correlated random walk theory for the diffusion of fluid mixtures through porous media, Langmuir, 28 (2011) 517-533.

[70] N. Nishiyama, D.H. Park, A. Koide, Y. Egashira, K. Ueyama, A mesoporous silica (MCM-48) membrane: preparation and characterization, J. Membr. Sci., 182 (2001) 235-244.

[71] J. Liu, J. Wei, Knudsen Diffusion in Channels and Networks, Chem. Eng. Sci., 111 (2014) 1-14.

[72] X. Gao, J.C. Diniz da Costa, S.K. Bhatia, Adsorption and transport of gases in a supported microporous silica membrane, J. Membr. Sci., 460 (2014) 46-61.

[73] X. Gao, J.C. Diniz da Costa, S.K. Bhatia, The transport of gases in a supported mesoporous silica membrane, J. Membr. Sci., 438 (2013) 90-104.

[74] S.K. Bhatia, D. Nicholson, Modeling mixture transport at the nanoscale: Departure from existing paradigms, Phys. Rev. Lett., 100 (2008) 236103.

[75] J. Kärger, F. Stallmach, S. Vasenkov, Structure-mobility relations of molecular diffusion in nanoporous materials, Magn. Reson. Imaging, 21 (2003) 185-191.

[76] A. Markovic, D. Stoltenberg, D. Enke, E.U. Schlünder, A. Seidel-Morgenstern, Gas permeation through porous glass membranes: Part I. Mesoporous glasses-effect of pore diameter and surface properties, J. Membr. Sci., 336 (2009) 17-31.

[77] R. Krishna, J.M. van Baten, Influence of segregated adsorption on mixture diffusion in DDR zeolite, Chem. Phys. Lett., 446 (2007) 344-349.

[78] A. Kapoor, R. Yang, Surface diffusion on energetically heterogeneous surfaces, AIChE J., 35 (1989) 1735-1738.

[79] S. Hwang, Interaction energy in surface diffusion, AIChE J., 14 (1968) 809-811.

[80] R. Srinivasan, S.R. Auvil, P.M. Burban, Elucidating the mechanism (s) of gas transport in poly [1-(trimethylsilyl)-1-propyne](PTMSP) membranes, J. Membr. Sci., 86 (1994) 67-86.

[81] A. Yamasaki, H. Inoue, Surface diffusion of organic vapor mixtures through porous glass, J. Membr. Sci., 59 (1991) 233-248.

[82] S. Hwang, K. Kammermeyer, Surface diffusion in microporous media, Can. J. Chem. Eng., 44 (1966) 82-89.

[83] S. Battersby, S. Smart, B. Ladewig, S. Liu, M.C. Duke, V. Rudolph, J.C. Diniz da Costa, Hydrothermal stability of cobalt silica membranes in a water gas shift membrane reactor, Sep. Purif. Technol., 66 (2009) 299-305.

[84] S. Battersby, B.P. Ladewig, M.C. Duke, V. Rudolph, J.C. Diniz da Costa, Membrane reactor modelling, validation and simulation for the WGS reaction using metal doped silica membranes, Asia Pac. J. Chem. Eng., 5 (2010) 83-92.

[85] S. Gopalakrishnan, J.C. Diniz da Costa, Hydrogen gas mixture separation by CVD silica membrane, J. Membr. Sci., 323 (2008) 144-147.

[86] M.J. Murphy, G.A. Voth, A.L. Bug, Classical and quantum transition state theory for the diffusion of helium in silica sodalite, J. Phys. Chem. B, 101 (1997) 491-503.

[87] D.G. Truhlar, B.C. Garrett, S.J. Klippenstein, Current status of transition-state theory, J. Phys. Chem., 100 (1996) 12771-12800.

[88] T.X. Nguyen, S.K. Bhatia, Determination of pore accessibility in disordered nanoporous materials, J. Phys. Chem. C, 111 (2007) 2212-2222.

[89] D. Dubbeldam, S. Calero, T.L.M. Maesen, B. Smit, Incommensurate diffusion in confined systems, Phys. Rev. Lett., 90 (2003) 245901.

[90] F. Jousse, S.M. Auerbach, Activated diffusion of benzene in NaY zeolite: Rate constants from transition state theory with dynamical corrections, J. Chem. Phys., 107 (1997) 9629-9639.

[91] D. Dubbeldam, R.Q. Snurr, Recent developments in the molecular modeling of diffusion in nanoporous materials, Mol. Simulat., 33 (2007) 305-325.

[92] T.X. Nguyen, S.K. Bhatia, Kinetic restriction of simple gases in porous carbons: transition-state theory study, Langmuir, 24 (2008) 146-154.

[93] U. Engberg, Y. Li, G. Wahnstrom, Some tests of basic assumptions in transition state theory for hydrogen diffusion in FCC-metals, J. Phys.: Condens. Matter., 5 (1993) 5543.

[94] T.X. Nguyen, H. Jobic, S.K. Bhatia, Microscopic observation of kinetic molecular sieving of hydrogen isotopes in a nanoporous material, Phys. Rev. Lett., 105 (2010) 085901.

[95] O.G. Jepps, S.K. Bhatia, D.J. Searles, Wall mediated transport in confined spaces: exact theory for low density, Phys. Rev. Lett., 91 (2003) 126102.

[96] A.V.A. Kumar, S.K. Bhatia, Mechanisms influencing levitation and the scaling laws in nanopores: Oscillator model theory, J. Phys. Chem. B, 110 (2006) 3109-3113.

[97] S.K. Bhatia, D. Nicholson, Transport of simple fluids in nanopores: Theory and simulation, AIChE J., 52 (2006) 29-38.

[98] S.K. Bhatia, O. Jepps, D. Nicholson, Tractable molecular theory of transport of Lennard-Jones fluids in nanopores, J. Chem. Phys., 120 (2004) 4472-4485.

[99] X. Zhang, W. Wang, G. Jiang, a potential model for interaction between the Lennard Jones cylindrical wall and fluid molecules, Fluid Phase Equilibr., 218 (2004) 239-246.

[100] W.A. Steele, M.J. Bojan, Simulation studies of sorption in model cylindrical micropores, Adv. Colloid Interfac., 76 (1998) 153-178.

[101] P.J.A.M. Kerkhof, M.A.M. Geboers, Analysis and extension of the theory of multicomponent fluid diffusion, Chem. Eng. Sci., 60 (2005) 3129-3167.

[102] R.E. Cunningham, R.J.J. Williams, Diffusion in gases and porous media, Plenum Press, New York, 1980.

[103] R. Jackson, Transport in porous catalysts Elsevier Sicentific Pub Co, Amsterdam, 1977.

[104] J.A. Wesselingh, R. Krishna, Mass Transfer in Multicomponent Mixtures, Delft University Press, Delft, The Netherlands, 2000.

[105] R.B. Evans III, G.M. Watson, E.A. Mason, Gaseous diffusion in porous media at uniform pressure, J. Chem. Phys., 35 (1961) 2076-2083.

[106] S. Chapman, T.G. Cowling, Mathematical Theory of Non-Uniform Gases, Cambridge University Press, Cambridge, 1939.

[107] R. Krishna, J.A. Wesselingh, The Maxwell-Stefan approach to mass transfer, Chem. Eng. Sci., 52 (1997) 861-911.

[108] X. Gao, M.R. Bonilla, J.C. Diniz da Costa, S.K. Bhatia, The transport of gases in macroporous α-alumina supports, J. Membr. Sci., 409-410 (2012) 24-33.

[109] X. Gao, M.R. Bonilla, J.C. Diniz da Costa, S.K. Bhatia, The transport of gases in a mesoporous γ-alumina supported membrane, J. Membr. Sci., 428 (2013) 357-370.

[110] X. Gao, J.C. Diniz da Costa, S.K. Bhatia, Understanding the diffusional tortuosity of porous materials: an effective medium theory perspective, Chem. Eng. Sci., 110 (2014) 55–71.

[111] S.K. Bhatia, D. Nicholson, Some pitfalls in the use of the Knudsen equation in modelling diffusion in nanoporous materials, Chem. Eng. Sci., 66 (2010) 284-293.

[112] J.C. Maxwell, On the dynamical theory of gases, Phil. Trans. R. Soc., (1867) 49-88.

[113] R. Krishna, J.M. van Baten, Unified Maxwell-Stefan description of binary mixture diffusion in micro-and meso-porous materials, Chem. Eng. Sci., 64 (2009) 3159-3178.

[114] T.J.H. Vlugt, J. van den Bergh, D. Dubbeldam, F. Kapteijn, Reconciling the Relevant Site Model and Dynamically Corrected Transition State Theory, Chem. Phys. Lett., 495 (2010) 77-79.

[115] J. van den Bergh, S. Ban, T.J.H. Vlugt, F. Kapteijn, Diffusion in zeolites: extension of the relevant site model to light gases and mixtures thereof in zeolites DDR, CHA, MFI and FAU, Sep. Purif. Technol., 73 (2010) 151-163.

[116] J. van den Bergh, S. Ban, T.J.H. Vlugt, F. Kapteijn, Modeling the loading dependency of diffusion in zeolites: the relevant site model extended to mixtures in DDR-type zeolite, J. Phys. Chem. C, 113 (2009) 21856-21865.

[117] J. van den Bergh, S. Ban, T.J.H. Vlugt, F. Kapteijn, Modeling the loading dependency of diffusion in zeolites: the relevant site model, J. Phys. Chem. C, 113 (2009) 17840-17850.

[118] S.K. Bhatia, D. Nicholson, Friction based modeling of multicomponent transport at the nanoscale, J. Chem. Phys., 129 (2008) 164709.

[119] G. Galliéro, C. Boned, A. Baylaucq, Molecular dynamics study of the Lennard-Jones fluid viscosity: Application to real fluids, Ind. Eng. Chem. Res., 44 (2005) 6963-6972.

[120] L. Onsager, Reciprocal relations in irreversible processes. I, Phys. Rev., 37 (1931) 405.

[121] L. Onsager, Reciprocal relations in irreversible processes. II, Phys. Rev., 38 (1931) 2265.

[122] D.G. Miller, Thermodynamics of Irreversible Processes. The Experimental Verification of the Onsager Reciprocal Relations, Chem. Rev., 60 (1960) 15-37.

[123] S. Kirkpatrick, Classical transport in disordered media: Scaling and effective-medium theories, Phys. Rev. Lett., 27 (1971) 1722-1725.

[124] M. Sheinman, C.P. Broedersz, F.C. MacKintosh, Nonlinear effective medium theory of disordered spring networks, Phys. Rev. E., 85 (2012) 021801.

[125] S.K. Bhatia, Directional autocorrelation and the diffusional tortuosity of capillary porous media, J. Catal., 93 (1985) 192-196.

[126] S.K. Bhatia, Stochastic theory of transport in inhomogeneous media, Chem. Eng. Sci., 41 (1986) 1311-1324.

[127] S.K. Bhatia, Capillary network models for transport in packed beds: considerations of pore aspect ratio, Chem. Eng. Commun., 154 (1996) 183-202.

[128] S.P. Friedman, N.A. Seaton, A corrected tortuosity factor for the network calculation of diffusion coefficients, Chem. Eng. Sci., 50 (1995) 897-900.

Chapter 3: The transport of gases in macroporous α-alumina substrates

The infiltration of fluids through the voids of porous materials is common place to several well established and emerging technologies, and optimizing their performance relies heavily on developing a deeper understanding of how the fluid flow is affected by the topology of the pore space. This is particularly challenging when the medium is unconsolidated, since it is not only the pore size distribution and pore network connectivity that must be considered, but also the pore aspect ratio distribution will often assume importance. In chapter, we introduce a modified Effective Medium Theory (EMT) where the effect of non-vanishing aspect ratios is considered in order to describe the transport mechanism of several light gases through unconsolidated macroporous α-alumina tubular substrates. It is confirmed that the tortuosity is not just a property of the medium, but also depends (weakly) on the operating conditions due to the combined effect of viscous and Knudsen contributions. The coordination number and average pore length are the only adjustable parameters in the theory, which allowed adequate prediction of the variation of the apparent tortuosity with temperature for the investigated gases.

3.1 Introduction

Since the discovery of MCM-41 and SBA-15 [1-3], much research has been devoted to the synthesis of inorganic nanoporous materials by the sol-gel process to tackle emerging and long-standing challenges in a variety of fields, such as gas separation, heterogeneous catalysis and drug delivery [4-7]. This has brought considerable attention to the modeling and simulation of the transport of fluids in nanoconfined spaces, due to its relevance for both process and materials design and optimization [8-11]. Nevertheless, little progress had been made until recently, and most of the work still largely relies on empirical modifications of the century-old Knudsen model [12], which ignores adsorption, to describe the effect of fluid-wall collision on diffusion [13]. Although the Knudsen model can qualitatively display some agreement with the experimental variation of the permeability with temperature, unrealistically high tortuosities are commonly obtained when applied under conditions in which adsorption is known to be important [14-17]. Furthermore, statistical mechanical theory [14, 15, 17] and molecular dynamics simulations (MD) [18, 19] have confirmed the overprediction of the diffusion coefficient estimated through the Knudsen approach for a variety of gases in 2 and 3 nm pore size silica membranes. The main reason for such overprediction in pores of a few molecular diameters is the assumption that no dispersive interactions exist between the fluid and the pore walls, which artificially increases the travel time of the fluid molecules between successive fluid-wall collisions and yields a higher diffusivity than that obtained when van der Waals interactions are incorporated [14, 15, 17]. However, for sufficiently wide pores, the effect of the pore walls field over the fluid particles can be safely ignored and the Knudsen model provides an adequate estimation of the (low-density) diffusion coefficient.

In practice, an inorganic membrane system consists of a thin selective ("active") layer with narrow pores in which separation occurs, and a relatively thick support with a wide average pore size so as to enhance mechanical resistance for industrial application while minimizing the resistance to flow. Porous asymmetric alumina discs and tubes consisting of a α-alumina substrate and a γ-alumina interlayer are usually chosen as the support [20-22]. The α-alumina substrate is made of packed crystal particles (~2 μm) to create macropores and provide mechanical resistance [23], while the crystal particles of γ-alumina are smaller(~0.05 μm) [24] and are coated over the surface of the α-alumina substrate to produce a uniform, defect-free surface over which the active layer is deposited. Due to the complex nature of transport through the membrane after dip-coating [25], modeling of fluid diffusion in the two different layers of the support is often based on the arbitrary assumption that the resistance to flow of the α-alumina substrate is negligible, thereby transferring all of the support resistance to the γ-alumina layer where, in addition, only the viscous contribution is considered. While these assumptions lead to reasonable tortuosities of the order of 3 - 4 [9, 26], they artificially transfer much of the active layer resistance to the support when the complete membrane system is analyzed, as recently shown by Bhatia and Nicholson [16].

For this reason, it is of great interest to understand the true nature and relative contribution of the different transport mechanisms through the substrate. This will in turn provide better understanding of the transport mechanism in the selective layer, since the real magnitude of the resistance offered by this layer can be determined from the (full) membrane permeation experiments if the support resistance is known. The current work aims to investigate the diffusion of several light gases in the α-alumina tubular substrate and the relationship between tortuosity and operating conditions by means of a modified EMT in which the aspect ratio, i.e. the ratio of pore radius to pore length, is different from zero [27, 28]. This is particularly important when analyzing unconsolidated media such as the α-alumina layer, since in these cases the pore length is expected to be of the same order of magnitude as the pore radius. The technique provides good agreement with the experimental data and proves valuable to extract information on how the materials morphology affects the transport.

3.2 Materials characterization and experiments

The α-alumina tubular substrates were obtained from Australia Chemtech Trading & Service Company, and are made of packed α-alumina particles sintered at high temperature. Permeation experiments were conducted on two substrate samples (arbitrarily labeled as substrate A and substrate B) having different pore size, by flowing six different gases (H_2, He, CH_4, N_2, CO_2 and Ar) through the substrate walls under the operating conditions listed in Table 3.1. It is noted that the permeation experiments was carried out from high temperature (573 K) to low temperature (293 K) to avoid any water blockage effect. A schematic drawing of the experimental setup and the direction of the gas flow through the substrate is shown in Figures 3.1a and 3.1b, respectively.

Table 3.1. operating conditions for single gas permeation in two tubular substrates.

Substrate	Inlet pressure, bar	Outlet pressure, bar	Temperature range, K
A	1.97	1.01	303 - 573
B	1.47	1.01	293 - 573

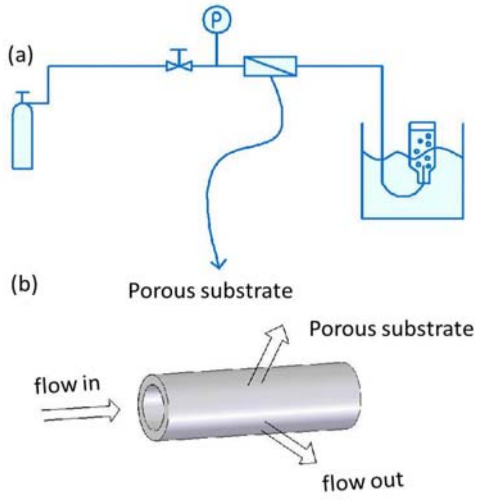

Figure 3.1 Sketch of (a) the experimental setup, and (b) substrate, for single gas permeation experiments.

The volumetric flow-rate is measured by water displacement method with a 1000 ml Schott bottle and a stop watch, and converted to molar flow-rate by means of an appropriate equation of state. It is noted that the permeate velocity of gases is extreme fast, thus the water resistance is negligible in such context and the measured flow rate has high accuracy, which is less than 5%, compared with the data based on bubble flow meter. The crystal particle size and pore size distribution of the α-alumina substrate were investigated by Scanning Electron Microscopy (SEM) and Mercury Porosimetry (Micrometrics, IV9500) and the results are depicted in Figures 3.2 and 3.3, respectively. In addition, the skeletal density of the substrate material was obtained by Helium Pycnometry, using a Micromeritics Accupyc 1330 instrument.

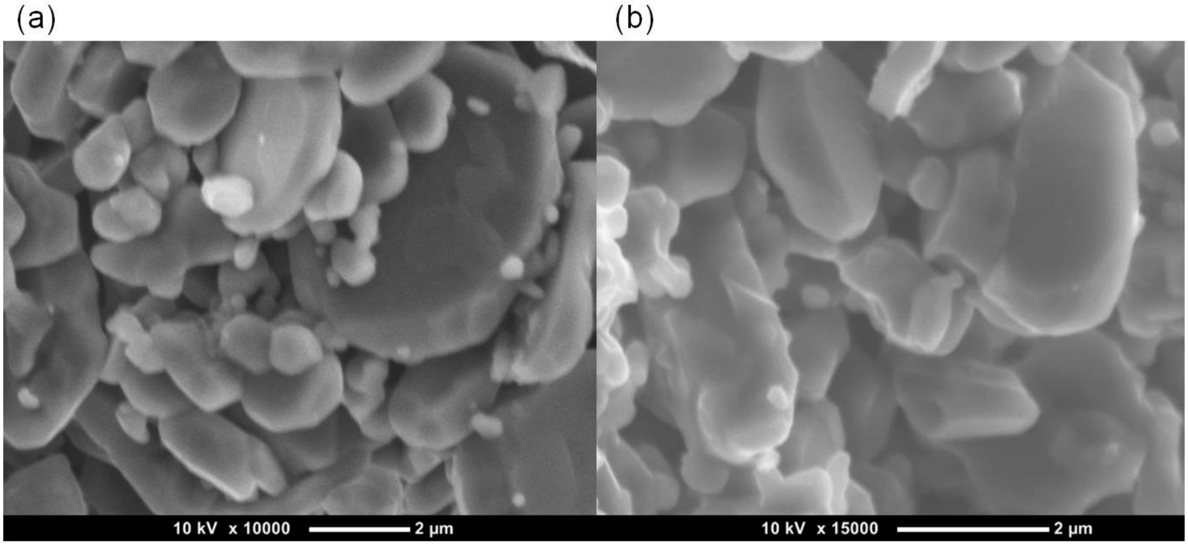

Figure 3.2 SEM images of the two substrates. (a) substrate A, and (b) substrate B.

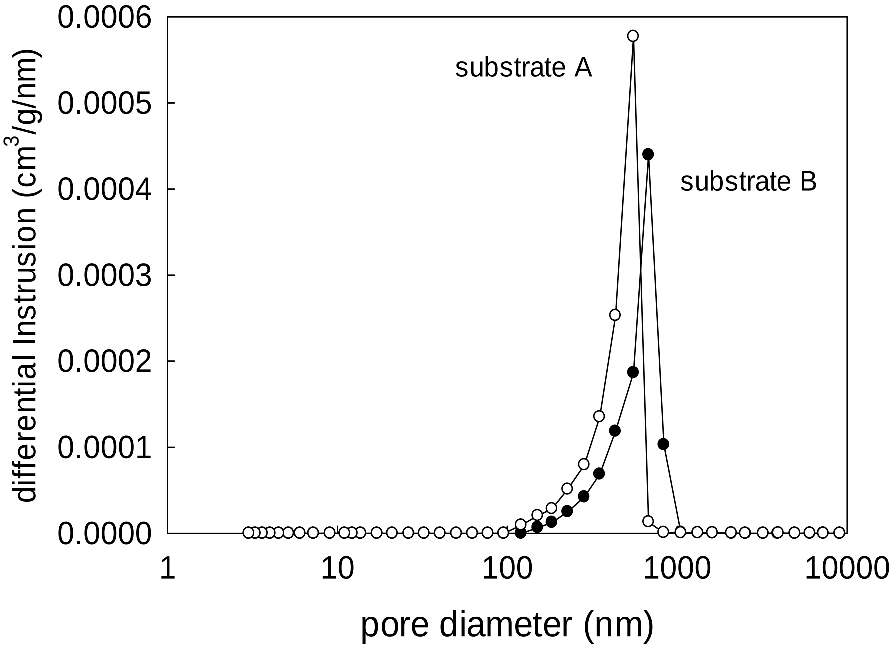

Figure 3.3 Pore size distributions of the two substrates, determined by mercury porosimetry.

The SEM results indicated that the two samples have similar particle sizes (1 - 3 μm). The porosity and apparent density of substrate A extracted from Mercury Porosimetry were 33.3% and 3.85 g/mL respectively, while the Helium Pycnometry yielded a skeletal density of 3.96 g/mL. For substrate B, the porosity and apparent density obtained from Mercury Porosimetry were 35.70% and 3.89 g/mL respectively, while its skeletal density was 3.91 g/mL. The similarity between the Mercury Porosimetry and Helium Pycnometry-based densities indicate that most of the void volume in the two samples corresponds to macropores, confirming the reliability of the pore size distribution determined through the Mercury Porosimetry technique. Figure 3.3 shows unimodal pore size distributions for both samples, with sharp peaks at 577.0 nm and 730.9 nm for substrates A and B, respectively, which will be taken as the representative pore diameters in the experimental calculations below.

3.3 Transport model

3.3.1 Flow mechanisms

Since all of the measured pore diameters exceed 100 nm, far above the range of the potential field produced by the wall, adsorption is negligible and a simple model superimposing Knudsen and viscous contributions is appropriate to describe the transport mechanism in the macropores. Assuming cylindrical pores, in the spirit of the Dusty Gas Model (DGM) [29, 30], the relationship between flow-rate and temperature can readily be expressed as [8]

$$F\sqrt{T} = \frac{\Delta P 2\pi L\varepsilon}{\tau_{app}\ln(r_o/r_i)}\left(\frac{\overline{r}_p^2\overline{P}}{8R_g\eta\sqrt{T}} + \frac{97\overline{r}_p}{R_g\sqrt{M}}\right) \tag{3.1}$$

in which the term $\ln(r_o/r_i)$ accounts for the change in curvature over the thickness of the substrate wall. Here F is flow rate, T is temperature; L is tube length; $\overline{P}$ is the average pressure through the substrate, η is viscosity, R_g is the gas constant, ΔP is the pressure drop, and r_o and r_i are the outer and inner pore radii respectively. Furthermore, $\overline{r}_p$ is the representative pore radius, M the fluid molar mass, ε the substrate porosity, and τ_{app} the (apparent) tortuosity coefficient, usually left as an adjustable parameter It is noted that the DGM has been criticized on the grounds that it uses conflicting frames of reference [15], with the frame of reference being the stationary solid phase in one step and the mixture centre of mass in another step of the derivation where the diffusion flux is defined. However, this inconsistency does not arise in the case of a pure component. Further, the DGM is based on the assumption of a non-interacting hard sphere gas and solid. However, this is not a concern in large pores (i.e. macropores), in which dispersive fluid-wall interactions may be neglected. Indeed, it is readily seen that the internally consistent Distributed Friction Model (DFM) of Bhatia and Nicholson [31] reduces to eqn. (3.1) for such pores.

From eqn. (3.1), plotting $F\sqrt{T}$ versus $1/\eta\sqrt{T}$ should yield a straight line whose intercept depends on the particular gas. Alternately, if we recast eqn. (3.1) as

$$F\sqrt{TM} = \frac{\Delta P 2\pi L\varepsilon}{\tau_{app}\ln(r_o/r_i)}\left(\frac{\overline{r}_p^2\overline{P}\sqrt{M}}{8R_g\eta\sqrt{T}} + \frac{97\overline{r}_p}{R_g}\right) \tag{3.2}$$

then, plotting $F\sqrt{TM}$ versus $\sqrt{M}/\eta\sqrt{T}$ may be expected to yield a straight line whose slope and intercept is independent of the particular gas species if τ_{app} is purely a structural parameter. The tortuosity, τ_{app}, may be readily determined from the slope or the intercept of the plots based on eqn. (3.1) or eqn. (3.2).

To avoid differences between the tortuosities obtained from the slope and intercept, τ_{app} is often obtained from eqn. (3.1), following

$$\tau_{app} = \frac{\Delta P 2\pi L\varepsilon}{F\sqrt{TM}\ln(r_o / r_i)}\left(\frac{\overline{r}_p^2\overline{P}\sqrt{M}}{8R_g\eta\sqrt{T}} + \frac{97\overline{r}_p}{R_g}\right) \tag{3.3}$$

3.3.2 Transport in pore networks

Effective medium theory (EMT) offers a convenient route to modeling transport in disordered pore networks, avoiding the uncertainty of choosing a representative pore size in eqs. (3.1)-(3.3). The fundamental principle behind EMT is replacing the actual network of disordered pores with randomly distributed conductances by a uniform network with the same overall resistance to flow as the original one. Bhatia and coworkers have recently used this technique to predict the variation of apparent tortuosity with adsorbate, temperature and pore size distribution parameters in silica microporous membranes, showing that the tortuosity is not exclusively determined by the pore structure but is also affected by the particular fluid and the operating conditions [14, 17]. However, the EMT formulation used in most of the previous works assumes infinitely long capillaries, i.e. vanishing aspect ratios [14, 17, 28, 32, 33]. This is not a reasonable assumption for the alumina substrate samples since, as depicted in Figure 3.2, the constituent particles are relatively "round" and, consequently, the interstitial pores will have diameters and lengths of similar order of magnitude. A modified EMT will be employed here considering non-vanishing aspect ratios [27, 28] to predict the apparent tortuosity in the macroporous alumina substrate.

For a pore of arbitrary radius r_p, the molecular current, i, is given in terms of the chemical potential gradient ($\nabla\mu$) by

$$i = \frac{\pi r_p^2 \rho_a D_o(r_p)}{R_g T}(-\nabla\mu) \tag{3.4}$$

At low bulk pressure, eqn. (3.4) may be rewritten, using the Gibbs-Duhem equation, as [14]

$$i = \frac{\pi r_p^2 K(r_p) D_o(r_p)}{R_g T l}\Delta P \tag{3.5}$$

Here, l is pore length and P is the pseudobulk pressure at which the bulk fluid will be in equilibrium with the adsorbate of density ρ_a. $K(r_p)$ is the equilibrium constant at the pseudo-bulk pressure and $D_o(r_p)$ is the corrected pore diffusivity, which includes fluid-wall and fluid-fluid interactions effects.

In the present development we neglect fluid-wall dispersive interactions for the substrate macropores, thereby taking the equilibrium constant $K(r_p)$ as unity and, following eqn. (3.1), $D_o(r_p)$ to be given by

$$D_o(r_p) = D_{vis}(r_p) + D_{Kn}(r_p) \tag{3.6}$$

where $D_{vis}(r_p)$ is the viscous diffusivity given by the well-known Hagen-Poiseuille equation,

$$D_{vis} = \frac{\overline{P} r_p^2}{8\eta} \tag{3.7}$$

and $D_{Kn}(r_p)$ is the Knudsen diffusivity, given by

$$D_{Kn} = 97.0 r_p \sqrt{\frac{T}{M}} \tag{3.8}$$

where r_p is the pore radius in metres, M is the molecular weight in g/mole, and D_{Kn} has the units of m^2/s. The conductance λ for a pore of radius r_p is defined as the ratio of the current to the potential difference. Following eqn. (3.5), this results in

$$\lambda = \frac{\pi r_p^2 D_o(r_p)}{l} \tag{3.9}$$

It is assumed that on the pore scale local equilibrium prevails, so that the pseudo-bulk pressure drop ΔP is considered to be pore size independent. The effective medium conductance λ_e is given by the solution to [14, 34]

$$\left\langle \frac{(\lambda - \lambda_e)}{(\lambda + (N/2 - 1)\lambda_e)} \right\rangle = 0 \tag{3.10}$$

where N is the coordination number, i.e., the number of pores meeting at an intersection and $\langle \cdot \rangle$ represents a number average over the pores. The pore number distribution $f_N(r_p)$ is related to the pore volume distribution $f_v(r_p)$ in Figure 3.3 by

$$f_v(r_p) = \pi r_p^2 l f_N \tag{3.11}$$

in which the pore volume distribution $f_v(r_p)$ satisfies

$$\varepsilon = \int_0^\infty f_v(r_p)\,dr_p \tag{3.12}$$

so that the number average is defined by

$$\langle h(r_p)\rangle = \frac{1}{N_t}\int_0^\infty h(r_p)\,f_N(r_p)\,dr_p \tag{3.13}$$

where N_t is the total density of pores, given by

$$N_t = \int_0^\infty f_N(r_p)\,dr_p = \frac{\varepsilon}{\pi\langle r_p^2 l\rangle} = \int_0^\infty \frac{f_v(r_p)}{\pi r_p^2 l}\,dr_p \tag{3.14}$$

For the effective medium, the directionally averaged flux in a pore of radius r_p may be expressed as [14]

$$j(r_p) = \frac{\lambda_e l}{\pi r_p^2 R_g T}\left(\frac{N-1}{N+1}\right)\overline{\cos^2(\theta)}\left(-\frac{dP}{dz}\right) \tag{3.15}$$

where z represents the coordinate along the macroscopic flux direction, $\overline{\cos^2(\theta)} = 1/3$ for long randomly oriented capillaries having a vanishing aspect ratio [27], and the factor (N-1)/(N+1) accounts for a correlation effect which arises because of the finite probability that a diffusing molecule returns to a pore that it has just traversed [35, 36]. For the porous substrates examined here, whose microstructure is depicted in Figure 3.2, the assumption of vanishingly small aspect ratio would not appear to be reasonable, and one has [27, 28]

$$\overline{\cos^2(\theta)} = g(x) = 1 + \frac{4x}{3(1+4x^2)} - \frac{2}{3(1+4x^2)^{1/2}} \tag{3.16}$$

where x ($=r_p/l$) is the aspect ratio. Eqn. (3.16) is derived on the assumption that in a pore of finite aspect ratio, the net flow direction is along the direction closest to the macroscopic diffusion direction, as depicted in Figure 3.4.

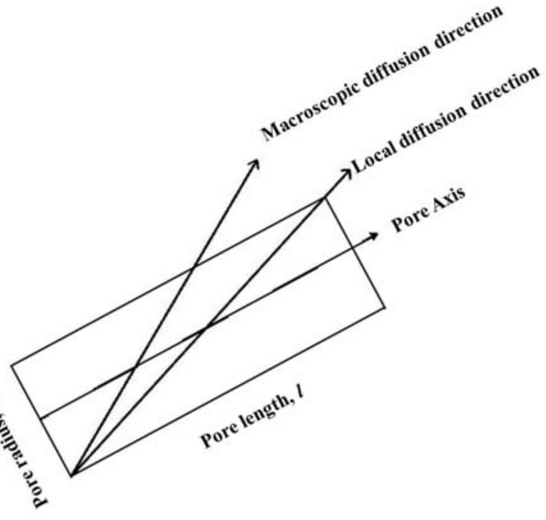

Figure 3.4 Diffusion directions in a pore with finite aspect ratio.

The macroscopic flux is given by

$$j_m = \int_0^\infty j(r_p) f_v(r_p) dr_p \tag{3.17}$$

which combines with eqs. (3.11)-(3.16) to provide

$$j_m = \frac{\varepsilon \lambda_e < l^2 g(x) >}{\pi < r_p^2 l > R_g T} \left(\frac{N-1}{N+1} \right) \left(-\frac{dP}{dz} \right) \tag{3.18}$$

In practice, when interpreting experimental data it is common to evaluate the diffusivity and flux considering only a single representative pore size, $\overline{r}_p$, such as a mean or modal pore size, and the phenomenological expression

$$j_m = \frac{\varepsilon D_o(\overline{r}_p)}{\tau_{app} R_g T} \left(-\frac{dP}{dz} \right) \tag{3.19}$$

where τ_{app} corresponds to the apparent tortuosity already defined in eqn. (3.1), and is obtained by fitting eqs. (3.1) or (3.2) to the experimental permeation measurements. Comparing eqs. (3.18) and (3.19), the theoretical value of the apparent tortuosity is found to be

$$\tau_{app} = \frac{\pi < r_p{}^2 l > D_o(\overline{r}_p)}{< l^2 g(x) > \lambda_e} \left(\frac{Z+1}{Z-1} \right) \tag{3.20}$$

The above equation will be used here to investigate the apparent tortuosity of the macroporous α-alumina substrate with pores of finite aspect ratio.

3.4 Results and discussion

3.4.1 Dependence of tortuosity on operating conditions

As mentioned above, plotting $F\sqrt{T}$ versus $1/\eta\sqrt{T}$ at constant mean pressure should yield a straight line whose slope and intercept provide independent estimates of the tortuosity. Figure 3.5 depicts the variation of $F\sqrt{T}$ with $1/\eta\sqrt{T}$ obtained from experimental permeation data (symbols) of several light gases at a mean pressure of 1.49 bar and 1.24 bar in substrates A and B, respectively, and the corresponding best linear fit (solid lines). The corresponding experimental error is evaluated as:

$$\left|\frac{\Delta\Omega}{\Omega}\right|_{\Omega=F\sqrt{T}}=\sqrt{(\frac{\Delta F}{F})^2+(\frac{\Delta T}{2T})^2} \tag{3.21}$$

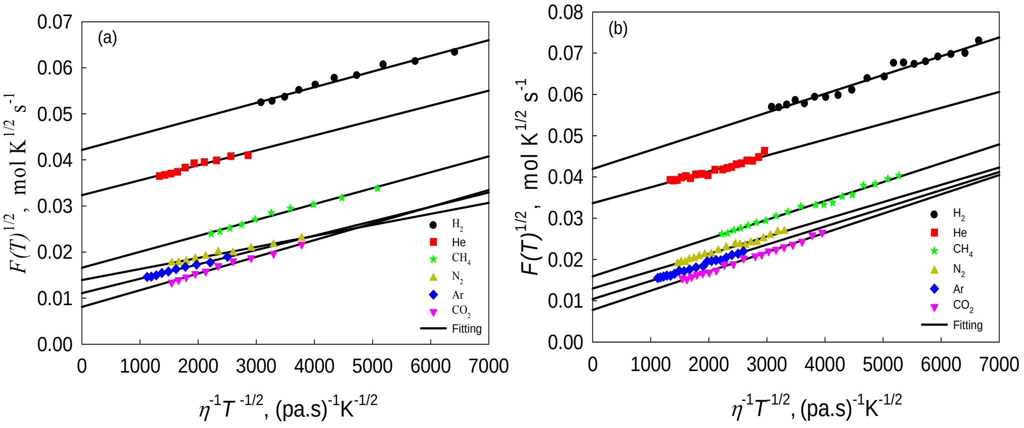

Figure 3.5 Variation of $F\sqrt{T}$ with $1/\eta\sqrt{T}$ for each gas. (a) substrate A, and (b) substrate B. The mean experimental error of $F\sqrt{T}$ is around 5%.

Considering the deviation of bottle volume (1.5 %), the stop watch uncertainty (0.01 s) and the reaction time (0.19 s) [37], the average error of flow rate ($\Delta F/F$) is around 3.5 %. Besides this, the temperature control accuracy of the Lindberg tube furnace is 1 K and the mean experimental temperature is around 440 K, thus the temperature relative error ($\Delta T/T$) is less than 1 %. It is evident that the experimental error for $F\sqrt{T}$ is less than 5 %. In the subsequent chapter, the setup is refined by a bubble flow meter using a wide glass tube (inner diameter around 6 cm) to get more accurate flow rates for the same substrate (sample A) under the same condition. The average flow rate deviation reduces to 2.8 %, which provides the experimental error for $F\sqrt{T}$ less than 4 %. On the other hand, on comparison of the two methods at the same condition, the average difference in flow rate is around 4 %, suggesting water resistance is negligible due to the extremely high velocity of gases from the permeate side. Thus the current water displacement approach is reliable.

The linearity of the data ($r^2 > 0.99$) suggests that eqn. (3.1) appropriately correlates the relationship between flow and temperature for the different gases. Following eqn. (3.1), it is readily seen that the intercept of the lines on the ordinate in Figure 3.5 is related with the relative weight of Knudsen diffusion to the overall flow. This Knudsen contribution corresponds to 30-80% of the total flow-rate in the two substrates for most gases, based on the Knudsen diffusion weights depicted in Figure 3.6. These results are in disagreement with the recent work of Ruthven et al. [26], who arbitrarily assume the viscous contribution to dominate the transport through a similar substrate with a much smaller average pore radius of 50 nm, where the Knudsen contribution is expected to be even larger.

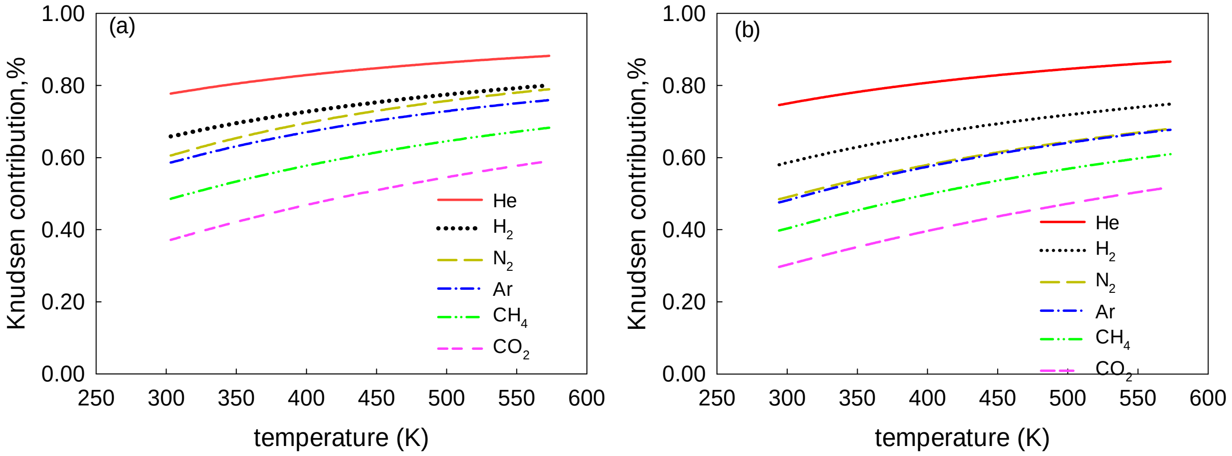

Figure 3.6 Relative contribution of Knudsen diffusion to transport through (a) substrate A, and (b) substrate B.

The intersection of the fitting lines for the different gases in Figure 3.5a reveals that the tortuosity is not gas independent. This is further confirmed by the tortuosity values extracted from the intercept (τ_i) and slope (τ_s) of the lines for each gas using the values of representative pore radius of 288.5 nm and 365.45 nm for substrates A and B, respectively, reported in Table 3.2. In all cases, the tortuosity is considerably lower than 3, which is characteristic of packed beds and, in general, of unconsolidated media [38-40]. It is also seen that there is considerable difference between τ_i and τ_s for both substrates and all of the gases, and that both τ_i and τ_s vary significantly from gas to gas. For instance, the difference in τ_i between N_2 and CO_2 in substrate A is 37%, and in substrate B this difference is 32%. Similarly, the difference between τ_i and τ_s for CO_2 is 26% for substrate A and 65% for substrate B.

Table 3.2 Tortuosity calculated according to slope and intercept of correlation.

Substrate A	τ_i	τ_s	Substrate B	τ_i	τ_s
He	1.77	1.89	He	1.73	1.64
H_2	1.92	1.80	H_2	1.96	1.39
CH_4	1.73	1.77	CH_4	1.83	1.38
N_2	1.56	2.56	N_2	1.70	1.51
Ar	1.64	1.96	Ar	1.77	1.44
CO_2	2.13	1.69	CO_2	2.25	1.36
all gases, Figure 3.7(a)	1.78	1.90	all gases, Figure 3.7(b)	1.91	1.39

To overcome this inconsistency of the tortuosities calculated from the slope and intercept of the linear correlation based on eqn. (3.1), we instead used the pore radius as a second fitting parameter. Thus, the slope and intercept for each gas were used to estimate a tortuosity and effective pore radius. Table 3.3 gives the values obtained for each gas by this procedure. Considerable variation in effective pore radius between different gases is seen in the Table, for each substrate. For example, the pore radius of substrate A based on CO_2 is almost twice that of N_2, while for substrate B it is higher by nearly 50%. In addition, the tortuosity shows considerable variation between gases, indicating that the approach is untenable.

Table 3.3 Mean pore radius and tortuosity of substrates for different gases, based on correlation using eqn. (3.1).

Gas	Substrate A		Substrate B	
	Mean pore radius, r_p (nm)	Tortuosity	Mean pore radius, r_p (nm)	Tortuosity
He	259	1.66	358	1.82
H_2	296	2.05	480	2.77
CH_4	270	1.69	448	2.41
N_2	179	1.08	381	1.91
Ar	231	1.37	418	2.18
CO_2	349	2.69	564	3.75

Alternatively, the tortuosity may be obtained by plotting the data for all of the gases together according to eqn.(3.2), which suggests that plotting $F\sqrt{TM}$ versus $\sqrt{M}/\eta\sqrt{T}$ should produce a straight line with intercept and slope that are independent of the particular gas. Such a plot is depicted in Figure 3.7, however the resulting intercept and slope-based tortuosities for the combined plot, reported in Table 3.2, show significant differences.

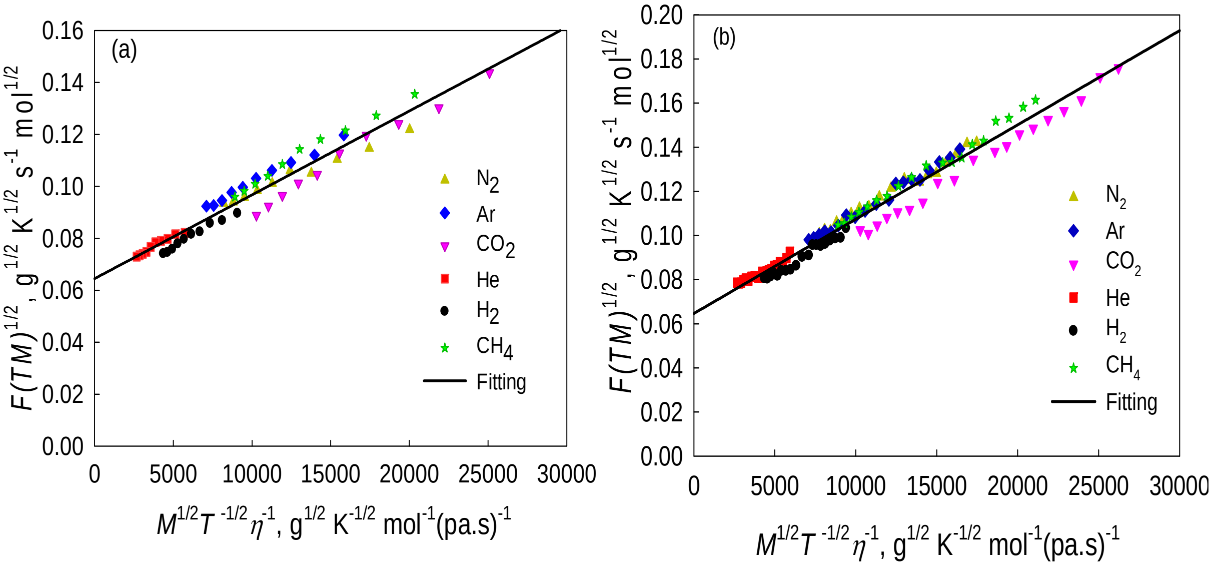

Figure 3.7 Variation of $F\sqrt{TM}$ with $\sqrt{M}/\eta\sqrt{T}$ for several gases in (a) substrate A, and (b) substrate B. The mean experimental error of $F\sqrt{TM}$ is around 5%.

In addition, systematic deviations from the linear fit are seen for different gases. For example, the data for CH_4 are consistently higher, while that for CO_2 is consistently lower. Nevertheless, the difference between τ_i and τ_s is somewhat less for substrate A than it is for substrate B, possibly due to the slightly narrower pore size distribution of former (c.f. Figure 3.2). Thus, the proper choice of representative pore size in the presence of a pore size distribution is an important issue which will affect the difference between the tortuosity values extracted from the slope and intercept of the linear correlation.

The discrepancies between τ_i and τ_s in the graphical methods are caused by the arbitrary choice of representative pore radius, and neglect of pore size distribution. In the case of the combined linear fits in Figure 3.7, the discrepancy is also affected by the assumption that tortuosity is independent of operating conditions, such as temperature, pressure and the particular gas species. As a result, it appears that it is not appropriate to calculate tortuosity by means of the above regression methods. In order to demonstrate the relationship between tortuosity and operating conditions, an apparent tortuosity at each temperature was calculated using eqn. (3.3), and was found to be gas-dependent and to increase with increase in temperature. As an example, the tortuosity for CO_2 in substrate B is plotted against temperature in Figure 3.8, clearly showing a systematic increase in the apparent tortuosity as the temperature increases, and this is not likely to be the consequence of a typical experimental error. When the data in Figure 3.8 were fitted by a linear correlation, the slope was 0.000684 with an error of 0.00015 within a 95% confidence interval. Thus, the slope is statistically significant, and different from zero. As further evidence for statistical significance of the positive effect of temperature on tortuosity, the data of Figure 3.8 was divided into 2 groups, one in which the tortuosity was above the overall average value (group A) and another in which the tortuosity was below this average (group B). Use of the t-test [40] showed the p-value for the null hypothesis (i.e. no difference between the two groups) to be 0.005, which is much smaller than the generally accepted value of 0.05 or less for rejecting the null hypothesis. Thus, the null hypothesis could be safely rejected, and a significant correlation between tortuosity and temperature exists. In the following section we explain the dependence of τ_{app} on T, using the modified EMT described above.

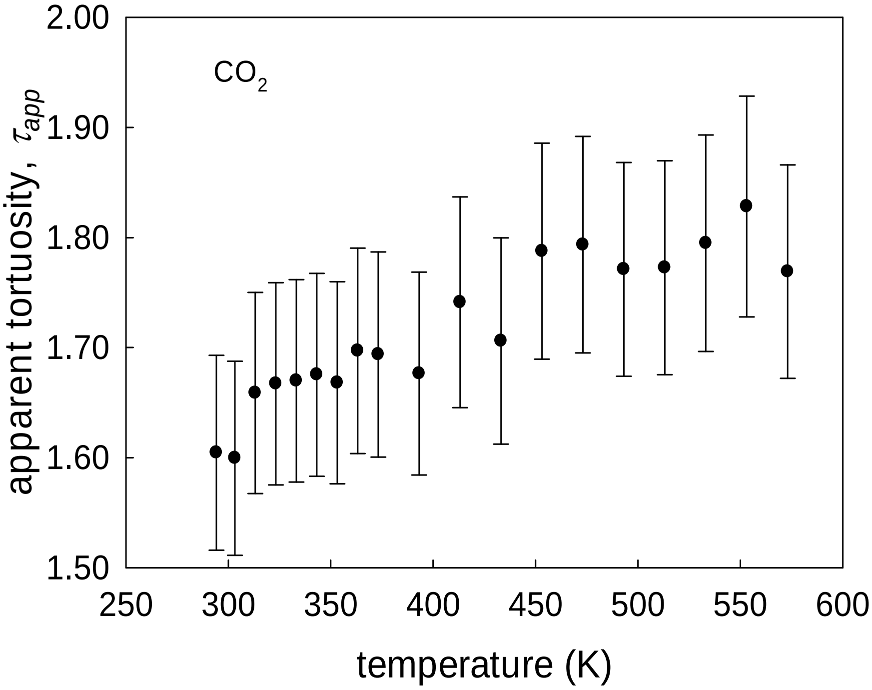

Figure 3.8 Variation of apparent tortuosity with temperature for CO_2 in substrate B, based on eqn. (3.3).

3.4.2 Data interpretation using effective medium theory

In order to investigate the variations of tortuosity of the substrates with temperature and diffusing gas, the modified EMT described in Section 3.3 is adopted. Since neither the pore length distribution nor the pore connectivity can be extracted from the characterization results, a constant length l is assumed and, along with the coordination number N, is taken as a fitting parameter. Figures 3.9a and 3.9b show the variation of $F\sqrt{T}$ with $1/\eta\sqrt{T}$ for the different gases using the best fit values of $N = 12$ and $l = 0.33$ µm for substrate A, and $N = 12$, $l = 0.30$ µm for substrate B. Such high values of the coordination number N are consistent with the close packing of spherical particles, such as in face-centred or hexagonal close packing. The modified EMT predicts well the experimental data for He, Ar, N_2 CH_4 and CO_2, and only marginally overpredicts the data for H_2, suggesting that the selected values for N and l adequately capture the substrate pore network topology. Nevertheless, it must be noted that the current theory assumes cylindrical, straight pores, while the real pores formed by the voids between the alumina particles are clearly irregular. In this sense, the values of N and l should be understood as the effective coordination number and pore length of an equivalent network comprised of ideal cylindrical pores that offers the same overall resistance to flow as the substrate samples.

The increase in the tortuosity with temperature depicted in Figure 3.8 for CO_2 was further verified for all of the gases, demonstrating that both Knudsen and viscous contributions play an important role in the transport through the substrate. As a matter of fact, if Knudsen flow was the only transport mechanism active during the experiments, it is clear that the effective conductance resulting from the solution of eqn. (3.10) would be proportional to $T^{1/2}$, canceling out to $T^{1/2}$, canceling out the $T^{1/2}$ factor from D_o in the numerator of eqn. (3.20) and yielding, as a consequence, a temperature-independent tortuosity. On the other hand, if D_o was purely viscous, it would be proportional again to some function of the temperature which, by a similar argument, would ultimately lead to a temperature-independent tortuosity. The subtle changes in tortuosity with increasing temperature observed in Figure 3.8 are not due to experimental uncertainty, since there is a systematic trend toward higher tortuosities; thus, they can only be due to the combined effect of the two transport mechanisms. However, it is expected to lead to the relative contribution of the two mechanisms to vary with temperature. At low temperatures the viscous contribution will have a higher weight than it has at higher temperatures, as noted in Figure 3.6. More interestingly, a single dominant transport mechanism would also cancel the effect of pressure (P) and molar mass (M), demonstrating the traditional concept of a purely material topology dependent tortuosity to be a limiting case.

Following eqn. (3.20), a tortuosity increasing with increasing T (with l assumed uniform) can only mean that the ratio $\pi < r_p^{\,2} > D_o(\overline{r}_p) / l\lambda_e$ increases with T. This is in fact not surprising since, as T increases, the relative contribution of Knudsen flow in the large pores becomes more important, whereas in the narrow pores, where Knudsen flow is dominant even at the lowest temperature, its relative contribution does not change significantly. Therefore, increasing T is essentially increasing the weight of the Knudsen contribution in the larger pores to the overall flow. However, in the large and highly conductive pores the drop in the viscous diffusion coefficient with temperature arising from an increasing viscosity overweighs the increase in the Knudsen diffusion coefficient, leading to a conductance increasing with temperature. On the contrary, the conductance increases slightly with temperature in the narrow pores as the viscous contribution is negligible. For the particular pore size distribution and connectivity of our sample, the decrease of conductance in the large pores dominates, and the effective conductance obtained from EMT tends to decrease with increase in temperature. At the mean pore radius the conductance was verified to increase with temperature for H_2 and He, and slowly decrease for the other investigated gases. Consequently, the ratio $D_0(\overline{r}_p)/\lambda_e$ increases with temperature, leading to the observed increase in the tortuosity.

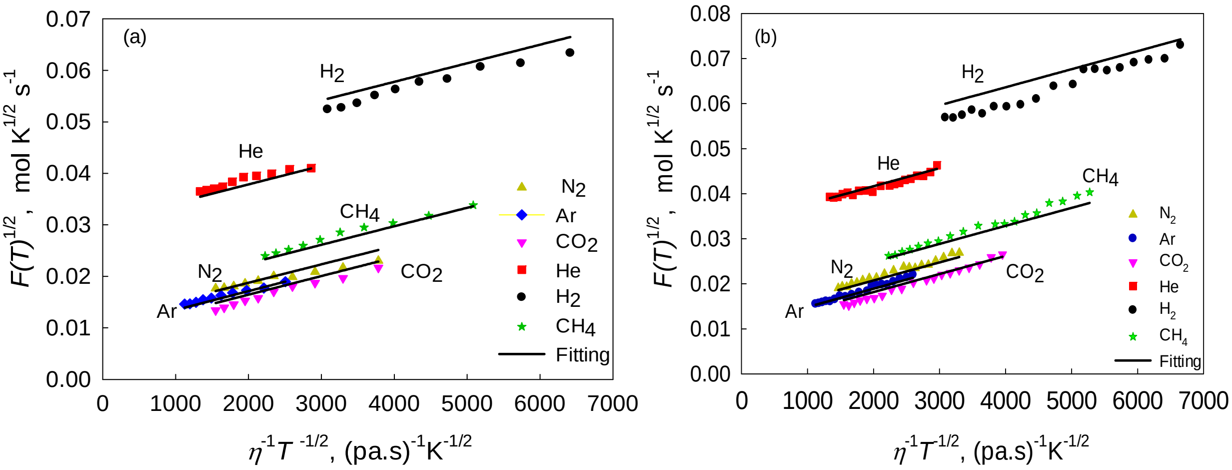

Figure 3.9 Variation of $F\sqrt{T}$ with $1/\eta\sqrt{T}$ in α-alumina substrates for each gas. The symbols represent experimental values, while the lines are model results, with (a) $l = 0.33$ μm and $N = 12$ for substrate A, and (b) $l = 0.30$ μm and $N = 12$ for substrate B. The mean experimental error of $F\sqrt{T}$ is around 5%

The above observations could explain the apparent success of Jareman et al [41] in modeling pure gas permeation as a combination of Knudsen and viscous flow in a MFI film by arbitrarily assuming a constant tortuosity in the γ-alumina interlayer. Due to the very weak changes in tortuosity with temperature and gas species, taking tortuosity constant, as noted in Jareman's work still yields a satisfactory fitting of experimental data. However, assuming viscous flow to dominate transport in the macroporous α-alumina substrate is seriously flawed when modeling supported membrane systems, since the consequence of this is that much of the membrane layer resistance will be transferred to the support. For example, in our case, the Knudsen resistance constitutes over

40-80% of the total resistance for most gases (c.f. Figure 3.6), even for a pore size as large as 500 nm, a pressure of 2 bars in the substrate side and a temperature of 300 K. On the other hand, the agreement between the theoretical and experimental tortuosities (well both below 3) confirms that the transport mechanism through the macroporous alumina is similar to that of a gas diffusing through a micron scale unconsolidated bed, where the aspect ratio plays an important role in the local diffusion direction.

The model pore length of about 0.30 μm is somewhat smaller than the particle size observed in the SEM, which is in the range of 1 - 3 μm (c.f. Figure 3.2). This is explained by the fact that the model pore is perfectly cylindrical, while the real pores synthesized by the packing of roughly spherical particles are irregular, having typically wide mouths of large diffusivity at the ends and a constricted region in the middle, as depicted in Figure 3.10. The large diffusivity mouths lead to an average short pore length when the real pores are idealized into perfectly cylindrical pores of constant diameter. The reason why the experiments with substrate *A* yielded a longer pore length than substrate *B* is because the particles comprising substrate *A* are a little larger than the particles in substrate *B*.

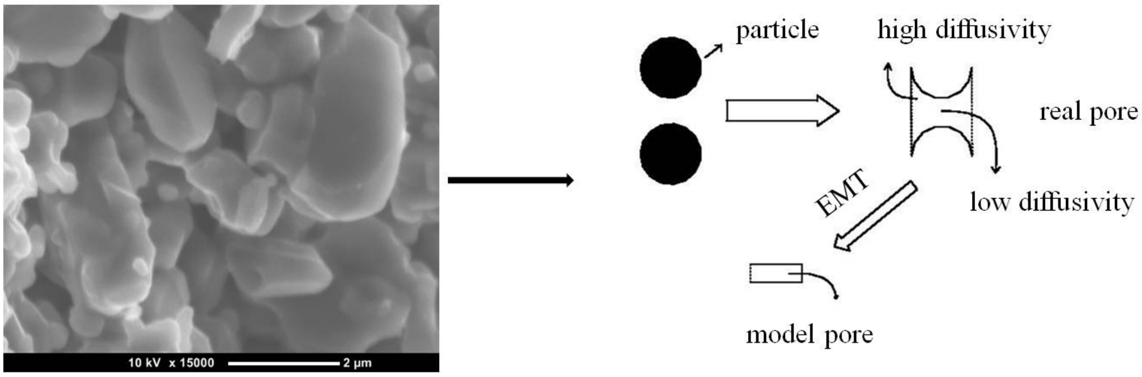

Figure 3.10 Relationship between real pore and idealized cylindrical pore.

3.4.3 Influence of operating conditions

The above results have shown that in the presence of combined Knudsen and viscous flow the apparent tortuosity is not a property of the porous medium alone, but depends also on operating variables such as temperature, pressure, and the gas species.

In the following, we explore the influence of the above factors on the apparent tortuosity by assuming a Rayleigh number pore radius density distribution [14, 17], which is expressed as:

$$f_N(r_p) = \frac{(r_p - r_o)}{(r_m - r_o)^2} e^{-[(r_p - r_o)^2/(r_m - r_o)^2]/2}, \qquad r_o \le r_p \le \infty \tag{3.22}$$

Here, r_o is the minimum pore radius, and r_m is the modal pore radius. The standard deviation of this distribution is readily seen to be

$$s_m = 0.7024(r_m - r_o) \tag{3.23}$$

Figure 3.11 depicts the variation of apparent tortuosity with the relative standard deviation according to eqn. (3.23) for (a) $N = 6$ and (b) $N = 12$ at 300 K and 200 kPa for N_2, Ar, CO_2, He, H_2 and CH_4 in pores with a uniform length of 900 nm. In this and all subsequent figures the reference pore radius $\overline{r}_p$ is taken as the number averaged radius. For $N = 6$ the tortuosity increases as the relative standard deviation increases. At a given mean pore radius, increasing the standard deviation is equivalent to decreasing the minimum pore radius, which in turn increases the availability of both narrow, poorly conductive and large, highly conductive pores as the distribution widens. This leads to the formation of short circuit paths that tend to increase the tortuosity. Furthermore, decreasing the minimum pore radius increases the population of low aspect ratio pores, which, as discussed above, contributes to increasing the tortuosity. However, for $N = 12$ the network availability is very high, and the increase in fraction of large pores dominates on increasing standard deviation, and this leads to decrease in tortuosity. Only subtle discrepancies between the tortuosities of the different gases exist, and such discrepancies vanish at very small standard deviation, indicating that it is the very existence of a pore size distribution that is responsible for a gas dependent tortuosity.

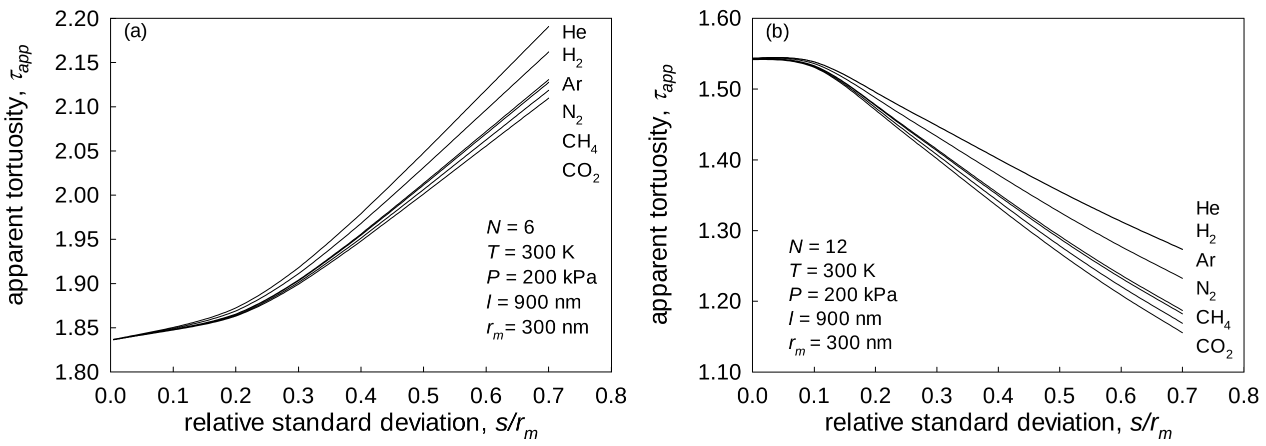

Figure 3.11 Variation of τ_{app} with relative standard deviation for several gases in porous medium following a Rayleigh distribution of pore radius, with (a) $N = 6$, $r_m = 300$ nm, and $l = 900$ nm, and (b) $N = 12$, $r_m = 300$ nm and $l = 900$ nm at $P = 200$ kPa, $T = 300$ K.

Figure 3.12 depicts the variation in tortuosity with (a) relative standard deviation and (b) temperature, for argon at different mean pore radius and at the indicated process conditions, which suggest that, at given pore length, decrease of pore radius will increase the tortuosity. On the other hand, the increase in tortuosity with temperature is in all cases very subtle, which is generally the case in those systems were adsorption is negligible. We notice that increasing the mean pore radius at constant relative standard deviation always decreases the tortuosity. This is not surprising since, as long as the width of the pore size distribution is held constant, it is only the aspect ratio that is the critical variable affecting the tortuosity and, as seen above; higher aspect ratios (wider pores) tend to decrease the tortuosity.

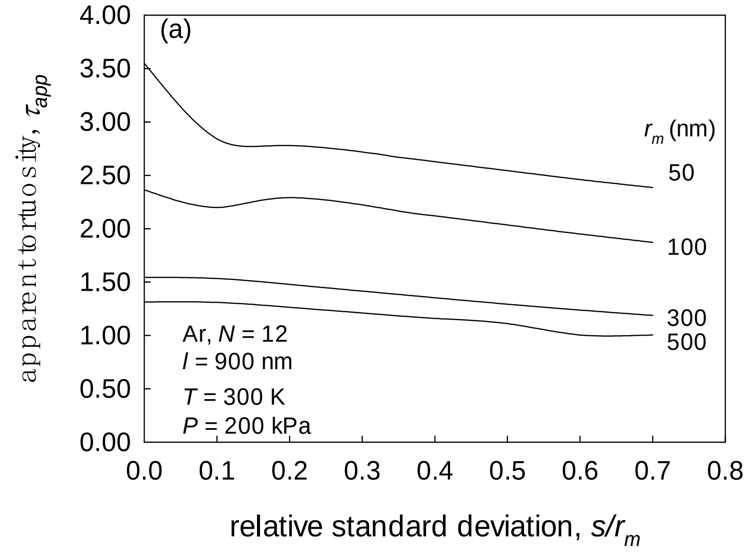

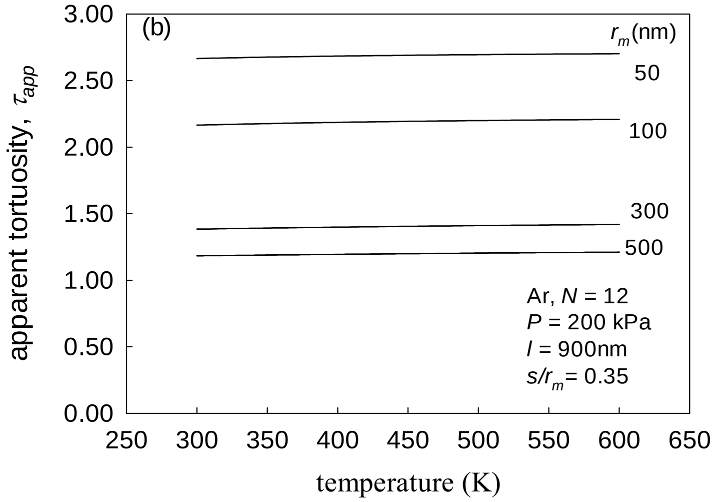

Figure 3.12 Variation of τ_{app} with (a) standard deviation, and (b) temperature for various pore radii in porous medium following a Rayleigh distribution, with N = 12 and l = 900 nm at P = 200 kPa for argon.

Figure 3.13 depicts the variation in tortuosity with temperature at (a) several coordination numbers and (b) several pore lengths, for argon at the indicated process conditions. The decrease of tortuosity with increasing coordination number is quite natural, since the higher N is, the more alternate paths are available at every intersection, decreasing the chance for a molecule to retrace its path. Figure 3.13b leads to an equivalent conclusion to that extracted from Figure 3.12a, confirming that lower aspect ratios tend to increase the tortuosity.

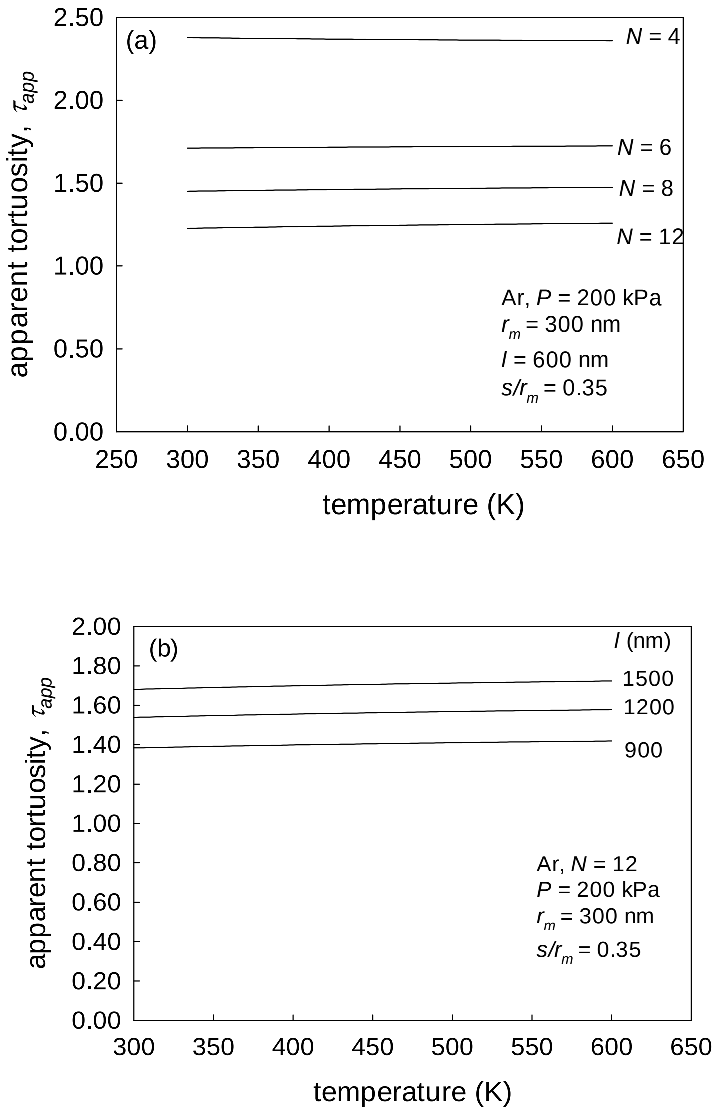

Figure 3.13 Variation of τ_{app} with temperature, for various values of (a) coordination number, and (b) pore length, in porous medium following a Rayleigh distribution of pore radius, with $r_m = 300$ nm and $s/r_m = 0.35$ at $P = 200$ kPa for argon.

Figure 3.14a illustrates the variation of effective conductance, λ_e, with temperature for several gases in a network following a Rayleigh distribution of pore radii with $N = 12$ and $r_\mathrm{m} = 300$ nm at the indicated operating condition. According to Figure 3.14a, the effective conductance decreases monotonically with temperature for all of the gases except for H_2 and He, which is due to the reduction in the viscous diffusion term, which makes the Knudsen contribution increasingly dominant, particularly in the wide pores. However, similar to what was discussed in the previous section, the total diffusion coefficient (i.e. $D_{\mathrm{vis}} + D_{\mathrm{Kn}}$) tends to decrease with increase in temperature in the largest pores because of the effect of increasing viscosity. Since the cross-section area of the widest pores is much larger than that of the narrowest pores, the decrease in conductance with temperature of the former overcomes the effect of the increase in conductance in the latter, leading to a decrease in effective conductance with increase in temperature. For H_2 and He, however, even the large pores are predominantly in the Knudsen regime at all temperatures, which causes an increase in conductance with temperature.

Figure 3.14b depicts the temperature variation of the diffusivity at the mean pore radius, $D_o(\overline{r}_p)$, determined using eqn. (3.6). The mean pore radius is taken here as the number averaged pore radius. In general, the trend is the same as that observed in the effective conductance, although the ratio $D_o(\overline{r}_p)/\lambda_e$ increases with T for all of the gases, leading to a tortuosity that increases with increase in temperature. However, at a coordination number of 4 the decrease in $D_o(\overline{r}_p)$ is faster than that in λ_e for argon, leading to a tortuosity that decreases with increase in temperature, as depicted in Figure 3.13a. This dependence of the temperature variation on the coordination number can be explained by noting that the more interconnected the network is, the greater the probability to have a wide pore in an intersection and, consequently, the stronger the effect of temperature changes is 'felt' over the whole structure.

Figure 3.15 depicts the variation in tortuosity with relative standard deviation at (a) several pressures and (b) several temperatures, for argon at the process conditions indicated in the plot. The apparent tortuosity decreases with increasing pressure (Figure 3.15a) and increases with increasing temperature (Figure 3.15b) in the whole range of relative standard deviation, which is a consequence of the interplay between the Knudsen and viscous contributions to diffusion. At the pressures considered in Figure 3.15a, viscous and Knudsen flow are always present; however, as the pressure increases the curves tend to converge to a limiting curve, termed the viscous limit, since viscous flow starts to become dominant and the tortuosity becomes progressively more independent of process conditions (P and T). The same argument explains the increase of tortuosity with temperature: as T is increased, since the relative contribution of Knudsen flow rises (c.f. Figure 3.6), particularly in the large pores, as discussed above. In the limit of low pressure only Knudsen flow is present and the apparent tortuosity reaches its maximum value, leading to the limiting curve termed the Knudsen limit. Similarly, at very high pressure only viscous flow is exists and the apparent tortuosity reaches its minimum possible value given by the viscous limit.

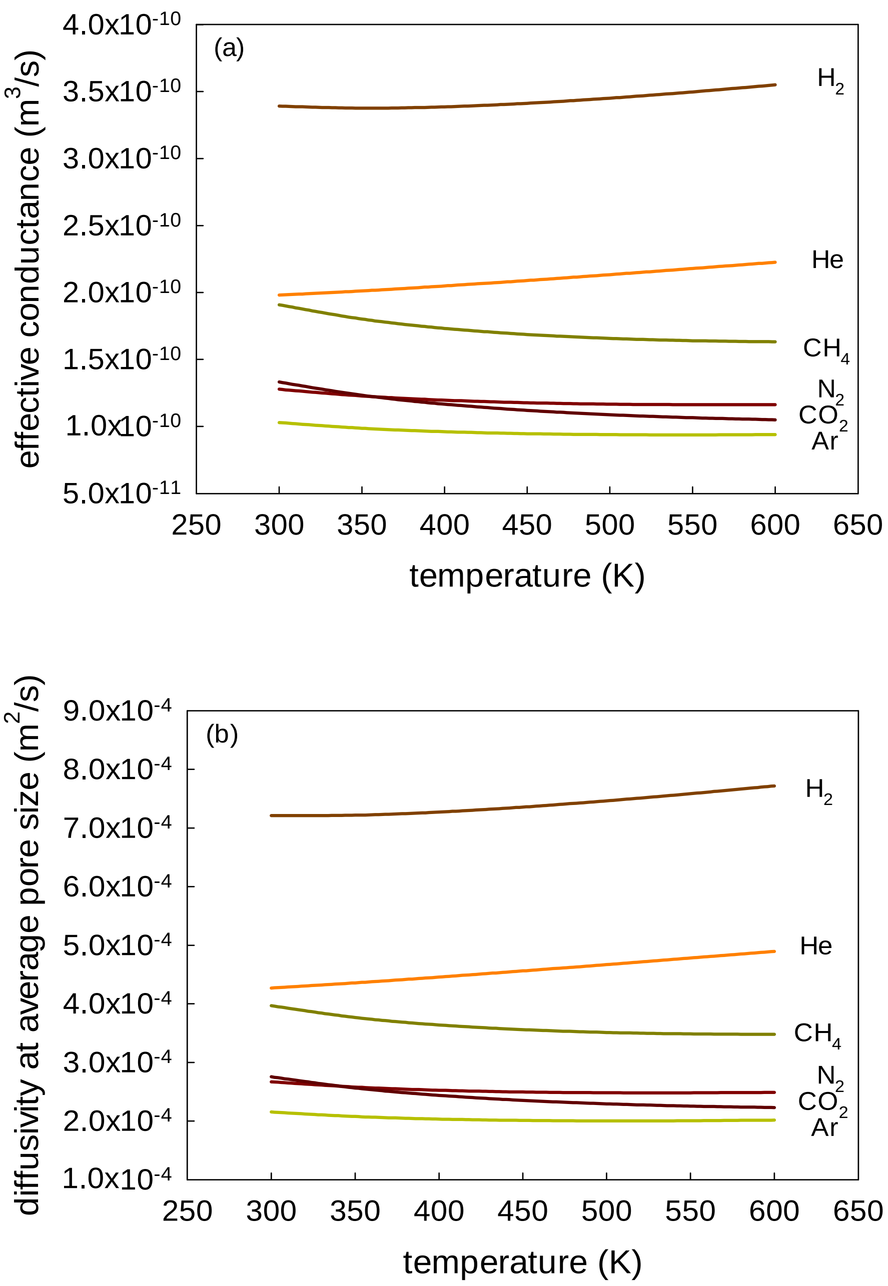

Figure 3.14 Variation of (a) effective conductance, and (b) diffusivity at the number averaged pore radius with temperature for various gases in a porous medium following a Rayleigh distribution of pore radii, with $N = 12$, $r_m = 300$ nm, $s/r_m = 0.35$ and $l = 900$ nm at P=200 kPa.

In summary, in the transition regime between Knudsen and viscous flow, the tortuosity is not only dependent on the properties of the medium but also on operating conditions such as temperature and pressure as well as gas species, due to the combined effect of viscous and Knudsen flows.

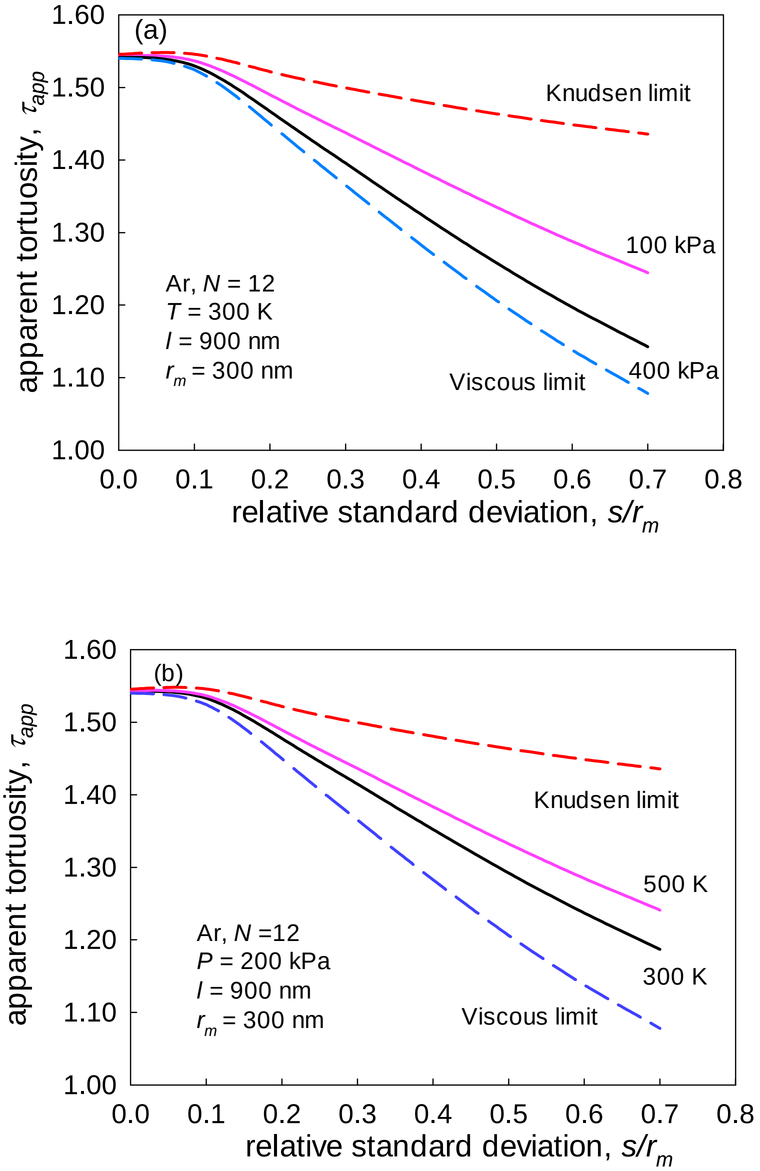

Figure 3.15 Variation of τ_{app} with relative standard deviation, for various values of (a) pressure, and (b) temperature in porous medium following a Rayleigh distribution of pore radius, with N = 12, r_m = 300 nm and l = 900 nm at P = 200 kPa for argon.

3.5 Conclusion

Single gas permeation experiments with six gases (N_2, Ar, CO_2, He, H_2 and CH_4) have been conducted over a wide temperature range in two tubular macroporous α-alumina substrates. The results show that the transport mechanism in the substrates is a combination of viscous and Knudsen flows when the feed pressure is below 2 bars. By using a modified effective medium theory considering the aspect ratio to explore the behavior of the apparent tortuosity for the different gases, it is shown that, in the presence of viscous and Knudsen flow the apparent tortuosity is not a porous medium property alone, but also depends on the operating conditions and the particular gas species. The average coordination number and pore length of the substrate samples constitute the only fitting parameters in the theory. Our results do not support the assumption that viscous flow is dominant in substrates with pore sizes around 50 nm and at low pressure. Instead, our work shows that the contribution of Knudsen flow for all gases in the two substrates, with even much larger average pore sizes, is as much as 80% at low pressure. It could be reasonably expected that, for substrate with much smaller pore size, the influence of viscous flow is negligible at the same pressures. Finally, by assuming a Rayleigh pore size distribution in the substrate, the influence of operating conditions and network parameters is theoretically investigated to show the interplay between aspect ratio and short circuiting effects. We find that, when the aspect ratio decreases, the apparent tortuosity increases, and the tortuosity tends to become more independent of operating conditions when one flow mechanism becomes dominant. Porous ceramic alumina substrates are extensively used in water treatment from contaminants and seawater desalination by liquid filtration [42-44], for which the fluid transport mechanism in pores is dominated by laminar flow. Thus apparent tortuosity based on the viscous limit is expected for such applications.

3.6 References

[1] C.T. Kresge, M.E. Leonowicz, W.J. Roth, J.C. Vartuli, J.S. Beck, Ordered mesoporous molecular sieves synthesized by a liquid-crystal template mechanism, Nature, 359 (1992) 710-712.

[2] D. Zhao, J. Feng, Q. Huo, N. Melosh, G.H. Fredrickson, B.F. Chmelka, G.D. Stucky, Triblock copolymer syntheses of mesoporous silica with periodic 50 to 300 angstrom pores, Science, 279 (1998) 548-552.

[3] Y. Wan, D. Zhao, On the controllable soft-templating approach to mesoporous silicates, Chem. Rev., 107 (2007) 2821-2860.

[4] C.J. Brinker, G.W. Scherer, Sol-Gel Science: The Physics and Chemistry of Sol-Gel Processing, Academic Pr., San Diego, CA, 1990.

[5] Y. Lu, G. Cao, R.P. Kale, S. Prabakar, G.P. López, C.J. Brinker, Microporous silica prepared by organic templating: relationship between the molecular template and pore structure, Chem. Mater., 11 (1999) 1223-1229.

[6] N.K. Raman, C.J. Brinker, Organic "template" approach to molecular sieving silica membranes, J. Membr. Sci., 105 (1995) 273-279.

[7] F. Ye, H. Guo, H. Zhang, X. He, Polymeric micelle-templated synthesis of hydroxyapatite hollow nanoparticles for a drug delivery system, Acta. Biomater., 6 (2010) 2212-2218.

[8] S. Higgins, W. DeSisto, D.M. Ruthven, Diffusive transport through mesoporous silica membranes, Micropor. Mesopor. Mat., 117 (2009) 268-277.

[9] D.M. Ruthven, Response to comments from S.K. Bhatia and D. Nicholson, Chem. Eng. Sci., 65 (2010) 4521-4522.

[10] J.C. Diniz da Costa, G.Q. Lu, V. Rudolph, Y.S. Lin, Novel molecular sieve silica (MSS) membranes: characterisation and permeation of single-step and two-step sol-gel membranes, J. Membr. Sci., 198 (2002) 9-21.

[11] S. Hwang, Fundamentals of membrane transport, Korean J. Chem. Eng., 28 (2011) 1-15.

[12] M. Knudsen, W.J. Fisher, The molecular and the frictional flow of gases in tubes, Phys. Rev., 31 (1910) 586-588.

[13] J. Xiao, J. Wei, Diffusion mechanism of hydrocarbons in zeolites-II. Analysis of experimental observations, Chem. Eng. Sci., 47 (1992) 1143-1159.

[14] S.K. Bhatia, Modeling pure gas permeation in nanoporous materials and membranes, Langmuir, 26 (2010) 8373-8385.

[15] S.K. Bhatia, M.R. Bonilla, D. Nicholson, Molecular transport in nanopores: a theoretical perspective, Phys. Chem. Chem. Phys., 13 (2011) 15350-15383.

[16] S.K. Bhatia, D. Nicholson, Comments on" Diffusion in a mesoporous silica membrane: Validity of the Knudsen diffusion model" by Ruthven, D.M., et al., Chem. Eng. Sci. 64 (2009) 3201-3203, Chem. Eng. Sci., 65 (2010) 4519-4520.

[17] S.K. Bhatia, D. Nicholson, Some pitfalls in the use of the Knudsen equation in modelling diffusion in nanoporous materials, Chem. Eng. Sci., 66 (2010) 284-293.

[18] R. Krishna, J.M. van Baten, An investigation of the characteristics of Maxwell-Stefan diffusivities of binary mixtures in silica nanopores, Chem. Eng. Sci., 64 (2009) 870-882.

[19] R. Krishna, J.M. van Baten, Unified Maxwell-Stefan description of binary mixture diffusion in micro-and meso-porous materials, Chem. Eng. Sci., 64 (2009) 3159-3178.

[20] D. Uhlmann, S. Liu, B.P. Ladewig, J.C. Diniz da Costa, Cobalt-doped silica membranes for gas separation, J. Membr. Sci., 326 (2009) 316-321.

[21] S. Battersby, T. Tasaki, S. Smart, B. Ladewig, S. Liu, M.C. Duke, V. Rudolph, J.C. Diniz da Costa, Performance of cobalt silica membranes in gas mixture separation, J. Membr. Sci., 329 (2009) 91-98.

[22] S. Battersby, S. Smart, B. Ladewig, S. Liu, M.C. Duke, V. Rudolph, J.C. Diniz da Costa, Hydrothermal stability of cobalt silica membranes in a water gas shift membrane reactor, Sep. Purif. Technol., 66 (2009) 299-305.

[23] K. Kusakabe, T. Kuroda, A. Murata, S. Morooka, Formation of a Y-type zeolite membrane on a porous-alumina tube for gas separation, Ind. Eng. Chem. Res., 36 (1997) 649-655.

[24] P. Patnaik, Handbook of inorganic chemicals, McGraw-Hill New York, 2003.

[25] D. Grosso, F. Cagnol, G.J.A.A. Soler-Illia, E.L. Crepaldi, H. Amenitsch, A. Brunet-Bruneau, A. Bourgeois, C. Sanchez, Fundamentals of mesostructuring through evaporation induced self assembly, Adv. Funct. Mater., 14 (2004) 309-322.

[26] D.M. Ruthven, W. DeSisto, S. Higgins, Diffusion in a mesoporous silica membrane: validity of the Knudsen diffusion model, Chem. Eng. Sci., 64 (2009) 3201-3203.

[27] S.K. Bhatia, Capillary network models for transport in packed beds: considerations of pore aspect ratio, Chem. Eng. Commun., 154 (1996) 183-202.

[28] S.P. Friedman, N.A. Seaton, A corrected tortuosity factor for the network calculation of diffusion coefficients, Chem. Eng. Sci., 50 (1995) 897-900.

[29] R.B. Evans III, G.M. Watson, E.A. Mason, Gaseous diffusion in porous media at uniform pressure, J. Chem. Phys., 35 (1961) 2076-2083.

[30] R.B. Evans III, G.M. Watson, E.A. Mason, Gaseous diffusion in porous media. II. effect of pressure gradients, J. Chem. Phys., 36 (1962) 1894-1902.

[31] S.K. Bhatia, D. Nicholson, Friction based modeling of multicomponent transport at the nanoscale, J. Chem. Phys., 129 (2008) 164709.

[32] S.V. Sotirchos, V.N. Burganos, Analysis of multicomponent diffusion in pore networks, AIChE J., 34 (1988) 1106-1118.

[33] P.D. Deepak, S.K. Bhatia, Transport in capillary network models of porous media: theory and simulation, Chem. Eng. Sci., 49 (1994) 245-257.

[34] M. Sahimi, Flow and transport in porous media and fractured rock: From classical methods to modern approaches, Wiley-VCH, 2011.

[35] S.K. Bhatia, Directional autocorrelation and the diffusional tortuosity of capillary porous media, J. Catal., 93 (1985) 192-196.

[36] S.K. Bhatia, Stochastic theory of transport in inhomogeneous media, Chem. Eng. Sci., 41 (1986) 1311-1324.

[37] I.J. Deary, D. Liewald, J. Nissan, A free, easy-to-use, computer-based simple and four-choice reaction time programme: The Deary-Liewald reaction time task, Behav. Res. Methods. , 43 (2011) 258-268.

[38] L. Zhang, N.A. Seaton, Prediction of the effective diffusivity in pore networks close to a percolation threshold, AIChE J., 38 (1992) 1816-1824.

[39] J.H. Kim, J.A. Ochoa, S. Whitaker, Diffusion in anisotropic porous media, Transport Porous Med., 2 (1987) 327-356.

[40] J.A. Currie, Gaseous diffusion in porous media. Part 2.-dry granular materials, Brit. J. Appl. Phys., 11 (1960) 318-324.

[41] F. Jareman, J. Hedlund, D. Creaser, J. Sterte, Modelling of single gas permeation in real MFI membranes, J. Membr. Sci., 236 (2004) 81-89.

[42] F. Patel, M.A. Baig, T. Laoui, Processing of porous alumina substrate for multilayered ceramic filter, Deslin. Water Treat., 35 (2011) 33-38.

[43] M.T.M. Pendergast, E.M.V. Hoek, A review of water treatment membrane nanotechnologies, Energ. Environ. Sci., 4 (2011) 1946-1971.

[44] F.F. Nazzal, M.R. Wiesner, pH and ionic strength effects on the performance of ceramic membranes in water filtration, J. Membr. Sci., 93 (1994) 91-103.

Chapter 4: The transport of gases in a mesoporous γ-alumina supported membrane

In this chapter, we investigate the low pressure diffusion of several gases in a mesoporous γ-alumina membrane of pore diameter 10.4 nm, coated on a macroporous α-alumina tubular substrate. Transport data for the uncoated substrate is also separately obtained and interpreted using the conventional slip flow correlation with a single representative pore size, and with effective medium theory while considering the entire pore size distribution. It is shown that the conventional correlation based on a single pore size yields significant anomalies in the tortuosity and pressure profile for all gases, which are eliminated on using the effective medium theory, demonstrating the importance of considering the pore size distribution (PSD). These anomalies lead to failure of the correlation for the membrane layer.

The effective medium theory is also extended to the disordered membrane layer, using the classical slip flow model and a version corrected for finite molecular size, as well as the Oscillator model developed in this laboratory. All the diffusion models fitted the experimental data accurately, without the artifacts observed with the commonly used single pore size model. The results make evident the importance of correctly taking the pressure profile into account, in any investigation for a multi-layered supported membrane (*i.e.* with a macroporous substrate and a mesoporous membrane layer). It is seen that the slip flow model leads to significantly higher apparent diffusivities than the Oscillator flow model at small pore sizes. Nevertheless, the performance of all three diffusion models is comparable, and it is not possible to distinguish between them for the large pore diameter of 10.4 nm of the mesoporous γ-alumina membrane layer. The results unequivocally show that it is critical to consider the full PSD for each layer rather than using a single representative pore size in modelling membrane transport, and in interpreting experimental permeability data.

4.1 Introduction

The achievement of technical advances in a variety of fields, such as catalysis, adsorptive separation and drug delivery requires a deep understanding of infiltration of fluids through nanoconfined spaces, as well as the development of porous materials with controllable structures, and the systematic tailoring of pore architecture [1-3]. In the last few decades numerous carbon-based [4, 5] and inorganic [6-8] nanoporous materials, and high quality membranes with a variety of applications have been synthesised by various methods such as sol-gel processing [9, 10], chemical vapour deposition (CVD) [11] and hydrothermal techniques [12]. All these developments have stimulated considerable interest in the modeling and simulation of fluid behaviour in such materials [13-17]. These works have highlighted significant deficiencies in existing approaches, which have been developed based on the assumption of negligible interaction between the fluid and solid. Nevertheless, the majority of modern work has followed the Dusty Gas Model (DGM), which utilises this assumption, while arbitrarily superposing the pore wall-affected and hydrodynamic fluxes [18].

When the pores are far larger than the range of the potential field of the wall, the pore wall-affected diffusion is dominated by fluid-wall collisions and represented by the classical Knudsen model [19, 20]. In that case, an appropriate estimate of the flow rate in tubular substrate is given by [2]

$$F\sqrt{T} = \frac{2\pi L\Delta P\varepsilon}{\tau_{app}\ln(R_o/R_i)}\left(\frac{\bar{r}_p^{\,2}\bar{P}}{8R_g\eta\sqrt{T}} + \frac{97\bar{r}_p}{R_g\sqrt{M}}\right) \tag{4.1}$$

or

$$F\sqrt{TM} = \frac{2\pi L\Delta P\varepsilon}{\tau_{app}\ln(R_o/R_i)}\left(\frac{\bar{r}_p^{\,2}\bar{P}\sqrt{M}}{8R_g\eta\sqrt{T}} + \frac{97\bar{r}_p}{R_g}\right) \tag{4.2}$$

Here, the term $\ln(R_o/R_i)$ accounts for the change in curvature over the thickness of the tube, with R_o (m) and R_i (m) the outer and inner tube radii, respectively. Further, T is temperature (K), L (m) is the tube length, $\bar{P}$ is the average pressure (Pa), η is fluid viscosity (Pa.s), M represents the fluid molar mass (g/mol), R_g is the gas constant, ε is the substrate porosity and τ_{app} the apparent tortuosity coefficient of the porous medium. $\bar{r}_p$ (m) is a selected representative pore radius in the porous medium, which is used as a reference to estimate the apparent tortuosity from measurements of F (moles/s).

Although the classical Knudsen model can successfully predict the experimental data for transport in macroporous materials at low pressures, the application of the Knudsen diffusion model in mesoporous materials has been the subject of criticism because the dispersive interaction between the fluid and the pore walls is not negligible [16, 21]. Indeed, it has been extensively found that interpretation of experimental data using the Knudsen model in such small pores leads to unrealistically high tortuosities, indicating significant overestimation of the diffusivity [22-24].

Molecular level modeling of the transport, in particular molecular dynamics (MD) simulation, is finding increasing use in predicting pore diffusivity, and has shown that the Knudsen approach overpredicts the diffusivity for 2 and 3 nm silica pores [16, 23, 25]. However, due to its computational intensity, the MD method is still impractical for use in interpreting experiment results in disordered materials, and a new tractable theory founded on molecular principles is of considerable interest. Extraordinary success has been achieved recently in this laboratory, with the development of a statistical mechanical theory [26, 27], termed as 'Oscillator model', which considers dispersive interactions, overcoming the limitations of the Knudsen model. By comparing the Knudsen and Oscillator model diffusivities with MD results for silica pores, it has been shown that the Knudsen equation overestimates the diffusivity even for a pore diameter of 10 nm [26]. This situation depends on the strength of the solid-fluid interaction, and the extent of the discrepancy will vary with the structure and chemical composition of the pore walls.

The application of any model to interpret data on the transport in a supported membrane requires individual consideration of the resistance of the membrane and support layers. In practice, an inorganic membrane system is fabricated in an asymmetric fashion, consisting of a thin selective ("active") top layer with narrow pores in the region of molecular sieving dimensions, in which separation occurs. The top layer is generally deposited on interlayers followed by a relatively thick substrate with wide pores to enhance mechanical resistance while minimising the resistance to flow. Asymmetric alumina tubes consisting of a α-alumina thick substrate (1 - 2 mm) and a γ-alumina interlayer are usually selected as the support [28-30]. The α-alumina layer is made of packed crystal particles (~ 3 μm) to create macropores and provide mechanical resistance [31], while the crystal particles of γ-alumina are much smaller (~0.05 μm) [32], and are coated over the surface of the α-alumina layer to produce a uniform, defect-free surface over which the active layer is deposited.

Since the interfacial pressures between layers are not directly measurable, the analysis of diffusion through the substrate and the interlayer is often based on arbitrary hypothesis regarding the dominant transport mechanism in the substrate. As an example, some authors assume dominance of viscous flow in the support [33], which permits a reasonable membrane tortuosity (around 3) but is in disagreement with straightforward theoretical estimates of the relative resistances for Knudsen and viscous flow [21, 34]. Depending on the pore structure of a material, the theoretical tortuosity range varies between unity and infinity; however, it is generally in the range of 4-10 for consolidated materials [35, 36], and below 2 for unconsolidated materials [37, 38].

Indeed, a recent study from this laboratory [2] has experimentally verified that such assumptions are incorrect, and that at low pressure Knudsen diffusion is the dominant transport mechanism in a symmetrical macroporous α-alumina substrate having a mean pore size of a few hundred nanometers [2]. Furthermore, most conventional correlations rely on the hypothesis that the tortuosity is fully determined by the material topology; however, in our previous work it has been extensively confirmed that tortuosity depends weakly on the operating conditions due to the interplay between Knudsen and viscous diffusion in the slip flow regime [2]. This makes the investigation of the diffusion in a supported membrane much more complicated, as a single tortuosity cannot be used to describe the transport of different gases at different temperatures. In addition, the thickness of the interlayer or membrane layer is generally kept very small (several microns) in order to permit high permeation rates [39, 40]. As a consequence, the interlayer pressure and the actual driving force through the membrane is unknown, and it is presumably quite sensitive to the gas species and operating conditions, differing significantly from values derived using empirical correlations which ignore the pore size distribution (PSD) or make arbitrary assumptions regarding the dominant flow resistance through the support.

As a result of the above complexities, it is important for the support resistance to be separately investigated, and correctly accounted for, in interpreting transport data for a supported membrane. Studies with a 2-layer system (γ-alumina interlayer over α-alumina substrate) will permit unequivocal understanding of the mechanism of fluid transport in the mesoporous γ-alumina layer coated on the macroporous substrate, and validate the applicability of the Knudsen model in the γ-alumina mesopores. This understanding will be critical to interpreting data for transport in a three-layer membrane, and obtaining fundamental insight into the mechanism and governing resistance for flow in the selective layer deposited over the γ-alumina interlayer. Therefore, following the steps of our previous work, we developed here three different methods to explore the diffusion mechanisms in a simple mesoporous γ-alumina supported membrane, while considering the resistance of the substrate and membrane layer. The technique provides good agreement with experimental data and proves to be valuable for extracting information on how the interlayer pressure and tortuosity is influenced by the operating conditions, such as temperature and gas species.

4.2 Materials characterization and experiments

The α-alumina tubular substrate was obtained from Australia Chemtech Trading & Service Company, and is made of packed α-alumina particles sintered at high temperature. The pore size distribution of the substrate was obtained using Mercury Porosimetry (Micrometrics, IV 9500), and is depicted in Figure 4.1. The porosity and skeletal density extracted from Mercury Porosimetry were 33.3% and 3.85 g/mL, respectively, very similar to the density of 3.96 g/mL obtained through Helium Pycnometry. The similarity between the Mercury Porosimetry and Helium Pycnometry-based densities reveals that most of the voids in the substrate correspond to macropores, confirming the reliability of the PSD determined through Mercury Porosimetry in Figure 4.1. The corresponding pore volume and surface area are 0.13 cm^3/g and 1.01 m^2/g, respectively, which were subsequently used to estimate the representative pore radius. To further understand the substrate structure, Scanning Electron Microscopy (SEM) images can be found in our recent work [2], which suggest that the size of the substrate particles was around 2-3 μm.

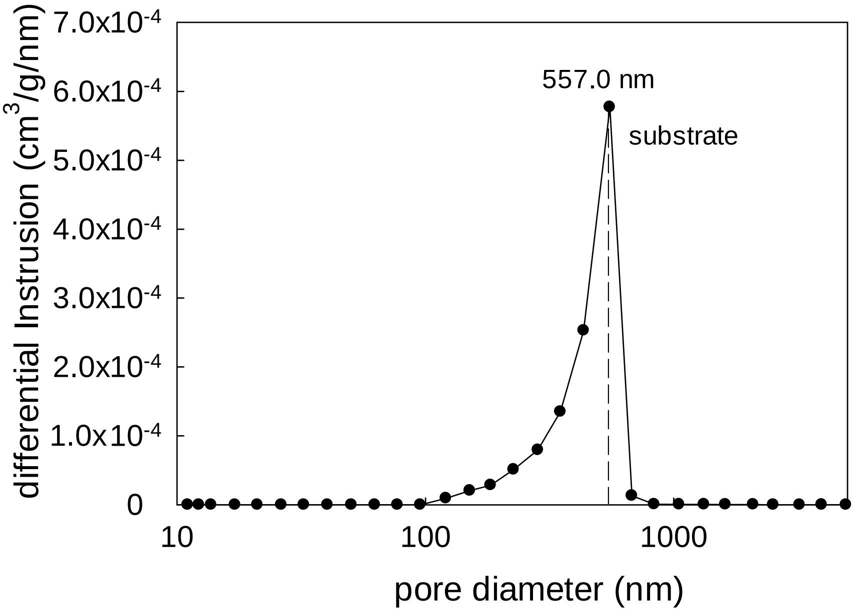

Figure 4.1 Pore size distribution of the substrate determined by mercury porosimetry.

The membrane layer was prepared from a γ-alumina solution (20 wt%) purchased from Sigma-Aldrich, with an average particle sizes of about 50 nm, as verified through the SEM micrograph in Figure 4.2.

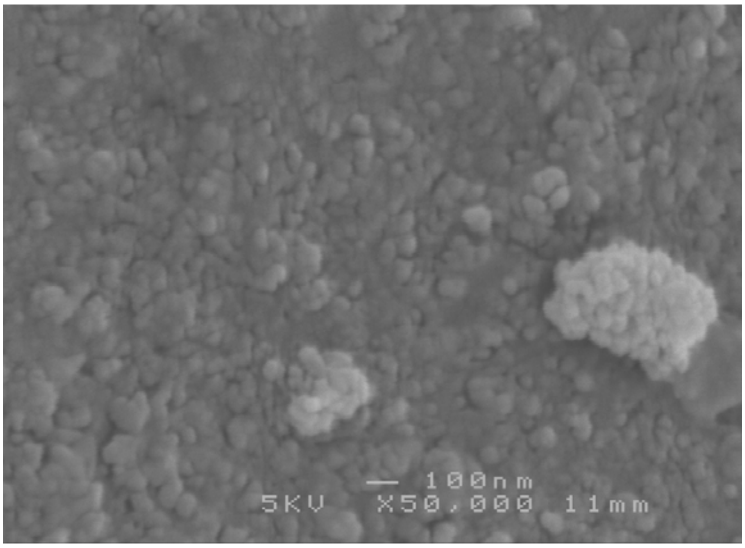

Figure 4.2 SEM image of the uncalcined γ-alumina powder

The γ-alumina solution was diluted to 2 wt% with deionized water, and coated onto the outer cylindrical substrate, while the inner surface was sealed during the dip-coating process. Subsequent to coating and drying in a temperature controlled oven at 40 ºC for 2 hours, the membrane was calcined at 700 ºC for 2.5 hours. In order to make a nearly defect-free membrane, ten alumina layers were coated over the outer surface of the substrate, where each layer was coated, dried and calcined under the same conditions as the first layer. The remaining diluted solution was dried and calcined under the same conditions as the supported membrane to obtain agglomerated γ-alumina powder, which was characterized by nitrogen adsorption at 77 K by using a Micrometrics ASAP2020. The pore size distribution of this agglomerated powder was taken to represent the pore structure of the γ-alumina membrane layer.

The N_2 adsorption isotherm was analyzed by nonlocal density function theory (NLDFT) assuming cylindrical pores with oxide surface, and the obtained pore size distribution is plotted in Figure 4.3.

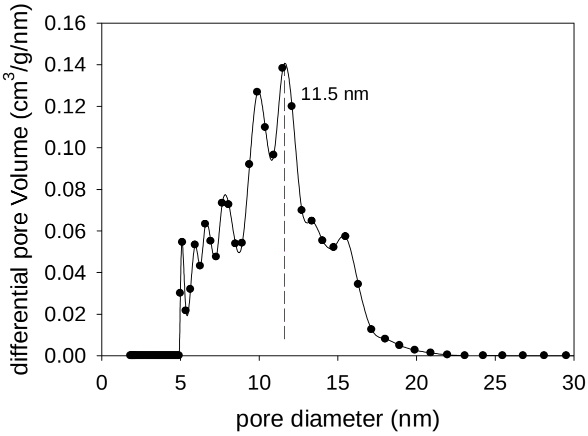

Figure 4.3 Pore size distribution of the calcined γ-alumina powder, obtained by nonlocal density function theory (NLDFT) interpretation of N_2 adsorption data.

The corresponding pore volume and surface area are 0.48 cm^3/g and 164.15 m^2/g, respectively, which were subsequently used to estimate the porosity and representative pore radius. The skeletal density of the γ-alumina powder measured by helium pycnometry was 3.09 g/mL, significantly smaller than the reference density between 3.6 and 4.0 g/mL [41], indicating the presence of voids inaccessible to He inside the γ-alumina particles or their agglomerates. The accessible porosity of the powder was determined by

$$\varepsilon = \frac{V_p \rho}{1 + V_p \rho} \tag{4.3}$$

in which V_p is the pore volume obtained through the NLDFT characterization, and ρ is the true density from Helium Pycnometry. Following eqn. (4.3), the accessible porosity of the alumina powder is estimated to be 0.57.

The thickness of the supported layer (*z*) is difficult to determine precisely since the boundary between the membrane layer and the substrate is somewhat diffuse. This is clearly demonstrated in the SEM micrographs (Figure 4.4), where the thickness varies between 1.37 and 2.32 μm. The variation in film thickness is attributed to the underlying topology of the α-alumina substrate, which varies in height and has a high roughness. As a result of the thin γ-alumina film coating, a more homogeneous and smooth layer is formed, although with slightly varying thickness. Based on these micrographs, an average value of $z = 2$ μm was considered a suitable estimate for the present calculations. In order to estimate an appropriate tortuosity, in this work a representative cylindrical pore size for the substrate and membrane layers in eqs. (4.1) and (4.2) is based on

$$\bar{r}_p = \frac{2V_p}{S} \tag{4.4}$$

where *S* is the surface area obtained through the Mercury Porosimetry or NLDFT characterization. This definition of the representative pore radius is perhaps the most common, although other alternatives such as the peak size of the PSD or number averaged pore radius have also been used [2]. Following eqn. (4.4), the obtained $\bar{r}_p$ is 257.05 nm for the substrate and 5.22 nm for γ-alumina membrane layer.

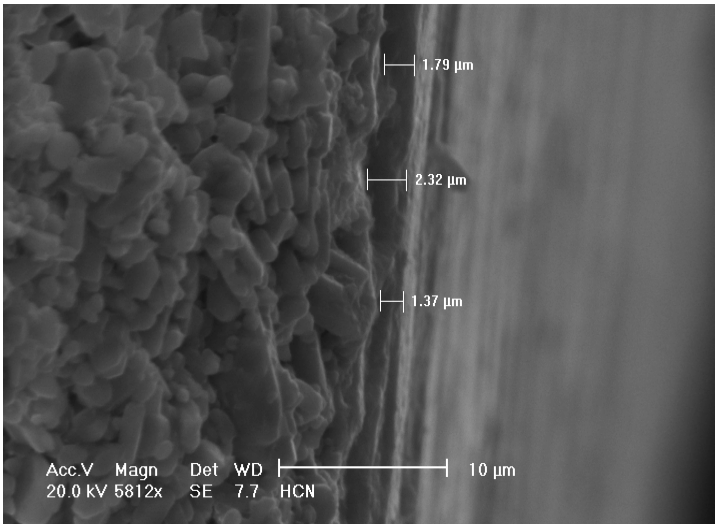

Figure 4.4 SEM image of the interfacial region between the substrate and the membrane layer.

The transport mechanism in the substrate has been previously examined based on the commonly used correlations in eqs. (4.1) and (4.2) with the flow rate measured by the water displacement method [2]. However, the resistance of water becomes increasingly more important when the membrane layer is deposited on the substrate surface. To minimize the experimental error, more accurate measurement of the flow rate through the substrate alone and the supported membrane were therefore made here using a bubble flow meter.

The membranes were tested in a dead-end mode, where one end of the membrane was sealed so gases had to diffuse through the membrane. Permeation experiments were conducted on the substrate and the supported membrane, respectively, by flowing six gases (H_2, He, CH_4, N_2, Ar and CO_2) at a constant feed pressure, P_F =1.97 bar, and several temperatures ranging from 30 to 300 ºC; the outlet pressure (P_o) corresponds to atmosphere pressure (1.01 bar). Schematic drawings indicating the direction of gas flow through the substrate and supported membrane are illustrated in Figure 4.5, in which the volumetric flow rate is measured by a bubble flow meter and later converted to molar flow rate by means of the ideal gas equation of state. In the sketch, P_1 represents the interfacial pressure between the α-alumina substrate and the γ-alumina layer. It is noted that the permeation experiments was carried out from high temperature (300 ºC) to low temperature (30 ºC) to avoid any water blockage effect.

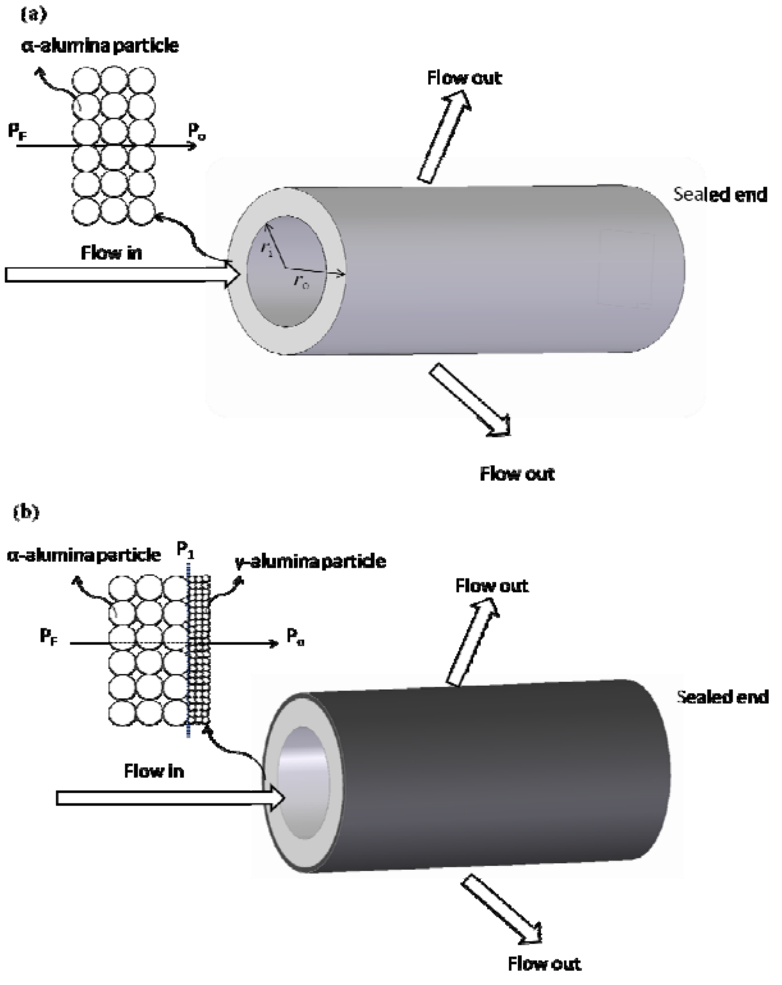

Figure 4.5 Schematic drawing of the flow direction in (a) the substrate, and (b) the supported membrane.

For clarity, the flow rate in the substrate and the membrane, although equal at steady state, are labeled as F_s and F_c, respectively. Besides, the structure parameters (porosity, tortuosity, tube length and average pore size) of the substrate and the membrane layer are identified by subscripts *s* and *c*, respectively, unless stated otherwise.

4.3 Transport models

4.3.1 Transport in a single pore

The gas diffusivity in a single pore is highly related to its pore size, which is defined in several different ways as depicted in Figure 4.6. For pores much larger than the fluid molecules for which the density is approximately constant along the radial coordinate (K=1), the diffusivity is estimated based on the geometrical radius (r_s), which is the distance between the centreline of the pore and the surface atoms on the walls.

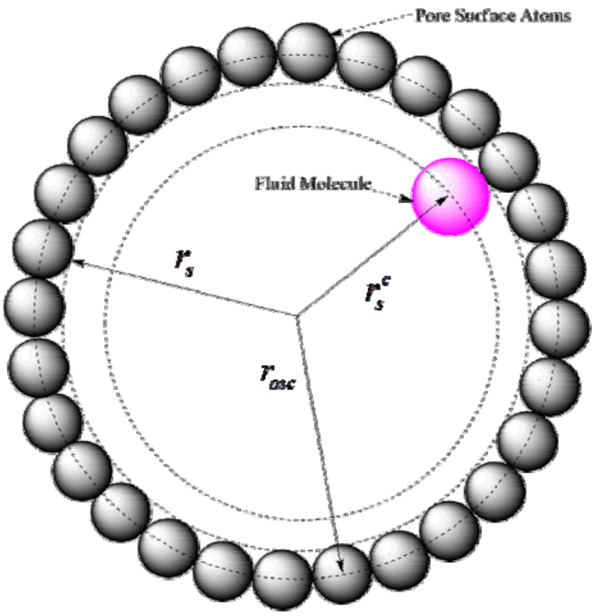

Figure 4.6 Illustration of different pore radii used in the classical Knudsen model (r_s), the corrected Knudsen model (r_s^c), and the Oscillator model (r_{osc}).

Slip flow has been extensively validated in the macroporous substrate at low pressure [2], for which the Knudsen (D_{Kn}) and viscous diffusivity (D_{vis}) are given by

$$D_{Kn} = 97 r_s \sqrt{\frac{T}{M}} \tag{4.5}$$

$$D_{vis} = \frac{\bar{P} r_s^2}{8\eta} \tag{4.6}$$

Since the macropores in the substrate are larger than 100 nm, based on the PSD in Figure 4.1, and are much larger than the fluid molecular size, eqs. (5) and (6) can be safely used to predict the apparent diffusivity ($D_o^a = D_{Kn} + D_{vis}$) in the substrate, neglecting any exclusion effects due to finite molecular size.

For smaller pores in which the finite size effect of the fluid molecules must be taken into account, the pore radius must be corrected as

$$r_s^c = r_s - \sigma_{ff}/2 \tag{4.7}$$

where σ_{ff} is the Lennard-Jones (LJ) fluid-fluid collision diameter, which is listed in Table 4.1 for the gases in this work. This applies to the mesopores in the membrane layer, for which the apparent diffusivity ($D_o^c = D_{Kn}^c + D_{vis}^c$) may be predicted based on the corrected pore radius (r_s^c) through eqs. (4.5) and (4.6), while neglecting adsorption and effects of inhomogeneity (i.e. considering that the equilibrium constant $K = 1$).

Table 4.1 Fluid-fluid Lennard-Jones parameters [23] used in the Oscillator model.

Parameters	H_2	He	CH_4	N_2	Ar	CO_2
σ_{ff} (nm)	0.2915	0.2551	0.381	0.3572	0.341	0.3472
ε_{ff}/k_B (K)	38.0	10.22	148.2	93.98	120.0	221.9

An alternative method to estimate the apparent diffusivity in the membrane layer is based on the recently developed Oscillator model [27], which considers the (low-density) radial density profile inside the pores. The pore radius used in the Oscillator model is the distance between the centreline of the pore and the centre of the surface atoms on the walls, r_{osc}, defined as

$$r_{osc} = r_s + \sigma_{ss}/2 \tag{4.8}$$

where σ_{ss} is the Lennard-Jones (LJ) solid-solid collision diameter. In the γ-alumina, the surface is assumed to consist of a surface layer of oxygen atoms, thus the oxygen atom radius, is be added to the geometrical pore radius r_s in Figure 4.3, to yield r_{osc}. According to the Oscillator model, for the diffusion of a LJ fluid under conditions of diffuse reflection in a cylindrical pore the diffusivity (D_{osc}) is given as

$$D_{osc} = \frac{2}{\pi m Q} \int_0^\infty e^{-\beta\varphi(r)} dr \int_0^\infty e^{-\frac{\beta p_r^2}{2m}} dp_r \int_0^\infty e^{-\frac{\beta p_r^2}{2mr^2}} dp_\theta \int_{r_{co(r,p_r,p_\theta)}}^{r_{cl}(r,p_r,p_\theta)} \frac{dr'}{p_r(r',r,p_r,r_\theta)} \tag{4.9}$$

where $\varphi(r)$ is the solid-fluid potential, m is fluid particle mass, $\beta = 1/k_B T$ and $Q = \int_0^\infty \exp(-\beta\varphi(r)) r dr$. Further, p_r and p_θ are the radial and angular components of the molecular momentum, while r_{cl} and r_{co} represent the radial bounds of a fluid molecule trajectory between consecutive diffuse reflections, extracted from the solution of $p_r(r', r, p_r, r_\theta) = 0$. Details of the derivation of eqn. (4.9) can be found elsewhere [1]. The equilibrium constant is given by

$$K = \frac{2}{r_{osc}^2} \int_0^{r_{osc}} e^{-\varphi(r)/k_B T} r dr \tag{4.10}$$

and the apparent diffusivity based on the pseudo-bulk concentration gradient is then estimated as $D_o^{osc} = D_{osc} K$, with viscous transport considered to be negligible in the mesoporous membrane layer. The value of $\varphi(r)$ depends strongly on the pore wall structure. In this work, the pore walls in the membrane layer are assumed to be infinitely thick and comprised of closely-packed LJ sites. The integration of the LJ interaction potential over the wall volume yields [42],

$$\varphi(r) = \pi^2 \varepsilon_{sf} \rho_v \sigma_{sf}^3 \left\{ \frac{7 F_h(-4.5, -3.5, 1; (r/r_{osc})^2)}{32 (r_{osc}/\sigma_{sf})^9 \left[1 - (r/r_{osc})^2\right]^9} - \frac{F_h(-1.5, -0.5, 1; (r/r_{osc})^2)}{(r_{osc}/\sigma_{sf})^3 \left[1 - (r/r_{osc})^2\right]^3} \right\} \tag{4.11}$$

Here σ_{sf} is the LJ solid-fluid collision diameter, ε_{sf} is the LJ potential well depth, ρ_v is the pore wall density (atoms per unit volume) and $F_h(x, y, z; w)$ is the Hypergeometric function. An alternate expression assuming a single layer pore wall has been derived elsewhere [43], and was used in recent work [23]; however, here we use the expression in eqn. (4.11), given the large size of the γ-alumina particles (~ 50 nm) comprising the pore walls compared to the length scale of the LJ interaction (~ $3\sigma_{sf}$). The Lennard-Jones (LJ) parameters of the different gases used in our experiments are given in Table 4.1, and the LJ parameters for the γ-alumina are taken from Blas et al. [44] as $\varepsilon_{ss}/k_B = 108.47$ K, $\sigma_{ss} = 0.303$ nm, with $\rho_v = 52.24$ nm^{-3}. The Lorentz-Berthelot mixing rules are employed to evaluate the fluid-solid LJ parameters ε_{sf} / k_B and σ_{sf} [26].

4.3.2 Transport in pore networks

As mentioned above, a key factor hindering the application of transport theories to the interpretation of experimental data or its incorporation in process design is the complexity of the material topology, which involves variables such as connectivity and PSD. Effective medium theory provides a method to account for these variables by replacing the nonuniform network with a uniform one where all pores offer the same resistance to flow. The inverse of that resistance is what is called the effective conductance. In our previous work [2], we have already applied this technique to model the transport in the substrate at low pressure, and the tortuosity was confirmed to vary with temperature due to the interplay between Knudsen and viscous diffusion. However, the previous methodology can only be used in the macroporous homogenous tubular substrate where the driving pressure gradient is well defined. For a heterogeneous supported membrane consisting of a macroporous substrate and a mesoporous γ-alumina layer the pressure gradient through each layer cannot be measured directly; consequently, the apparent tortuosity for each layer cannot be determined and the methodology is untenable. In order to eliminate the uncertainty on the tortuosities, a method based on flow rate is developed here, which is applicable for the homogenous substrate by itself as well as to each layer of a supported membrane having two or more layers (i.e. the substrate and membrane layers).

For a pore of radius r_p, the conductance λ is defined as the ratio of the current to the driving force:

$$\lambda = \frac{\pi r_p^2 K(r_p) D_o(r_p)}{l} \tag{4.12}$$

where $D_o(r_p)$ is the pore diffusivity, and $K(r_p)$ is the equilibrium constant, based on the relevant pore radius as defined above. Thus, $D_o(r_p) = D_o^a$ or D_o^c for the classical slip flow and corrected slip flow model, respectively, which will be applied for the substrate as well as membrane layers. For the membrane layer, the Oscillator model provides the alternative $D_o(r_p) = D_o^{osc}$. Further, $K\left(r_p\right) = 1$ for the large substrate macropores for which the Knudsen model is considered to hold.

The effective medium conductance λ_e is obtained from the solution to [45, 46]

$$\left\langle \frac{(\lambda - \lambda_e)}{(\lambda + (N/2-1)\lambda_e)} \right\rangle = 0 \tag{4.13}$$

where N is the coordination number, *i.e.*, the number of pores meeting at an intersection and $\langle\ \rangle$ represents a number average over the pores. The directionally averaged local flux in a pore of radius r_p may be expressed as [45]

$$j(r_p) = \frac{\lambda_e l}{\pi r_p^2 R_g T}\left(\frac{N-1}{N+1}\right)\overline{\cos^2(\theta)}\left(-\frac{dP}{dz}\right) \tag{4.14}$$

where z represents the coordinate along the macroscopic flux direction, $\overline{\cos^2(\theta)}$ accounts for the local diffusion direction, which is not necessarily axial [47], and the factor $(N\text{-}1)/(N\text{+}1)$ stands for a correlation effect which arises because of the finite probability that a diffusing molecule returns to a pore that it has just traversed [35, 36]. For unconsolidated materials such as the substrate depicted in Figure 4.4, with non-vanishing aspect ratio $x = r_p/l$, the local direction of flow is assumed close to the macroscopic transport direction, and the expression for $\overline{\cos^2(\theta)}$ can be written as [37, 47]

$$\overline{\cos^2(\theta)} = g(x) = 1 + \frac{4x}{3(1+4x^2)} - \frac{2}{3(1+4x^2)^{1/2}} \tag{4.15}$$

The overall flux in the equivalent uniform network can be obtained by integration over the pore volume distribution, giving [2]

$$J = \frac{\varepsilon\lambda_e < l^2 g(x) >}{\pi < r_p^2 l > R_g T}\left(\frac{N-1}{N+1}\right)\left(-\frac{dP}{dz}\right) \tag{4.16}$$

For a given layer, the apparent tortuosity is obtained by equating the flux in eqn. (4.16) to the empirical model $J = \varepsilon K(\overline{r}_p) D_o(\overline{r}_p)(-dP/dz)/\tau_{app} R_g T$, yielding [2]

$$\tau_{app} = \frac{\pi < r_p{}^2 l > K(\overline{r}_p) D_o(\overline{r}_p)}{< l^2 g(x) > \lambda_e}\left(\frac{N+1}{N-1}\right) \tag{4.17}$$

where $\overline{r}_p$ is a representative pore radius, such as that defined in eqn. (4.4).

Since the tortuosity cannot be directly measured experimentally and the flux, J, varies with radial position in tubular materials, it is more suitable to choose the flow rate, F, as the variable for the analysis of the transport mechanism in the substrate or the membrane, since F is experimentally measurable and always constant across the substrate and the membrane layer. The expression for F is derived from integration of eqn. (4.16) over the substrate (or the membrane) thickness

$$F = \frac{2\varepsilon\lambda_e L < l^2 g(x) >}{< r_p^2 l > \ln(R_o/R_i) R_g T}\left(\frac{N-1}{N+1}\right)(-\Delta P) \tag{4.18}$$

which can be rewritten as

$$F = \frac{2\varepsilon\lambda_e L < l^2 g(x) >}{< r_p^2 l > \ln(1 + z_c/R_i) R_g T}\left(\frac{N-1}{N+1}\right)(-\Delta P) \tag{4.19}$$

where z_c is the thickness of the substrate or membrane layer.

Since the thickness of the substrate tube (z_c = 2.13 mm) is comparable to R_i (R_i = 4.25 mm), no further simplifications can be done on eqn. (4.19). On the other hand, the thickness of the membrane layer ($z_c \approx 2$ μm) is much smaller than its inner radius (R_o = 6.38 mm), so that $\ln(1+z_c/R_o) \approx z_c/R_o$, and the flow rate expression reduces to

$$F = \frac{2\varepsilon R_o \lambda_e L < l^2 g(x) >}{z_c < r_p^2 l > R_g T}\left(\frac{N-1}{N+1}\right)(-\Delta P) \tag{4.20}$$

Since neither the pore length distribution nor the pore connectivity can be extracted from the characterization results, a constant length l is assumed and, along with the coordination number N, is taken as an adjustable parameter obtained by fitting the flow rate through the following objective optimization function

$$Q(N,l) = \frac{1}{n}\sum_{i=1}^{n}\frac{(F_{mi} - F_{ei})^2}{F_{ei}^2} \tag{4.21}$$

where n is the number of experimental flow rate points for all gases, F_{ei} is the experimental flow rate value for data point i, and F_{mi} is the theoretical value of the flow rate obtained by effective medium theory corresponding to the same operating conditions in F_{ei}. For clarity, the structure related parameters (coordination number, pore length and model tortuosity) of the substrate and the membrane layer are distinguished by subscripts s and c, respectively, unless stated otherwise.

For the pure substrate by itself, operating conditions such as temperature and pressure can be directly monitored in the experiments, so the driving pressure drop, ($-\Delta P$), is available, and the coordination number (N_s) and pore length (l_s) can readily be obtained by fitting the model in eqn. (4.18), based on minimization of $Q(N_s, l_s)$. On the other hand, the interfacial pressure, P_1, in the heterogeneous supported membrane is undetectable, so the driving force, ($-\Delta P$), in each layer is not directly available. However, the adjustable parameters for the coated membrane layer (N_c and l_c) can be indirectly obtained by solving the relationship

$$F_s\left(P_F, P_1\right) = F_c\left(P_1, P_o\right) \tag{4.22}$$

to obtain P_1, and subsequently minimizing $Q(N_c, l_c)$. Here F_s is the flow rate predicted by eqn. (4.18) for the substrate as part of the supported membrane, and F_c is the flow rate predicted by eqn. (4.20) for the membrane layer.

In this way, the interfacial pressure, P_1, is estimated theoretically, and the structure parameters (N_c and l_c) of the supported membrane layer are optimized based on eqn. (4.21).

4.4 Results and discussion

4.4.1 Failure of conventional correlations based on a single pore size

We first examine the use of the commonly used correlation in eqs. (4.1) and (4.2), for the flow through the substrate alone, using a single representative pore size, as is often the practice in the experimental literature. Thus, the presence of a pore size distribution is overlooked in the diffusion modeling. According to eqn. (4.1), plotting $F_s\sqrt{T}$ versus $1/\eta\sqrt{T}$ at constant mean pressure should yield a straight line whose slope and intercept provide independent estimates of the tortuosity, termed as τ_s and τ_i, respectively. Such a plot is depicted in Figure 4.7(a), where the deviation between the regression line (solid lines) and the experimental data (symbols) is observed to be very small for all the gases, indicating the model adequately fits the experimental data. However, the regression lines are not parallel to each other as a purely material-dependent tortuosity would suggest, and the lines corresponding to some of the heaviest gases (N_2, Ar and CO_2) even cross over each other. Alternatively, the tortuosity can be obtained by plotting $F_s\sqrt{TM}$ versus $\sqrt{M}/\eta\sqrt{T}$ for all the gases together according to eqn. (4.2), and a straight line with intercept and slope that are independent of the particular gas should be observed. Such plot is shown in Figure 4.7(b), where it is evident that some of gases (CH_4 and H_2) systematically deviate from the regression line. Moreover, the tortuosity varies slightly from gas to gas, as is evident from the fitting results given in Table 4.2.

Table 4.2 Fitted apparent tortuosity based on use of a single representative pore size.

Parameters	H_2	He	CH_4	N_2	Ar	CO_2	Overall tortuosity based on Figure 4.7(b)
τ_i	1.59	1.66	1.50	1.46	1.59	1.72	1.66
τ_s	1.79	1.36	1.56	1.69	1.45	1.35	1.38

To investigate the transport in the membrane layer, the interfacial pressure (P_1) can be estimated from the measured flow rate by using eqn. (4.1) with the apparent substrate tortuosity given in Table 4.2. Assuming the Knudsen model to hold, a straight line through the origin should then be obtained upon plotting the membrane layer permeance ($\pi = J/\Delta P$) against $1/\sqrt{TM}$ following eqn. (2), since viscous flow is negligible for the narrow pore size range of 5-25 nm of the membrane layer (c.f. Figure 4.3). Using the individual τ_i and τ_s for each gas, the estimated interfacial pressure is illustrated in Figure 4.8(a), in which anomalous behavior with temperature is observed, with the interfacial pressure increasing with temperature under some conditions. Furthermore, unexpected crossover between gases is observed. The corresponding regression line for the membrane layer is depicted in Figure 4.8(b), in which the obtained apparent tortuosity of this layer is about 2.92. However, large systematic deviation of the different gases from the regression line is seen, and the behavior of all the gases is nonlinear. Similar behaviour is obtained by using the overall tortuosities for τ_i and τ_s for all gas together in the substrate, given in Table 4.2. As shown in Figures 4.8(c) and 4.8(d), the obtained interfacial pressure and the corresponding regression line are now significantly different, and yield a higher value of tortuosity (τ_{app} = 3.58), but with similar pattern of deviation from the expected linear behavior.

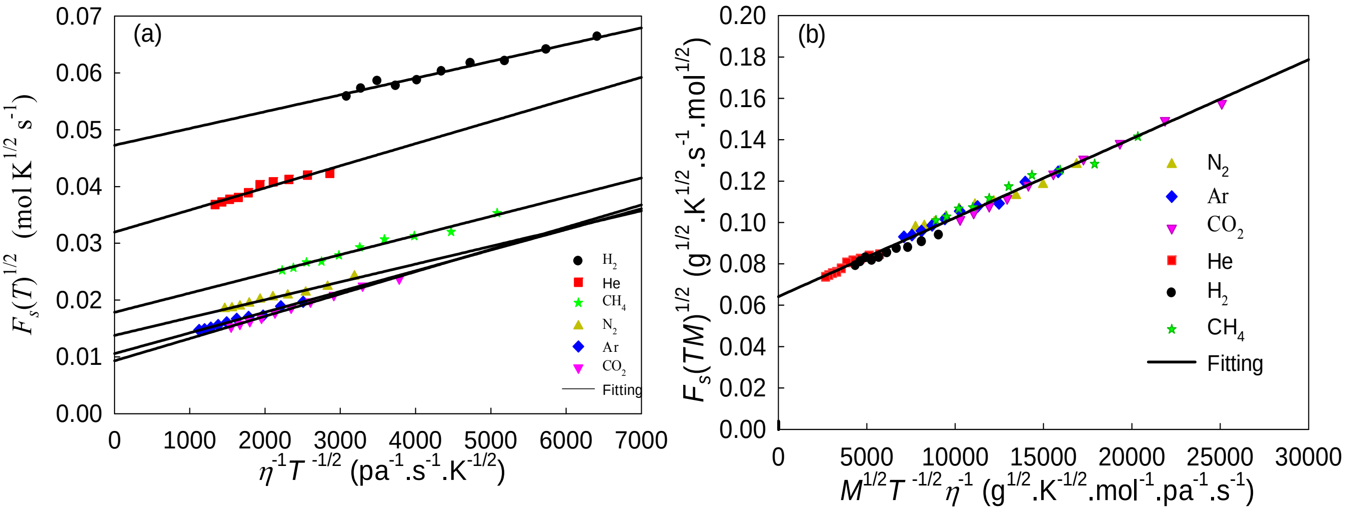

Figure 4.7 (a) Variation of $F_s\sqrt{T}$ with $1/\eta\sqrt{T}$, and (b) variation of $F_s\sqrt{TM}$ with $\sqrt{M}/\eta\sqrt{T}$ for several gases in the uncoated substrate. The symbols are the experimental points, and the lines are the regression results obtained using eqs. (4.1) and (4.2).

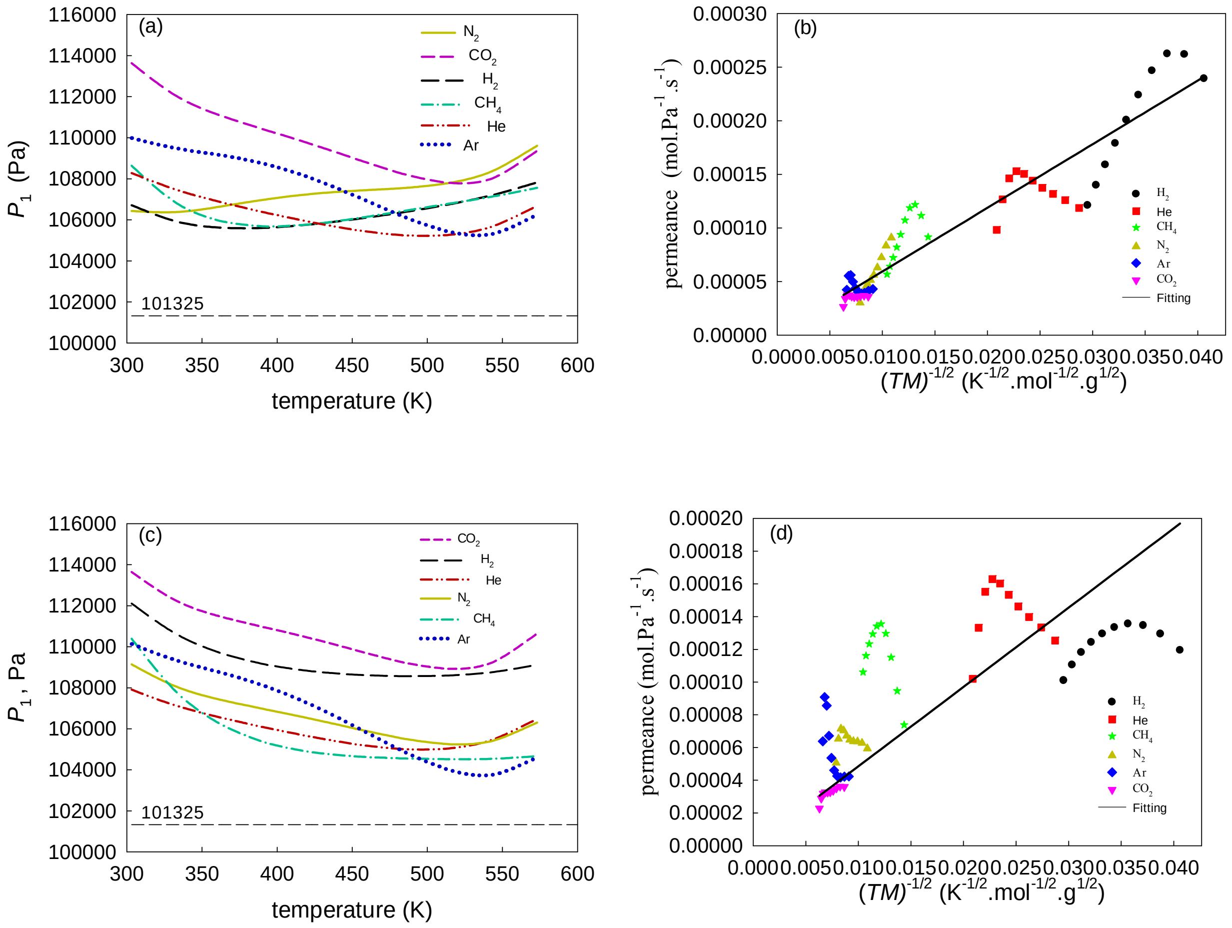

Figure 4.8 Variation of interfacial pressure with temperature and linear regression results for the membrane layer according to eqs. (4.1) and (4.2), using fitted tortuosities given in Table 4.2. (a) The interfacial pressure obtained using individual gas tortuosities, (b) linear regression using individual gas tortuosities, (c) the interfacial pressure obtained using the combined overall tortuosity, and (d) linear regression using the combined overall tortuosity. The symbols are the experimental points, and the lines are the model results obtained using eqs. (4.1) and (4.2).

The diffusion in the membrane layer can now be investigated by equating the flow rates through the substrate and membrane layers, using the interfacial pressure indicated in Figure 4.8(a) or 4.8(c) and assuming a suitable flow mechanism in this layer. To demonstrate the results of this method, the three models discussed in Section 4.3.1 are used to estimate the apparent tortuosity in the membrane layer; these include the Knudsen, the corrected Knudsen (corrected for pore size as in eqn. (4.7) and the Oscillator models, using the interfacial pressure in Figure 4.8(a). For the classical and corrected Knudsen models, the corresponding apparent tortuosity variation with temperature in the membrane layer is depicted in Figures 4.9(a) and 4.9(b) respectively, showing the apparent tortuosity to vary strongly with temperature, lying between 2 and 5 in the temperature range investigated. Similar behavior is seen for the Oscillator model, as depicted in Figure 4.9(c), with significant tortuosity variation (between 1.5 and 4). Although variation of tortuosity with both temperature and gas is expected based on the Oscillator model when adsorption is strong [23], such variations of tortuosity should be very small for large pores for which adsorption is negligible. Thus, a nearly constant tortuosity should be expected for the pore size of 5.22 nm for all the gases, in contradiction of the results in Figures 4.9(a)-4.9(c).

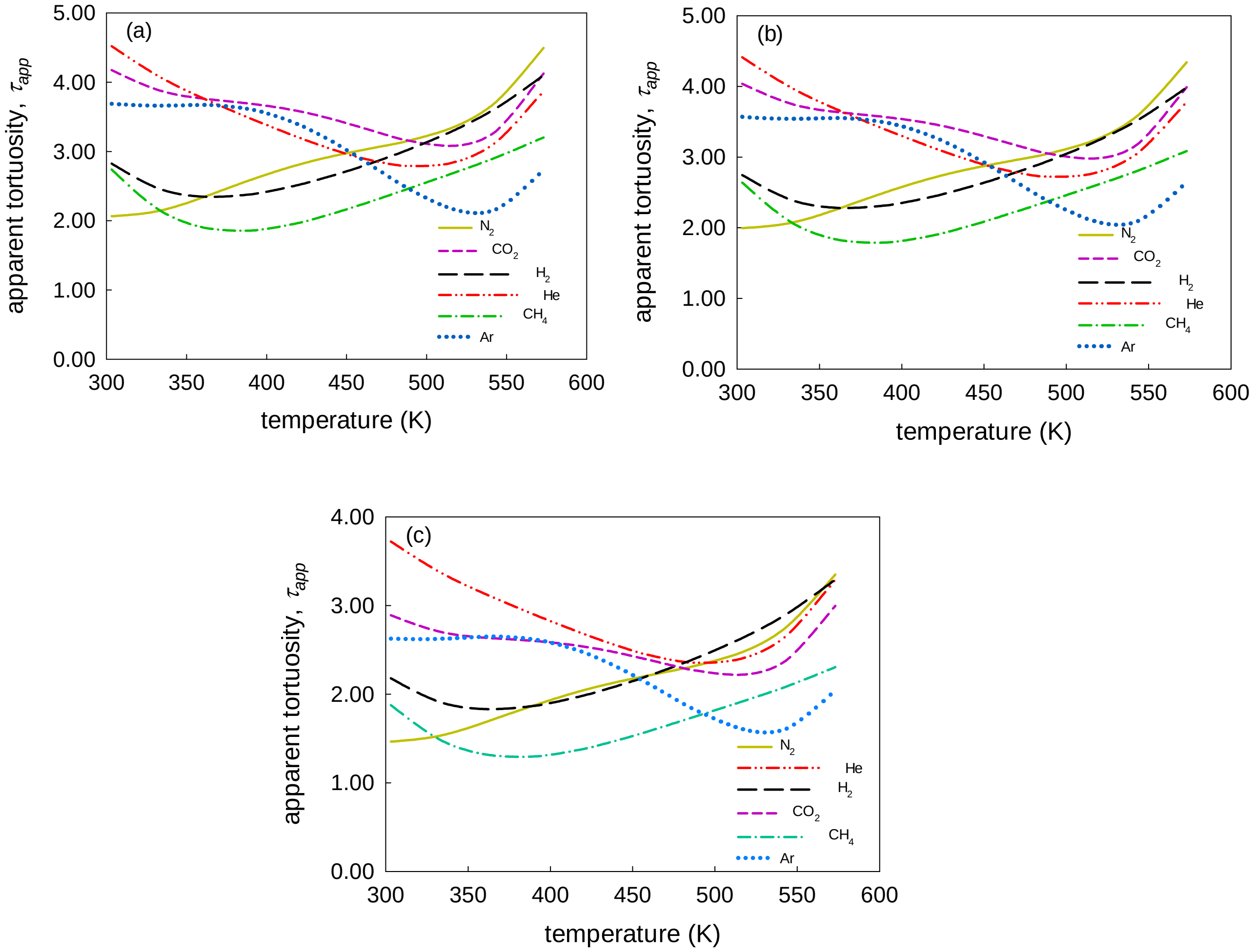

Figure 4.9 Variation of apparent tortuosity with temperature for the membrane layer, using individual fitted tortuosities for each gas in the substrate given in Table 4.2, and ignoring the pore sized distribution. (a) classical Knudsen model, (b) corrected Knudsen model, and (c) Oscillator model.

It is important to note that the above anomalous results are not necessarily an indication of failure of the flow models, but are most likely a result of using a representative pore radius in the substrate - the commonly used main assumption in the analysis - rather than considering the pore size distribution. In fact, it has been theoretically validated that the tortuosity is not only directly influenced by pore topology, but also affected by the conditions of the fluid flow in the pores [2, 45, 46]. For instance, in the slip flow regime, the apparent substrate tortuosity varies with temperature when using a representative pore radius due to the different contributions of viscous and Knudsen flow in pores of different sizes [2]. The same phenomenon is also evident here, as shown in Figure 4.10 for N_2 in the uncoated substrate, and a mild temperature dependency for tortuosity is observed, with a slight decrease in tortuosity with increase in temperature. This tortuosity has been estimated from the measured flow rate at each temperature, using eqn. (4.1). As evidence for statistical significance of the effect of temperature on tortuosity, the data in Figure 4.10 was divided into 2 groups according to temperature. Application of one-way analysis of variance (ANOVA) [48] showed the *p*-value for the null hypothesis (i.e. no difference between two groups) to be 0.02. This is significantly smaller than the generally accept value of 0.05 for rejecting the null hypothesis, indicating there is a significant relationship between temperature and tortuosity. Interestingly, the present observation is different from our previous work, in which an increase in tortuosity with temperature was found. The different trend is due to the different representative pore radius used here. In the present work this radius is estimated based on eqn. (4.4), while in the earlier work we had used the number averaged pore radius [2]. Thus, it is clear that the choice of representative pore size has an important bearing on the relationship between tortuosity and temperature, when the contributions of both viscous and wall-mediated diffusive flow are important.

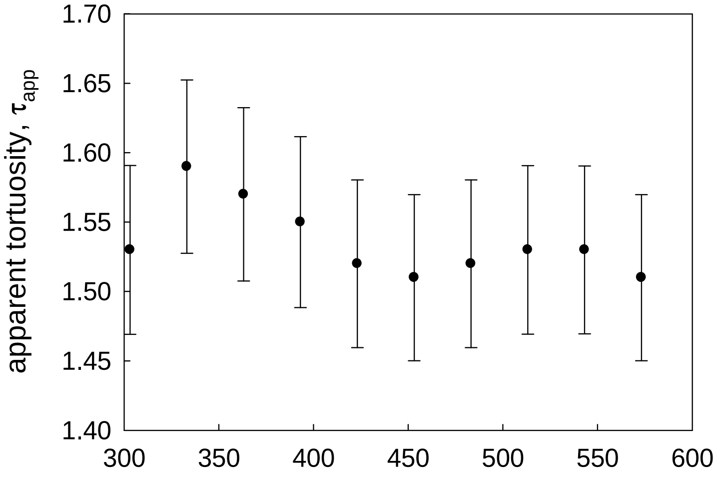

Figure 4.10 Variation of apparent tortuosity with temperature for N_2 flow in the substrate, based on eqn. (4.1) and using the representative pore radius define in eqn. (4.4).

It is evident that the commonly used model, based on eqs. (4.1) and (4.2) with a single pore size, can only crudely explain the results and further improvements are needed. As shown in our earlier work, such anomalies can be explained by the use of a pore size distribution with a suitable network model [2, 36, 45]. Here we use effective medium theory (EMT) for this purpose, exploring the transport in the membrane layer with this powerful method in the next section.

4.4.2 Application of effective medium theory

4.4.2.1 Transport in uncoated substrate

Given the above inconsistencies in the tortuosity values based on eqs. (4.1) or (4.2), we employed effective medium theory for the transport in the uncoated substrate. The advantage of this method is that it accounts for the pore size distribution, rather than using a single arbitrary representative pore size such as in eqn. (4.4).

Instead of fitting the apparent tortuosity, the effective medium theory described in eqs. (4.12)-(4.19) establishes a direct relation between the experimental flow rate and the macroscopic driving force. The structure parameters N_s and l_s were obtained by minimizing the objective function defined in eqn. (4.21), covering all the gases and temperature points at which measurements were made. Figure 4.11(a) depicts the variation of F with T obtained from experimental permeation data (symbols) and the corresponding best fit (solid lines) obtained using the structure parameters $N_s = 12$ and $l_s = 300$ nm for several light gases. The slip flow model with the Knudsen and viscous contributions given in eqs (4.5) and (4.6) was used for individual pores. It is readily seen that the new model can accurately predict the fluid behavior in the substrate except for a slight overestimation of the data for H_2, suggesting that the selected values for N_s and l_s adequately capture the substrate pore network topology. Nevertheless, we note that the current theory assumes straight cylindrical pores, somewhat different from the real pores formed by the irregular voids between the alumina particles. In this sense, the values of N_s and l_s should be understood as the effective coordination number and pore length of an equivalent network comprised of ideal cylindrical and straight pores providing the same overall resistance to flow as the actual substrate.

The model pore length ($l_s = 300$ nm) is only slightly shorter than the one reported in our previous work $l_s = 330$ nm, for the same substrate by fitting the experimental tortuosity to the model tortuosity provided by eqn. (4.17) [2]. The difference is mainly due to the greater accuracy of the current measurements, and to a smaller extent due to the fitting of the flow rate rather than the tortuosity. The bubble flow meter expectedly provides more accurate results; because of this, we will continue to take $l_s = 300$ nm in the ensuing calculations. The model pore length is only about 10% of the real particles size, because the real pore space between the aggregated alumina particles is not perfectly cylindrical but has wide mouths and a central constriction, so the model pore length must be shortened to produce an equivalent uniform diffusivity [2]. The variation of tortuosity with temperature for all gases is illustrated in Figure 4.11(b), using the representative pore radius of 257.05 nm in eqn. (4.17), showing a decrease in tortuosity with increase in temperature. This is consistent with the experimentally observed behavior illustrated in Figure 4.10. Such variation is a consequence of the combination of Knudsen and viscous flows, as discussed in our previous work [2].

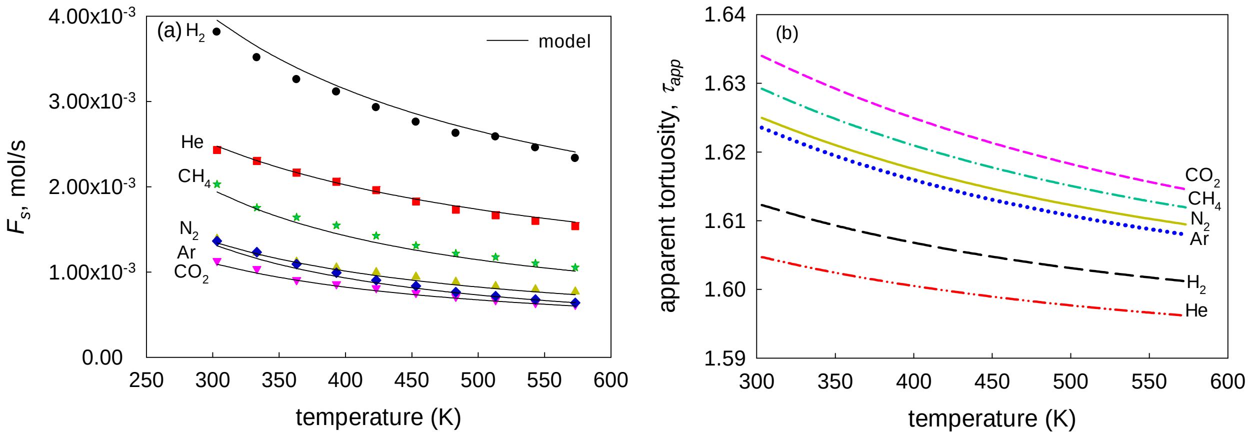

Figure 4.11 (a) Variation of F_s with temperature, and (b) variation of apparent tortuosity with temperature, for the uncoated substrate. The symbols are the experimental points, and the lines are the model results obtained using eqs. (4.17) or (4.18) with $N_s = 12$, $l_s = 300$ nm, and the classical slip flow model in the substrate.

The systematic decrease is due to a different representative pore radius, which leads to decrease of the ratio of the apparent diffusivity $D_o(\overline{r}_p)$ to the effective conductance λ_e with increase in temperature. The model parameters for the substrate ($N_s = 12$ and $l_s = 300$ nm) will be used in the prediction of the transport in the supported membrane.

4.4.2.2 Transport in the coated membrane layer

All of the above results rely on the understanding of the fluid behavior within individual pores in the pore space to produce appropriate diffusivity estimates to be used along with effective medium theory. Although the slip flow model was extensively validated for macrospores in the substrate [2], the flow mechanisms in the mesopores remains controversial [22]. To interpret data obtained here for the coated membrane, three different flow models (classical slip flow model, corrected slip flow and Oscillator model) were applied to reference the transport in the mesopores, as follows.

4.4.2.2.1 Slip flow in the membrane layer

In this case, we assumed the classical slip flow model in the mesopores described by eqs. (4.5) and (4.6). The structural parameters of the coated membrane layer were obtained by fitting the flow rate versus temperature data, by minimizing the objective function in eqn. (4.21). Figure 4.12(a) shows the variation of flow rate with temperature for the different gases in the supported membrane, using the fitted values of N_c = 12 and l_c = 5 nm for the coated membrane layer and N_s = 12 and l_s = 300 nm, as fitted above for the substrate. The symbols correspond to the experimental data, and the lines to the model results. As noted in our recent work [2], such high values of the coordination number N, of 12, are consistent with the close packing of spherical particles, such as in face-centred or hexagonal close packing. This agreement is to be expected given the unconsolidated nature of the substrate and the membrane layers, and provides support for the EMT approach adopted. The model pore length of 5 nm is around 10% of the particle size (~50 nm) of the unconsolidated porous medium of the coated membrane layer, yielding the same particle size to pore length ratio as obtained for the substrate.

Since the model predicted the experimental data well except for marginal overprediction for H_2 as illustrated in Figure 4.12(a), it is meaningful to examine the corresponding interfacial pressure, P_1. The variation of P_1 with temperature for several gases is depicted in Figure 4.12(b). The interfacial pressure (P_1) decreases monotonically with increase in temperature for all the gases, and represents a significant improvement over the results obtained using the correlation in eqs. (4.1) or (4.2) with the tortuosity parameters in Table 4.2. The latter leads to an increase in interfacial pressure above a temperature of about 500 K, as illustrated in Figure 4.8(a). This apparent increase is clearly due to the use of a single representative pore size in the modeling, while neglecting the PSD. Figure 4.12(b) shows that the interfacial pressure profile is significantly different for each of the gases, with the following order, from the highest to the lowest interfacial pressure, observed at all temperatures: $CO_2 > CH_4 > N_2 > Ar > H_2 > He$. This is clearly indicative of a higher relative resistance of the substrate for the lighter gases.

Accordingly, the driving force in the membrane layer varies significantly from gas to gas and with temperature for any given species. For instance, at low temperature (303 K) the pressure gradient for CO_2 is almost twice as much as the one for He since the outlet pressure is about 1 bar, and the pressure gradient for CO_2 at low temperature (303 K) is almost 30% higher than that at 573 K. Figure 4.12(c) indicates that the relative pressure drop over the substrate constitutes most of the driving force (more than 95%) through the supported membrane for all the gases. This is a consequence of the substrate thickness being considerably larger than the thickness of the membrane layer. Therefore, it is of paramount importance to correctly take the pressure drop through each of the layers into account for similar supported membranes before analyzing the transport, as it is not uncommon to neglect the resistance offered by the substrate based only on its (typically) large mean pore size.

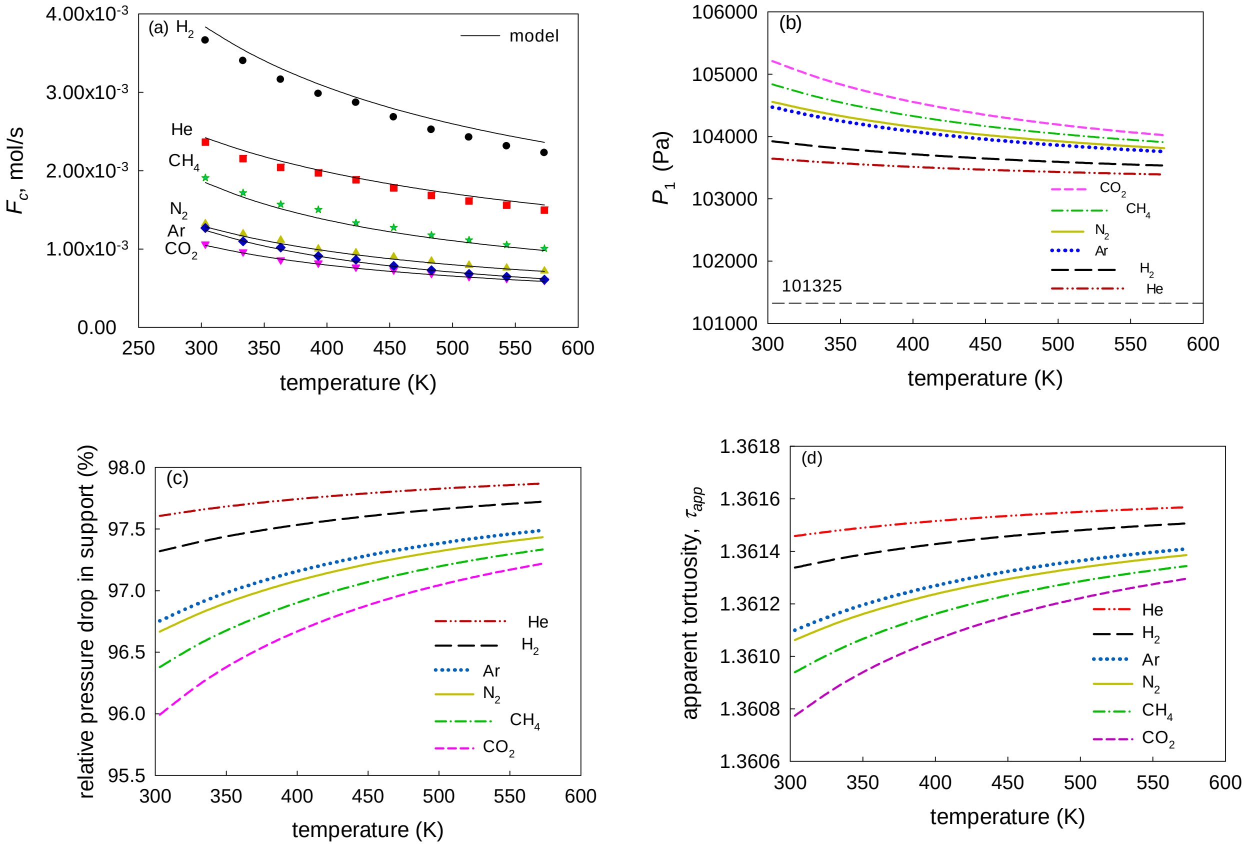

Figure 4.12 (a) Variation of F_c with temperature, (b) variation of interfacial pressure, P_1, with temperature, (c) variation of the relative pressure drop in the substrate with temperature, for flow of different gases in the supported membrane, and (d) the variation of model tortuosity, τ_{app}, with temperature for membrane layer. The symbols are the experimental points, and the lines are the model results obtained using eqs. (4.20) and (4.22) with $N_c = 12$, $l_c = 5$ nm, and the classical slip flow model in the membrane layer.

Figure 4.12(d) depicts the apparent tortuosity variation with temperature for the membrane layer based on eqn. (4.17), indicating negligible tortuosity variation (between 1.360 and 1.362) with temperature and gas when effective medium theory is used. This tortuosity variation is much smaller than that obtained through the empirical correlation method discussed above (2-5), indicating the importance of considering the PSD. The low value of the membrane layer tortuosity, of around 1.36, is also more reasonable given the unconsolidated nature of the α-alumina layer (c.f.

Figure 4.2), and is in the range reported for packed beds [43]. On the other hand high values, such as those in the range of 2-5, obtained here using a single representative pore size, are far too large for unconsolidated porous media, but are commonly accepted in the literature because they are fortuitously in the range expected for long cylindrical pores. Nevertheless, the inadequacy of the single pore size approach is evident from the anomalous behavior with respect to temperature. The nearly constant tortuosity for the membrane layer obtained using effective medium theory can be explained by noting that the viscous flow contribution to the overall diffusivity, given by eqn. (4.6), varies with r_p^2, and is negligible in the narrow mesopores of the membrane layer (i.e. $D_o^a \approx D_{Kn}$). In the absence of viscous effects, the factor $(T)^{1/2}$ appearing in the terms λ_e and $D_o(\overline{r}_p)$ in eqn. (4.17) cancels out, leading to a constant tortuosity that depends only on the pore size distribution [2].

The interfacial pressure variation with temperature or gas can be found by equating the model flow rate for the substrate and the membrane, as given in eqs. (4.18) and (4.20), to obtain

$$P_1 = (P_F + \omega \frac{\lambda_e^c}{\lambda_e^s} P_o) \Big/ (1 + \omega \frac{\lambda_e^c}{\lambda_e^s}) \tag{4.23}$$

where $\omega = \dfrac{\varepsilon_s < l_s g_s(x) > z < r_c^2 >}{\varepsilon_c R_o < l_c g_c(x) >< r_s^2 > \ln(R_o/R_i)}$ is a property of the supported membrane (ω=87,137.64 in this work), λ_e^c is the effective conductance for the coated membrane layer and λ_e^s is the effective conductance for the substrate.

Since ω is temperature independent, it is readily seen that it is the ratio of the effective conductance between the substrate and the membrane ($\lambda_e^c / \lambda_e^s$) that determines the interfacial pressure at any temperature. Figure 4.13 depicts the variation of interfacial pressure with the conductance ratio, $\lambda_e^c / \lambda_e^s$. Both λ_e^c and λ_e^s, as well as their ratio $\lambda_e^c / \lambda_e^s$, decrease with increasing temperature, which makes the interfacial pressure lower at higher temperature. In this sense, although the flow rate for He is lower than the flow rate for H_2 in both substrate and membrane, $\lambda_e^c / \lambda_e^s$ is lower for H_2 than it is for He, which makes H_2 to have higher interfacial pressure than He.

In the above estimations based on the classical slip flow model in eqs. (4.5) and (4.6), it is assumed that the size of the fluid molecules is negligible. However, in the narrow pores of the membrane layer with PSD depicted in Figure 4.3, the fluid molecule can make a considerable fraction of the smallest pores inaccessible. By taking the fluid molecule size into account, a corrected slip flow model ($D_o^c = D_{Kn}^c + D_{vis}^c$) can be used to examine the transport in the membrane layer. Nevertheless, very similar results are obtained compared to those provided by the classical slip flow model as shown in Figure 4.14(a), with exactly the same values of the fitted structural parameters ($N_c = 12$, $l_c = 5$ nm). This is because the fluid molecule size represents a small fraction of the pore volume for pores above a size of about $10\sigma_{ff}$. In Figure 4.14(b), the predicted interfacial pressure, P_1, is slightly larger than that obtained through the classical method for the same gas species, however, the difference between pressure gradients in membrane layer is not completely negligible for the two models, especially at low temperature. For instance, the driving force in the membrane layer for N_2 obtained by the corrected slip flow model is 10% larger than that obtained by the classical slip flow model at 303 K, in the membrane layer. Additionally, the corrected flow model yields the same order for the gases from the highest to the lowest P_1 at every temperature, and the pressure loss in the substrate is still dominant for all gases (above 95%) as shown in Figure 4.14(c).

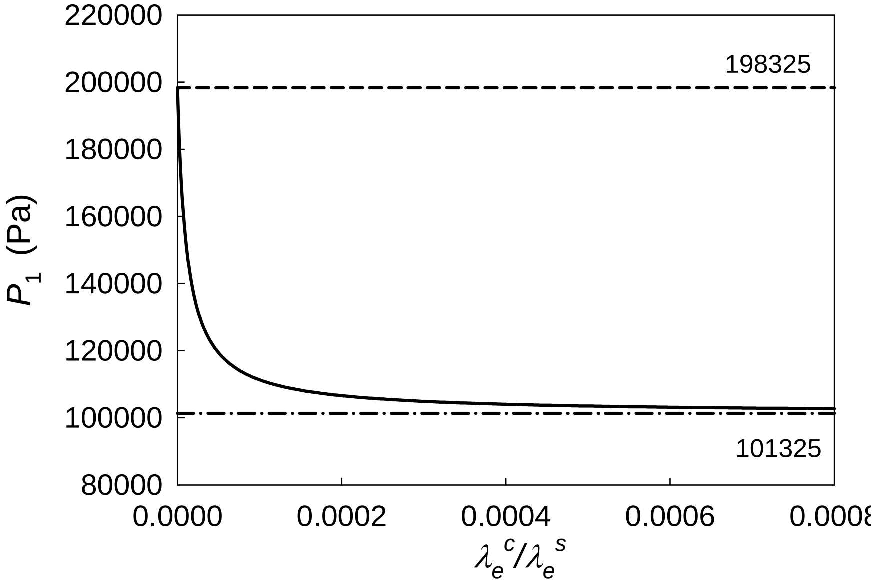

Figure 4.13 Variation of P_1 with effective conductance ratio in the supported membrane, based on eqn. (4.23).

The predicted apparent tortuosity using the corrected slip flow model is also almost constant with temperature for each gas, but slightly varies between the gases, lying between 1.44 and 1.47 as illustrated in Figure 4.14(d). The variation of tortuosity between the different gases is mainly caused by the effect of the correction to the pore radius on the conductance, which depends on the gas species. The slight tortuosity increase compared to the classical slip flow model is due to the disproportionate decrease in conductance of the small pores on correcting the pore radius, compared to the large pores. This leads to the large pore offering short circuit paths, thereby increasing the tortuosity. This tortuosity increase is larger for the larger molecules.

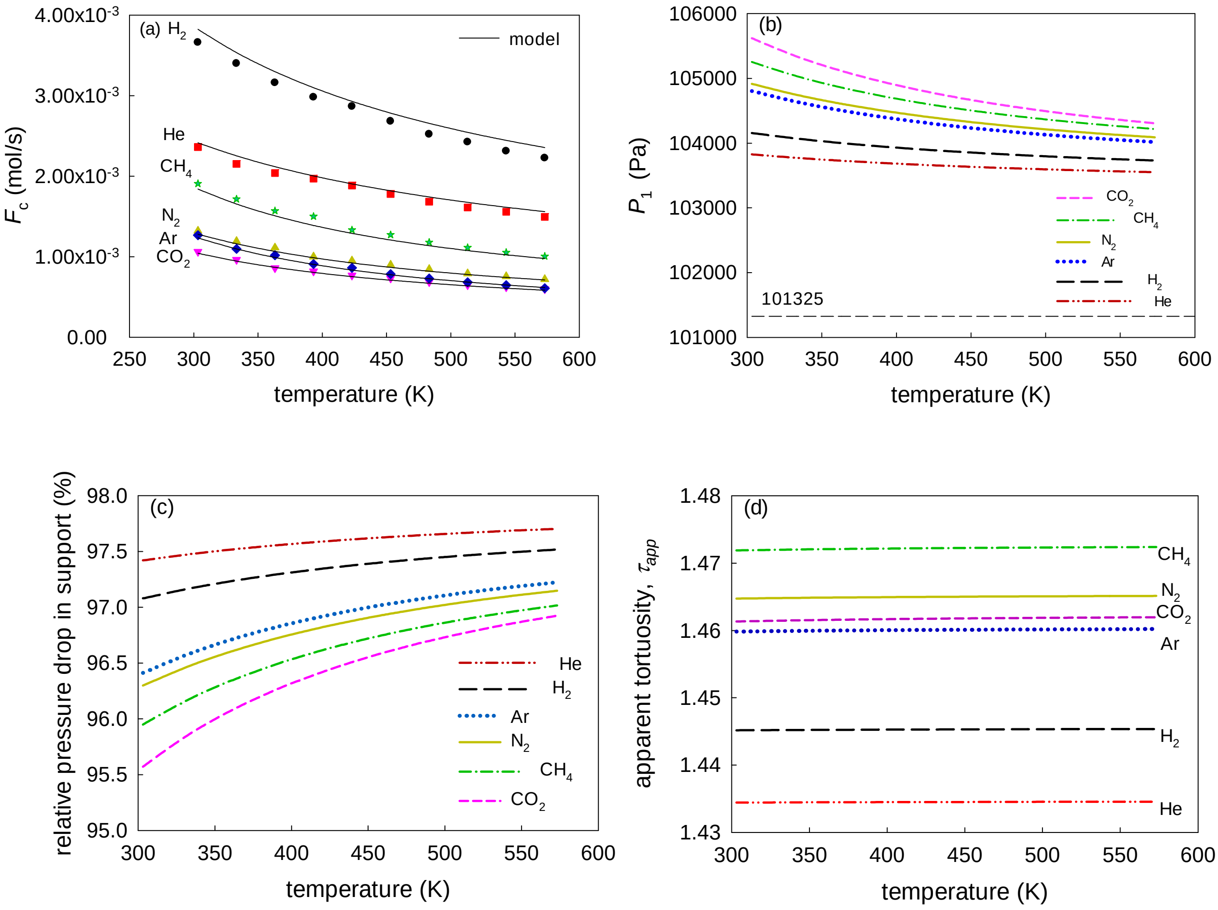

Figure 4.14 (a) Variation of F_c with temperature, (b) variation of interfacial pressure, P_1, with temperature, (c) variation of the relative pressure drop in the substrate with temperature, for flow of different gases in the supported membrane, and (d) the variation of model tortuosity, τ_{app}, with temperature for membrane layer. The symbols are the experimental points, and the lines are the model results obtained using eqs. (4.20) and (4.22) with $N_c = 12$, $l_c = 5$ nm, and the corrected slip flow model in the membrane layer.

Although the above results based on the slip flow model for the membrane layer accurately predicted the experimental data and produced a reasonable tortuosity, it is important to note that the models for transport at the single pore level employed so far cannot be unequivocally validated, as direct measurement of the interfacial pressure P_1 is not possible. Thus the models may still produce accurate flow rates by adjusting the corresponding coordination number and pore length even when the slip flow fails. The interfacial pressures are the true ones only when the actual diffusion mechanism is provided. However, since the models have explained the data for several gases with the same membrane parameters, a high degree of confidence in these results is expected. Nevertheless, the above results (slip flow or corrected slip flow models) constitute just two ‘explanations’ to the experiments, and it is meaningful to apply the Oscillator model as an alternative to explore the diffusion mechanism and seek out another explanation to the experimental data.

4.4.2.2.2 Oscillator model in the membrane layer

In this case, the Oscillator model is applied in the pores of the membrane layer, with viscous flow neglected at this scale. The variation of flow rate with temperature obtained for the supported membrane is illustrated in Figure 4.15(a), showing the Oscillator model to yield similar results as the slip flow model, with only slight overestimation for the case of H_2. The fitted structure parameters are $N_c = 12$ and $l_c = 5$ nm, matching those obtained with the prior models. This indicates that both the slip flow model and the Oscillator model are adequate for the system under study.

The interfacial pressures estimated through the Oscillator model are plotted in Figure 4.15(b), where the pressure again decreases monotonically with temperature for each gas, and the order of interfacial pressures from highest to lowest is exactly the same as before, *i.e.* $CO_2>CH_4>N_2>Ar>H_2>He$. The interfacial pressure predicted by the Oscillator model is significantly higher than that derived from the slip flow model for each gas, since the diffusivity obtained from the Oscillator model is smaller than that provided by the slip-flow model [23, 45]. Nevertheless, the overall pressure drop is still dominated by the substrate part for all the gases, as illustrated in Figure 4.15(c). The estimated apparent tortuosities are depicted in Figure 4.15(d), in which a slightly smaller tortuosity (in the range of 1.28-1.29) is seen. The apparent tortuosity obtained by this flow model demonstrates a very weak dependence on temperature and gas species, and different temperature tendencies. For example, the tortuosity decreases with temperature for H_2 and He, but increases with temperature for CH_4, N_2, Ar and CO_2. The above results are not surprising since the temperature dependence in the Oscillator model is much more complex than that in the Knudsen model, and the temperature dependence of the conductance at the average pore radius (effectively of $K(\overline{r}_p)D_o(\overline{r}_p)$), is different from that of the effective conductance, λ_e in eqn. (4.17). This leads to the complex behavior of the tortuosity-temperature relationship, discussed at length elsewhere [45].

From the above results, it is clear that the diffusivity in the pores influences the obtained interfacial pressure very significantly, so it is meaningful to compare the apparent diffusivity between the three flow models. The pore radius (center-center) for the membrane is in the range of 1 to 12 nm based on the pore size distribution in Figure 4.3, and the corresponding apparent diffusivities in this range provided by the two models (classical, corrected slip flow and Oscillator models) are plotted in

Figure 4.16 for a light gas (H_2), a gas of intermediate mass (CH_4) and a heavy gas (Ar), at low temperature (300 K) and high temperature (500 K).

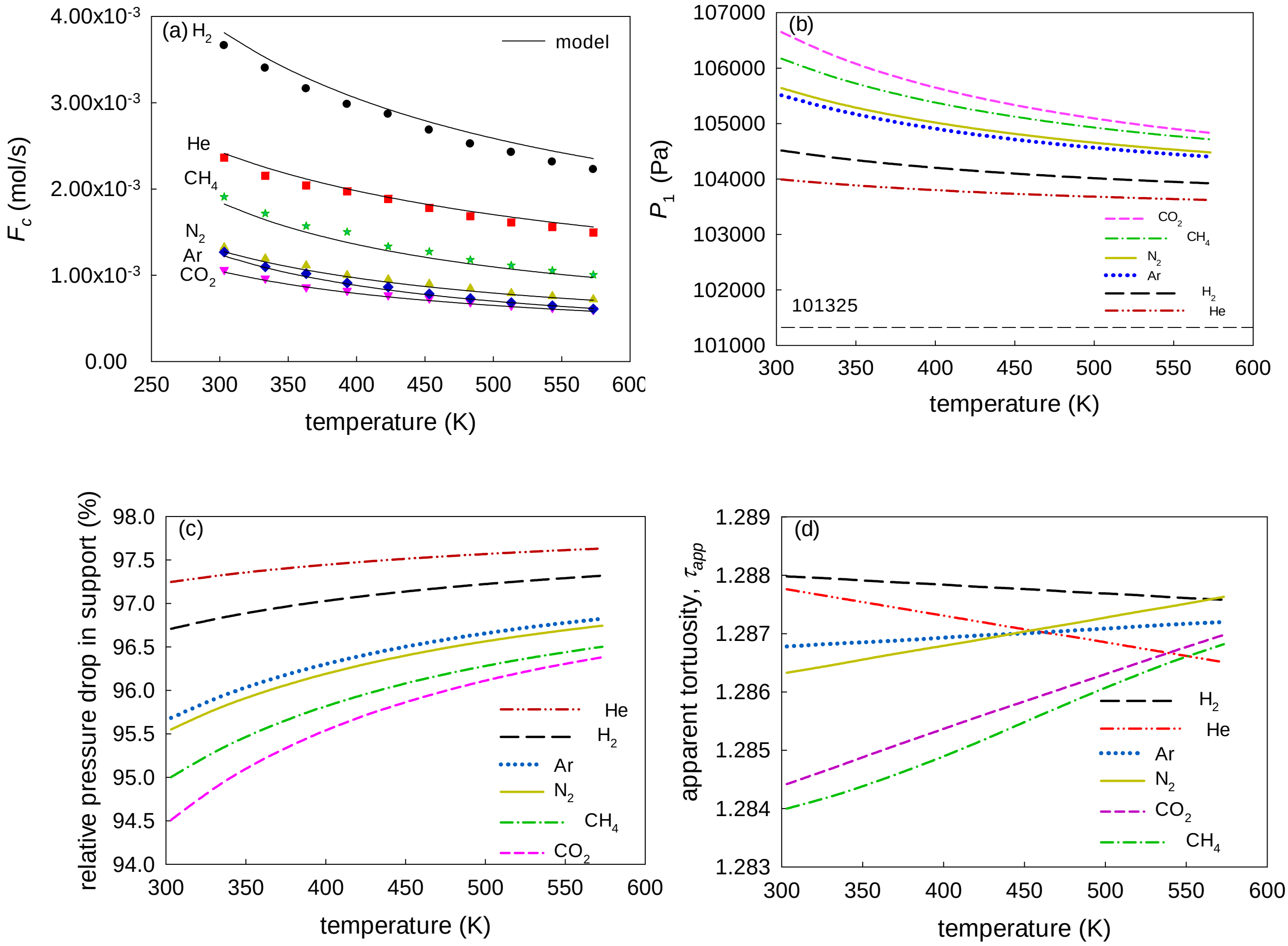

Figure 4.15 (a) Variation of F_c with temperature, (b) variation of interfacial pressure, P_1, with temperature, (c) variation of the relative pressure drop in the substrate with temperature, for flow of different gases in the supported membrane, and (d) the variation of model tortuosity, τ_{app}, with temperature for membrane layer. The symbols are the experimental points, and the lines are the model results obtained using eqs. (4.20) and (4.22) with $N_c = 12$, $l_c = 5$ nm, and the Oscillator model in the membrane layer.

It is noted the two models predict almost the same apparent diffusivity when the pore radius is larger than 6 nm. For narrower pores, the diffusivity between two models is significantly different, though this difference appears less prominent on the logarithmic scale used for the ordinate in Figures 4.16(a) and 4.16(b). The above observation explains the difference in interfacial pressure obtained by the two models. The comparison of apparent diffusivity of the corrected slip flow and Oscillator model is given in Figures 4.16(c) and 4.16(d), and shows that the corrected slip flow model provides an apparent diffusivity (D_o^c) larger than the Oscillator model (D_o^{osc}) by 10-50% in the selected pore size range at both temperatures. On the other hand, it is important to mention that the equilibrium constant, *K*, based on eqn. (4.10) is close to unity for all the gases even at low temperature (300 K), suggesting very weak adsorption in the alumina pores.

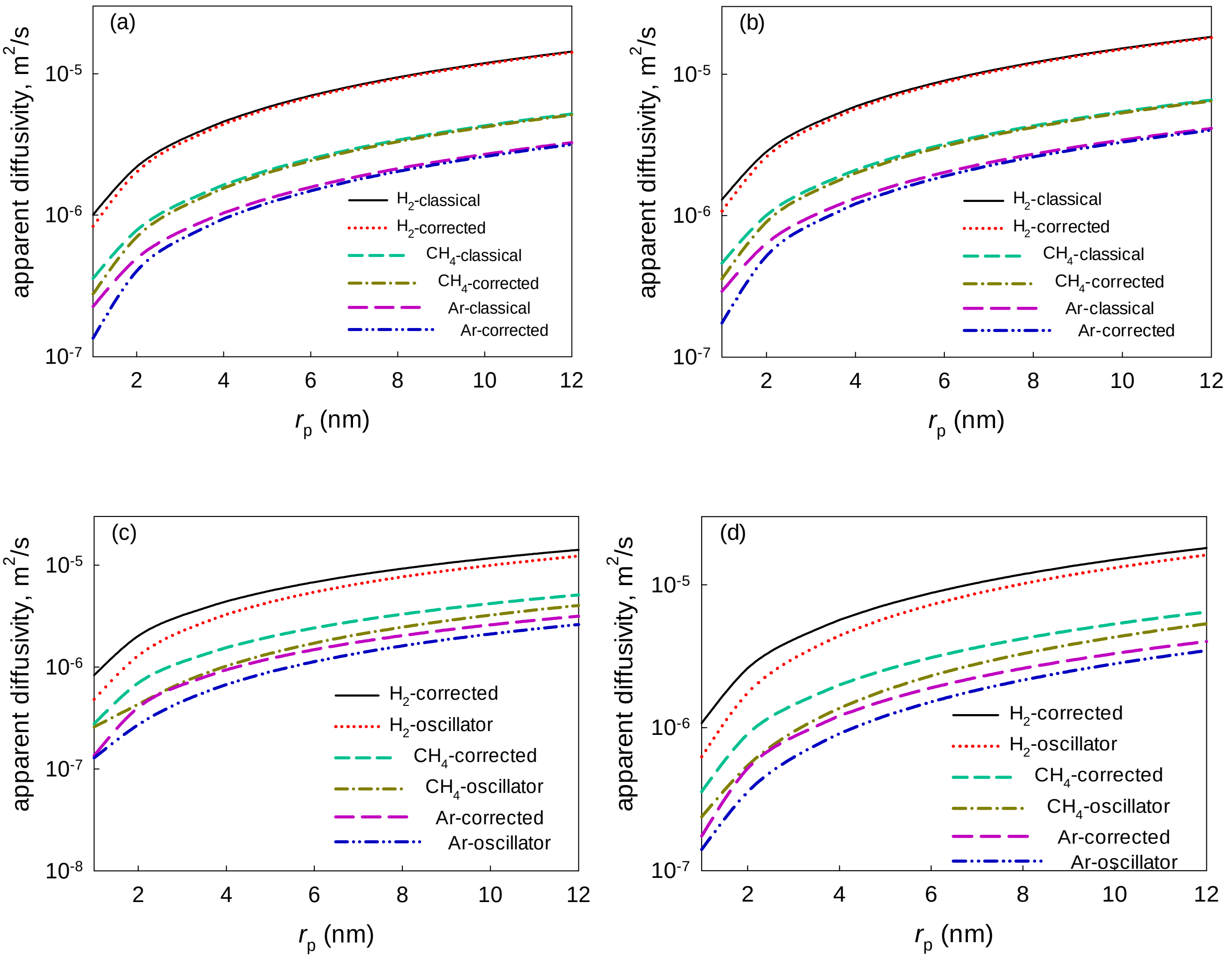

Figure 4.16 Variation of apparent diffusivity with pore radius (center to center) based on the classical, corrected slip flow model and Oscillator model for H_2, CH_4 and Ar. (a) classical and corrected slip flow models at 300 K, (b) classical and corrected slip flow models at 500 K, (c) corrected slip flow model and Oscillator model at 300 K, and (d) corrected slip flow model and Oscillator model at 500 K.

4.5 Summary and Conclusions

Single gas permeation experiments with six gases (N_2, Ar, CO_2, He, H_2 and CH_4) have been conducted over a wide range of temperatures (30 to 300 ºC) in a tubular macroporous α-alumina substrate and a supported mesoporous γ-alumina membrane. The transport through both substrate and membrane layers were examined by both conventional correlations and a rigorous effective medium theory method based on three different diffusion models. The results of the conventional correlation method show that while it can capture the transport mechanism in the substrate, it fails to adequately model the behavior because of the assumption of a temperature-independent tortuosity and the use of a single representative pore size while neglecting details of the pore size distribution. These simplifications lead to artifacts in the interfacial pressure variation with temperature, and to failure of the correlation in the membrane layer. For the rigorous EMT method, the fluid behavior was examined by fitting the theoretical and experimental flow rates for the substrate to obtain the corresponding structure parameters ($N_s = 12$ and $l_s = 300$ nm) using the classical slip flow model in the macropores. Based on this, both slip flow models (classical and corrected) and the Oscillator model have been used to predict the apparent diffusivity in the membrane layer, providing three possible explanations for the transport in the membrane layer. These confirm that the effective medium theory method adequately predicts the fluid transport in the substrate and membrane layer by using only two adjustable structure parameters in each layer.

Using the EMT for each layer, all the three diffusion models predict a monotonic decrease in interfacial pressure with temperature and a nearly constant tortuosity for the membrane layer, in which the pressure gradient significantly varies with gas species and temperature. Further, the pressure drop along the substrate is dominant for all the gases (greater than 95% of the overall drop). The estimated apparent pore length for the substrate, and the membrane layer using the three diffusion models, is 10% of the alumina particle size in each case. The different interfacial pressure predicted by the three models was explained by comparing the corresponding apparent diffusivity among the three models, and showed the difference of apparent diffusivity predicted by the classical and corrected slip flow models is not negligible for pores smaller than 6 nm – thus consideration of the finite molecular size is important in such pores. Comparing the apparent diffusivity based on the corrected slip flow and the Oscillator model, the corrected slip flow provides apparent diffusivity larger by 10-50% for pores between 1 and 12 nm (center to center) than the Oscillator model. The near-unity value of the equilibrium constant according to eqn. (4.10) indicated very weak adsorption for alumina materials even at low temperature and small pore size.

For the large pore size of the membrane layer, of about 10.4 nm diameter, there is little difference between the Knudsen (and its corrected form) and Oscillator models, and it is not possible to distinguish their performance. In smaller pore membranes the difference may be expected to be more significant, and this will be demonstrated in a forthcoming paper. The significance of the above results verifies that effective medium theory is an efficient and accurate way to explore the diffusion in supported multi-layer membranes to obtain structure parameters that can be used to predict the transport behavior, avoiding the pitfalls of neglecting the pore size distribution. The parameters determined here will be used in modeling the transport in supported three-layer membranes in our future work.

4.6 References

[1] S.K. Bhatia, M.R. Bonilla, D. Nicholson, Molecular transport in nanopores: a theoretical perspective, Phys. Chem. Chem. Phys., 13 (2011) 15350-15383.

[2] X. Gao, M.R. Bonilla, J.C. Diniz da Costa, S.K. Bhatia, The transport of gases in macroporous α-alumina supports, J. Membr. Sci., 409-410 (2012) 24-33.

[3] M.R. Bonilla, S.K. Bhatia, The low-density diffusion coefficient of soft-sphere fluids in nanopores: accurate correlations from exact theory and criteria for applicability of the Knudsen model, J. Membr. Sci., 382 (2011) 339-349.

[4] W. Zhou, X. Bai, E. Wang, S. Xie, Synthesis, structure, and properties of single walled carbon nanotubes, Adv. Mater., 21 (2009) 4565-4583.

[5] E.T. Thostenson, Z. Ren, T.W. Chou, Advances in the science and technology of carbon nanotubes and their composites: a review, Compos. Sci. Technol., 61 (2001) 1899-1912.

[6] P. Selvam, S.K. Bhatia, C.G. Sonwane, Recent advances in processing and characterization of periodic mesoporous MCM-41 silicate molecular sieves, Ind. Eng. Chem. Res., 40 (2001) 3237-3261.

[7] M.E. Davis, Ordered porous materials for emerging applications, Nature, 417 (2002) 813-821.

[8] P. Kumar, V.V. Guliants, Periodic mesoporous organic–inorganic hybrid materials: Applications in membrane separations and adsorption, Micropor. Mesopor. Mat., 132 (2010) 1-14.

[9] R.M. De Vos, H. Verweij, Improved performance of silica membranes for gas separation, J. Membr. Sci., 143 (1998) 37-51.

[10] J.C. Diniz da Costa, G.Q. Lu, V. Rudolph, Y.S. Lin, Novel molecular sieve silica (MSS) membranes: characterisation and permeation of single-step and two-step sol-gel membranes, J. Membr. Sci., 198 (2002) 9-21.

[11] S. Gopalakrishnan, J.C. Diniz da Costa, Hydrogen gas mixture separation by CVD silica membrane, J. Membr. Sci., 323 (2008) 144-147.

[12] J. Caro, M. Noack, Zeolite membranes-recent developments and progress, Micropor. Mesopor. Mat., 115 (2008) 215-233.

[13] Y. Wan, D. Zhao, On the controllable soft-templating approach to mesoporous silicates, Chem. Rev., 107 (2007) 2821-2860.

[14] X. Wang, Q. Li, J. Xie, Z. Jin, J. Wang, Y. Li, K. Jiang, S. Fan, Fabrication of ultralong and electrically uniform single-walled carbon nanotubes on clean substrates, Nano Lett., 9 (2009) 3137-3141.

[15] A.K. Cheetham, G. Férey, T. Loiseau, Open framework inorganic materials, Angew. Chem. Int. Edit, 38 (1999) 3268-3292.

[16] R. Krishna, J.M. van Baten, An investigation of the characteristics of Maxwell-Stefan diffusivities of binary mixtures in silica nanopores, Chem. Eng. Sci., 64 (2009) 870-882.

[17] S.K. Bhatia, D. Nicholson, Friction based modeling of multicomponent transport at the nanoscale, J. Chem. Phys., 129 (2008) 164709.

[18] E.A. Mason, A.P. Malinauskas, R.B. Evans III, Flow and diffusion of gases in porous media, J. Chem. Phys., 46 (1967) 3199-3216.

[19] R.B. Evans III, G.M. Watson, E.A. Mason, Gaseous diffusion in porous media at uniform pressure, J. Chem. Phys., 35 (1961) 2076-2083.

[20] R.B. Evans III, G.M. Watson, E.A. Mason, Gaseous diffusion in porous media. II. effect of pressure gradients, J. Chem. Phys., 36 (1962) 1894-1902.

[21] S.K. Bhatia, D. Nicholson, Comments on" Diffusion in a mesoporous silica membrane: Validity of the Knudsen diffusion model" by Ruthven, D.M., et al., Chem. Eng. Sci. 64 (2009) 3201-3203, Chem. Eng. Sci., 65 (2010) 4519-4520.

[22] A. Markovic, D. Stoltenberg, D. Enke, E.U. Schlünder, A. Seidel-Morgenstern, Gas permeation through porous glass membranes: Part I. Mesoporous glasses-effect of pore diameter and surface properties, J. Membr. Sci., 336 (2009) 17-31.

[23] S.K. Bhatia, D. Nicholson, Some pitfalls in the use of the Knudsen equation in modelling diffusion in nanoporous materials, Chem. Eng. Sci., 66 (2010) 284-293.

[24] J. Kärger, F. Stallmach, S. Vasenkov, Structure-mobility relations of molecular diffusion in nanoporous materials, Magn. Reson. Imaging, 21 (2003) 185-191.

[25] R. Krishna, J.M. van Baten, Unified Maxwell-Stefan description of binary mixture diffusion in micro-and meso-porous materials, Chem. Eng. Sci., 64 (2009) 3159-3178.

[26] O.G. Jepps, S.K. Bhatia, D.J. Searles, Wall mediated transport in confined spaces: exact theory for low density, Phys. Rev. Lett., 91 (2003) 126102.

[27] S.K. Bhatia, O. Jepps, D. Nicholson, Tractable molecular theory of transport of Lennard-Jones fluids in nanopores, J. Chem. Phys., 120 (2004) 4472-4485.

[28] D. Uhlmann, S. Liu, B.P. Ladewig, J.C. Diniz da Costa, Cobalt-doped silica membranes for gas separation, J. Membr. Sci., 326 (2009) 316-321.

[29] S. Battersby, T. Tasaki, S. Smart, B. Ladewig, S. Liu, M.C. Duke, V. Rudolph, J.C. Diniz da Costa, Performance of cobalt silica membranes in gas mixture separation, J. Membr. Sci., 329 (2009) 91-98.

[30] S. Battersby, S. Smart, B. Ladewig, S. Liu, M.C. Duke, V. Rudolph, J.C. Diniz da Costa, Hydrothermal stability of cobalt silica membranes in a water gas shift membrane reactor, Sep. Purif. Technol., 66 (2009) 299-305.

[31] K. Kusakabe, T. Kuroda, A. Murata, S. Morooka, Formation of a Y-type zeolite membrane on a porous-alumina tube for gas separation, Ind. Eng. Chem. Res., 36 (1997) 649-655.

[32] P. Patnaik, Handbook of inorganic chemicals, McGraw-Hill New York, 2003.

[33] D.M. Ruthven, W. DeSisto, S. Higgins, Diffusion in a mesoporous silica membrane: validity of the Knudsen diffusion model, Chem. Eng. Sci., 64 (2009) 3201-3203.

[34] F. Jareman, J. Hedlund, D. Creaser, J. Sterte, Modelling of single gas permeation in real MFI membranes, J. Membr. Sci., 236 (2004) 81-89.

[35] S.K. Bhatia, Directional autocorrelation and the diffusional tortuosity of capillary porous media, J. Catal., 93 (1985) 192-196.

[36] S.K. Bhatia, Stochastic theory of transport in inhomogeneous media, Chem. Eng. Sci., 41 (1986) 1311-1324.

[37] S.P. Friedman, N.A. Seaton, A corrected tortuosity factor for the network calculation of diffusion coefficients, Chem. Eng. Sci., 50 (1995) 897-900.

[38] E. Iglesia, S.L. Soled, J.E. Baumgartner, S.C. Reyes, Synthesis and catalytic properties of eggshell cobalt catalysts for the Fischer-Tropsch synthesis, J. Catal., 153 (1995) 108-122.

[39] H.L. Castricum, R. Kreiter, H.M. van Veen, D.H.A. Blank, J.F. Vente, J.E. ten Elshof, High-performance hybrid pervaporation membranes with superior hydrothermal and acid stability, J. Membr. Sci, 324 (2008) 111-118.

[40] M.C. Duke, J.C. Diniz da Costa, G.Q. Lu, M. Petch, P. Gray, Carbonised template molecular sieve silica membranes in fuel processing systems: permeation, hydrostability and regeneration, J. Membr. Sci., 241 (2004) 325-333.

[41] R.A. Silva, C.F. Diniz, M.M. Viana, S.L. Abreu, T.G.F. Souza, N.D.S. Mohallem, T.D.S. Mohallem, Preparation of thin films using freeze drier alumina, Braz. J .Phys, 39 (2009) 236-238.

[42] G.J. Tjatjopoulos, D.L. Feke, J. Adin Mann, Molecule-micropore interaction potentials, J. Phys. Chem., 92 (1988) 4006-4007.

[43] X. Zhang, W. Wang, G. Jiang, a potential model for interaction between the Lennard Jones cylindrical wall and fluid molecules, Fluid Phase Equilibr., 218 (2004) 239-246.

[44] F.J. Blas, L.F. Vega, K.E. Gubbins, Modeling new adsorbents for ethylene/ethane separations by adsorption via π-complexation, Fluid Phase Equilibr., 150 (1998) 117-124.

[45] S.K. Bhatia, Modeling pure gas permeation in nanoporous materials and membranes, Langmuir, 26 (2010) 8373-8385.

[46] M. Sahimi, Flow and transport in porous media and fractured rock: From classical methods to modern approaches, Wiley-VCH, 2011.

[47] S.K. Bhatia, Capillary network models for transport in packed beds: considerations of pore aspect ratio, Chem. Eng. Commun., 154 (1996) 183-202.

[48] R. Bailey, Design of comparative experiments, Cambridge Univeristy Press, 2008.

Chapter 5: The transport of gases in a supported mesoporous silica membrane

In this chapter, we investigate the low pressure transport of several gases in a disordered mesoporous silica membrane of mean pore diameter 3.70 nm, deposited on a porous tubular asymmetric support. The transport data for the supported membrane is examined using three different diffusion models, the classical Knudsen model, a version corrected for finite molecular size, as well as the Oscillator model developed in this laboratory, using a representative pore size in each layer. We show that the correlation by the Knudsen approach, or its modification for finite molecular size, overestimates the diffusion coefficient in the membrane layer, and yields unrealistically high tortuosities, which vary with temperature and gas species. The apparent tortuosity is significantly reduced to a more reasonable range based on Oscillator model, which accounts for dispersive fluid-solid interaction and the effect of adsorption on the transport.

In order to overcome the lack of transferability associated with fitting of a variable tortuosity, effective medium theory is used to model the transport in the different layers, while considering the entire pore size distribution for each layer, using only fundamental structural parameters. It is found that the classical and corrected Knudsen models yield significant deviations even with an unrealistically high thickness for the membrane layer, due to the overestimation of the diffusivity. The most satisfactory results are obtained with the Oscillator model, in which the fitting error is significantly reduced with acceptable membrane thickness. The results indicate that the Knudsen model fails to represent the transport for the mesopores of mean size of 3.70 nm in silica, and that the Oscillator model provides a more accurate apparent diffusivity which accounts for the effects of adsorption. We also show that use of the effective medium theory provides a satisfactory option to model the transport, using only fundamental structural parameters that are transferable.

5.1 Introduction

Mass transport in confined spaces is fundamental to the application of porous materials in areas such as adsorption, separation and catalysis. In the last decade, interest in the subject has been considerably enhanced by the rapid emergence of new nanoporous materials which are believed to hold promise for such applications [1-5]. The Knudsen model, developed a century ago, is still the primary tool to examine the diffusion of gases in porous materials when the pore diameter exceeds the (arbitrary) IUPAC micropore limit of 2 nm [6-8]. However, direct verification of the Knudsen model was originally performed at low density with relatively large tubes of 33–145 μm diameter [9], in which the diffusion is dominated by the fluid-wall diffuse reflection, with negligible influence of the dispersive force exerted by the wall [10]. On the other hand, most porous materials are often examined under conditions in which inter-molecular collisions are also of importance.

Thus, the viscous contribution also needs to be considered; this is often represented by Hagen-Poiseuille equation.

The most successful approach based on this principle is the Dusty Gas Model (DGM) of Mason and his workers, , which arbitrarily superposes pore wall-affected diffusion and hydrodynamic fluxes [11]. When adsorption is negligible, the pore wall-affected diffusion is often represented by the Knudsen model, which is supplemented by a surface diffusion contribution when adsorption is significant, with the hydrodynamic contribution assumed negligible [12, 13]. Although it lacks a firm molecular basis, the DGM approach is commonly applied by researchers [14-16] due to its simplicity; this is generally done by empirically correlating experimental data using a representative pore radius. For instance, several nanoporous materials are highly disordered, and the use of structure-related fitting parameters such as tortuosity is generally required. Use of a single representative pore size is a major shortcoming of this method, as the pore size distribution (PSD) has significant influence for nanoscale porous materials [12]. In addition, unambiguous confirmation of the validity of the Knudsen model in narrow pores with nanoscale dimension, to which the Knudsen model is frequently applied, has never been obtained. Although it can successfully correlate experimental data for various nanoscale materials, the interpretation of experimental data using the Knudsen model in such narrow pores leads to unrealistically high tortuosities, which mask the failure of the diffusion model and indicate significant overestimation of the diffusivity [17-19].

The failure of the Knudsen model in the mesopores is believed to be due to the neglect of dispersive solid-fluid interactions during the transport. However, when the pores are much larger than the range of potential field exerted by the wall, the classical Knudsen model can be safely employed to represent the fluid-wall diffusion, and the DGM can be applied to model the transport. For instance, in macroporous tubular substrate where the pores radius is in the range of hundreds of nanometers, the relationship between the flow rate (F) and temperature can readily expressed as [20]

$$F\sqrt{T} = \frac{2\pi L(-\Delta P)\varepsilon}{\tau_{app}\ln(R_o/R_i)}\left(\frac{\bar{r}_p^{\,2}\bar{P}}{8R_g\eta\sqrt{T}} + \frac{97\bar{r}_p}{R_g\sqrt{M}}\right) \tag{5.1}$$

Here, the term $\ln(R_o/R_i)$ accounts for the change in curvature over the thickness of the tube, and R_o (m) and R_i (m) are the outer and inner tube radii, respectively. Furthermore, T represents temperature (K), L (m) is the tube length, $\bar{P}$ is the average pressure (Pa), η is fluid viscosity (Pa.s), M is the fluid molar mass (g/mol) and R_g is the gas constant. ε is the substrate porosity and τ_{app} the apparent tortuosity coefficient, which is normally obtained through correlation based on the experimental data.

Molecular dynamics (MD) simulations do not suffer from many of the uncertainties arising from the assumptions and simplifications introduced in theoretical models, and have become an invaluable recourse for predicting pore diffusivity; this is particularly important when direct measurements are either impossible or inadequate. According to the simulation results, not only does the Knudsen approach overestimate the diffusivity for mesopores [21-23], but also misinterprets the fluid density profile across the pore radius. The latter is not uniform and identical to the bulk conditions, but is strongly affected by the pore radius and pore structure due to the potential field produced by the pore walls [21-23].

On the other hand, MD is still impractical for routine use due to its high computational demand, and the quest for a tractable theory founded on molecular principles is therefore of much importance. Considerable efforts have been devoted to modify the Knudsen model by introducing an Arrhenius-type factor containing an activation energy term [24-27], so as to incorporate a stronger temperature dependence, but this approach is somewhat empirical and lacks molecular basis. On the other hand, considerable success has been achieved in this laboratory, through the development of the 'Oscillator model', which considers the solid-fluid dispersive interaction before collision, and the density profile difference between the pores and bulk is represented by the equilibrium constant [28-30]. The new theory has been extensively validated against the MD results and some experimental data [6], and is extremely efficient from a computational standpoint, requiring only 2-5 min of CPU time, in contrast to 10-24 hours for MD simulations. Nevertheless, the model needs further confirmation, which constitutes one of the aims of this article.

A significant challenge attending the application of any theory to experimental transport data is the intricacy of the pore network, including the connectivity and pore shape as well as the presence of non-uniform pore size, especially in disordered and heterogeneous porous materials. For instance, a typical supported silica membrane system is fabricated in an asymmetric fashion, comprising a thin selective top layer with narrow pores, in which the separation occurs, coated on a relative thick porous support. A thick porous α-alumina tube coated with a thin γ-alumina interlayer is usually selected as the asymmetric support [31-33]. The α-alumina substrate is made of unconsolidated micron sized (~3 μm) crystal particles, to obtain a macroporous structure with good mechanical resistance. The γ-alumina crystal particles in the interlayer are much smaller (~0.05 μm) and deposited on the surface of the α-alumina substrate to create a smooth, defect-free surface over which the active silica layer is coated. The 'traditional' method to model the transport in the supported membrane is based on empirical fitting in the spirit of DGM, by choosing a representative pore for each layer. However, the interfacial pressures between layers are not directly measurable, and the analysis of diffusion through each layer is often based on arbitrary assumptions, regardless of the variation of controlling mechanism with operating conditions, including temperature and gas species [7].

Besides, considering the large pore size in the substrate (a few hundred nanometers), some authors assume dominance of viscous flow even at low pressure conditions [14, 15, 34], which permits a reasonable membrane tortuosity but is contradicted by straightforward theoretical analysis [35]. Indeed, substantial experiments have verified that such assumption is incorrect, and both Knudsen flow and viscous flow are of importance in the macroporous substrate at low pressure [16, 20, 36-38]. Furthermore, most conventional correlations based on the DGM rely on the hypothesis that the tortuosity is solely determined by the topology of the medium; however, our previous work has extensively shown that the apparent tortuosity can be significantly influenced by the diffusion mechanism in the pores [12, 16]. In addition, the apparent tortuosity is not directly measurable, but is obtained based on an arbitrarily chosen representative pore radius that may be evaluated by various prescriptions (e.g. from pore volume to surface area ratio, or peak of pore size distribution). Thus, any correlation based on such a representative pore radius cannot be used to unequivocally validate the corresponding transport mechanism in a disordered material.

As a result of the above uncertainties, it is of interest to develop a new approach which can be unambiguously applied to model the transport in disordered supported porous membranes, with the resistance for each layer correctly accounted for, in interpreting experimental data. Effective medium theory (EMT) provides the necessary machinery for resolving the above issues, and in this method, a nonuniform network with a distribution of conductance is replaced by a uniform one in which each conductance is assigned an effective value [39-42]. This approach has been successfully employed to examine the transport in unconsolidated materials and in a heterogeneous supported γ-alumina membrane [20], in which the macroscopic parameters can be directly predicted, so it does not suffer from the uncertainties arising from an arbitrary apparent tortuosity in the empirical method. In this spirit, we apply this technique to explore the diffusion mechanisms in a typical mesoporous amorphous silica membrane, having a mean pore diameter of 3.70 nm, coated on an asymmetric alumina support, while considering the resistance of each layer. The results permit unequivocal understanding of the mechanism of fluid transport in the mesoporous silica layer, and demonstrate the inadequacy of the Knudsen model in representing the diffusion in this layer.

5.2 Materials synthesis, characterization and membrane permeation experiments

5.2.1 Macroporous substrate

The α-alumina tubular substrate was obtained from Australia Chemtech Trading & Service Company, and is made of packed α-alumina particles sintered at high temperature. The tube has an inner radius of 4.25 mm and an outer radius of 6.38 mm, and a length of 8.20 cm. Since the pore structure of the substrate mainly comprises interstitial voids between the α-alumina crystals, the particle size has dramatically influence on the size of the pores. Before conducting any pore size characterization, the substrate was investigated by Scanning Electron Microscopy (SEM), showing the particle size to be round 3 μm, and the pore space to comprise macropores. A more accurate pore size distribution was then characterized by mercury porosimetry (Micrometrics, IV 9500), and the mean pore radius was found to be around 250 nm. The details of the characterization of the pore network for the substrate can be found in our recent work [16]. We note here that the permeation experiments with the pure substrate, coated asymmetric support, and coated silica membrane, were conducted using three separate 8.2 cm long piece cut from the same 2 m piece of the substrate tube. The structural characterizations presented here were done on a sample from this large tube, and are considered representative of the properties of all the shorter tubes cut from this.

5.2.2 Mesoporous interlayer

The asymmetric support was synthesized in this laboratory by dip-coating the α-alumina substrate in a γ-alumina solution (20 wt%) purchased from Sigma-Aldrich, with an average particle size of about 50 nm. For the dip-coating the solution was diluted to 2 wt% with deionized water, and the inner surface of the substrate was sealed. The dip-coating was performed at a rate of 10 cm/min using a dip-coating apparatus, and the coated tube subsequently oven-dried at 40 ^{o}C for 2 hours. The as-synthesized asymmetric support was then calcined at 700 °C for 2.5 hours. In order to make a nearly defect-free membrane, ten γ-alumina layers were coated over the substrate, in which each interlayer was coated, dried and calcined under the same conditions as the first layer. The remaining diluted solution was processed under the same conditions as the asymmetric support to obtain an agglomerated γ-alumina powder, which was characterized by nitrogen adsorption at 77 K using a Micrometrics ASAP2020. The indicative pore radius was around 5.2 nm, and the pore structure of this agglomerated powder was taken to represent the pore structure of the γ-alumina on the substrate. The thickness of the interlayer was then examined by SEM, giving a value of around 2 μm. The details of characterization of the pore network of the interlayer can be found in our previous publication [20].

5.2.3 Mesoporous silica

The silica membrane layer was synthesized using a tetraethylorthosilica (TEOS) silica sol templated with Pluronic P123 ($EO_{20}PO_{70}EO_{20}$, MW= 5800, Sigma-Aldrich), a non-ionic block copolymer. A mixture of 27.00 mL H_2O, 27.00 mL diluted HCl (2.30 mol/L), 44.35 mL ethanol, 56.00 mL TEOS was stirred vigorously for 20 min, then a mixture of P123 and ethanol was added to the solution and the stirring continued until the P123 completely dissolved.

The as-synthesized tubular asymmetric support was dipped into the solution, using the dip-coating apparatus, at a rate of 10 cm/min, and subsequently oven-dried at 40 °C for 2 hours. The surfactant was then removed by calcination at 600 °C for 2.5 hours with a heating/cooling rate 1 °C/min, which was confirmed to be sufficient to vaporize the surfactant by thermogravimetric analysis (TGA). As seen in Figure 5.1(a), the organic surfactant began to decompose at 180 °C and is completely removed by 600 °C. The completely disappearance of the surfactant was further demonstrated by Fourier transform infrared spectroscopy (FTIR). As depicted in Figure 5.1(b), the characteristic bands of CH_3 (2980 cm^{-1}), CH_2 (2922 cm^{-1}), and CH (2851 cm^{-1}) in P123 are entirely eliminated after calcining, indicting the absence of any organic residuals in the silica gel [43]. To ensure complete coverage of the membrane, ten silica layers were deposited over the asymmetric support, and each silica layer was coated, dried and calcined under the same conditions as the first layer. The remaining silica sol was processed under the same conditions as the membrane to obtain porous silica powder, which was taken to represent the pore structure of the silica membrane layer.

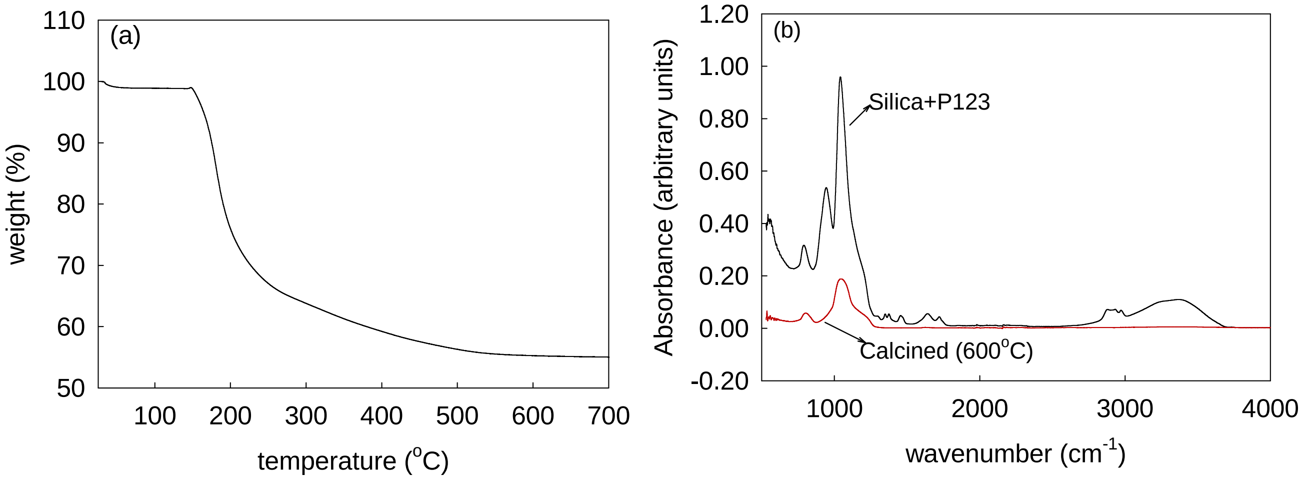

Figure 5.1 (a) Thermogravimetric analysis curve for the uncalcined silica xerogel, and (b) the Fourier transform infrared spectroscopy (FTIR) of the calcined and uncalcined silica xerogel.

The obtained porous silica powder was characterized by nitrogen adsorption at 77 K, and the pore size distribution was examined by nonlocal density function theory (NLDFT) assuming cylindrical pores with an oxide surface. The pore size distribution for the calcined silica gel is illustrated in Figure 5.2, indicating that majority of the pores are within the mesoporous range, and the corresponding pore volume and surface area are 0.48 cm^3/g and 519.87 m^2/g respectively, which were subsequently used to estimate the porosity and average pore radius.

The pore structure of the silica powder was investigated by Transmission electron microscopy (TEM) as in Figure 5.3, showing that the diameter of most pores is less than 5 nm in accord with the PSD determined by NLDFT. The skeletal density of the silica powder measured by Helium Pycnometry was 2.23 g/cm^3, close to the theoretical density of around 2.3 g/cm^3 [44], indicating that essentially all voids in the sample are accessible. The accessible porosity of the powder was determined by

$$\varepsilon = \frac{V_p \rho}{1 + V_p \rho} \tag{5.2}$$

in which V_p is the pore volume obtained through the NLDFT characterization, and ρ is the true density from Helium Pycnometry. Following eqn. (5.2), the accessible porosity of the silica powder is estimated to be 0.52.

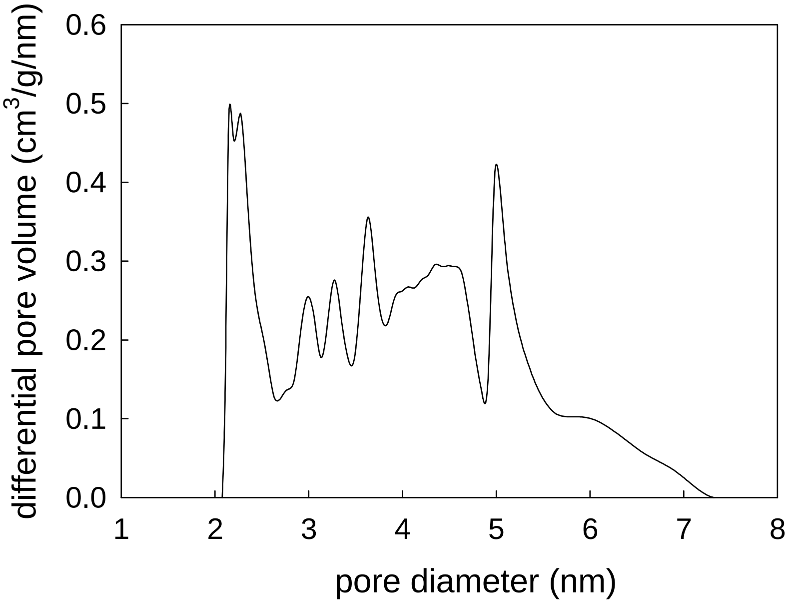

Figure 5.2 Pore size distribution of the calcined silica powder, obtained by nonlocal density function theory (NLDFT) interpretation of N_2 adsorption data.

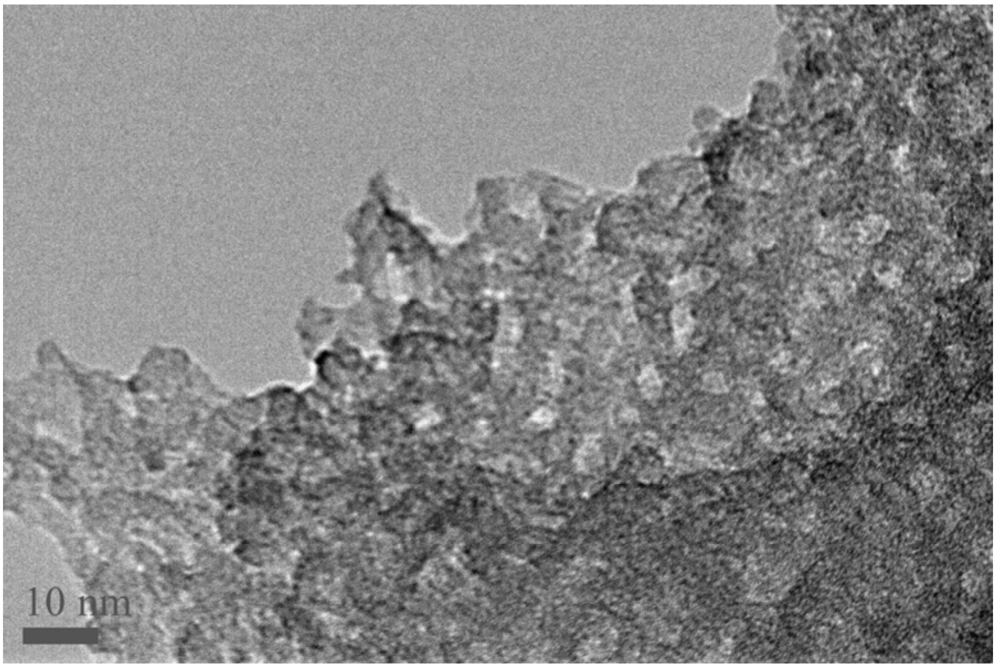

Figure 5.3 Transmission electron microscopy image of the porous silica powder.

In order to estimate an appropriate tortuosity for each layer based on the correlation using eqn. (5.1), in this work an average cylindrical pore radius is evaluated following:

$$\overline{r}_p = \frac{2V_p}{S} \tag{5.3}$$

where S is the surface area determined through the NLDFT characterization or Mercury Porosimetry. This definition of the representative pore radius is perhaps the most common, although other alternatives such as the peak size of the PSD or number averaged pore radius have also been used. Following eqn. (5.3), the obtained $\overline{r}_p$ is 257.05 nm for the substrate, 5.22 nm for interlayer, and 1.85 nm for the silica layer.

The value of the thickness for each layer is critical in modeling the transport in the supported membrane, while considering the resistance for each layer. For the macroporous substrate, the thickness can be directly measurable by a caliper; for the mesoporous interlayer and membrane layer, the corresponding thickness is only several microns, and has to be evaluated through the SEM images. Since the boundaries between the layers are ill-defined and somewhat diffuse, the thickness of the interlayer and membrane layer cannot be precisely evaluated. As depicted in the Scanning Electron Microscopy (SEM) images in Figure 5.4, the thickness of the silica membrane layer varies between 12 and 18 μm (after accounting for the thickness of the interlayer of 2 μm) due to the underlying uneven topology of the asymmetric support, which varies in height and has some surface roughness, and an average membrane thickness of 15 μm was taken for the transport data analysis.

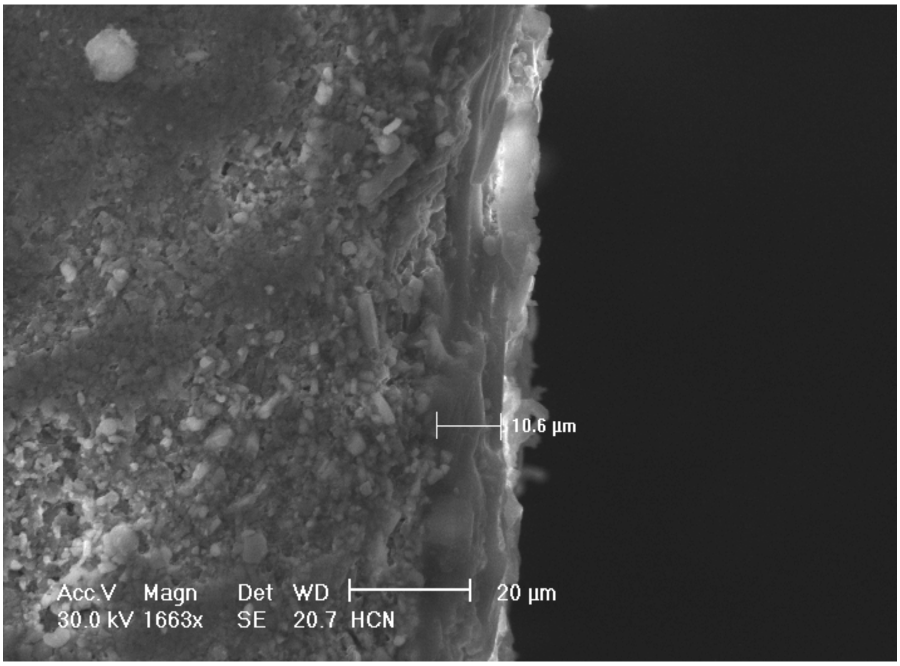

Figure 5.4 Scanning electron microscopy image of the supported silica membrane layer.

5.2.4 Single gas membrane permeation experiments

The transport mechanism in the homogenous substrate and asymmetric support has been previously investigated independently in our previous work [20] by conducting two sets of single gas permeation experiments. It was confirmed that the transport in the macroporous substrate can be adequately modeled as slip flow, with both Knudsen and viscous contributions being important. The corresponding transport mechanism for the interlayer could be represented by three diffusion models, including the classical slip flow, a correction version for finite molecular size and the Oscillator model.

To explore the diffusion in the narrower pore silica membrane deposited on the asymmetric support, single gas permeation experiments were performed here under the same conditions as in the earlier study [20], as illustrated in Figure 5.5.

The flow of six different gases (H_2, He, CH_4, N_2, Ar and CO_2) was investigated, with the gas entering from the substrate side at a constant feed pressure, P_F =1.97 bar, permeating through the interlayer, and finally leaving from the silica layer side, where the outlet pressure (P_o) corresponds to atmosphere pressure (1.01 bar). The operating temperature was varied from 30 to 300°C. The volumetric flow rate was measured by a bubble flow meter and later converted to molar flow rate by means of the ideal gas equation of state. In the transport modeling discussed below, the interfacial pressure between the substrate and the interlayer is arbitrarily labeled as P_1, and the interfacial pressure between the interlayer and the silica membrane layer is represented by P_2. It is noted that the permeation experiments was carried out from high temperature (300 °C) to low temperature (30 °C) to avoid any water blockage effect.

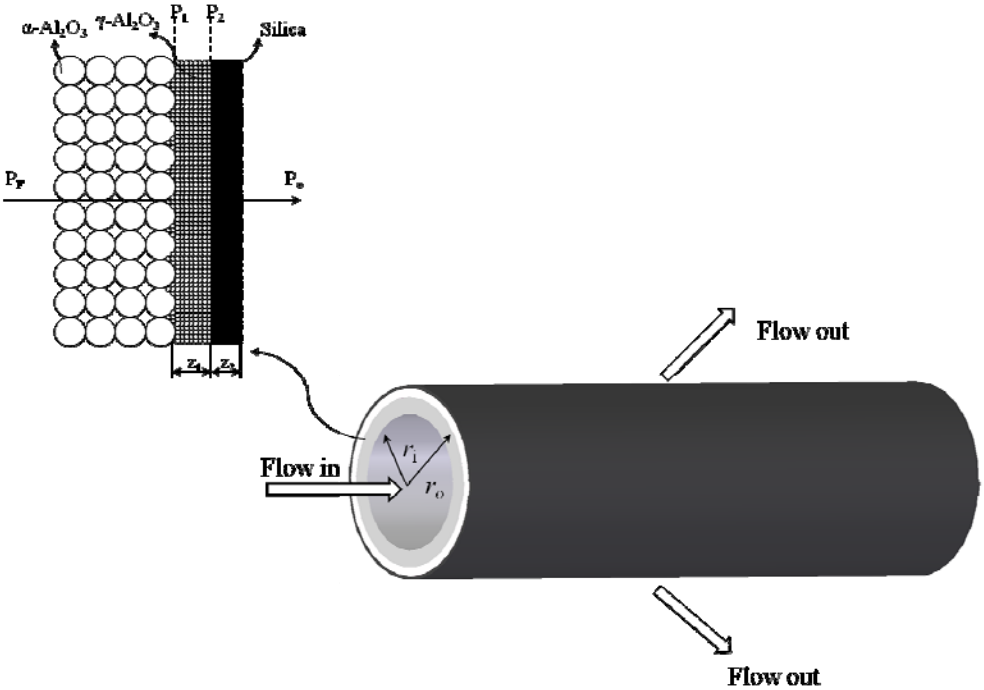

Figure 5.5 Schematic drawing of the flow direction in the supported silica membrane and the interface between different layers.

For clarity, the flow rates in the substrate, interlayer and the silica membrane layer, although equal at steady state, are labeled respectively as F_s, F_c and F_m. Besides, the structural parameters (porosity, tortuosity, tube length and average pore radius) for the substrate, interlayer and the silica membrane layer are identified by subscripts *s*, *c* and *m*.

5.3 Transport models

5.3.1 Transport in a single pore

Following our previous work, an important aim of this article is to explore the transport of adsorbates in a narrow pore mesoporous silica material having a disordered network, with various flow mechanisms employed at the single pore level. To distinguish the diffusivity estimated by different models, the pore radius used for each model must be precisely defined. As suggested in Figure 5.6, there are several ways to define a pore radius, which will be extensively discussed in the following.

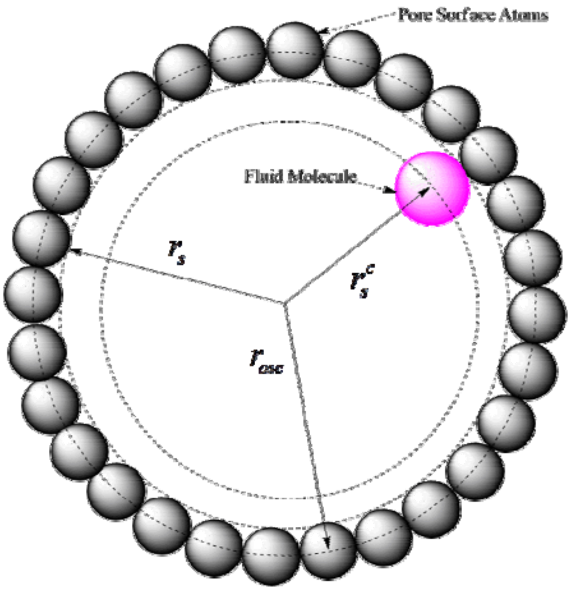

Figure 5.6 Illustration of different pore radii used in the classical Knudsen model (r_s), the corrected Knudsen model (r_s^c), and the Oscillator model (r_{osc}).

5.3.1.1 Classical slip flow model

In the classical slip flow model, the diffusivity is estimated based on the geometrical pore radius (r_s), defined as the distance between the centerline of the pore and the surface of atom on the walls, with the fluid molecular size considered negligible compared to the pore radius, which is reasonable for macropores (r_s > 25 nm). The classical slip flow model has been extensively validated at low pressure, for which the Knudsen (D_{Kn}) and viscous diffusivity (D_{vis}) are respectively represented as

$$D_{Kn} = 97 r_s \sqrt{\frac{T}{M}} \tag{5.4}$$

$$D_{vis} = \frac{\overline{P} r_s^2}{8\eta} \tag{5.5}$$

with the variables having the same units as in eqn. (5.1). Besides, the density profile along the radial coordinate is considered to be constant and identical to the bulk, therefore, the equilibrium constant is always unity for Knudsen and viscous diffusion (K=1). Since the pores in the substrate are larger than 100 nm, the slip flow model with an apparent diffusivity $(D_o^a = D_{Kn} + D_{vis})$ can be safely used for the transport in the substrate, without exclusion effects due to the relatively small molecular size.

5.3.1.2 Corrected slip flow model

For smaller pores, the exclusion effect of fluid molecules should be taken into account, and pore radius is corrected as

$$r_s^c = r_s - \sigma_{ff}/2 \tag{5.6}$$

where σ_{ff} is the Lennard-Jones (LJ) fluid-fluid collision diameter, listed in Table 5.1 for the gases relevant to in this article. The apparent diffusivity ($D_o^c = D_{Kn}^c + D_{vis}^c$) is estimated based on the corrected pore radius (r_s^c) through eqs. (5.4) and (5.5), taking the equilibrium constant as unity. Since the finite fluid molecular size can lead to a considerable fraction of the smallest pores becoming inaccessible in the interlayer and silica membrane, the corrected slip flow model is applied to predict the alternative apparent diffusivity for the pores in these layers so as to fully confirm the validity of the Knudsen model at the corresponding pore sizes.

Table 5.1 Fluid-fluid Lennard-Jones parameters used in the Oscillator model.

parameters	H_2	He	CH_4	N_2	Ar	CO_2
σ_{ff} (nm)	0.2915	0.2551	0.381	0.3572	0.341	0.3472
ε_{ff}/k_B (K)	38.0	10.22	148.2	93.98	120.0	221.9

5.3.1.3 Oscillator model

An alternative way to evaluate the apparent diffusivity in the interlayer and silica membrane layer is based on the Oscillator model [23], which considers the (low-density) radial density profile inside the pores. However, the pore radius used in the Oscillator model is different from the ones used in the slip flow model, and is the distance between the centreline of the pore and the centre of the surface atoms on the walls, r_{osc}, following

$$r_{osc} = r_s + \sigma_{ss}/2 \tag{5.7}$$

where σ_{ss} is the LJ solid-solid collision diameter of the atoms on the pore walls.

In the Oscillator model, the diffusivity of a LJ fluid under conditions of diffuse reflection in a cylindrical pore, D_{osc}, is estimated as

$$D_{osc} = \frac{2}{\pi m Q} \int_0^\infty e^{-\beta\varphi(r)} dr \int_0^\infty e^{-\frac{\beta p_r^2}{2m}} dp_r \int_0^\infty e^{-\frac{\beta p_\theta^2}{2mr^2}} dp_\theta \int_{r_{co(r,p_r,p_\theta)}}^{r_{cl}(r,p_r,p_\theta)} \frac{dr'}{p_r(r',r,p_r,p_\theta)} \tag{5.8}$$

where $\varphi(r)$ is the solid-fluid potential, m is fluid particle mass, $\beta = 1/k_B T$ and $Q = \int_0^\infty re^{-\beta\varphi(r)}dr$. Further, p_r and p_θ are the radial and angular components of the molecular momentum, and r_{cl} and

r_{co} represent the radial bounds of a fluid molecule trajectory between consecutive diffuse reflections, determined through the solution of $p_r(r',r,p_r,p_\theta)=0$. Here, $p_r(r?\,r,\,p_r,\,p_\theta)$ is its radial momentum when it is at radial position, r', given that it has radial momentum p_r at r, and is obtained from

$$p_r(r?\,r,\,p_r,\,p_\theta)=\left(2m\left[\varphi(r)-\varphi(r')\right]+\frac{p_\theta^2}{r^2}\left[1-\left(\frac{r}{r'}\right)^2\right]+p_r^2(r)\right)^{1/2} \tag{5.9}$$

The equilibrium constant (K) for Oscillator model is readily obtained from

$$K=\frac{2}{r_{osc}^2}\int_0^{r_{osc}} e^{-\varphi(r)/k_BT}\,rdr \tag{5.10}$$

The value of the interaction potential, $\varphi(r)$, strongly depends on the pore wall composition and structure. For γ-alumina, the pore is assumed to have infinitely thick walls comprising randomly distributed oxygen ions, and these ions are considered to dominate the interaction between the fluid and the pore walls. Assuming LJ interaction between the fluid molecules (taken as a single LJ site) and the oxygen ions in the wall, the interaction potential profile, $\varphi(r)$, is given by [45]

$$\varphi(r)=\pi^2\varepsilon_{sf}\rho_v\sigma_{sf}^3\left\{\frac{7F_h(-4.5,-3.5,1;(r/r_{osc})^2)}{32(r_{osc}/\sigma_{sf})^9\left[1-(r/r_{osc})^2\right]^9}-\frac{F_h(-1.5,-0.5,1;(r/r_{osc})^2)}{(r_{osc}/\sigma_{sf})^3\left[1-(r/r_{osc})^2\right]^3}\right\} \tag{5.11}$$

Here σ_{sf} is the LJ solid-fluid collision diameter, ε_{sf} is the LJ potential well depth, ρ_v is the oxygen density in the wall (ions per unit volume) and $F_h(x,y,z;w)$ is the Hypergeometric function. The LJ parameters for the gases used in our experiments are listed in Table 5.1, and the LJ parameters for the γ-alumina are taken from Blas et al. [46] as $\varepsilon_{ss}/k_B = 108.47$ K, $\sigma_{ss} = 0.303$ nm, with $\rho_v = 52.24$ nm^{-3}. For silica, the pore is composed of a single layer wall, in which the interaction between fluid and pore walls is considered to be dominated by a surface layer of oxygen ions, leading to the interaction energy profile [47]

$$\varphi(r)=4\pi^2\varepsilon_{sf}\rho_s\sigma_{sf}^2\left\{\frac{63F_h(-4.5,-4.5,1;(r/r_{osc})^2)}{128(r_{osc}/\sigma_{sf})^{10}\left[1-(r/r_{osc})^2\right]^{10}}-\frac{3F_h(-1.5,-1.5,1;(r/r_{osc})^2)}{4(r_{osc}/\sigma_{sf})^4\left[1-(r/r_{osc})^2\right]^4}\right\} \tag{5.12}$$

where ρ_s is the pore wall surface density (atoms per unit area). The LJ parameters for the silica layer are evaluated based on the results from Neimark et al. [48] as $\varepsilon_{ss}/k_B = 492.7$ K, $\sigma_{ss} = 0.28$ nm, with $\rho_s = 10.47$ nm^{-2}. The Lorentz-Berthelot mixing rules are employed to estimate the solid-fluid LJ parameters ε_{sf}/k_B and σ_{sf} [28]. Finally, the apparent low density diffusivity based on the pseudo-bulk concentration gradient is then estimated as $D_o^{osc} = D_{osc} K$, ignoring the viscous contribution due to fluid-fluid interaction.

5.3.2 Transport in pore networks

A critical factor impeding the application of any transport theory in disordered nanoporous materials is the complexity of material topology, involving the variables such as connectivity, pore structure and pore size distribution. This is clearly evident in the typical supported silica membrane, which comprises the macroporous α-alumina substrate, mesoporous γ-alumina interlayer and mesoporous or microporous amorphous silica layer. In the substrate and interlayer, the pores form the spaces between unconsolidated crystal particles, and not only must the pore size distribution and pore network connectivity be considered but also the pore aspect ratio distribution assumes importance [16].

Effective medium theory (EMT) offers a convenient tool to account for these complexities of the network for each layer by replacing the nonuniform pore network with an effective one having pores of uniform conductance. With a hybrid model combining the correlated random walk theory (CRWT) and EMT on this effective network, the macroscopic flow rate can be precisely predicted for the interpretation of experimental data. In our previous work [16], we have already applied this technique to model the transport in the macroporous substrate and confirmed the variation of tortuosity with operating conditions due to the combined effects of the Knudsen and viscous contributions (which have different associated tortuosities in the limiting regimes where they govern the transport). The methodology has been further extended to predict the transport properties of an asymmetric support comprised of the macroporous substrate and the mesoporous interlayer [20]. The results clearly demonstrated that the classical and corrected slip flow models, or the Oscillator model, can adequately represent the transport in the interlayer, and confirmed that the pressure gradients vary significantly with operating conditions and gases. Following the line of our previous works, we utilize this methodology to model the transport for the silica layer coated on the asymmetric support while the taking the resistance for each layer into account, and investigate the validity of the classical Knudsen diffusion model in the silica mesopores, which are considerably narrower than those of the γ-alumina interlayer..

For a pore of radius of r_p, the conductance, λ, is defined as the ratio of the molecular current to the pressure gradient driving force, following

$$\lambda = \frac{\pi r_p^2 D_o(r_p) K(r_p)}{l} \tag{5.13}$$

where $D_o(r_p)K(r_p)$ is the apparent diffusivity, including both the diffusivity and equilibrium constant (K) based on the relevant pore radius as provided above, and l is the pore length. For the macroporous substrate, the combination of classical Knudsen and viscous diffusivity is used to estimate the apparent diffusivity ($D_o = D_{Kn} + D_{vis}$), with $K = 1$, and for interlayer and membrane layer, the apparent diffusivity can be estimated based on this expression or with pore size correction following eqn. (5.7) for the corrected slip flow model. The Oscillator model provides the alternative $D_o = D_o^{osc}$, with the viscous contribution being neglected, and $K(r_p)$ following eqn. (5.10).

Assuming that local equilibrium prevails in the pores, the effective medium conductance, λ_e is determined through the solution to [39]

$$\left\langle \frac{(\lambda - \lambda_e)}{(\lambda + (N/2-1)\lambda_e)} \right\rangle = 0 \tag{5.14}$$

where N represents the coordination number, *i.e.*, the average number of pores meeting at each node, and $\langle \cdot \rangle$ is an average over the pore number distribution. The flux in a pore of radius, r_p, is assessed as

$$j(r_p) = \frac{\lambda_e l}{\pi r_p^2 R_g T} \left(\frac{N-1}{N+1} \right) \overline{\cos^2(\theta)} \left(-\frac{dP}{dz} \right) \tag{5.15}$$

where z represents the coordinate along the macroscopic flux direction, $\overline{\cos^2(\theta)}$ accounts for the local diffusion direction, which is not necessarily axial [49], and the factor (N-1)/(N+1) stands for a correlation effect which arises because of the finite probability that a diffusing molecule returns to a pore that it has just passed through [50, 51]. For unconsolidated media such as the macroporous substrate and mesoporous interlayer, the pore radius is comparable to the pore length, and the diffusion direction in the pore is not purely axial; consequently the aspect ratio effect must be taken into account. By assuming the local transport direction to be that closest to the macroscopic flux direction, the expression for $\overline{\cos^2(\theta)}$ can be rewritten as [49, 52]

$$\overline{\cos^2(\theta)} = g(x) = 1 + \frac{4x}{3(1+4x^2)} - \frac{2}{3(1+4x^2)^{1/2}} \tag{5.16}$$

where x is the aspect ratio (r_p/l). Upon assuming the pseudo pressure to be locally uniform in the network, the net flux in the equivalent uniform network is obtained upon integration of eqn. (5.15) over the pore volume distribution, to yield

$$J = \frac{\varepsilon \lambda_e < l^2 g(x) >}{\pi < r_p^2 l > R_g T} \left(\frac{N-1}{N+1} \right) \left(-\frac{dP}{dz} \right) \tag{5.17}$$

In practice, experimental data is commonly interpreted phenomenologically, while using a representative pore radius, $\bar{r}_p$, and introducing a tortuosity, following

$$J = \frac{\varepsilon D_o(\bar{r}_p)K(\bar{r}_p)}{\tau_{app} R_g T}\left(-\frac{dP}{dz}\right) \tag{5.18}$$

where τ_{app} is an apparent tortuosity that is generally obtained by fitting the experimental flux. Comparing eqs. (5.17) and (5.18), the theoretical prediction of apparent tortuosity is given by

$$\tau_{app} = \frac{\pi < r_p^2 l > D_o(\bar{r}_p)K(\bar{r}_p)}{< l^2 g(x) > \lambda_e}\left(\frac{N+1}{N-1}\right) \tag{5.19}$$

In the present work we use eqn. (5.3) to define the representative pore radius, $\bar{r}_p$.

In the tubular supported membrane, the steady state flow rate (F) is constant across the substrate, interlayer and membrane layer, and integration of eqn. (5.17) over the radial coordinate for each layer, yields

$$F = \frac{2\varepsilon\lambda_e L < l^2 g(x) >}{< r_p^2 l > \ln(R_o/R_i) R_g T}\left(\frac{N-1}{N+1}\right)(-\Delta P) \tag{5.20}$$

where R_i and R_o are the inner and outer radius of the layer, respectively. Since the thickness of the substrate tube (2.13 mm) is comparable to R_i ($R_i = 4.25$ mm), no further simplifications can be done on eqn. (5.20). For the interlayer, the thickness of this interlayer ($z_c \approx 2$ μm) is much smaller than the outer radius of the tube ($R_o = 6.38$ mm), so that $\ln(R_i/R_o) \approx z_c/R_o$, and the expression for the flow rate simplified to

$$F = \frac{2\varepsilon R_o \lambda_e L < l^2 g(x) >}{z_c < r_p^2 l > R_g T}\left(\frac{N-1}{N+1}\right)(-\Delta P) \tag{5.21}$$

In addition to its very small thickness, the silica membrane layer is consolidated, so that the pores in this layer are not interstitial voids between particles. Assuming long cylindrical pores, the aspect ratio may be considered small for the silica layer, and the flow rate in this layer is then obtained as

$$F = \frac{2\varepsilon R_o \lambda_e L < l^2 >}{3 z_m < r_p^2 l > R_g T}\left(\frac{N-1}{N+1}\right)(-\Delta P) \tag{5.22}$$

It is to be noted that the flow rate in the silica layer is independent of l (as the effective conductance, λ_e, is inversely proportional to l). This is not the case for the substrate and interlayer, for which the function $g(x)$ is a nonlinear function of l. For clarity, the structural parameters (coordination number, pore length and apparent tortuosity) of the substrate, interlayer and silica layer are distinguished by subscripts *s*, *c* and *m*.

The above model may be readily applied to the interpretation of membrane transport data. In the present case, the silica membrane thickness, z_m, and coordination number, N_m, are taken as the adjustable parameters, and can be determined by minimization of the error

$$Q(N,l) = \frac{1}{n}\sum_{i=1}^{n}\frac{(F_{mi} - F_{ei})^2}{F_{ei}^2} \tag{5.23}$$

where n is the number of experimental flow rate points for all gases, F_{ei} is the experimental flow rate value for data point i, and F_{mi} is the corresponding model flow rate obtained by effective medium theory. The estimation of the theoretical flow rate requires solving the flow rate relationships for the three layers:

$$F_s\left(P_F, P_1, N_s, l_s\right) = F_c\left(P_1, P_2, N_c, l_c\right) = F_m\left(P_2, P_o, N_m, z_m\right) \tag{5.24}$$

to determine the interfacial pressures, P_1 and P_2. The structural parameters of the substrate (N_s, l_s) and interlayer (N_c, l_c) have been determined in our prior study [20], and have the values $N_s = N_c = 12$, $l_s = 300$ nm, $l_c = 5$ nm. These values have been used in the present work in conjunction with effective medium theory.

5.4 Results and discussion

5.4.1 Comparison of permeance of the different layers in the membrane

The individual diffusion resistance for each layer of the membrane cannot be characterized from overall permeation experiments on the 3-layer composite membrane, as the interfacial pressures between the layers are unknown. However, the apparent permeance ($\pi = J/(-\Delta P)$) of the substrate, asymmetric support and the 3-layer membrane can be determined from the corresponding permeation experiments separately conducted with these.

In chapter 4 [20] we presented flow rate versus temperature results for the substrate and for the γ-alumina coated asymmetric support, for the six different gases used here, at pressures similar to those used here. Figure 5.7 depicts the variation of the permeance with gas molecular size (taken as the LJ size parameter), for the substrate and the asymmetric γ-alumina coated support, based on the earlier data [20], and for the 3-layer composite membrane based on the data obtained here, for (a) 30 °C, and (b) 300 °C. In estimating the flux based on the measured flow rates, we have taken the outer surface of the alumina substrate as the standard area. It is evident from Figure 5.7 that the difference of the apparent permeance between the substrate and the asymmetric support is very small, around 5% in both cases, and that the main resistance in the asymmetric support is provided by the macroporous substrate rather than the mesoporous interlayer. On the other hand, the apparent permeance of the supported silica membrane ranges from 10 to 15% of the apparent permeance of the asymmetric support, indicating that the main resistance is provided by the silica membrane layer but the resistance of the support is also significant.

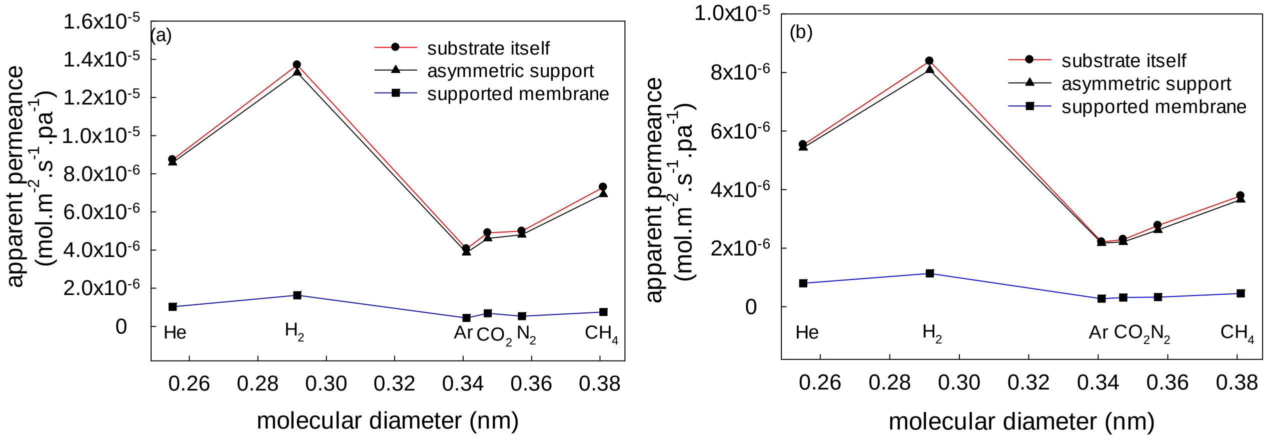

Figure 5.7 Variation of the apparent permeance with gas molecular size for the substrate, the asymmetric support and supported membrane, at (a) 30 °C, and (b) 300 °C, respectively.

5.4.2 Correlation of membrane transport data using single pore size in each layer

It is important to note that the above apparent permeance analysis of each layer is largely qualitative, which is only indicative of the relative importance of their resistance. These must depend on temperature and, for the substrate, also depend on pressure, due to the significance of viscous transport in this layer [16]. In order to correctly account for the resistance of each layer and explore the transport for the membrane layer, the interfacial pressures, P_1 and P_2 (c.f. Figure 5.5), must be specified. Here, we will first attempt to use the ‘traditional’ correlation based on a mean pore radius to investigate the interfacial pressures and transport mechanism for the silica membrane layer in the 3-layer composite membrane. For this we will appeal to our recent data for permeation through the uncoated substrate and the asymmetric support without the silica membrane layer [20], to permit evaluation of the interfacial pressures in the 3-layer membrane system, while using eqn. (5.3) to provide the mean pore radius.

Assuming the classical slip flow model of eqn. (5.1) in the substrate, the interfacial pressure, P_1, for the 3-layer system is estimated by comparing the flow rate data for the substrate itself with that for the substrate as part of the supported membrane. Thus, following eqn. (5.1), we use

$$\left(\frac{J\sqrt{T}}{(P_F-P_O)\left(\frac{\bar{r}_p^{\,2}(P_F+P_O)}{16R_g\eta\sqrt{T}}+\frac{97\bar{r}_p}{R_g\sqrt{M}}\right)}\right)_{\substack{\text{substrate}\\ \text{alone}}} = \left(\frac{J\sqrt{T}}{(P_F-P_1)\left(\frac{\bar{r}_p^{\,2}(P_F+P_1)}{16R_g\eta\sqrt{T}}+\frac{97\bar{r}_p}{R_g\sqrt{M}}\right)}\right)_{\substack{\text{support}\\ \text{in membrane}}} \tag{5.25}$$

to estimate P_1 for the asymmetric support, and for the 3-layer membrane. This assumes that the tortuosity of the substrate is unchanged and transferable to the substrate part in the 3-layer membrane. Subsequently, using these values of P_1 we adopt a similar method for the γ-alumina layer to estimate P_2 in the 3-layer system (c.f. Figure 5.5), following

$$\left(\frac{J\sqrt{T}}{(P_1-P_O)}\right)_{\substack{\text{asymmetric}\\ \text{support}}} = \left(\frac{J\sqrt{T}}{(P_1-P_2)}\right)_{\substack{\text{3-layer}\\ \text{system}}} \tag{5.26}$$

assuming negligible viscous contribution in the pores of the γ-alumina (~11.5 nm dia. [20]). J represents the flux based on the outer radius of the tube as $F/(2\pi R_o L)$.

Figure 5.8 depicts the variation of interfacial pressures, P_1 (Figure 5.8(a)) and P_2 (Figure 5.8(b)) with temperature, for the 3-layer membrane, based on the flow rate versus temperature data obtained here and that for the substrate and asymmetric support obtained in our recent work [20]. This flux versus temperature data for the various gases, obtained here and obtained in our recent work [20], is tabulated in the Supplementary Information. It is evident from Figure 5.8(a) that the estimated interfacial pressure generally decreases with increase in temperature for all the gases, similar to the results in our recent work [20]. However, the curves do show some fluctuation, largely arising from experimental scatter, with cross-over between gases. As will be subsequently evident the anomalous crossover results from the use of a single pore size in the substrate. As illustrated in Figure 5.8 (b), similar behavior is observed for P_2. Further, based on the feed pressure, P_F, of 1.97 bar and the permeate pressure, P_o, of 1.01 bar in our experiments, it is evident from the results in Figure 5.8 that the dominant pressure drops in the supported membrane lie in the mesoporous silica layer (around 90%) and in the macroporous substrate (around 9%), suggesting the pressure loss in the interlayer is negligible (around 1%). This is consistent with the above analysis based on the apparent permeance in Figure 5.7.

Once the interfacial pressures are obtained, the pressure driving force in the silica layer can be readily evaluated, and the apparent tortuosity of this layer can be explicitly examined for each gas at any temperature based on an appropriate diffusion mechanism. In what follows we extensively test the validity of the three diffusion models discussed above (the classical Knudsen model, a corrected version for finite molecular size, and the Oscillator model), for the silica layer using a single representative mean pore size as defined in eqn. (5.3) and a membrane thickness of 15 μm based on the SEM micrograph (Figure 5.4).

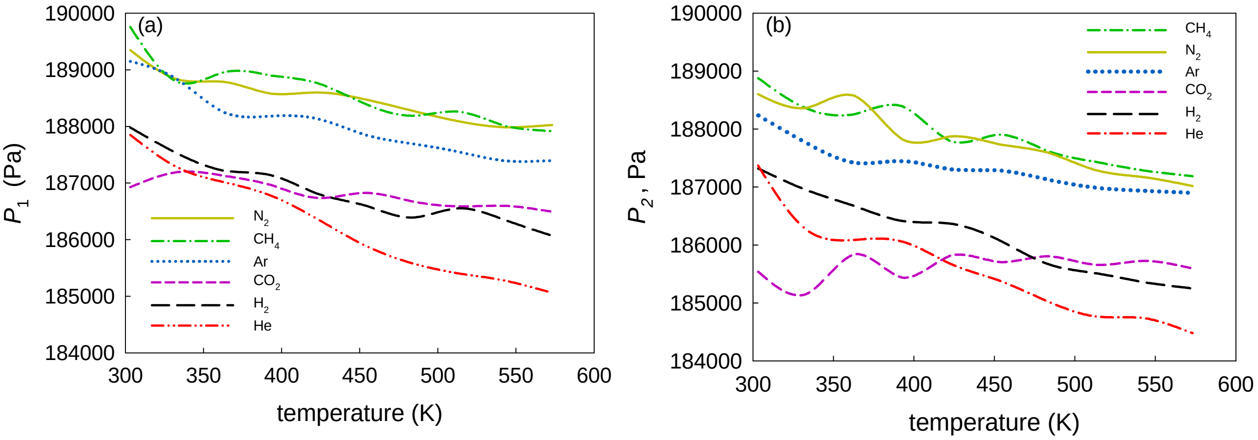

Figure 5.8 Variation of the interfacial pressures, P_1 and P_2 with temperature based on eqn. (5.1), using a representative pore radius for each layer. (a) Interfacial pressure, P_1, and (b) interfacial pressure, P_2.

5.4.2.1 Classical and corrected Knudsen model-based correlation

For the silica layer, having pores in the size range of 2-7 nm diameter, the viscous contribution to the flow may be neglected, and the tortuosity at each temperature point may be readily evaluated from eqn. (5.1). Figure 5.9(a) depicts the variation of tortuosity with temperature for the active silica layer in the membrane, using the estimated values of P_2 depicted in Figure 5.8(b), and the mean pore radius defined by eqn. (5.3). It is evident that the estimated tortuosities are unreasonably high (between 8 and 19), and have a strong temperature and gas dependence, following the order He > H_2 > $N_2 \simeq$ Ar > CH_4 > CO_2, which is observed at each temperature. As mentioned in Chapter 4, the extreme high tortuosity only occurs to the material in which the pores are poorly connected with each other, i.e., the pore coordination number is close to unity. However, according to the work of Seaton based on percolation theory from N_2 adsorption, the pore coordination number for silica is in the range between 3 and 6, which indicates that the maximum intrinsic tortuosity for silica is around 4 [53-55]. It is also evident from Figure 5.9(a) that the trend of the tortuosity variation with temperature is sensitive to the gas species, showing a tortuosity increase with increase in temperature for the heavier gases (Ar, N_2, CH_4 and CO_2), a decrease for He, and little change for H_2. Such variation of tortuosity with temperature and gas species is unexpected for the Knudsen model, for which a constant, purely pore structure-dependent, tortuosity is predicted [12, 20], as $D_o(r) \propto \sqrt{T/M}$ with K = 1 in this case, so that eqs. (5.13), (5.14) and (5.19) lead to a constant tortuosity.

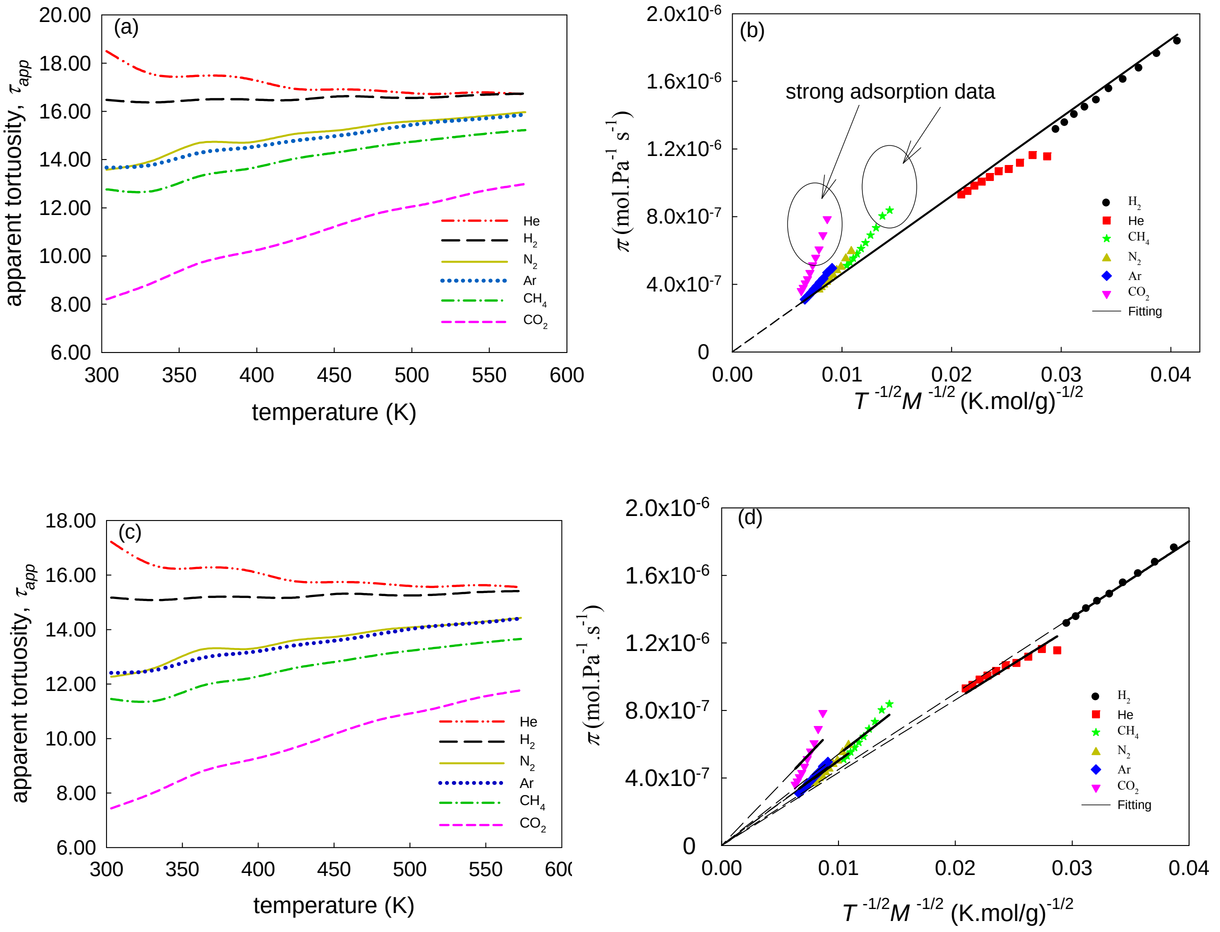

Figure 5.9 (a) Empirical variation of the apparent tortuosity for the silica layer with temperature, obtained using the classical Knudsen diffusion model, (b) linear regression for all the gases based on the classical Knudsen diffusion model in the silica layer, (c) variation of the apparent tortuosity with temperature for the silica layer, obtained using the corrected Knudsen diffusion model, and (d) linear regression for all the gases based on the corrected Knudsen diffusion model in silica layer. The symbols are the experimental points, and the lines are the model results using eqn. (5.18), taking the membrane thickness as z_m = 15 μm based on the SEM image.

However, the behavior observed here is completely consistent with that predicted using the Oscillator model with effective medium theory [12], including even the ordering of the gases with increasing tortuosity. This provides strong support for the validity of the latter approach. As an alternative, one may obtain an overall tortuosity for the silica layer based on eqn. (5.18) by plotting the permeance ($\pi = J/(-\Delta P)$) versus $1/\sqrt{TM}$. A linear correlation passing through the origin is then expected if the Knudsen model is valid, and the apparent tortuosity may then be evaluated from the slope. Such a plot is illustrated in Figure 5.9(b), where it is evident that some of gases (CH_4 and CO_2) systematically deviate from the regression line, especially at low temperature. As marked in the ellipses, much of the experimental data for the heavier gases (CO_2 and CH_4) is significantly higher than the regression line, indicating that strong adsorption occurred for these gases at low temperature, for which the density difference between the pore and bulk fluids is significant. In addition, the apparent tortuosity obtained from the slope is 16.2, which is extremely high. This high a tortuosity mainly arises from the overestimation of apparent diffusivity by the Knudsen model [6, 12], and to a smaller extent from the neglect of the pore size distribution for each layer.

A reduced diffusivity in the membrane layer may be obtained by considering the exclusion effect due to finite molecular size following eqn. (5.6), and the corrected Knudsen model is used to estimate the tortuosity for each gas, with the fluid LJ parameters given in Table 5.1. The variation of the apparent tortuosity with temperature obtained using by this model is depicted in Figure 5.9(c), where it is seen that the apparent tortuosity is only slightly reduced for each gas. It is evident that the tortuosity values are still unreasonably high (between 7 and 17), and a systematic dependence on temperature is still evident with this method. To eliminate the temperature dependence for each gas, the apparent tortuosity can be empirically obtained as above from a linear correlation of the permeance with $1/\sqrt{TM}$. Such a plot is illustrated in Figure 5.9(d), with the estimated apparent tortuosities given in Table 5.2, showing significant variation with gas and having the same order as before, *i.e.*, He > H_2 > N_2 ≃ Ar > CH_4 > CO_2. For instance, the difference in apparent tortuosity for He and CO_2 is more than 150%, in contradiction to theory, which predicts that the apparent tortuosity should be independent of temperature, and only marginally different between gases for the corrected Knudsen model due to molecular size differences [20].

Table 5.2 Apparent tortuosity of silica layer for various gases based on empirical correlation using the corrected Knudsen model.

tortuosity	H_2	He	CH_4	N_2	Ar	CO_2
τ_{app}	15.3	16.1	12.4	13.4	13.4	9.4

The above anomalies indicate that neither the classical nor the corrected Knudsen equation is able to satisfactorily model the transport in the silica layer based on a single representative pore radius. Besides the neglect of the pore size distribution, both fail due to the significant overestimation of the apparent diffusivity and the neglect of adsorption, which leads to an unreasonably high estimated tortuosity.

5.4.2.2 Oscillator model-based correlation

The Oscillator model provides an alternative approach to correlate the experimental flux in the silica layer, in which the apparent diffusivity (KD_{osc}) is estimated using eqs. (5.8) and (5.10) while considering the fluid-solid interaction with the LJ parameter given in Table 5.1. The variation of apparent tortuosity with temperature, estimated using eqn. (5.18), is depicted in Figure 5.10(a), showing the tortuosity to be dramatically decreased for each gas compared to that estimated using the Knudsen or corrected Knudsen approach. In addition, the tortuosity variation with temperature and gas species is consistent with the prediction by theory [12], due to the more complex dependence of flux on temperature and fluid molecular parameters in the Oscillator model. As with the Knudsen model, a linear correlation of permeance ($\pi = J/(-\Delta P)$) against $D_{osc}(\overline{r}_p)K(\overline{r}_p)/T$ was performed for each gas in accordance with eqn. (5.18), as depicted in Figure 5.10 (b), and the tortuosity derived from the slope. It evident that the correlation arising from the Oscillator model is much more satisfactory than the Knudsen approach, without the anomalies arising from the strong adsorption of CH_4 and CO_2 at low temperature observed in the Knudsen approach. This suggests that the adsorption is correctly considered in the equilibrium constant, *K*, using the Oscillator model. The apparent tortuosity for each gas is given in Table 5.3, in which a strong gas dependence is observed, with similar order as before, *i.e.,* He > H_2 > N_2 ≃ Ar > CH_4 > CO_2. This dependence of tortuosity on diffusing species is consistent with theoretical predictions, and our previous observation that more strongly adsorbed gases have lower tortuosity except at sub-nanometer sizes [6].

Table 5.3 Apparent tortuosity of silica layer for various gases based on empirical correlation using the Oscillator model.

tortuosity	H_2	He	CH_4	N_2	Ar	CO_2
τ_{app}	8.94	10.37	7.66	7.59	7.64	6.00

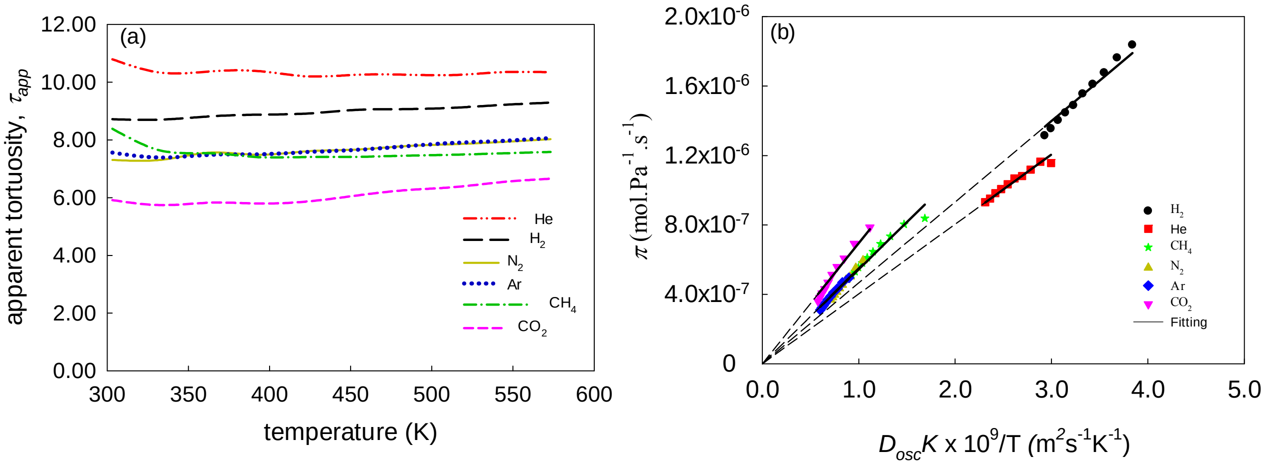

Figure 5.10 (a) Empirical variation of the apparent tortuosity with temperature for the silica layer, obtained using the Oscillator model, and (b) linear regression for all gases based on the Oscillator model in the silica layer.

The above success of the Oscillator model can be explored by examining the difference of apparent diffusivity and equilibrium constant for each model at the mean pore radius, $\overline{r}_p$, defined by eqn. (5.3). Figures 5.11 (a) and (b) illustrate the variation of apparent diffusivity with gas molecular size for the classical Knudsen model, its corrected version accounting for finite molecular size, and for the Oscillator model, at 30 °C and 300 °C, respectively. It is evident that the apparent diffusivity is only decreased by about 10% by the exclusion due to finite molecular size in the corrected Knudsen model for each gas, but almost halved by the Oscillator model, indicating that the diffusivity is greatly overestimated by the Knudsen model at the mean pore of the silica layer. Since the equilibrium constant (*K*) reflects the adsorption intensity, it is interesting to investigate the influence of factors such as gas species and temperature on *K*. Such a plot is depicted in Figure 5.11(c), and it is evident that the adsorption equilibrium constant is strongly depended on the gas species and temperature. For the strongly adsorbed gases (CH_4 and CO_2), the value of *K* is as high as 5-7 at 30 °C, but decreases to almost unity at 300 °C. For the moderately adsorbing gases (N_2 and Ar), the value of *K* is around 2.5 at 30 °C, and falls to almost unity at 300°C, while for the most weakly adsorbed gases (He and H_2), the value of *K* is almost unity at both temperatures. These results are consistent with the observations based on Figures 5.9(b) and 5.9(d), where the adsorption effect is seen to be most significant for the heavier gases at low temperature. On the other hand the adsorption of the lighter gases is very weak even at very low temperature, indicating that the densities of the pore and bulk fluid are almost identical at all temperatures, thus, the correlation can provide good agreement with the experimental data over the whole temperature range.

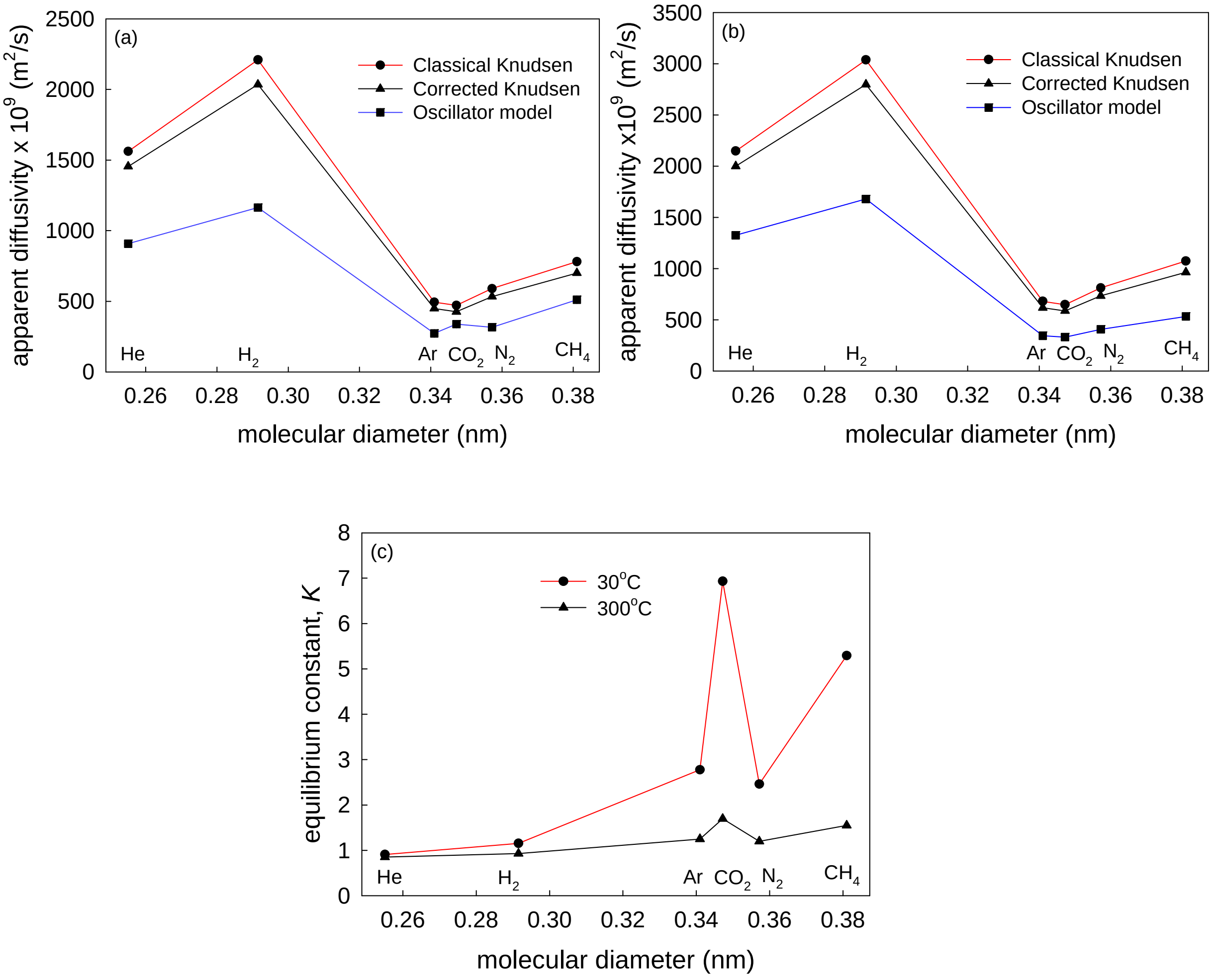

Figure 5.11 Variation of the apparent diffusivity with gas molecular size predicted by the classical Knudsen model, a correction version for finite molecular size, and by the Oscillator model, at (a) 30 °C, and (b) 300 °C respectively, at a pore radius r_p = 1.85 nm for silica, and (c) variation of the equilibrium constant with gas molecular size at 30 °C and 300 °C.

Although a more acceptable apparent tortuosity of membrane layer is permitted by Oscillator model for each gas, it is evident that the methodology, based on a single pore size, can only qualitatively explain the results, and some anomalies occur in the correlation results. For instance, unexpected crossover of tortuosities between some of the heavier gases (N_2, Ar and CH_4) is observed, and the tortuosity for He is still very high (around 11). In addition, the above analysis while demonstrating better agreement for the Oscillator model is correlative and cannot be used predicatively, since the tortuosity is found not to be transferable between different fluids and temperatures. We have previously shown that our hybrid correlated random walk-effective medium analysis in eqs. (5.13)-(5.22) [6, 12, 40] can successfully predict fluxes and tortuosities for the macroporous substrate and the interlayer having large mesopores of size about 11.5 nm diameter [16, 20], using fundamental structural parameters of the solid (pore coordination number,

N, and pore length l) while accounting for the whole pore size distribution. We therefore next explore the application of this approach to the current data for the narrower pore size silica layer, using the three different diffusion models (Knudsen, corrected Knudsen and the Oscillator model) at the single pore level.

5.4.3 Application of effective medium theory

Given the high tortuosity and its lack of transferability based on the empirical correlation using a single pore size, effective medium theory is next utilized to investigate the transport using an appropriate diffusion models for each layer. The advantage of this method is that it accounts for the entire pore size distribution for each layer, rather than using an arbitrary single pore size as in eqn. (5.18). Here we have used the pore volume distribution for each layer, $f_v(r_p)$, determined as described in Section 5.2, with the corresponding number distribution, $f_N(r_p)$, for use with the effective medium theory following

$$f_N(r_p) = \frac{f_v(r_p)}{\pi r_p^2 l} \tag{5.27}$$

By utilizing the relationship between pore structure and macroscopic flow rate in eqn. (5.20), the diffusion model can be directly validated, with the coordination number (N), and membrane thickness (z) or pore length (l) as the fitting parameters. In the 3-layer composite membrane, the diffusion mechanisms and structural parameters for the substrate and interlayer must be determined in advance before investigating the transport in the silica layer. For unconsolidated media such as the substrate and interlayer, the aspect ratio plays an important role in the local transport, and the coordination number and pore length are used as the fitted parameters; these have been determined in our prior study [20], with the values $N_s = N_c = 12$, $l_s = 300$ nm, $l_c = 5$ nm. For the consolidated silica layer, the pore aspect ratio is assumed to be negligibly small (*i.e.* $x = 0$, $g(x) = 1/3$), so that the local transport direction in the pore is purely axial, the fitted structural parameters are the coordination number (N_m) and membrane thickness (z_m) based on eqn. (5.22) by equating the flow rate between each layer as described in eqn. (5.24). Following our previous work, the classical slip flow model, its corrected version for finite molecular size, and the Oscillator model are employed in this methodology to independently investigate the diffusion in the silica layer.

5.4.3.1 Slip flow in the membrane layer

With the classical slip flow model used in each layer (substrate, interlayer and membrane layer), the structural parameters of the silica layer were obtained by minimizing the fitting error of the flow rate, given in eqn. (5.23). For this eqn. (5.24) was solved to obtain the interlayer pressures with the substrate and interlayer parameters as determined previously [20] and given above. Figure 5.12(a) illustrates the variation of flow rate with temperature for the experimental permeation data (symbols), and the corresponding best fit (lines) obtained using the silica membrane layer structural parameters of $N_m = 3$ and $z_m = 22.5$ μm, for several gases. As seen in Figure 5.12(a), the model flow rates for the light gases (H_2 and He) are significantly larger than the experimental values, despite the high value of the fitted membrane thickness compared to the actual value of about 15 μm. This indicates that the corresponding apparent diffusivity is still significantly overestimated for these gases. For instance, the model flow rate for He is 25% higher than the experimental value at 30 °C.

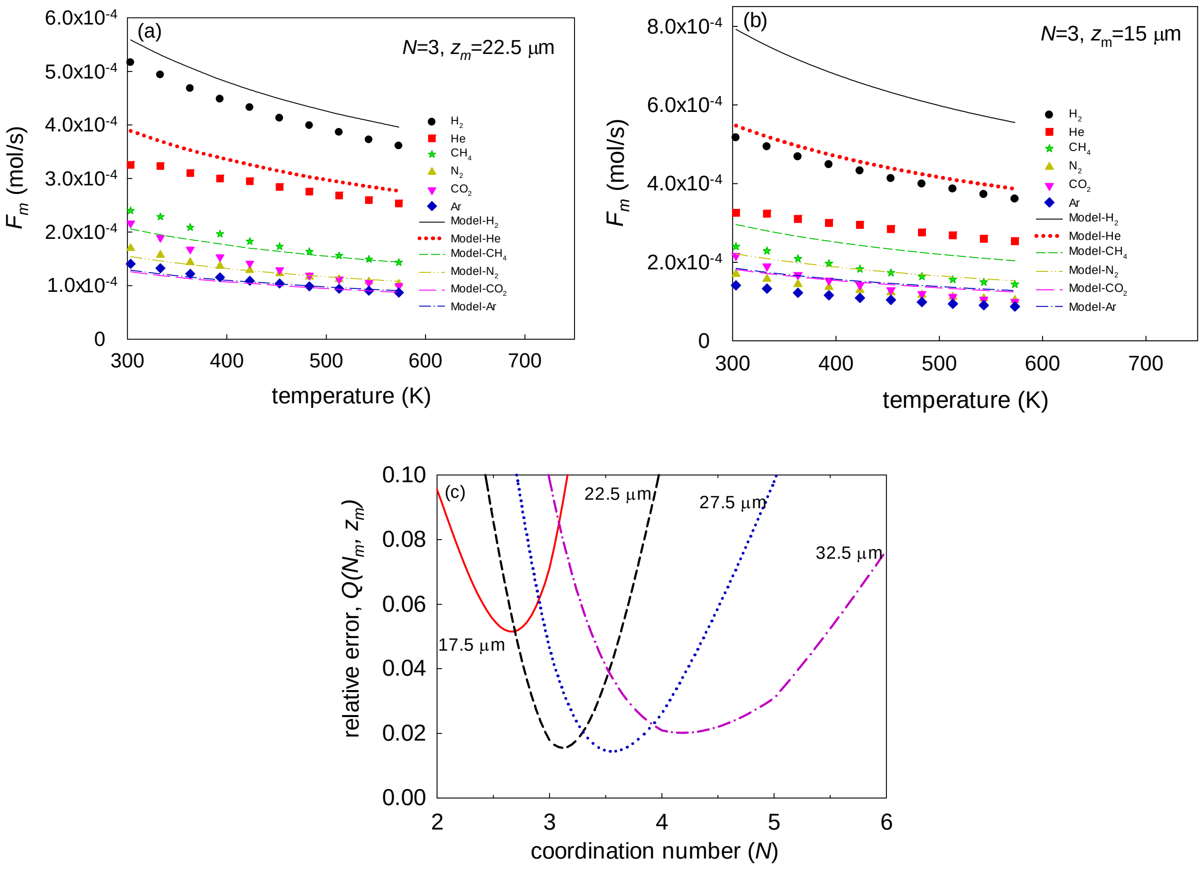

Figure 5.12 Variation of (a), (b) flow rate with temperature obtained from experimental permeation data (symbols) and the corresponding best fit (lines) based on the classical slip flow model in the silica layer, using the structural parameters of $N_m = 3$, with (a) $z_m = 22.5$ μm and (b) $z_m = 15$ μm, and (c) the relative error, $Q(N_m, z_m)$, with coordination number for several values of membrane thickness.

In addition, the model generally underestimates the flow rate for the strongly adsorbed gas (CO_2 and CH_4) at low temperature, which is mainly due to the neglect of the effect of adsorption. For example, the model flow rate for CO_2 is 40% lower than the experimental one at 30 °C. On the other hand, the model does provide good agreement with the experimental results for the moderately adsorbed gas (N_2 and Ar); however, it may be recognised that this is achieved by the use of an unrealistically large membrane thickness - this masks the overestimation of the diffusivity for these gases. As is evident from Figure 5.4, the membrane thickness varies between 12 and 18 μm. Figure 5.12(b) compares the variation of the flow rate with temperature for the experimental permeation data (symbols) and the corresponding model curve (lines) obtained using a membrane thickness of 15 μm and coordination number $N_m = 3$. It is evident that the model flow rate is significantly higher than the experimental one for all the gases, and the relative deviation is even larger than 60% for some conditions, confirming the overprediction of the apparent diffusivity by the classical slip flow model in the silica pores. The failure of this diffusion model is further demonstrated by the plot of the relative fitting error, $Q(N_m, z_m)$, versus coordination number (N_m) for several membrane thickness (z_m), depicted in Figure 5.12(c). It is evident that any arbitrary changes of the thickness (z_m) and coordination number (N_m) increase the error significantly compared to the best fit model results in Figure 5.12(a). Thus, it is clear that the diffusivity is significantly overestimated by the Knudsen model due to the neglect of the dispersive force exerted by the wall.

Similar overprediction is also observed for the corrected slip flow model, in which the effective pore size is adjusted to account for finite molecular size, following eqn. (5.6). Figure 5.13(a) compares the variation of the flow rate with temperature for the different gases, for the experimental permeation data (symbols) and the corresponding best fit (lines) obtained using the structural parameters of $N_m = 3$ and $z_m = 17.5$ μm. It is evident that the fitted membrane thickness (17.5 μm) is reduced to a more realistic value, and the model provides better agreement with experimental data for the weakly adsorbed gases (H_2 and He).

Nevertheless, the total deviation for the other heavier gases is still very large and the corresponding flow rate is systematically underestimated by the model due to the high membrane thickness. Figure 5.13(b) depicts the comparison between the data and the model results using the mean value of $z_m =$ 15 μm and $N_m = 3$. In this case the model provides good agreement with experimental data for the moderately adsorbed gases (N_2 and Ar), but the flow rate for the weakly adsorbed gases (He and H_2) and the strongly adsorbed gases (CH_4 and CO_2) shows significant deviation, exceeding 30% at low temperature. Figure 5.13(c) depicts the sensitivity of the relative error, $Q(N_m, z_m)$, to coordination number (N_m) and membrane thickness (z_m). As for the uncorrected slip flow model, the error is very sensitive to the coordination number, and any change in assumed membrane thickness from the best fit value of 17.5 μm increases the fitting error. Thus, it is clear that neither the slip flow model nor its corrected version can satisfactorily interpret the data.

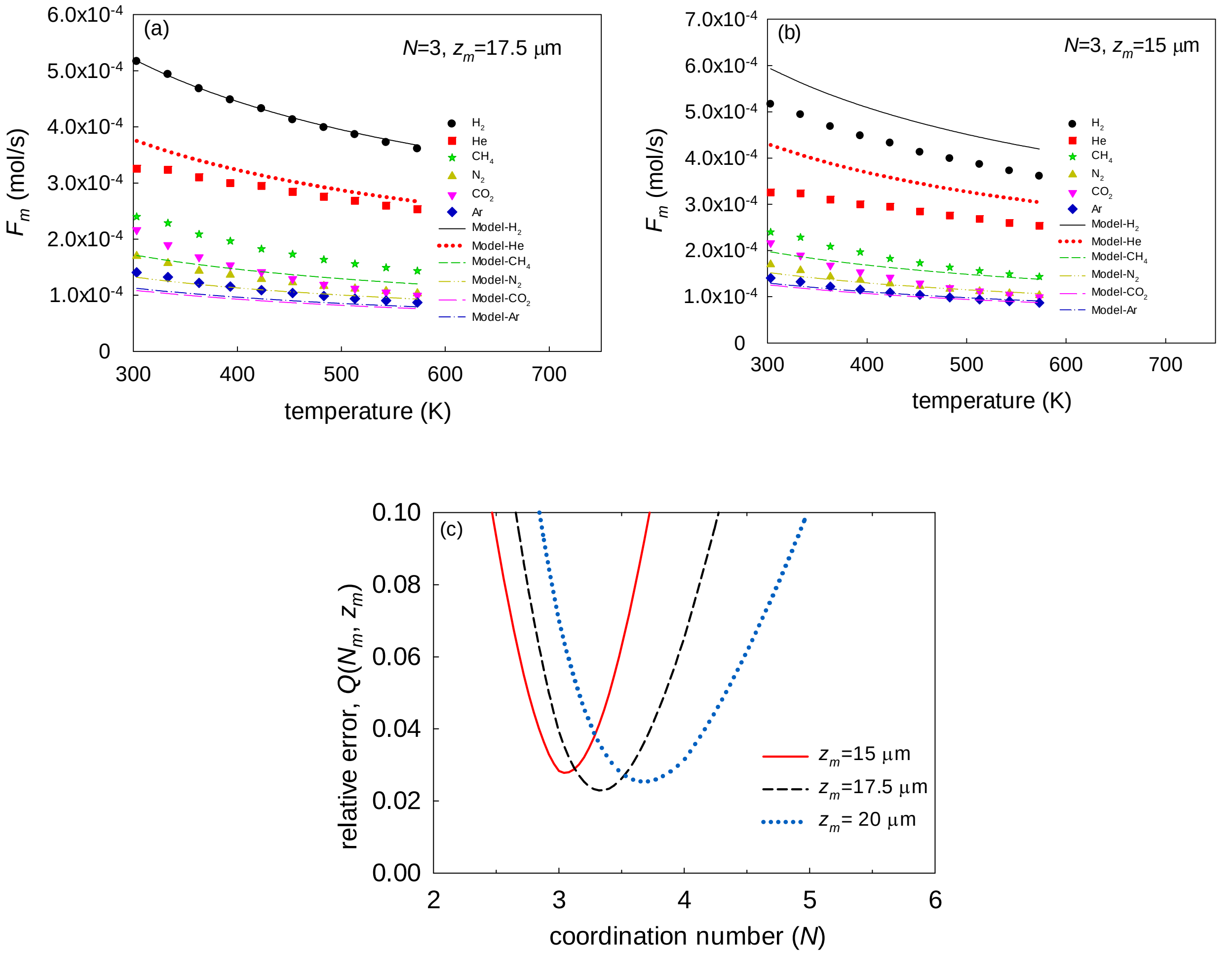

Figure 5.13 Variation of (a), (b) flow rate with temperature obtained from experimental permeation data (symbols) and the corresponding best fit (lines) based on the corrected slip flow model in the silica layer, using the structural parameters of $N_m = 3$, with (a) $z_m = 17.5$ µm and (b) $z_m = 15$ µm, and (c) the relative error, $Q(N_m, z_m)$, with coordination number for several values of membrane thickness.

5.4.3.2 Oscillator model in the membrane layer

The apparent diffusivity (KD_{osc}) can be directly evaluated by the Oscillator model with the adsorption effect represented by the equilibrium constant, K. Figure 5.14 (a) illustrates the comparison of the variation of the flow rate with temperature between the experimental permeation data (symbols) and the model (lines) using the best fit structural parameters of $N_m = 3$ and $z_m = 15$ µm, for the different gases. It is evident that the fitted membrane thickness reduces to a more reasonable value, consistent with that observed in the SEM image, in comparison to the Knudsen model or its corrected form. In addition, the agreement between the model line and the experiment value is much better, especially for the heavier gases at low temperature. For instance, the flow rate for CO_2 is higher than N_2 at low temperature (30 °C) for the experiment, but cannot be predicted by the Knudsen model. However, this behavior is found for the Oscillator model, since the equilibrium constant for CO_2 is much higher than N_2 in the silica pores at low temperature as indicated in Figure 5.11(c); this leads to a higher apparent diffusivity for CO_2 compared to that for N_2 at low temperature. Further, it is important to note that the current theory assumes straight cylindrical pores with smooth surfaces, which is different from the real voids formed in the silica matrix, in which the pore shape is irregular with a rough surface as seen in Figure 5.3. Thus the values of N_m should be understood as the effective coordination number of an equivalent network comprised of ideal cylindrical and straight pores, with a smooth surface providing the same overall resistance to flow as the actual silica layer.

On the other hand, it is evident that Oscillator model marginally underestimates the flow rate for all the gas except He, for which a small overprediction occurs. The discrepancy can be justified that the real voids with roughness surface can provides extra resistance, which is not included in any part of the effective medium theory. The resistance caused by the surface roughness is not considered here, and may be expected to be related to the molecular size, with the smaller molecules such as He being more sensitive to the surface texture and thereby facing greater resistance. Thus the model slightly overestimates the flow rate for He, for which the resistance is underestimated. The success of the Oscillator model is further demonstrated by plotting the relative error function, $Q(N_m, z_m)$, versus coordination number (N_m) for several membrane thickness (z_m). As seen in Figure 5.14(b), the error is 50% less than that for the Knudsen approach, indicating that the diffusion in the silica mesoporous membrane is more accurately represented by the Oscillator model.

We note here that we have used the membrane thickness as a fitting parameter to illustrate the reliability of the method, which leads to an optimum value of the thickness in excellent agreement with the average value obtained from the SEM image. This provides convincing evidence for the validity of the Oscillator model at this pore size scale, while the Knudsen model requires an unrealistically large membrane thickness due to its overprediction. Thus when the membrane thickness can be specified based on the independent measurements, the coordination number need be the only fitting parameter when interpreting membrane transport data based on the Oscillator model. However, in practice accurate specification of the membrane thickness is somewhat difficult because the interlayer boundaries are often diffuse, with some interpenetration. In such circumstances it may be pertinent to use effective membrane thickness as a fitting parameter. In the present case it is evident that a consistent membrane thickness is obtained for all gases when using the Oscillator model, but not when using the Knudsen model for the transport in the silica layer.

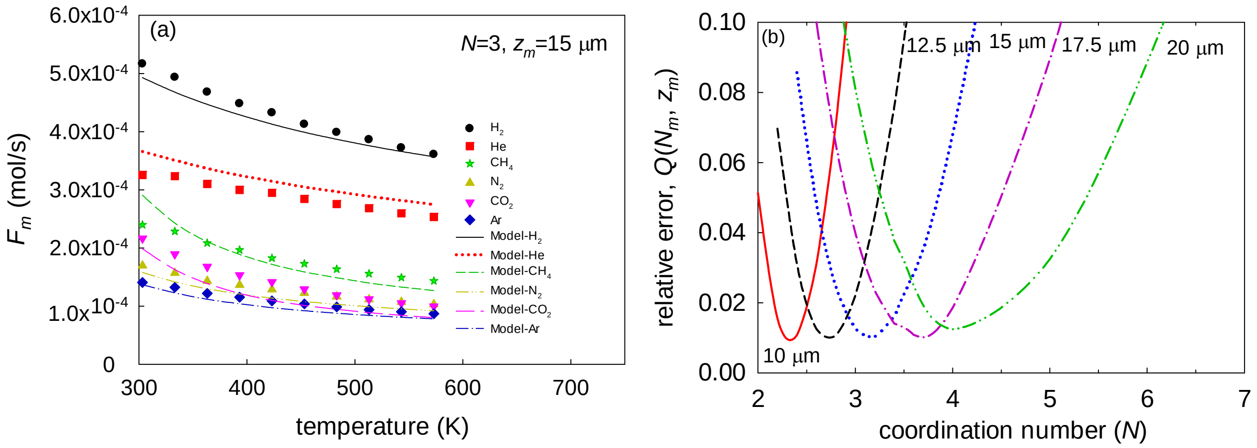

Figure 5.14 Variation of (a) flow rate with temperature, obtained from experimental permeation data (symbols) and the corresponding best fit (lines) based on the Oscillator model in the silica layer, obtained using the structural parameters of $N_m = 3$ and $z_m = 15$ μm, and (b) the relative error, $Q(N_m, z_m)$, with coordination number for several values of membrane thickness.

Figure 5.15(a) depicts the relative pressure drop in the silica layer, for the parameters $N_m = 3$ and $z_m = 15$ μm corresponding to the best fit. It is evident that most of the pressure drop (85-90%) in the 3-layer membrane lies in the silica layer consistent with the conclusions based on Figure 5.7. The balance of the pressure drop essentially lies in the α-alumina substrate, as depicted in Figure 5.15(b). Interestingly, for the weakly adsorbed gases He and H_2 the relative pressure drop in the silica decreases, while that in the substrate increases, with increase in temperature, which is contrary to the behavior for the other gases. This is readily seen to be because of the larger increase in the apparent diffusivity (KD_{osc}) in the silica layer with increase in temperature compared to that in the substrate (in which the Knudsen model is adequate), for He and H_2, due to the effect of fluid-solid interaction (c.f. Figure 5.11). It may be noted that the equilibrium constant is close to unity for He and H_2, and nearly constant, so that the increase in apparent diffusivity for these gases is essentially due to the increase in pore diffusivity. On the other hand for the other more strongly adsorbed gases the apparent diffusivity with increase in temperature is much more modest due to the decrease in the equilibrium constant, evident in Figure 5.11(c). This leads to the increase in relative pressure drop in the silica layer with increase in temperature for these gases seen in Figure 5.15(a). This increase is the largest for the most strongly adsorbed gases, CH_4 and CO_2, for which the equilibrium constant reduces the most with increase in temperature.

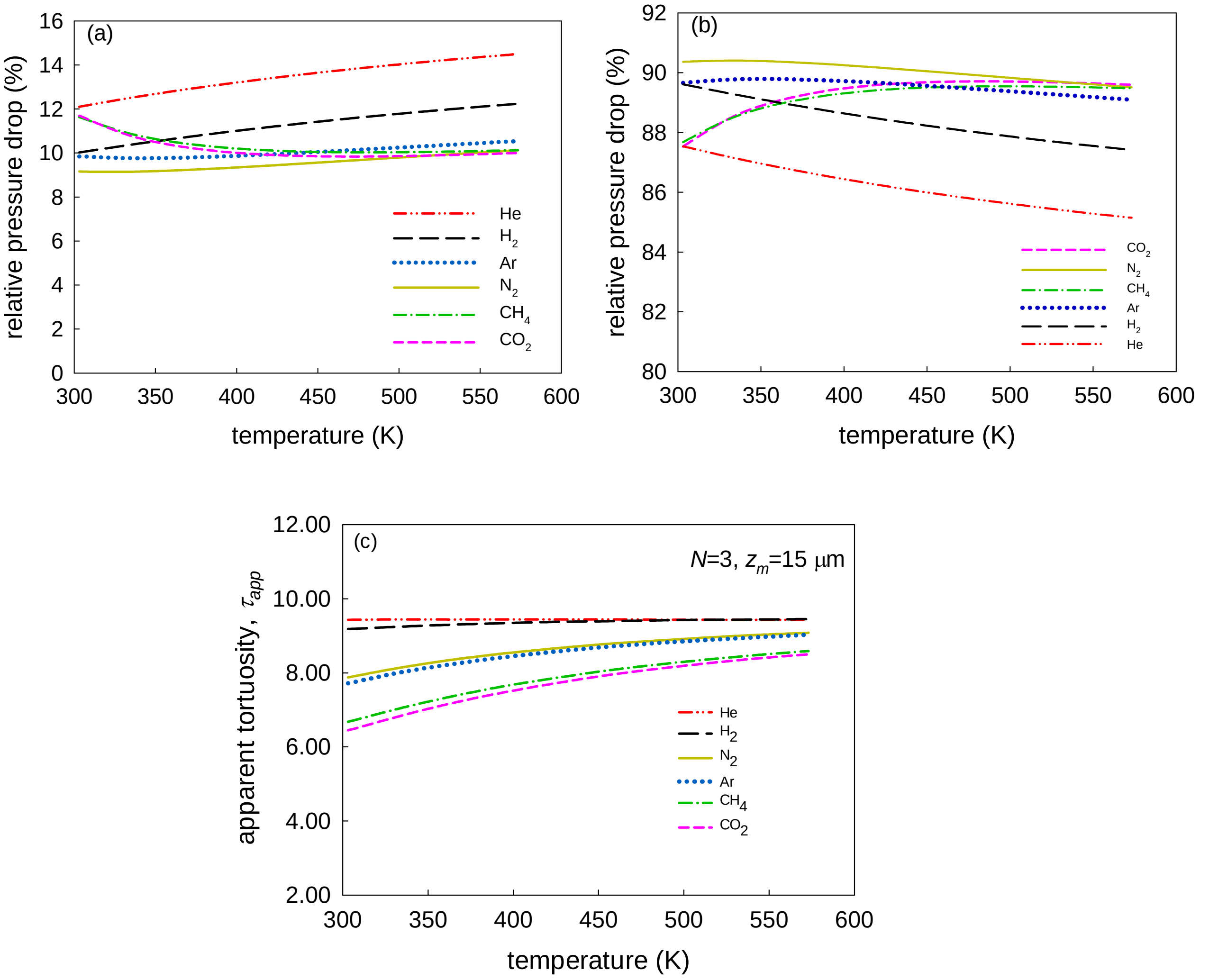

Figure 5.15 Variation of (a), (b) relative pressure drop over (a) the substrate layer, and (b) the silica membrane layer, and (c) the apparent silica layer tortuosity with temperature for various gases, based on eqn. (19) and the Oscillator model in the silica layer, with the fitted structural parameters ($N_m = 3$ and $z_m = 15$ μm).

5.5 Summary and conclusions

Single gas permeation experiments with six gases (N_2, Ar, CO_2, He, H_2 and CH_4) have been carried out over a wide range of temperature (30-300 °C) in a mesoporous silica membrane coated on an asymmetric support. The transport through the silica membrane layer has been examined using both conventional correlations based on a single representative pore radius, and a more rigorous effective medium theory considering the pore size distribution for each layer. The correlation results demonstrate that the classical Knudsen diffusion model, and a version corrected for finite molecular size, significantly overpredict the diffusivity, which leads to very high apparent tortuosities (between 8 and 19). In addition, it is seen that adsorption effects are important for all gases except

He and H_2, particularly at low temperature, and should be taken into account. On the other hand the Oscillator model, which considers the adsorption, leads to a significantly lower apparent diffusivity, and correlates the experimental flux versus temperature data much more accurately for all the gases in comparison to the Knudsen model.

To more precisely investigate and validate the transport mechanism in silica layer, the various diffusion models are tested using a more rigorous methodology based on effective medium theory while considering the pore size distribution for each layer. The failure of classical Knudsen approach and its version corrected for finite molecular size is also demonstrated through the effective medium approach, with the flow rate overestimated for all the gases by over 30%. Use of the Oscillator model which considers dispersive fluid solid interaction in the interlayer and the silica layer, leads to significantly lower diffusivities, and better fit of the experimental data compared to the Knudsen approach, with deviation for each gas around 8%. It is found that the resistance of the interlayer is negligible in the supported 3-layer membrane, and the governing resistance lies in the silica layer with about 85-90% of the total pressure drop lying in this layer, and about 10% in the substrate. In addition, the apparent tortuosity for each gas is examined, and at all the temperatures the order from the highest to the lowest is He > H_2 > N_2 > Ar > CH_4 > CO_2. It is found that the tortuosity depends strongly on gas species, and increases with temperature due to increased short circuiting by larger pores at higher temperatures. This increase is the weakest for the least adsorbing gases, He and H_2, whose adsorption equilibrium constant is nearly constant and close to unity. For the more strongly adsorbing gases, the opposing effects of increase in temperature on pore diffusivity and equilibrium constant lead to a stronger increase in the apparent diffusivity with increase in temperature for larger pores, while the short circuiting effect in smaller pores is reduced at high temperature, and more gas molecules tend to flow through larger pores, therefore the tortuosity increases.

5.6 Supplementary Information

Table S5.1. The flux of substrate at various temperatures for different gases

Temp (K)	J (mol/s/m^2)					
	N_2	Ar	CO_2	He	H_2	CH_4
303.15	0.49520015	0.40312937	0.48616747	0.86608515	1.35833801	0.72309871
333.15	0.43667650	0.36940182	0.43944222	0.82025366	1.25175594	0.62516186
363.15	0.39933599	0.32311737	0.38972287	0.77160313	1.16068288	0.58507987
393.15	0.37452932	0.30620888	0.35393779	0.73365756	1.10886142	0.55135365
423.15	0.35557893	0.28921078	0.32242618	0.69859865	1.04372773	0.50779876
453.15	0.33691473	0.26942380	0.29772046	0.65114431	0.98249758	0.46685162
483.15	0.31501382	0.25291510	0.27293985	0.61712999	0.93580213	0.43433344
513.15	0.29759884	0.23858587	0.25587612	0.59382309	0.92140214	0.41905203
543.15	0.28424579	0.22717799	0.24117920	0.57019720	0.87510145	0.39276950
573.15	0.27496583	0.21928021	0.22758014	0.54831055	0.83117165	0.37546227

Table S5.2 The flux of asymmetric support at various temperatures for different gases

Temp (K)	J (mol/s/m^2)					
	N_2	Ar	CO_2	He	H_2	CH_4
303.15	0.46573097	0.37442462	0.44680899	0.83275210	1.29014429	0.67215916
333.15	0.42075383	0.33935171	0.38672006	0.75850884	1.19788896	0.60481156
363.15	0.39244378	0.30321197	0.35881971	0.71889278	1.11391324	0.55332011
393.15	0.35252719	0.28927002	0.32083612	0.69451766	1.05004455	0.52913606
423.15	0.33534942	0.27119178	0.30393695	0.66379717	1.01004519	0.46983187
453.15	0.31732624	0.25784413	0.27653614	0.62737456	0.94531570	0.44889732
483.15	0.29817064	0.24214149	0.25767504	0.59319014	0.88856566	0.41549542
513.15	0.27936031	0.22854335	0.24056459	0.56793474	0.85397814	0.39258637
543.15	0.26654230	0.21940116	0.22750873	0.54924176	0.81485358	0.37120874
573.15	0.25389082	0.21106526	0.21425656	0.52681416	0.78396216	0.35469704

Table S5. 3 The flux of 3-layer silica membrane at various temperatures for different gases

Temp (K)	J (mol/s/m^2)					
	N_2	Ar	CO_2	He	H_2	CH_4
303.15	0.05196507	0.04305573	0.06617804	0.09951732	0.15791272	0.07335468
333.15	0.04806602	0.04048572	0.05796064	0.09887448	0.15091598	0.06992954
363.15	0.04385377	0.03729710	0.05130041	0.09479313	0.14309578	0.06379910
393.15	0.04176024	0.03535106	0.04692214	0.09167631	0.13702039	0.06010757
423.15	0.03934275	0.03336190	0.04331483	0.09012524	0.13220444	0.05580689
453.15	0.03755143	0.03175853	0.03945077	0.08695103	0.12615169	0.05292282
483.15	0.03564948	0.03012621	0.03642936	0.08426269	0.12195880	0.05004419
513.15	0.03416740	0.02868790	0.03423884	0.08204317	0.11808398	0.04772105
543.15	0.03284644	0.02761597	0.03210244	0.07939264	0.11383636	0.04565234
573.15	0.03154827	0.02655736	0.03042637	0.07744164	0.11032010	0.04385890

5.7 References

[1] J.C. Diniz da Costa, G.Q. Lu, V. Rudolph, Y.S. Lin, Novel molecular sieve silica (MSS) membranes: characterisation and permeation of single-step and two-step sol-gel membranes, J. Membr. Sci., 198 (2002) 9-21.

[2] Y. Wan, D. Zhao, On the controllable soft-templating approach to mesoporous silicates, Chem. Rev., 107 (2007) 2821-2860.

[3] N.K. Raman, C.J. Brinker, Organic "template" approach to molecular sieving silica membranes, J. Membr. Sci., 105 (1995) 273-279.

[4] S. Higgins, R. Kennard, N. Hill, J. DiCarlo, W.J. DeSisto, Preparation and characterization of non-ionic block co-polymer templated mesoporous silica membranes, J. Membr. Sci., 279 (2006) 669-674.

[5] C.J. Brinker, G.W. Scherer, Sol-Gel Science: The Physics and Chemistry of Sol-Gel Processing, Academic Pr., San Diego, CA, 1990.

[6] S.K. Bhatia, D. Nicholson, Some pitfalls in the use of the Knudsen equation in modelling diffusion in nanoporous materials, Chem. Eng. Sci., 66 (2010) 284-293.

[7] D.M. Ruthven, W. DeSisto, S. Higgins, Diffusion in a mesoporous silica membrane: validity of the Knudsen diffusion model, Chem. Eng. Sci., 64 (2009) 3201-3203.

[8] R.T. Yang, Gas separation by adsorption processes, Butterworth Publishers,Stoneham, MA, 1986.

[9] M. Knudsen, W.J. Fisher, The molecular and the frictional flow of gases in tubes, Phys. Rev., 31 (1910) 586-588.

[10] S.K. Bhatia, M.R. Bonilla, D. Nicholson, Molecular transport in nanopores: a theoretical perspective, Phys. Chem. Chem. Phys., 13 (2011) 15350-15383.

[11] E.A. Mason, A.P. Malinauskas, R.B. Evans III, Flow and diffusion of gases in porous media, J. Chem. Phys., 46 (1967) 3199-3216.

[12] S.K. Bhatia, Modeling pure gas permeation in nanoporous materials and membranes, Langmuir, 26 (2010) 8373-8385.

[13] S. Hwang, Fundamentals of membrane transport, Korean J. Chem. Eng., 28 (2011) 1-15.

[14] S. Higgins, W. DeSisto, D.M. Ruthven, Diffusive transport through mesoporous silica membranes, Micropor. Mesopor. Mat., 117 (2009) 268-277.

[15] F. Jareman, J. Hedlund, D. Creaser, J. Sterte, Modelling of single gas permeation in real MFI membranes, J. Membr. Sci., 236 (2004) 81-89.

[16] X. Gao, M.R. Bonilla, J.C. Diniz da Costa, S.K. Bhatia, The transport of gases in macroporous α-alumina supports, J. Membr. Sci., 409-410 (2012) 24-33.

[17] H. Preising, D. Enke, Relations between texture and transport properties in the primary pore system of catalyst supports, Colloids Surf. A, 300 (2007) 21-29.

[18] A. Markovic, D. Stoltenberg, D. Enke, E.U. Schlünder, A. Seidel-Morgenstern, Gas permeation through porous glass membranes: Part I. Mesoporous glasses-effect of pore diameter and surface properties, J. Membr. Sci., 336 (2009) 17-31.

[19] J. Kärger, F. Stallmach, S. Vasenkov, Structure-mobility relations of molecular diffusion in nanoporous materials, Magn. Reson. Imaging, 21 (2003) 185-191.

[20] X. Gao, M.R. Bonilla, J.C. Diniz da Costa, S.K. Bhatia, The transport of gases in a mesoporous γ-alumina supported membrane, J. Membr. Sci., 428 (2013) 357-370.

[21] R. Krishna, J.M. van Baten, Influence of segregated adsorption on mixture diffusion in DDR zeolite, Chem. Phys. Lett., 446 (2007) 344-349.

[22] R. Krishna, J.M. van Baten, An investigation of the characteristics of Maxwell-Stefan diffusivities of binary mixtures in silica nanopores, Chem. Eng. Sci., 64 (2009) 870-882.

[23] S.K. Bhatia, O. Jepps, D. Nicholson, Tractable molecular theory of transport of Lennard-Jones fluids in nanopores, J. Chem. Phys., 120 (2004) 4472-4485.

[24] J. Xiao, J. Wei, Diffusion mechanism of hydrocarbons in zeolites-I. Theory, Chem. Eng. Sci., 47 (1992) 1123-1141.

[25] J. Xiao, J. Wei, Diffusion mechanism of hydrocarbons in zeolites-II. Analysis of experimental observations, Chem. Eng. Sci., 47 (1992) 1143-1159.

[26] R.S.A. De Lange, J.H.A. Hekkink, K. Keizer, A.J. Burggraaf, Formation and characterization of supported microporous ceramic membranes prepared by sol-gel modification techniques, J. Membr. Sci., 99 (1995) 57-75.

[27] J.C.S. Wu, H. Sabol, G.W. Smith, D.L. Flowers, P.K.T. Liu, Characterization of hydrogen-permselective microporous ceramic membranes, J. Membr. Sci., 96 (1994) 275-287.

[28] O.G. Jepps, S.K. Bhatia, D.J. Searles, Wall mediated transport in confined spaces: exact theory for low density, Phys. Rev. Lett., 91 (2003) 126102.

[29] M.R. Bonilla, S.K. Bhatia, The low-density diffusion coefficient of soft-sphere fluids in nanopores: accurate correlations from exact theory and criteria for applicability of the Knudsen model, J. Membr. Sci., 382 (2011) 339-349.

[30] S.K. Bhatia, D. Nicholson, Transport of simple fluids in nanopores: Theory and simulation, AIChE J., 52 (2006) 29-38.

[31] D. Uhlmann, S. Liu, B.P. Ladewig, J.C. Diniz da Costa, Cobalt-doped silica membranes for gas separation, J. Membr. Sci., 326 (2009) 316-321.

[32] S. Battersby, T. Tasaki, S. Smart, B. Ladewig, S. Liu, M.C. Duke, V. Rudolph, J.C. Diniz da Costa, Performance of cobalt silica membranes in gas mixture separation, J. Membr. Sci., 329 (2009) 91-98.

[33] H.L. Castricum, R. Kreiter, H.M. van Veen, D.H.A. Blank, J.F. Vente, J.E. ten Elshof, High-performance hybrid pervaporation membranes with superior hydrothermal and acid stability, J. Membr. Sci, 324 (2008) 111-118.

[34] N. Nishiyama, D.H. Park, A. Koide, Y. Egashira, K. Ueyama, A mesoporous silica (MCM-48) membrane: preparation and characterization, J. Membr. Sci., 182 (2001) 235-244.

[35] S.K. Bhatia, D. Nicholson, Comments on" Diffusion in a mesoporous silica membrane: Validity of the Knudsen diffusion model" by Ruthven, D.M., et al., Chem. Eng. Sci. 64 (2009) 3201-3203, Chem. Eng. Sci., 65 (2010) 4519-4520.

[36] W. Jin, S. Li, P. Huang, N. Xu, J. Shi, Preparation of an asymmetric perovskite-type membrane and its oxygen permeability, J. Membr. Sci., 185 (2001) 237-243.

[37] F.T. De Bruijn, L. Sun, Ž. Olujić, P.J. Jansens, F. Kapteijn, Influence of the support layer on the flux limitation in pervaporation, J. Membr. Sci., 223 (2003) 141-156.

[38] O. Schramm, A. Seidel-Morgenstern, Comparing porous and dense membranes for the application in membrane reactors, Chem. Eng. Sci., 54 (1999) 1447-1453.

[39] V.N. Burganos, S.V. Sotirchos, Diffusion in pore networks: effective medium theory and smooth field approximation, AIChE J., 33 (1987) 1678-1689.

[40] P.D. Deepak, S.K. Bhatia, Transport in capillary network models of porous media: theory and simulation, Chem. Eng. Sci., 49 (1994) 245-257.

[41] S. Kirkpatrick, Classical transport in disordered media: Scaling and effective-medium theories, Phys. Rev. Lett., 27 (1971) 1722-1725.

[42] M. Sahimi, Flow and transport in porous media and fractured rock: From classical methods to modern approaches, Wiley-VCH, 2011.

[43] S. Cao, Y. Zhu, J. Wu, K. Wang, Q. Tang, Preparation and sustained-release property of triblock copolymer/calcium phosphate nanocomposite as nanocarrier for hydrophobic drug, Nanoscale Res. Lett., 5 (2010) 781-785.

[44] K. Vollmayr, W. Kob, K. Binder, Cooling-rate effects in amorphous silica: A computer-simulation study, Phys. Rev. B, 54 (1996) 15808-15827.

[45] X. Zhang, W. Wang, G. Jiang, a potential model for interaction between the Lennard Jones cylindrical wall and fluid molecules, Fluid Phase Equilibr., 218 (2004) 239-246.

[46] F.J. Blas, L.F. Vega, K.E. Gubbins, Modeling new adsorbents for ethylene/ethane separations by adsorption via π-complexation, Fluid Phase Equilibr., 150 (1998) 117-124.

[47] W.A. Steele, M.J. Bojan, Simulation studies of sorption in model cylindrical micropores, Adv. Colloid Interfac., 76 (1998) 153-178.

[48] A.V. Neimark, P.I. Ravikovitch, M. Grün, F. Schüth, K.K. Unger, Pore size analysis of MCM-41 type adsorbents by means of nitrogen and argon adsorption, J. Colloid. Interf. Sci., 207 (1998) 159-169.

[49] S.K. Bhatia, Capillary network models for transport in packed beds: considerations of pore aspect ratio, Chem. Eng. Commun., 154 (1996) 183-202.

[50] S.K. Bhatia, Directional autocorrelation and the diffusional tortuosity of capillary porous media, J. Catal., 93 (1985) 192-196.

[51] S.K. Bhatia, Stochastic theory of transport in inhomogeneous media, Chem. Eng. Sci., 41 (1986) 1311-1324.

[52] S.P. Friedman, N.A. Seaton, A corrected tortuosity factor for the network calculation of diffusion coefficients, Chem. Eng. Sci., 50 (1995) 897-900.

[53] L. Zhang, N.A. Seaton, Prediction of the effective diffusivity in pore networks close to a percolation threshold, AIChE J., 38 (1992) 1816-1824.

[54] H. Liu, L. Zhang, N.A. Seaton, Determination of the connectivity of porous solids from nitrogen sorption measurements—II. Generalisation, Chem. Eng. Sci., 47 (1992) 4393-4404.

[55] N.A. Seaton, Determination of the connectivity of porous solids from nitrogen sorption measurements, Chem. Eng. Sci., 46 (1992) 1895-1909.

Chapter 6: Understanding the diffusional tortuosity of porous materials: an effective medium theory perspective

The interpretation of experimental data on transport in porous materials is often based on the use of a single representative pore size, overlooking effects of the pore size distribution (PSD) and pore network connectivity, and fitting a tortuosity into which all such uncertainties are consigned. In this chapter, using literature data on the diffusion of N_2, Xe and i-C_4H_{10} in mesoporous Shell silica spheres, we demonstrate that the tortuosity depends on the choice of the representative pore radius as well as gas species. Both the Knudsen model and the Oscillator model considering dispersive fluid-solid interactions, developed in this laboratory, are found to adequately interpret the data in conjunction with effective medium theory (EMT) by fitting a network coordination number instead of tortuosity. This insensitivity to model is due to the large mean mesopore radius of 7.4 nm for this silica; however, the Oscillator model is found to yield a value of the coordination number closer to the range of values expected for this material.

Using the EMT we demonstrate that the tortuosity is dependent on temperature and diffusing species, because of differences in temperature dependence between the conductance at the representative pore radius and the true conductance which depends on the network connectivity and PSD. In the slip flow regime, which is obtained at large pore size, we show that the superposition of Knudsen and viscous mechanisms leads to temperature and species dependence of tortuosity, because of the different pore size dependence of the two contributions. This leads to different limiting tortuosities and PSD dependence in the Knudsen and viscous flow regimes. These critical aspects are largely unappreciated in the literature, and even systematic variations of tortuosity with temperature or diffusing species usually overlooked, often leading to misrepresentation of the underlying mechanism.

6.1 Introduction

Advances in templating methods and techniques of nanomaterials synthesis have led to the rapid growth of a vast array of novel nanoporous materials, which hold potential for applications in areas such as adsorption and gas storage, membrane separation, heterogeneous catalysis and drug delivery [1-5]. These developments have stimulated considerable interest in the modeling of adsorption and fluid transport in the confined spaces of such materials, which is central to their applications [6-8]. The most common approach in the modeling of transport in nanoporous materials relates the flux (J) to an effective diffusion coefficient (D_e) and the bulk pressure gradient (∇P) through the phenomenological relation [9-11]:

$$J = \frac{D_e}{R_g T}(-\nabla P) \tag{6.1}$$

where R_g is the gas constant and T is the temperature. Since nanoporous materials often comprise a network of pores that is disordered and has a pore size distribution, the interpretation of the effective diffusivity therefore generally involves pore network parameters, such as porosity (ε), and an apparent tortuosity (τ_{app}). In general, the various theories developed to estimate the effective diffusivity based on the properties of the fluids and the porous medium, have the form [12-16]

$$D_e = \frac{\varepsilon \bar{D}_a}{\tau_{app}} \tag{6.2}$$

where $\bar{D}_a$ is the apparent pore diffusivity, commonly evaluated using an appropriate diffusion models while choosing an appropriate representative pore size. Although the porosity can be extracted from gas adsorption or mercury porosimetry analysis [17], the apparent tortuosity is often empirically estimated by fitting experimental flux data to a correlation suggested by an assumed transport model.

Apparent success of the correlation (e.g. effective diffusivity versus $\sqrt{T/M}$, where M is molecular weight, as per the established Knudsen model), and proximity of the fitted tortuosity to the theoretical value of 3 for a random walk, is often used as a criterion to validate assumptions regarding transport mechanisms in disordered nanoporous materials; however, this approach has been criticized on fundamental grounds [18, 19]. Nevertheless, due to its simplicity, the above approach has become routine in investigations of diffusion in the newly-synthesized nanoporous materials [5, 6, 20]. In this spirit, the most commonly used model is the Dusty Gas Model (DGM) of Mason and coworkers [13], which arbitrarily superposes pore wall-affected diffusion and hydrodynamic fluxes. When adsorption is negligible, the pore wall-affected diffusion is often represented by the Knudsen model, which is supplemented by a surface diffusion contribution when adsorption is significant [21].

Although the DGM based approach utilizing the Knudsen diffusion model has been successfully used to correlate experimental data, its validity for multicomponent systems has been criticized by Kerkhof and Geboers [22] and Bhatia et al.[15], who demonstrate internal inconsistencies in its development. Nevertheless, while not inconsistent in pure component systems, it yields unphysical parameter values when adsorption effects are not negligible, and the fluid molecular size is not insignificant in comparison to the pore size. Under these conditions, very high tortuosities are often obtained for mesoporous materials if the Knudsen diffusivity is utilized in the DGM approach [23-26]; this is attributed to the overprediction of the diffusivity by the Knudsen model, due to its neglect of the dispersive force exerted by the wall [15, 17-19, 27-29]. As a result there is much interest in the development of new diffusion models that consider the potential field of the walls [18, 30-32]. Significant success has been achieved in this laboratory through the development of the 'Oscillator model' which considers the effect of the solid-fluid dispersive interaction on the diffusion as well as on the adsorption [31, 33, 34].

Another key deficiency of the DGM approach is that the apparent tortuosity is incorporated as an effective parameter, which is assumed to be exclusively determined by the properties of the porous medium, and is considered constant. However, it has been experimentally confirmed that the apparent tortuosity can be influenced by the operating conditions such as temperature and gas species [16, 17, 28]. For instance, in the slip flow regime in macroporous materials, to which the DGM is frequently applied, the apparent tortuosity of the macroporous network varies (albeit weakly) with temperature and gas species due to the combined effects of viscous flow and Knudsen diffusion [28]. At the mesopore scale, where viscous flow is negligible at low pressures, the experimentally observed variation of tortuosity with temperature and gas species can be reconciled by the effect of the fluid-wall interaction, and the resulting differences in temperature dependence of the diffusivity in pores of different size as predicted by the Oscillator model [17, 28]. This leads to short circuiting effects by pores of higher conductance in the network, and to the dependence of the apparent tortuosity on temperature and gas species, as well as pressure [27]. This shortcoming of the DGM, which considers the tortuosity to be dependent only on the porous medium, has been demonstrated through experiments with a multi-layered supported mesoporous membrane [17, 28, 29], whereby the transport properties of the composite were sequentially investigated as each layer was added. Rigorous layer-by-layer analysis showed the combination of the Oscillator model with an effective medium theory treatment of network effects to be the most successful approach in modeling the transport in each layer [29].

Effective medium theory (EMT) offers a convenient route to model transport in disordered nanoporous materials, while considering the entire pore size distribution, by replacing the actual random network with an effective one having a uniform conductance in each pore. One advantage of this method is that it enables rigorous analysis of the relationship between apparent tortuosity and the pore structure as well as properties of the diffusing fluid. Thus, its application in conjunction with an appropriate diffusion model, such as the Knudsen or Oscillator models [31], has been key to the interpretation of membrane data and the resolution of the temperature and species dependence of the tortuosity of disordered nanomaterials and membranes [17, 19, 27-29].

In our recent studies [17, 28], we have demonstrated this technique along with the Knudsen or Oscillator model, to satisfactorily represent the transport in a macroporous substrate and in a mesoporous γ-alumina membrane having mean pore radius of 5 nm, as well as a mesoporous silica membrane having a mean pore radius of 1.85 nm [29]. In addition, our results showed significant differences in predicted dependence of tortuosity on temperature for a given macroporous network in the slip flow regime, when the representative pore radius was based on either the number averaged pore size or on the volume to surface area ratio [17, 28]. Further, in mesoporous silica materials, the trend of the predicted dependence of tortuosity on temperature varies with the gas for the Oscillator model when the representative pore radius is defined based on the volume to the surface area ratio [29], differing from our previous finding that the tortuosity increases with temperature for all the investigated gases when the representative pore radius is represented by the peak of the number distribution [19, 27]. This raises the important question of how the tortuosity trends depend on choice of representative pore radius, when the details of the pore size distribution are overlooked, as is common in interpreting experimental data. Therefore, in the current work, we use this powerful technique (EMT) to investigate how the tortuosity and its variation with temperature is affected by the pore network structure and the choice of representative pore radius in different flow regimes. As an example to illustrate these effects, we examine published data on the diffusion of various gases in mesoporous silica spheres, with the results for this material providing the motivation for further study to better understand these complex effects on transport in such disordered nanoporous materials.

6.2 Materials characterization

Mesoporous silica spheres of diameter 2.7 mm were obtained from ExxonMobil Corporate Research laboratories; these spheres were internally labeled Shell S980B at ExxonMobil. The sample was characterized by mercury porosimetry (Micrometrics, IV9500), and the pore size distribution (PSD) is illustrated in Figure 6.1, in which a sharp peak is observed at around a pore radius of 6 nm, indicating the majority of the pores are within the mesoporous range. The corresponding pore volume (V_p) and surface area (S_g) by this method are 0.96 cm^3/g and 258.67 m^2/g respectively. Similar values have been obtained by Reyes et al [35] for this silica using N_2 physisorption in which the pore volume and surface area are 1.16 cm^3/g and 204 m^2/g respectively. However, the mean pore radius obtained here of 7.4 nm ($2V_p/S_g$) is substantially different from the value of 3.5 nm quoted by Reyes et al. [35]. The basis of the value of 3.5 nm given by Reyes et al. is not known, as the value of $2V_p/S_g$ based on their own reported data is 11.4 nm. It may be noted that in a separate article, based on measured liquid imbibition rates, Iglesia et al. [36] estimate the pore radius of the Shell silica S980B spheres as 8.5 nm, in good agreement with the current value of

7.4 nm. In light of these results it was concluded that the value of 3.5 nm is incorrect. To further confirm our result, the silica spheres were examined by Transmission electron microscopy (TEM). The micrograph depicted in Figure 6.2 shows the solid phase to be highly consolidated, and majority of the pores to lie between 5 nm and 10 nm, in accord with the mercury porosimetry-based PSD. The similarity of pore volumes between different methods indicates that most of the void volume is accessible to mercury; thus, in what follows, the pore size distribution in Figure 6.1 is taken to represent that of the pore network of the sample.

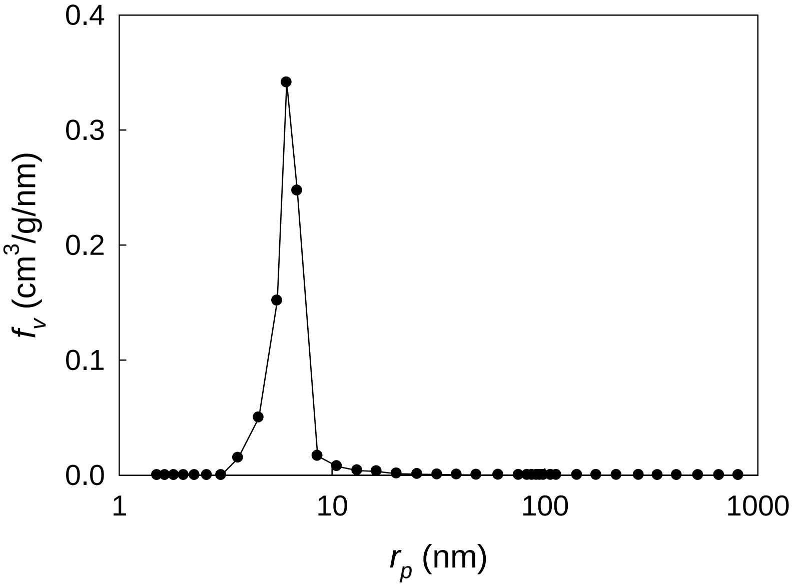

Figure 6.1 Pore size distribution of mesoporous Shell silica spheres, determined by mercury porosimetry.

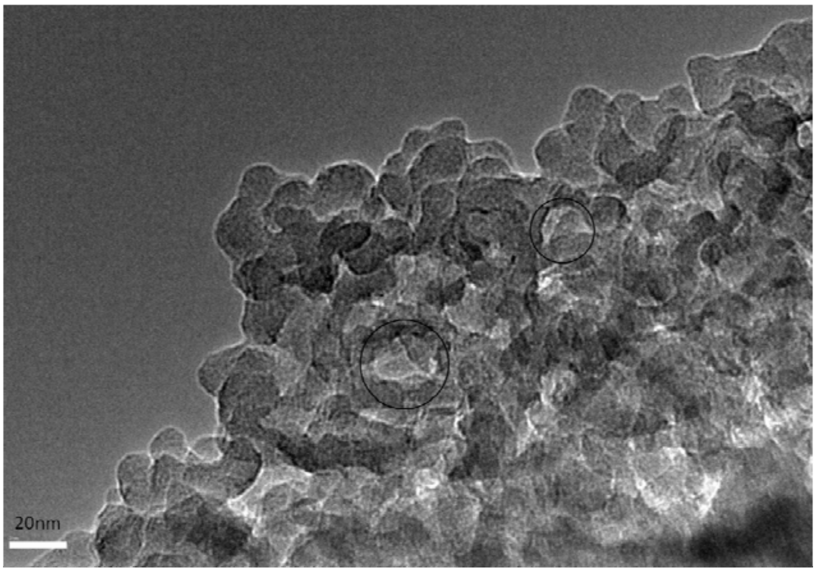

Figure 6.2 Transmission electron microscopy image of Shell mesoporous silica spheres.

The skeletal density of the silica spheres measured by Helium Pycnometry was 2.22 g/cm^3, which is very close to the theoretical density of around 2.30 g/cm^3 [37], suggesting that most of voids in the sample are accessible by the gas. The accessible porosity (ε) of the powder was estimated to be 0.68, following

$$\varepsilon = \frac{V_p \rho}{1 + V_p \rho} \qquad (6.3)$$

in which V_p is the pore volume obtained through the characterization by mercury porosimetry, and ρ is the true density from Helium Pycnometry.

6.3 Transport models

6.3.1 Transport in a single pore

Central to the work reported here is the effective medium theory to predict the apparent tortuosity for disordered nanoporous materials by considering the entire pore size distribution, with the diffusivity represented by a suitably chosen model at the single pore level. To estimate the diffusivity using different models, the pore radius used for each model must be precisely defined. As illustrated in Figure 6.3, there are several ways to define a representative pore radius, which will be extensively addressed for the corresponding diffusion models, as it must depend on the interaction potential. All of the models discussed below are based on the assumption of the flow of a pure fluid.

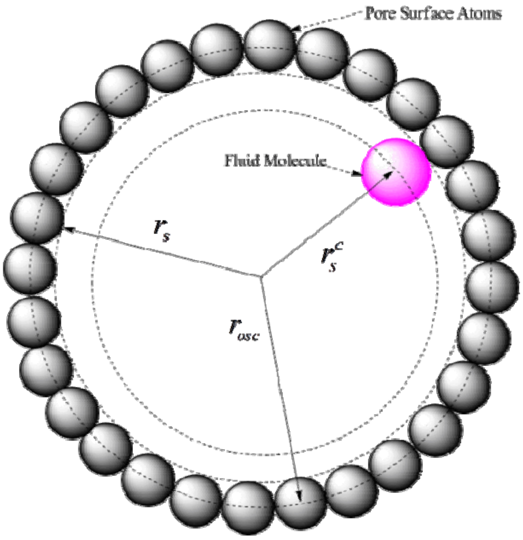

Figure 6.3 Illustration of the different pore radii used in the classical Knudsen model (r_s), the corrected Knudsen model (r_s^c), and the Oscillator model (r_{osc}).

6.3.1.1 Slip flow model

For pores much larger than the size of fluid molecules, the exclusion effect is negligible, and the density along the radial coordinate is uniform, and identical to the bulk density (K=1), which effectively implies a hard sphere interaction potential. In this case the diffusivity is estimated based on the geometrical pore radius (r_s), which is the radial distance from the pore center to the wall surface. The slip flow model is extensively employed to represent the diffusivity in macroporous materials, for which the Knudsen (D_{Kn}) and viscous diffusivity (D_{vis}), are given by

$$D_{Kn} = \frac{4r_s}{3}\sqrt{\frac{2k_BT}{\pi m}} = 97r_s\sqrt{\frac{T}{M}} \tag{6.4}$$

$$D_{vis} = \frac{\bar{P}r_s^2}{8\eta} \tag{6.5}$$

here M represents the fluid molar mass (g/mol), η is fluid viscosity (Pa.s) and $\bar{P}$ is the average pressure (Pa). The apparent diffusivity (D_a) is regarded as the combination of D_{Kn} and D_{vis} ($D_a = D_{Kn} + D_{vis}$). For pores smaller than $10\sigma_{ff}$, the molecular size must be taken into account, and the pore radius is corrected to be r_c by

$$r_c = r_s - \sigma_{ff}/2 \tag{6.6}$$

where σ_{ff} is the Lennard-Jones (LJ) fluid-fluid collision diameter, which is listed in Table 6.1 for the gases in this article [19, 27, 38]). The apparent diffusivity ($D_a^c = D_{Kn}^c + D_{vis}^c$) is evaluated based on the corrected pore radius through eqs. (6.4) and (6.5), and the inhomogeneity of the density profile in the pore is neglected (i.e. considering the equilibrium constant K=1).

Table 6.1 Fluid-fluid Lennard-Jones parameters used in the Oscillator model

Parameters	He	CH_4	N_2	i-butane	Xe
σ_{ff} (nm)	0.2551	0.381	0.3572	0.5278	0.4047
ε_{ff}/k_B (K)	10.22	148.2	93.98	330.1	231.0

The relative importance of viscous flow may be assessed by examining the ratio D_{Kn}/D_{vis} for the hard sphere fluid. Use of the kinetic theory result $\eta = 5(\pi m k_B T)^{1/2}/16\pi\sigma_{ff}^2$ and the definition of the mean free path $\lambda = k_BT/\sqrt{2}\pi\sigma_{ff}^2 P$ [39], leads to $D_{Kn}/D_{vis} = (20/3)\lambda/r_s$. Thus, as an approximation, the viscous contribution is nearly insignificant for conditions under which the mean free path exceeds the pore size. As an example, for Ar, for which, $\sigma_{ff} = 0.34$ nm, the mean free path is estimated as 40.3 nm at a pressure of 2 bar at 300 K. Thus, under these conditions viscous flow is negligible in pores smaller than about 40 nm in radius, but must be considered in larger pores.

6.3.1.2 Oscillator model

As the pore size is reduced, the dispersive force exerted by the walls plays an important role in the fluid diffusion. In this case, not only does the Knudsen approach fail to evaluate the single pore diffusivity accurately, but also the density profile in the pore becomes nonuniform and differs from the bulk value [33, 40]. In this case, the Oscillator model provides an alternative to estimate the diffusivity and adsorption effect in the pores, in which the corresponding pore radius is the half distance of the center-to-center pore diameter, i.e.

$$r_{osc} = r_s + {}^{\sigma_{ss}}\!/_{2} \tag{6.7}$$

where σ_{ss} is the LJ solid-solid collision diameter of the atoms on the pore walls. For a cylindrical pore, at low density, the Oscillator model diffusivity (D_{osc}) of a LJ fluid particle under the conditions of diffuse reflection is given as [31, 33]

$$D_{osc} = \frac{2}{\pi m Q}\int_0^\infty e^{-\beta\phi(r)}dr\int_0^\infty e^{-\frac{\beta p_r^2}{2m}}dp_r\int_0^\infty e^{-\frac{\beta p_\theta^2}{2mr^2}}dp_\theta\int_{r_{co}(r,p_r,p_\theta)}^{r_{cl}(r,p_r,p_\theta)}\frac{dr'}{p_r(r',r,p_r,p_\theta)} \tag{6.8}$$

where $p_r(r?\ r,\ p_r,\ p_\theta)$ is the radial momentum of the particle at r':

$$p_r(r?\ r,\ p_r,\ p_\theta) = \left(2m\left[\phi_{fs}(r) - \phi_{fs}(r')\right] + \frac{p_\theta^2}{r^2}\left[1 - \left(\frac{r}{r'}\right)^2\right] + p_r^2(r)\right)^{1/2} \tag{6.9}$$

given that it has radial momentum p_r at r. Here p_θ is the angular momentum, ϕ_{fs} is the one-dimensional fluid-solid potential, m is fluid particle mass, $\beta = 1/k_BT$ and $Q = \int_0^\infty re^{-\beta\phi(r)}dr$. Further, r_{cl} and r_{co} are the radial bounds of the trajectory of the particle, determined through the solution of $p_r(r', r, p_r, p_\theta) = 0$. A detailed derivation of eqn. (6.8) can be found elsewhere [31].

An advantage of the Oscillator model is that it considers the whole adsorbed phase in the pore under the influence of the fluid-solid potential, with its continuous density profile based on the canonical energy distribution, within a single framework without approximating it as comprising a liquid-like surface phase and a bulk gas phase in the remainder of the pore. The latter approximation of the adsorbate in terms of two uniform phases has frequently been used in the past [21, 41], with the liquid-like phase assumed to undergo surface diffusion. This empiricism is avoided in the Oscillator model.

The adsorption effect is represented by the equilibrium constant (*K*) in the Oscillator model, and is readily obtained using

$$K = \frac{2}{r_{osc}^2} \int_0^{r_{osc}} e^{-\phi(r)/k_B T} r dr \tag{6.10}$$

and the apparent low density diffusivity based on the pseudo-bulk concentration gradient is then estimated as $D_a^{osc} = D_{osc}$, with viscous transport considered to be negligible. The value of the interaction potential, $\phi(r)$, strongly depends on the pore wall composition and structure. In this work, the pore walls in the silica spheres are assumed to be infinite thick and comprised of closely-packed LJ sites, with the interaction between the fluid particles and the pore wall being dominated by oxygen ions. The assumption of interaction purely with oxygen in silica is commonly made [42, 43] since oxygen ions are predominant on the surface and effectively screen the interaction of the silicon. The interaction energy profile is estimated by [44]

$$\phi(r) = \pi^2 \varepsilon_{fs} \rho_v \sigma_{fs}^3 \left\{ \frac{7F_h(-4.5,-3.5,1;(r/r_{osc})^2)}{32(r_{osc}/\sigma_{fs})^9 \left[1-(r/r_{osc})^2\right]^9} - \frac{F_h(-1.5,-0.5,1;(r/r_{osc})^2)}{(r_{osc}/\sigma_{fs})^3 \left[1-(r/r_{osc})^2\right]^3} \right\} \tag{6.11}$$

Here σ_{fs} is the LJ fluid-solid collision diameter, ε_{fs} is the LJ potential well depth, ρ_v is the pore wall density (atoms per unit volume) and $F_h(x,y,z;w)$ represents the Hypergeometric function. The LJ parameters of the different gases used in this work is given in Table 6.1, and the LJ parameters for the silica are taken from Kumar et al. [45] as $\varepsilon_{ss}/k_B = 165.0$ K, $\sigma_{ss} = 0.27$ nm, with $\rho_v = 46.57$ nm^{-3}. The Lorentz-Berthelot mixing rules are employed to estimate the fluid-solid LJ parameters ε_{fs}/k_B and σ_{fs} . We note here that the model assumes a structureless wall with diffuse reflection, as in the Knudsen model, and an LJ diffusing species. These are clearly simplifications, and in particular the simple LJ assumption will not be satisfactory for complex molecules such as long chain alkanes or for aromatics.

6.3.2 Transport in pore networks

An important aim of this article is to investigate the transport in disordered mesoporous materials using diffusion models at the single pore level, for which the apparent tortuosity can be theoretical evaluated based on the effective medium theory [46]. Considering a random network of interconnected pores having a coordinate number, *N*, the predicted apparent tortuosity can be derived as follows.

For a pore radius r_p, the conductance, λ, is defined as the ratio of the molecular current to the driving force (taken here as the pseudo-bulk density gradient), i.e.

$$\lambda = \frac{\pi r_p^2 D_o(r_p) K(r_p)}{l} \tag{6.12}$$

where $D_o(r_p)K(r_p)$ is the apparent diffusivity, including both the diffusivity and equilibrium constant (K) based on the relevant pore radius as provided in Figure 6.3, and l is the pore length. The presence of the equilibrium constant K in eqn. (6.12) is due to the choice of the pseudo-bulk density gradient as the driving force, since the diffusivity $D_o(r_p)$ is based on an adsorbed phase density gradient driving force. The pseudo-bulk density is defined as the density of the bulk phase that would be in equilibrium with the adsorbed phase. For macroporous materials, the combination of the classical Knudsen and viscous diffusivity is used to estimate the apparent diffusivity ($D_o = D_a$), with $K = 1$. For narrower pores the apparent diffusivity is estimated based on the corrected pore size ($D_o = D_a^c$), with $K = 1$, and the Oscillator model provides an alternative apparent diffusivity ($D_o = D_o^{osc}$), with $K(r_p)$ defined in eqn. (6.10).

Assuming the pseudo-bulk pressure drop ($-\Delta P$) is independent of the pore size, the effective medium conductance, λ_e is given by the solution of [12, 14]

$$\left\langle \frac{(\lambda - \lambda_e)}{(\lambda + (N/2 - 1)\lambda_e)} \right\rangle = 0 \tag{6.13}$$

where $\langle \cdot \rangle$ is an average over the pore number distribution, and N is the pore network coordination number (i.e. number of pores meeting at an intersection). Physically, this is an effective parameter that represents the connectivity of the pore network, which has been found useful in consistently explaining the adsorption of molecules of different size [47], as well as adsorption hysteresis [48] and the transport of gases in membranes and supports [17, 28, 29]. For the effective medium, the pore flux is estimated as [9]

$$j(r_p) = \frac{\lambda_e l}{\pi r_p^2 R_g T} \left(\frac{N-1}{N+1} \right) \overline{\cos^2(\theta)} \left(-\frac{dP}{dz} \right) \tag{6.14}$$

where z represents the coordinate along the macroscopic flux direction, $(N-1)/(N+1)$ stands for a correlation effect due to the finite possibility that a diffusing molecule re-enters a pore that it has just left, and the factor $\overline{\cos^2(\theta)}$ accounts for the local diffusion direction, which is not necessarily axial but depends on the pore aspect ratio ($x=r_p/l$). For unconsolidated media, pores are formed from the space between the consolidated crystal particles in which the pore size is comparable to the pore length, so the diffusion direction in the pore is not axial but dependent on the aspect ratio.

By assuming that the local diffusion follows the closest path to the macroscopic flux, the expression of $\overline{\cos^2(\theta)}$ is obtained as [9, 49]

$$\overline{\cos^2(\theta)} = g(x) = 1 + \frac{4x}{3(1+4x^2)} - \frac{2}{3(1+4x^2)^{1/2}} \tag{6.15}$$

For consolidated materials, the pore aspect ratio is negligibly small, so that the local diffusion direction is axial, and upon taking $x = 0$, we obtain $g(x) = 1/3$.

The net flux in the equivalent uniform network is obtained upon integration of eqn. (6.14) over the pore volume, to yield

$$J = \frac{\varepsilon \lambda_e < l^2 g(x) >}{\pi < r_p^2 l > R_g T}\left(\frac{N-1}{N+1}\right)\left(-\frac{dP}{dz}\right) \tag{6.16}$$

In practice, it is common to interpret the experimental data phenomenologically based on the effective diffusivity at a mean pore radius, $\overline{r_p}$, so that eqs. (6.1) and (6.2) yield

$$J = \frac{\varepsilon D_o(\overline{r_p}) K(\overline{r_p})}{\tau_{app} R_g T}\left(-\frac{dP}{dz}\right) \tag{6.17}$$

where $\bar{D}_a$ is replaced by $D_o(\overline{r_p})K(\overline{r_p})$. Combining eqs. (6.16) and (6.17), the theoretical apparent tortuosity is obtained as

$$\tau_{app} = \frac{\pi < r_p^2 l > D_o(\overline{r_p}) K(\overline{r_p})}{< l^2 g(x) > \lambda_e}\left(\frac{N+1}{N-1}\right) \tag{6.18}$$

This is the tortuosity an experimentalist would be expected to obtain, when interpreting experimental data using a single representative pore size, r_p. As is evident from eqn. (6.18), the representative pore radius, $\overline{r_p}$, critically affects the estimated apparent tortuosity and its variation with diffusing species and temperature; this is due to the difference in temperature dependence between $D_o(\overline{r_p})K(\overline{r_p})$ and λ_e, and this difference will depend on the fluid. This representative pore radius can be chosen in several ways. In experimental work, the most commonly used representative pore radius is estimated based on the ratio of pore volume and surface area, following

$$\overline{r_p} = \frac{2V_p}{S_g} \tag{6.19}$$

where S_g is the surface area determined through gas adsorption or mercury porosimetry. In addition, the number average radius provides another alternative, and is defined by

$$\overline{r_p} = \frac{\int_0^\infty r_p f_N(r_p) dr_p}{\int_0^\infty f_N(r_p) dr_p} \tag{6.20}$$

where $f_N(r_p)$ is the pore number distribution. The relationship between the pore volume distribution, $f_v(r_p)$, and $f_N(r_p)$ is given as

$$f_N(r_p) = \frac{f_v(r_p)}{Hr_p^2} \tag{6.21}$$

where $H = \int_0^\infty [f_v(r_p)/r_p^2]dr_p$. Further, the peak of the pore volume distribution, $f_v(r_p)$, is also frequently taken as the representative pore radius. Finally, the peak of the number distribution, $f_N(r_p)$, provides another choice of representative pore radius to be investigated here in estimating tortuosity. For clarity, the representative pore radii defined in eqs. (6.19) and (6.20) are labelled as $\overline{r_v}$ and $\overline{r_n}$ respectively, while we define r_v and r_n as the peaks of the pore volume and number distribution respectively. In the following, the above pore radii are employed to predict the apparent tortuosity, and to investigate the effect of choice of representative pore size on this tortuosity.

6.4 Results and discussion

We first examine the data of Reyes et al. [35] for the diffusion of N_2, Xe and i-C_4H_{10} in mesoporous Shell silica spheres, showing that while the different models are applicable at the large pore sizes prevalent in this material, the pore size distribution and network topology, usually neglected in interpretations of diffusion data, has critical influence on the tortuosity. Further, we demonstrate that in narrower pore size structures, where the pore wall interaction influences the transport significantly so that the Knudsen model is inapplicable, the apparent tortuosity varies with gas and operating conditions, and this variation depends on the choice of representative pore radius in a non-trivial way.

6.4.1 Diffusion in mesoporous silica spheres

The intraparticle diffusivity in the mesoporous Shell silica spheres was obtained from the work of Reyes et al. [35], who studied the diffusion of N_2, Xe and i-C_4H_{10} in this material over a wide range of temperature, by the frequency response technique. The authors reported that the diffusion is in the Knudsen regime as the experimental temperature and gas species dependence of the diffusivities followed a $\sqrt{T/M}$ dependence. This conclusion was further supported by Ruthven et al. [30] by correlating the measured diffusivity with the Knudsen diffusivity using a representative pore radius of 3.5 nm, to derive an acceptable apparent tortuosity (τ_{app} = 4.2). However, as illustrated in Figures 6.1 and 6.2, the mean pore radius of the sample is clearly much larger than 3.5 nm, so the estimation of the tortuosity requires reconsideration based on a more relevant pore size. Further, it is instructive to re-examine the transport mechanism in the silica spheres using the different representative pore radii (r_n, $\bar{r}_n$, r_v and $\bar{r}_v$) with different diffusion models. It was found that the values of the pore radii r_n, $\bar{r}_n$ and r_v are very close to each other for the pore size distribution given in Figure 6.1, so only the results based on $\bar{r}_v$ and $\bar{r}_n$ are discussed in the following section.

6.4.1.1 Classical Knudsen model

Figure 6.4(a) and (b) depicts the correlation results based on the classical Knudsen model with $K(\bar{r}_p) = 1$, using $\bar{r}_v$ (7.4 nm) and $\bar{r}_n$ (6.1 nm), in which high apparent tortuosities of 9.3 and 7.7 respectively are extracted from the regression line. These tortuosities are significantly larger than the value of about 4.2 quoted by Ruthven using an unrealistically low pore radius of 3.5 nm [30], highlighting the effect of the choice of representative pore radius. It is readily seen that the three tortuosities of 9.3, 7.7 and 4.2 vary linearly with the associated representative pore radius, which is to be expected given the proportionality of the Knudsen diffusion coefficient to this pore radius. These tortuosities may be interpreted by effective medium theory, with the diffusivity represented by the classical Knudsen model. Considering that the mesoporous silica sphere is highly consolidated, the aspect ratio is taken as $x = 0$, so that $g(x) = 1/3$, and the coordination number, N, is the only adjusted parameter for a chosen representative pore radius ($\bar{r}_v$ or $\bar{r}_n$).

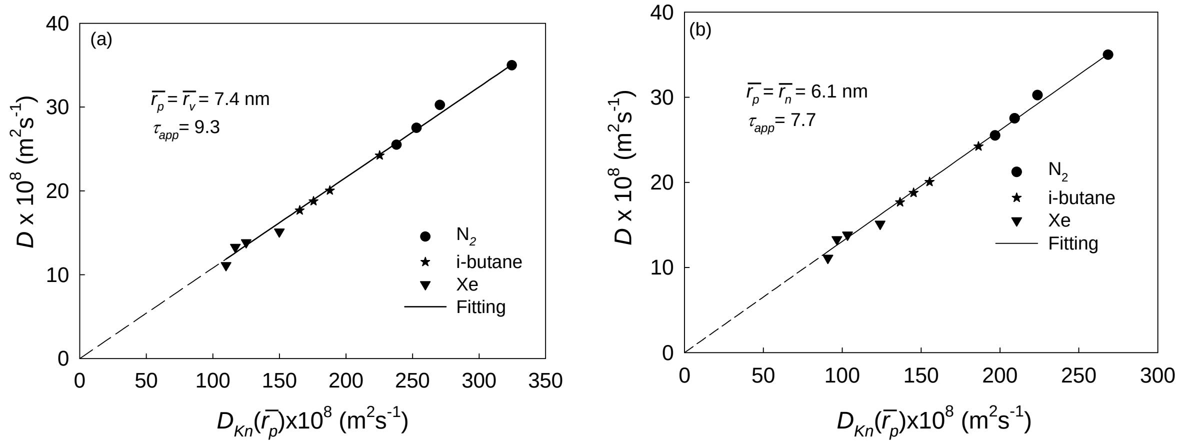

Figure 6.4 Correlation of the diffusivity in mesoporous Shell silica spheres based on the classical Knudsen model using different representative pore radii. (a) $\bar{r}_v$ and (b) $\bar{r}_n$. Experimental pressure used is 2.13 kPa [35].

According to the effective medium theory, for the Knudsen model for which $K(\bar{r}_p) = 1$, the predicted tortuosity should be independent of temperature and gas species, since the factor $(T/M)^{1/2}$

appearing in the terms λ_e and $D_o(\overline{r_p})$ in eqn. (6.18), cancels out [28]. Such a plot for $\overline{r_v}$ is depicted in Figure 6.5, in which the predicted τ_{app} decreases with increase in coordination number, and the fitted value of the coordination number for the tortuosity in Figure 6.4(a) is 2.92. The same coordination number may be estimated for all choices of representative pore radius with the pore size distribution in Figure 6.1, because of the linearity between tortuosity and this representative pore size for the Knudsen model. In general, a value between 3 and 6 has been found for the value of *N* for consolidated silica materials based on interpretation of N_2 adsorption data using percolation theory [48, 50, 51], and the present value is in the low end of this range. Based on the linearity in Figure 6.4 for all gases the Knudsen model appears to be satisfactory for the large mesopore sizes pertinent to the Shell silica sample; however, the low value of *N* given the high porosity of 68% of this silica suggests that this may be an artifact [19]. Consequently, it is important to explore the interpretation of the data using the other models discussed in Section 6.3.1.

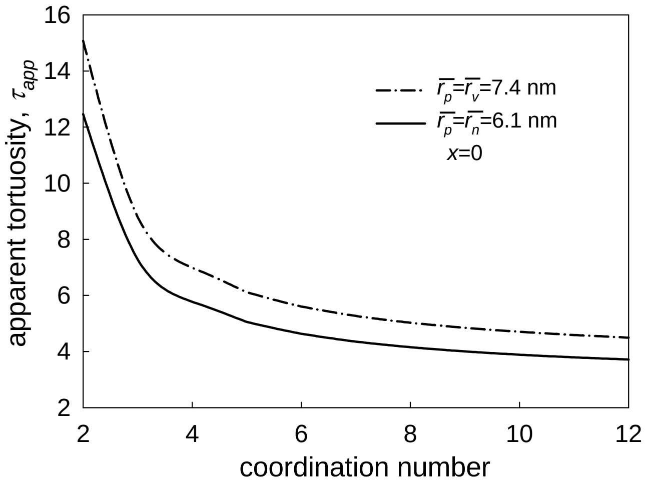

Figure 6.5 Variation of apparent tortuosity with coordination number for mesoporous Shell silica spheres, based on the classical Knudsen model using different representative pore radii. (a) $\overline{r_v}$ and (b) $\overline{r_n}$.

6.4.1.2 Corrected Knudsen model

Since the Knudsen diffusion model appears adequate for the large pore size of the silica based on the linearity in Figure 6.4, it may be expected that the corrected Knudsen and Oscillator models will also be satisfactory. In the above Knudsen model-based correlation the tortuosity is exclusively determined by the porous medium and is independent of the gas and temperature. However, as demonstrated in our previous results [17], the tortuosity and its variation with temperature and gas is significantly affected by the choice of diffusion model. For instance, the apparent tortuosity varies with gas species for the corrected Knudsen model, due to the effect of the different molecular size correction to the pore radius on the conductance. Therefore it is of interest to examine the tortuosity for the corrected Knudsen model based on $\bar{r}_v$ and $\bar{r}_n$ by introducing the molecular exclusion effect, using the LJ parameters listed in Table 6.1. Such plots are depicted in Figures 6.6(a) and (b), in which the apparent tortuosity is extracted from the slope of the correlation for each gas using the corrected Knudsen model with $K(\bar{r}_p)=1$. As shown in Figure 6.6(a), the apparent tortuosity based on $\bar{r}_v$ is only slightly reduced and differs only marginally between the gases; similar behavior is observed for $\bar{r}_n$ in Figure 6.6(b) albeit with smaller tortuosities than those in Figure 6.6(a). The trend of dependence of tortuosity on gas species is in accord with the prediction for the corrected Knudsen model using effective medium theory, in which the tortuosity variation with gas is mainly caused by the different correction to the pore radius, with larger molecules showing higher tortuosity [17].

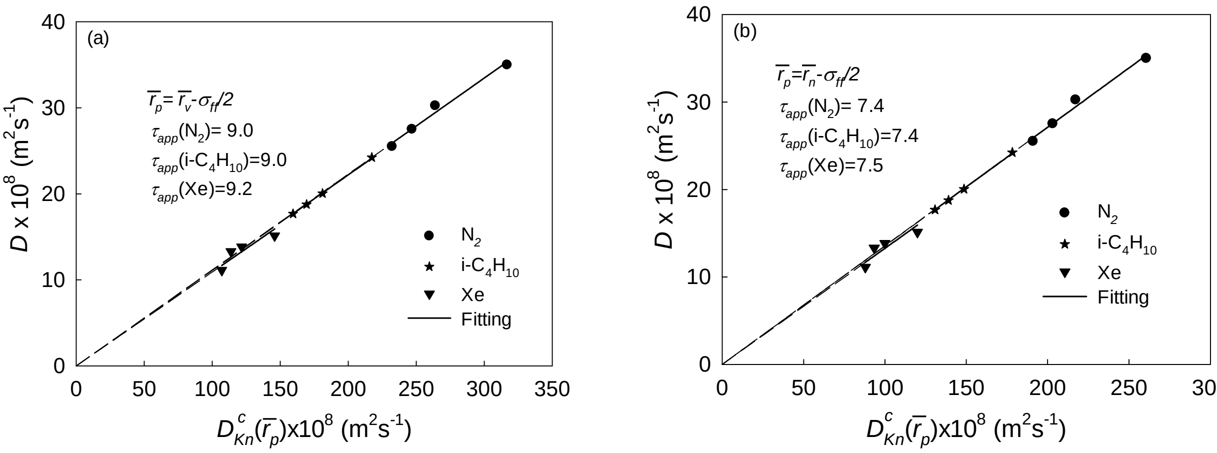

Figure 6.6 Correlation of the diffusivity in mesoporous Shell silica spheres based on the corrected Knudsen model using different representative pore radii. (a) $\bar{r}_v$ and (b) $\bar{r}_n$. Experimental pressure used is 2.13 kPa [35].

To further examine the exclusion effect, the tortuosity versus coordination number based on $\bar{r}_v$ and $\bar{r}_n$ is plotted in Figures 6.7(a) and (b) respectively, using eqn. (6.18) with $K(\bar{r}_p)=1$, in which the predicted tortuosity is expected to be independent of temperature but to vary slightly between gases. As shown in Figure 6.7(a) τ_{app} decreases with increase in coordination number, and the fitted coordination number for the tortuosity values in Figure 6.6(a) is 3.25. This is slightly larger than that based on the classical Knudsen model, but still in the low end of the range of typical values obtained for silica based on percolation theory interpretations of N_2 adsorption data [50]. Figure

6.7(b) depicts the apparent tortuosity versus coordination number for representative pore radius taken as $\bar{r}_n$, yielding a fitted coordination number of 3.24 for the tortuosities in Figure 6.6(b), very similar to the value provided by $\bar{r}_v$. However, it is noted that for all coordination numbers the predicted order of the tortuosity for the gases in Figure 6.7 is i-butane $\simeq$ Xe>N_2, which is different from the experimental order, Xe>i-butane $\simeq$ N_2, in Figure 6.6. This inconsistency can only be attributed to experimental scatter, as the tortuosity variation between gases is small, and such differences may not be accurately resolved by the experiments.

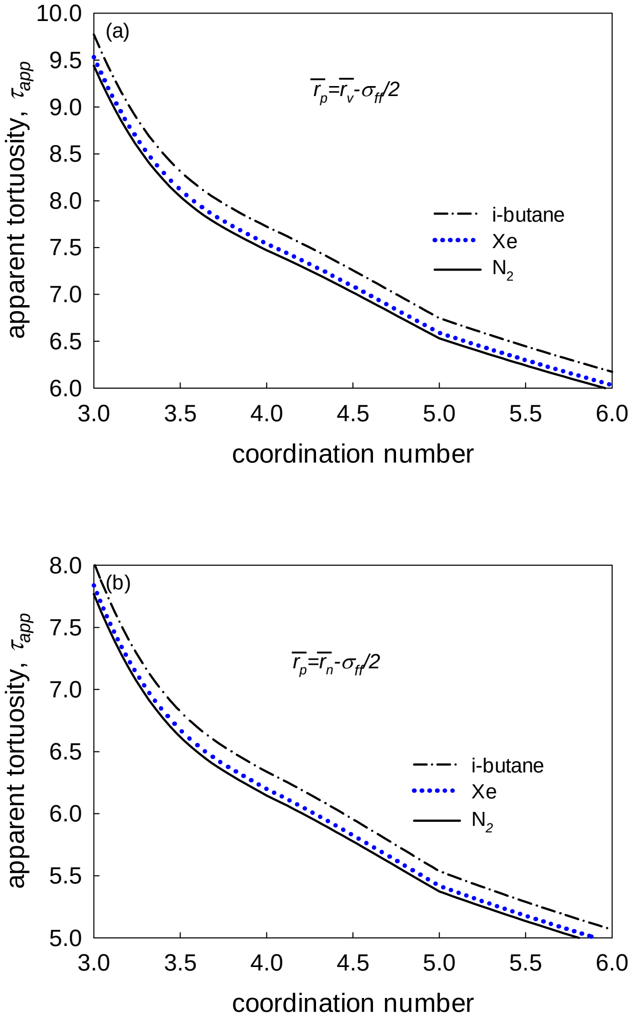

Figure 6.7 Variation of apparent tortuosity with coordination number for mesoporous Shell silica spheres, based on the corrected Knudsen model using different representative pore radii. (a) $\bar{r}_v$ and (b) $\bar{r}_n$.

6.4.1.3 Oscillator model

The Oscillator model from this laboratory was also applied to interpret the experimental data with the LJ interaction parameters given in Table 6.1, and the experimental tortuosity evaluated from the ratio between the model-based diffusivity and the observed diffusivity, with $K(\overline{r}_p)$ predicted by eqn. (6.10). In this approach, the experimental tortuosity varies with temperature and species, which is expected for the Oscillator model since the dependence of the conductance on the gas is much more complex for the Oscillator model than for the Knudsen model for in which the temperature and gas dependence term $(T/M)^{1/2}$ cancels out of eqn. (6.18). This leads to the complex tortuosity dependence on gas and temperature as discussed elsewhere [29]. The results based on $\overline{r}_v$ and $\overline{r}_n$ are plotted in Figures 6.8 and 6.9 respectively, with the symbols representing the experimental tortuosities, and the lines are the model results obtained using eqn. (6.18). We note here that for the frequency response analysis used by Reyes et al. [35] their reported diffusivity represents that based on a gas phase concentration gradient, and must be interpreted as $\overline{K}D_o / \tau_{exp}$, where $\overline{K}$ is the mean equilibrium constant, defined as

$$\overline{K} = \frac{1}{V_p}\int_0^\infty K(r_p) f_v(r_p) dr_p \tag{6.22}$$

and τ_{exp} is the experimental tortuosity.

As shown in Figure 6.8, the experimental tortuosity based on $\overline{r}_v$ is below the values obtained for the Knudsen model or its version corrected for molecular size, and varies slightly with gas and temperature following the order $N_2 \simeq$ Xe > i-butane. The predicted tortuosities based on EMT decrease with increase in coordination number but slightly increase with increase in temperature for all the gases. The estimated coordination number consistent with the results for all the gases is around 4.0, which is somewhat larger than the value obtained using the Knudsen based approach, and in accord with values from percolation theory-based interpretations of nitrogen adsorption isotherms on silicas [50].

Similar results are obtained for $\overline{r}_n$ in Figure 6.9, although the apparent tortuosities are even smaller than those in Figure 6.8. The estimated coordination number using $\overline{r}_p = \overline{r}_n$ is very similar to that based on $\overline{r}_v$, at 4.0. Besides, the predicted tortuosity order of the gases in both cases follows the pattern $N_2 \simeq$ Xe > i-butane for all coordination numbers. This is clearly indicative of a higher tortuosity (albeit only very slightly) for the more weakly adsorbed gases. Such tortuosity dependence on gas is expected for the Oscillator model where stronger adsorption in small pores enhances their conductance at low temperature, mitigating the short circuiting effects of larger pores, and therefore leading to a lower tortuosity [19, 27, 29]. Nevertheless, the pore sizes in the mesoporous Shell silica spheres are sufficiently large that the short circuiting effect is not as prominent as that in small pores (less than 2 nm), and the tortuosity difference between i-butane and Xe or N_2 is therefore small.

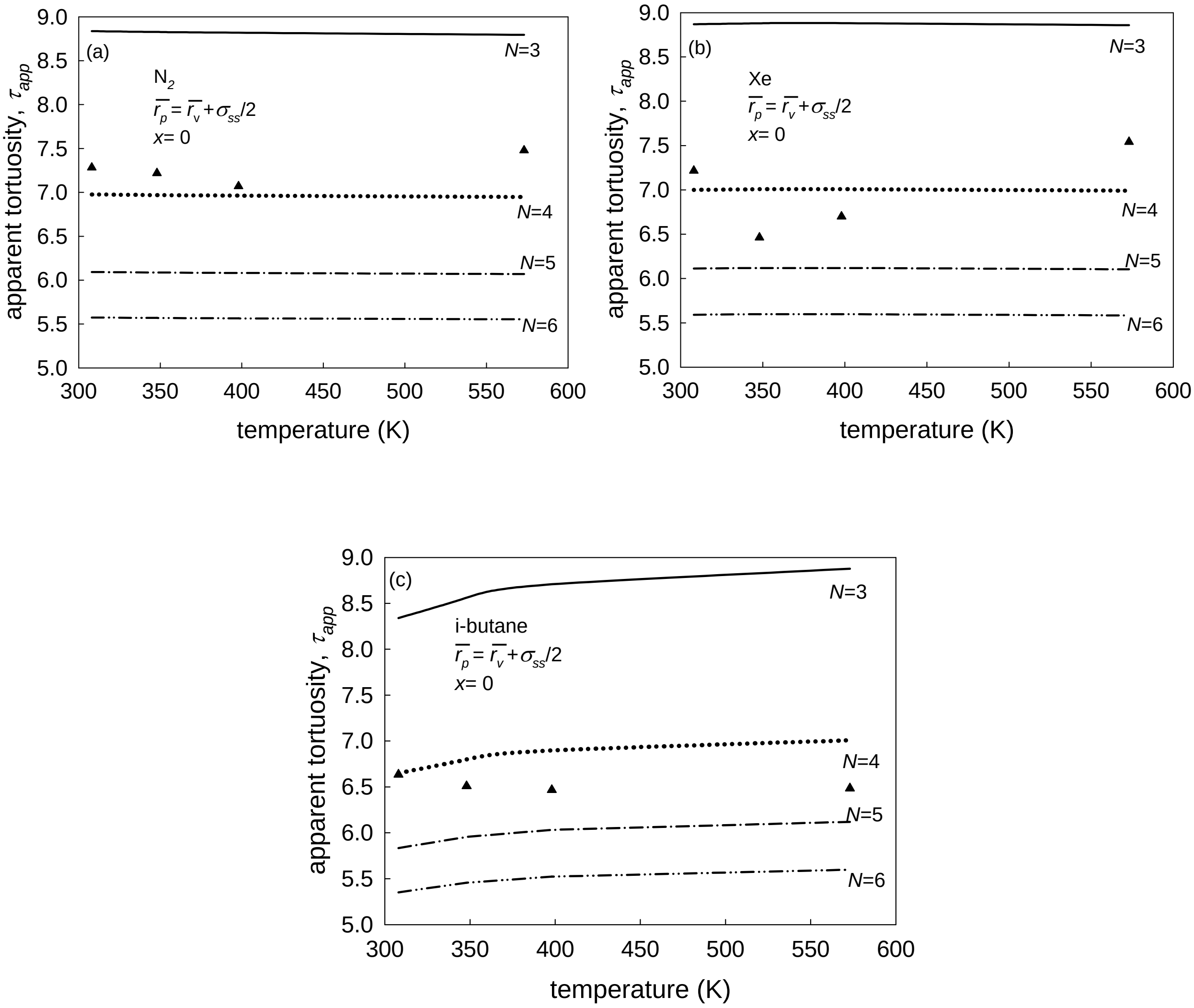

Figure 6.8 Variation of apparent tortuosity with temperature for mesoporous Shell silica spheres, using representative pore radius, $\overline{r_v}$, for different gases. (a) N_2, (b) Xe, and (c) i-butane. The symbols represent the experimental tortuosity and lines the theoretical results based on the Oscillator model with EMT, for different coordination numbers, in the Henry's Law region.

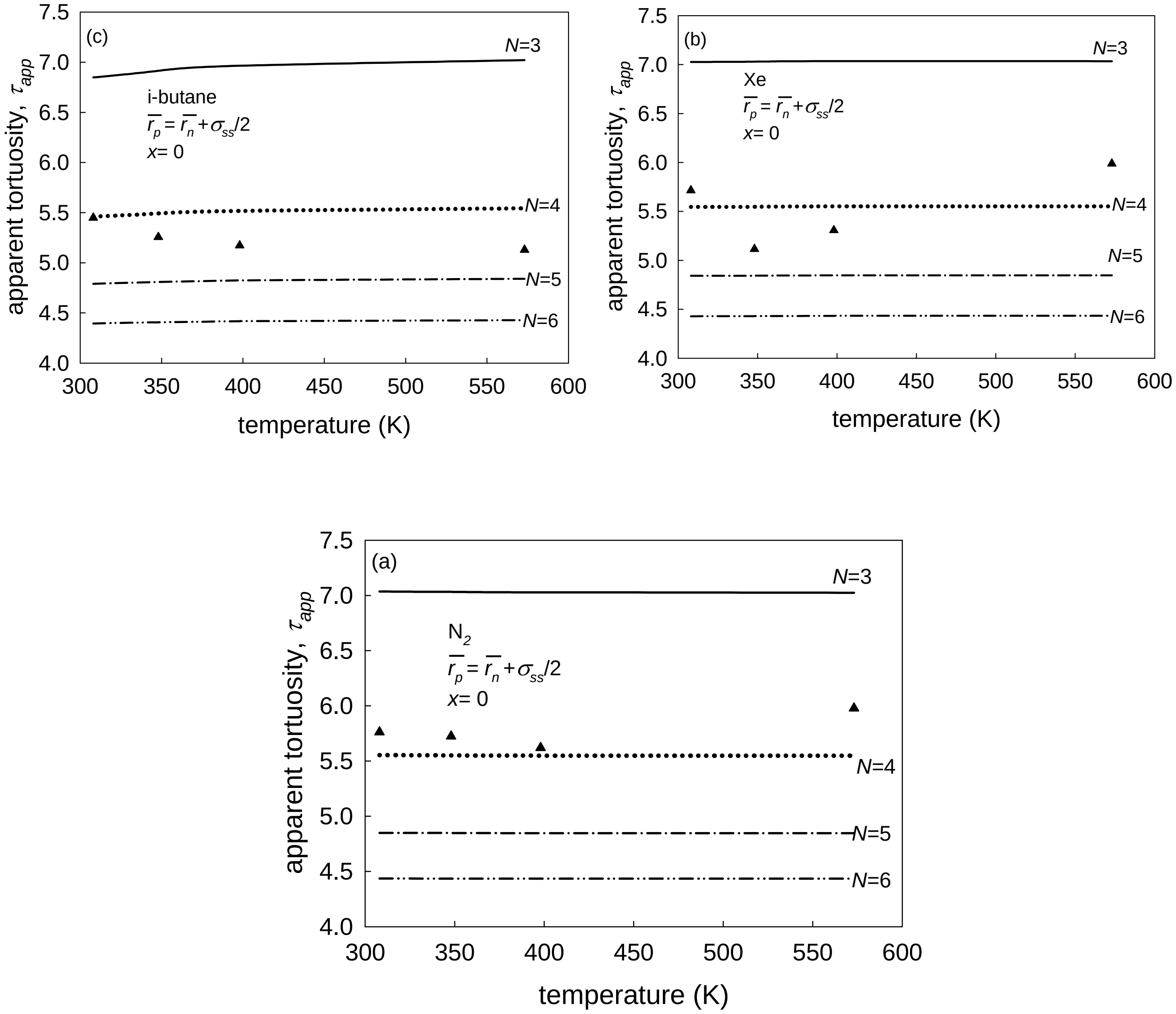

Figure 6.9 Variation of apparent tortuosity with temperature for mesoporous Shell silica spheres, using representative pore radius, $\overline{r}_n$, for different gases. (a) N_2, (b) Xe, and (c) i-butane. The symbols represent the experimental tortuosity and lines the theoretical results based on the Oscillator model with EMT, for different coordination numbers, in the Henry's Law region.

The small tortuosity variation with gas can be explained by plotting the variation of pore conductance, represented as λl, with the pore radius for each gas, as illustrated in Figure 6.10 for the lowest and highest temperature (308 K and 573 K). It is evident that the conductance monotonically increases with increase in pore radius in a similar way for all three gases, indicating that short circuiting effects by large pores are similar for all gases, and their tortuosities therefore differ only marginally. Further, adsorption is not strong even at low temperature, and the variation of conductance with pore size is similar for both temperatures; thus the tortuosities are almost constant over the temperature range as given in Figures 6.8 and 6.9.

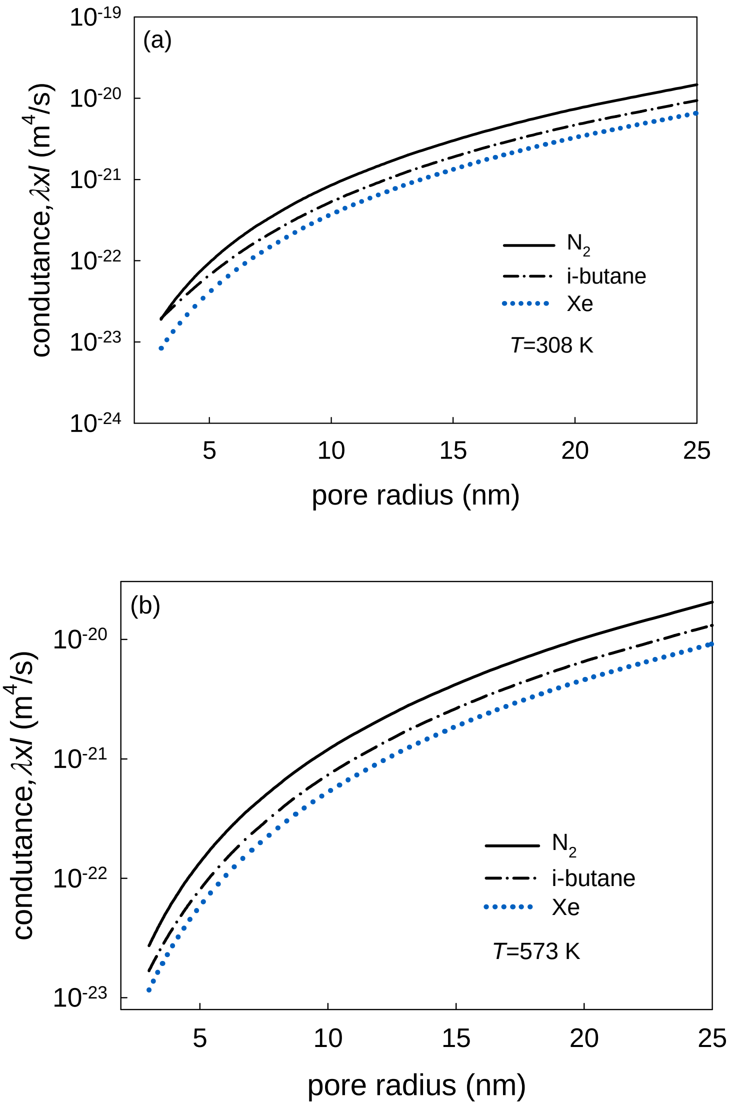

Figure 6.10 Variation in conductance (as λl) with pore radius, for different gases, at (a) 308 K, and (b) 573 K.

It is clear from the above that the diffusion mechanism in the mesoporous silica spheres is satisfactorily represented by the Oscillator model. Thus, it would appear that all three models (Knudsen, corrected Knudsen and the Oscillator model) can be used for the large pore sizes of the mesoporous Shell silica. Nevertheless, the larger fitted coordination number of 4 based on the Oscillator model would appear somewhat more reasonable given the high porosity of 68% of this silica.

6.4.2 Influence of pore structure

Our recent results have shown that the tortuosity is not exclusively determined by the properties of the porous medium, but also significantly dependent on the diffusing gas and process conditions as well as the diffusion model adopted [16, 17, 19, 27, 29]. The present results have shown that it also depends on the choice of representative pore radius, as this affects the intrinsic diffusivity values based on which the tortuosity is determined. In this section we investigate these features and the diverse variety of behavior that results from different choices of the representative pore radius. Assuming a Rayleigh distribution, the relationship between the pore radius, r_p, and number density, $f_N(r_p)$, is given by

$$f_N(r_p) = \frac{(r_p - r_o)}{(r_n - r_o)^2} e^{-[(r_p - r_o)^2 / 2(r_n - r_o)^2]} \tag{6.23}$$

here, r_o is the minimum pore radius and r_n is the peak of the number distribution (or modal pore radius). The standard deviation of this distribution is readily seen to be

$$s = 0.7024(r_n - r_o) \tag{6.24}$$

The mean pore radius, $\overline{r_v}$, based on the ratio between the pore volume and surface area, is expressed as

$$\overline{r_v} = \frac{\int_{r_o}^{\infty} r_p^2 l f_N(r_p) dr_p}{\int_{r_o}^{\infty} r_p l f_N(r_p) dr_p} \tag{6.25}$$

Further, r_v is the peak of the pore volume distribution, $f_v(r_p)$, which follows

$$f_v(r_p) = \frac{r_p^2 l f_N(r_p)}{\int_{r_o}^{\infty} r_p^2 l f_N(r_p) dr_p} V_p \tag{6.26}$$

Figures 6.11(a) and (b) depict the pore number and volume distribution for macroporous networks, with modal pore radii r_n = 50 nm and 200 nm respectively.

The minimum pore radius, r_o is taken such that the relative standard deviation, s/r_n, has a value of 0.50, and the different choices of representative pore radii for each pore network are marked. Significant differences between the various possible choices for representative pore radii are evident. For instance, the difference between $\overline{r_n}$ and r_n is around 20%, and increases to 40% between r_v and r_n. To examine the influence of modal pore radius on the representative pore radii, distributions having modal radii of r_n = 2 nm and 8 nm, with the same relative standard deviation of 0.5, are depicted in Figures 6.11(c) and (d). The relative difference of the representative pore radii is almost identical to that obtained for the macroporous network; thus, the variation of representative pore radius is also considerable in mesoporous networks with wide pore size distributions. Much smaller differences were found for the mesoporous Shell silica, in which the number average, $\overline{r}_n$, is very close to the peaks r_v and r_n due to its pore size distribution being much narrower.

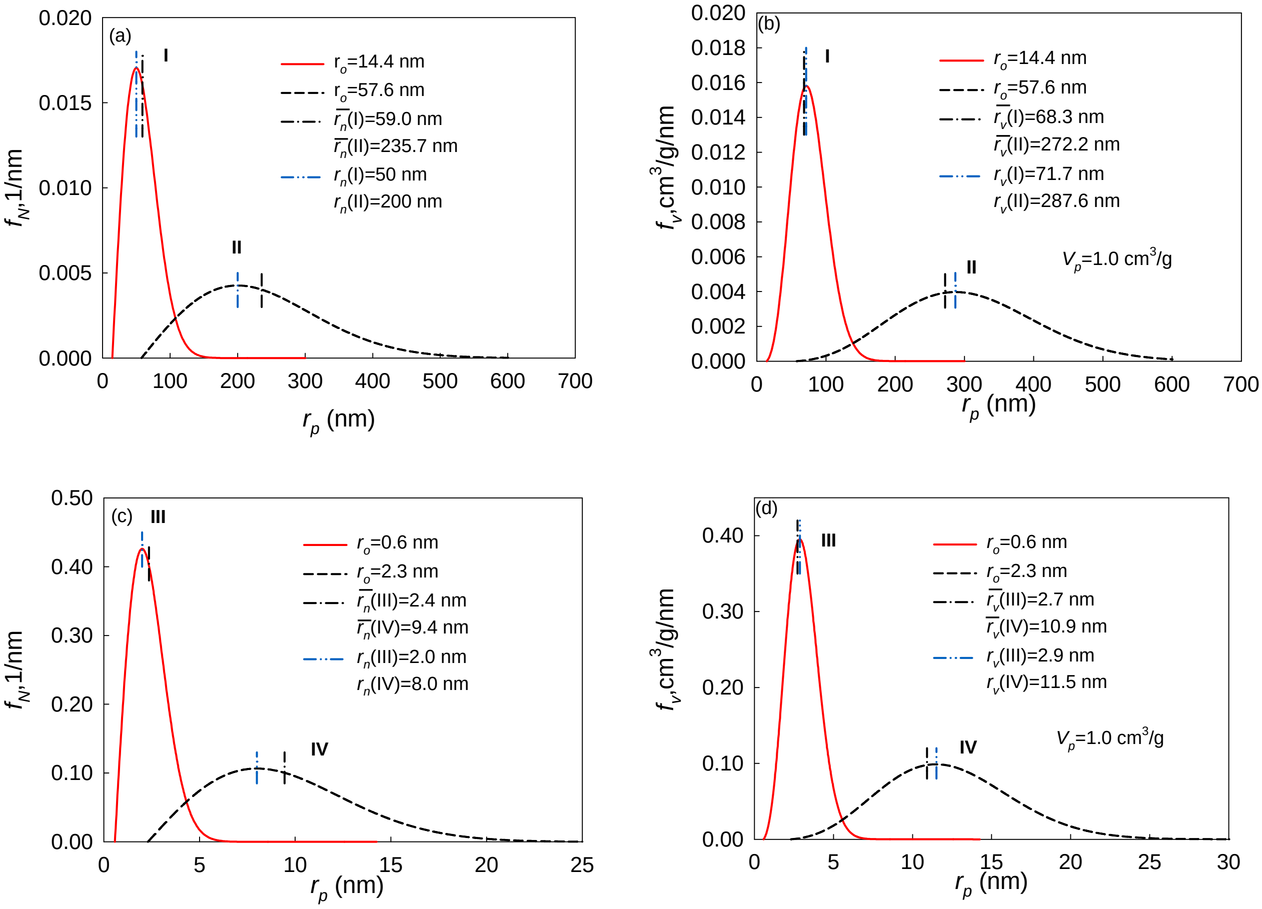

Figure 6.11 Illustration of different representative pore radii for the Rayleigh pore number distribution with various modal pore radii, and the corresponding pore volume distribution, for s/r_n=0.50. (a) Representative pore radii $\overline{r}_n$ and r_n, corresponding to a Rayleigh pore number distribution for macroporous networks I and II. (b) Representative pore radii $\overline{r}_v$ and r_v, and pore volume distribution, for macroporous networks I and II. (c) Representative pore radii, $\overline{r}_n$ and r_n, corresponding to a Rayleigh pore number distribution for mesoporous networks III and IV. (d) Representative pore radii $\overline{r}_v$ and r_v, and pore volume distribution, for mesoporous networks III and IV.

To investigate the effect of representative pore radii on different nanoporous networks, the pore network with the modal pore radius of 200 nm is assumed to represent macroporous materials, in which the transport is adequately represented by slip flow [28], and the pore network with a modal pore radius 2 nm is assumed to represents mesoporous materials in which the diffusion is better represented by the Oscillator model [19, 27, 29, 34].

6.4.2.1 Macroporous network

In macroporous media having length scale of a few hundred nanometers, the pores are either formed by voids between large crystallites (micron sized) or the space created by the emulsion templates in the sol-gel technique [52]. In the first type of pore, the radius is comparable to the pore length, and the aspect ratio ($x \neq 0$) effect must be taken into account [28]; while in the second type, the pore radius is far less than the pore length, and the aspect ratio is small, i.e. $x \simeq 0$ [29]. Unconsolidated macroporous materials are often employed as the substrate to provide the main mechanical resistance for the membrane layer in industrial practice [29]. For such materials, the aspect ratio is considered here and the tortuosity trends with operating conditions are examined using various representative pore radii to demonstrate what an experimentalist may be expected to observe in this type of material.

Figure 6.12 depicts the variation of tortuosity with temperature for argon for several coordination numbers based on eqn. (6.18), using different representative pore radii, and constant pore length and pressure. The apparent diffusivity comprises a combination of Knudsen and viscous diffusion, following the slip flow model. It is evident that the tortuosity trends strongly depend on the representative pore radius and coordination number. At low coordination number (N=3) in Figure 6.12(a), the tortuosity monotonically decreases with increase in temperature for all the pore radii, and increases with increase in the representative pore radius. With increase in coordination number the tortuosity is reduced, as seen in Figures 6.12(b)-(d), which is because of the reduction in short circuiting effects with increase in connectivity.

In addition, a variety of trends in tortuosity, both increasing and decreasing with respect to temperature, are obtained. Nevertheless, at the macropore sizes chosen the temperature effect is weak due to the dominance of the viscous flow mechanism. It is clear from the EMT expression in eqn. (6.18) that when either Knudsen or viscous flow dominates, the temperature and gas-specific factors will cancel, and the tortuosity will be dependent on the properties of the pore network only. When both viscous and Knudsen contributions are important, the variation of tortuosity will depend on the difference between the temperature dependence of $D_o(\overline{r}_p)K(\overline{r}_p)$ and λ_e. With increase in $\overline{r}_p$

the temperature dependence of $D_o(\overline{r}_p)K(\overline{r}_p)$ will be weaker, leading to a milder increase or even reduction in tortuosity with increase in temperature.

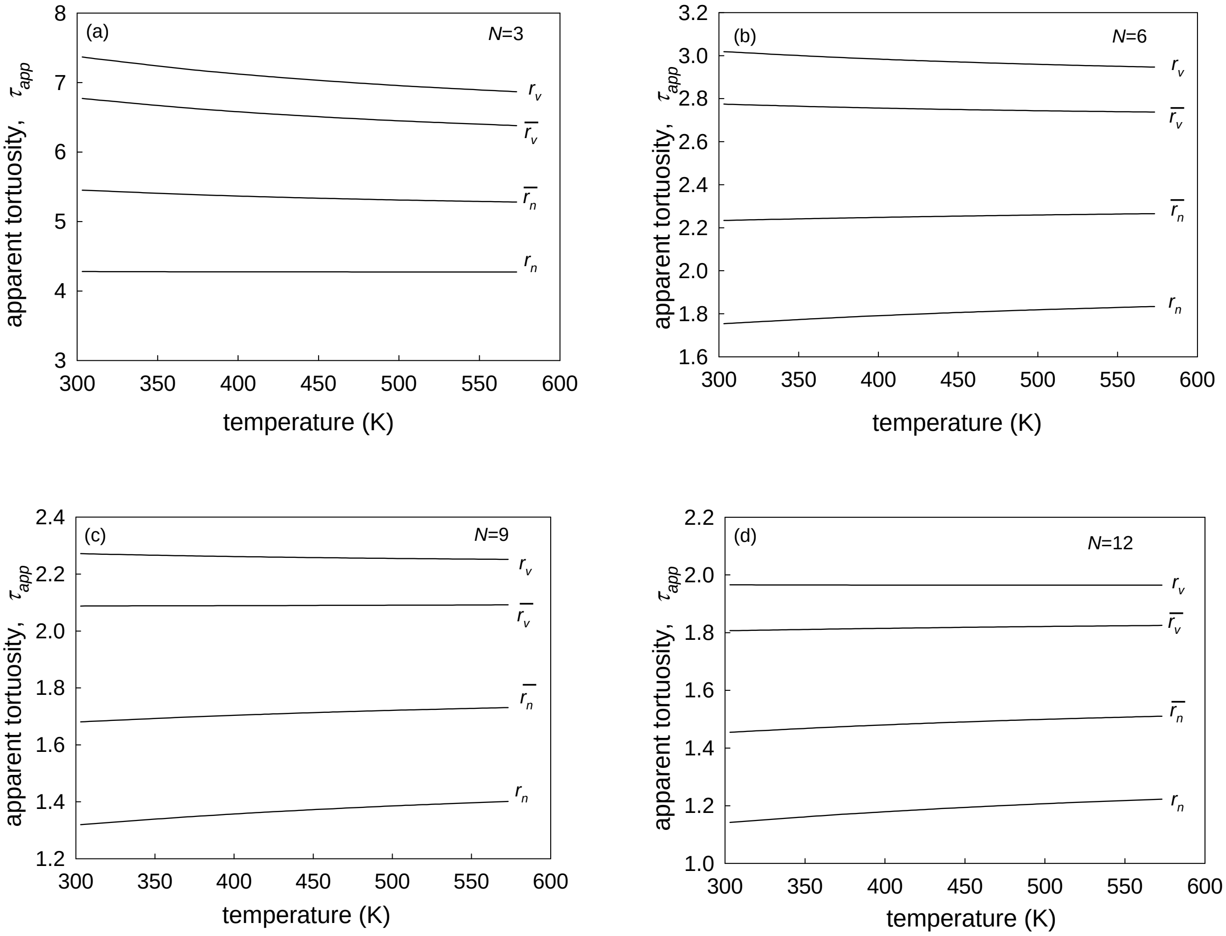

Figure 6.12 Variation of apparent tortuosity with temperature for different representative pore radii and several coordination numbers, based on slip flow in an unconsolidated porous medium following a Rayleigh pore number distribution, with r_n = 200 nm, l = 800 nm, and s/r_n=0.50 at P=200 kPa, for argon. (a) N=3, (b) N=6, (c) N=9 and (d) N=12.

As shown above, different representative pore radii can result in different tortuosity trends with temperature for the same pore network, due to the difference in temperature dependence of $D_o(\overline{r}_p)K(\overline{r}_p)$ and λ_e arising from the combination of Knudsen and viscous diffusion. For larger representative pore radius the tortuosity tends to decrease with increase in temperature, while for smaller representative pore radius the trend is a decreasing one.

To further explore this phenomenon, the effect of relative standard deviation using the largest (r_v) and the smallest (r_n) representative pore radius was investigated at different temperature and pressure for N = 6, as depicted in Figures 6.13(a) and (b). It is seen that either decrease in temperature or increase in pressure yields a higher tortuosity over the given relative standard deviation range investigated, indicating that stronger viscous flow leads to higher tortuosity. This is due to the quadratic dependence of the viscous flow diffusivity on pore radius, evident in eqn. (6.5), as opposed to the linear dependence of the Knudsen diffusivity in eqn. (6.4); this leads to greater short circuiting by larger pores when viscous flow dominates. From Figure 6.13 it is also evident that the temperature dependence of the apparent tortuosity in slip flow is mainly caused by the different tortuosity limits for pure Knudsen or viscous diffusion. For representative pore radius r_v, the tortuosity increases with increase in relative standard deviation in both the viscous and Knudsen limits, which is because of increase in r_v with increase in the relative standard deviation, evident from Figure 6.12. Consequently, with increase in r_v, $D_o(r_v)K(r_v)$ increases faster with increase in the relative standard deviation compared to λ_e, leading to increase in tortuosity with increase in relative standard deviation following eqn. (6.18). However, this increase in tortuosity is stronger for viscous flow compared to Knudsen diffusion because of the quadratic dependence on pore size leading to stronger short circuiting by larger pores.

On the other hand, when r_n is chosen as the representative pore radius the tortuosity instead reduces with increase in the relative standard deviation, with the Knudsen limit now being higher than the viscous limit, as seen in Figures 6.13(c) and (d). This is because r_n, and therefore $D_o(r_n)K(r_n)$, is unchanged with increase in relative standard deviation, while λ_e continues to increase due to larger fraction of large pores. This increase is larger in the viscous limit, and dominates over the short circuiting effects of large pores, because of the quadratic dependence of the viscous flow diffusivity on pore size. As a result, the tortuosity in the viscous limit is lower than that in the Knudsen limit, and reduces with increase in the relative standard deviation of the PSD.

As shown in Figure 6.12, the tortuosity-temperature relationship is strongly influenced by the coordination number. Figure 6.14 depicts the variation of tortuosity with coordination number in the Knudsen and viscous limits, for the porous network given in Figure 6.12, based on eqn. (6.18) and different representative pore radii. It is evident that the tortuosity decreases with increase in coordination number in both limits, and at sufficiently small coordination number the tortuosity in the viscous limit is always higher. This is because of the greater short circuiting when the network connectivity is reduced, and the stronger effect of the reduced connectivity on the short circuiting in the viscous limit due to its quadratic pore size dependence. With increase in representative pore size the cross-over of the Knudsen limit-based tortuosity to higher values occurs at higher coordination numbers because of this quadratic increase of the viscous flow diffusivity with this pore size in contrast to the linear increase of the Knudsen diffusivity.

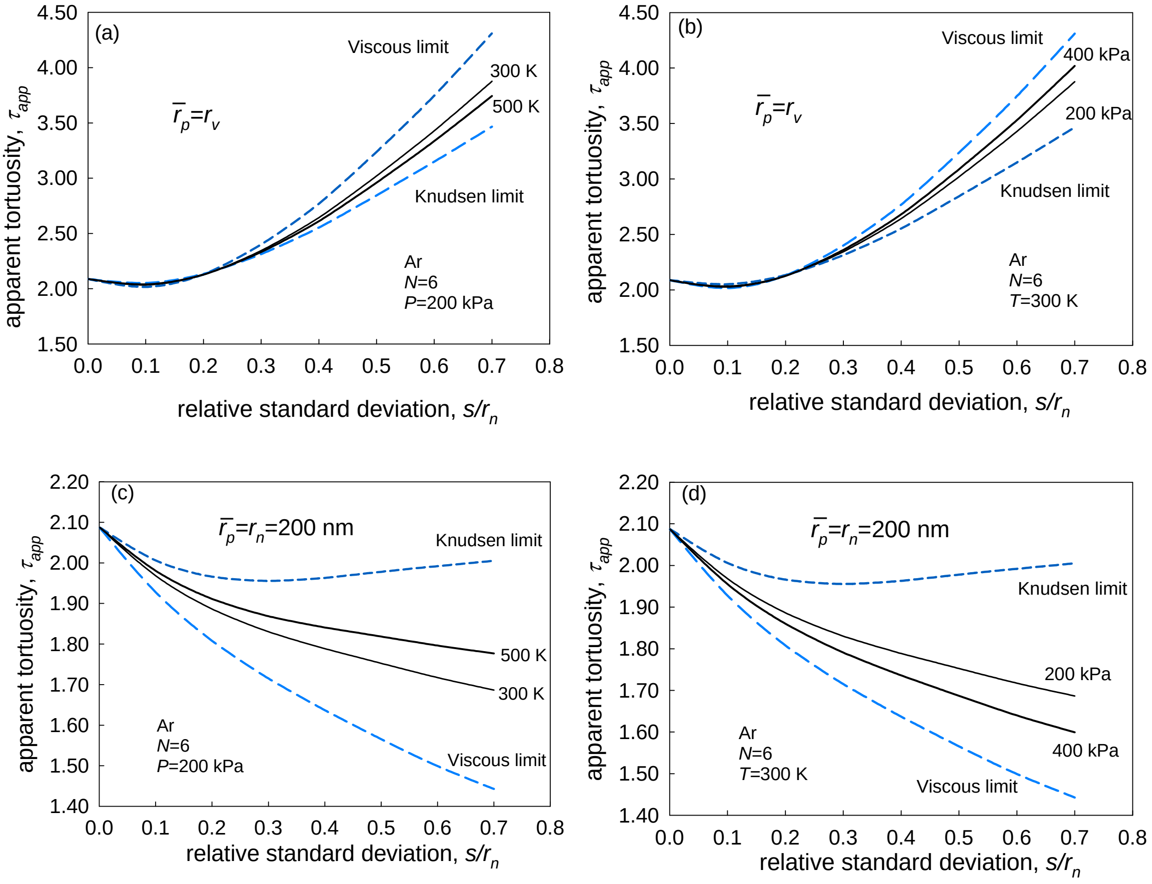

Figure 6.13 Variation of apparent tortuosity with relative standard deviation for argon, using representative pore radius r_v, for different (a) temperature, and (b) pressure, and using representative pore radius r_n, for different (c) temperature, and (d) pressure. Based on slip flow in an unconsolidated porous medium following a Rayleigh pore number distribution, with N=6, r_n = 200 nm and l=800 nm.

The changes in relative importance of viscous flow and Knudsen diffusion lead to the increase or decrease of apparent tortuosity with temperature for different representative pore radii. Since the relative importance of these two modes depends on the gas, it is of interest to compare the apparent tortuosity of various gases. Such plots are given in Figures 6.15(a) and (b), using r_v and r_n for N=6, for a light gas (H_2), an intermediate gas (CH_4) and two heavier gases (Ar and CO_2).

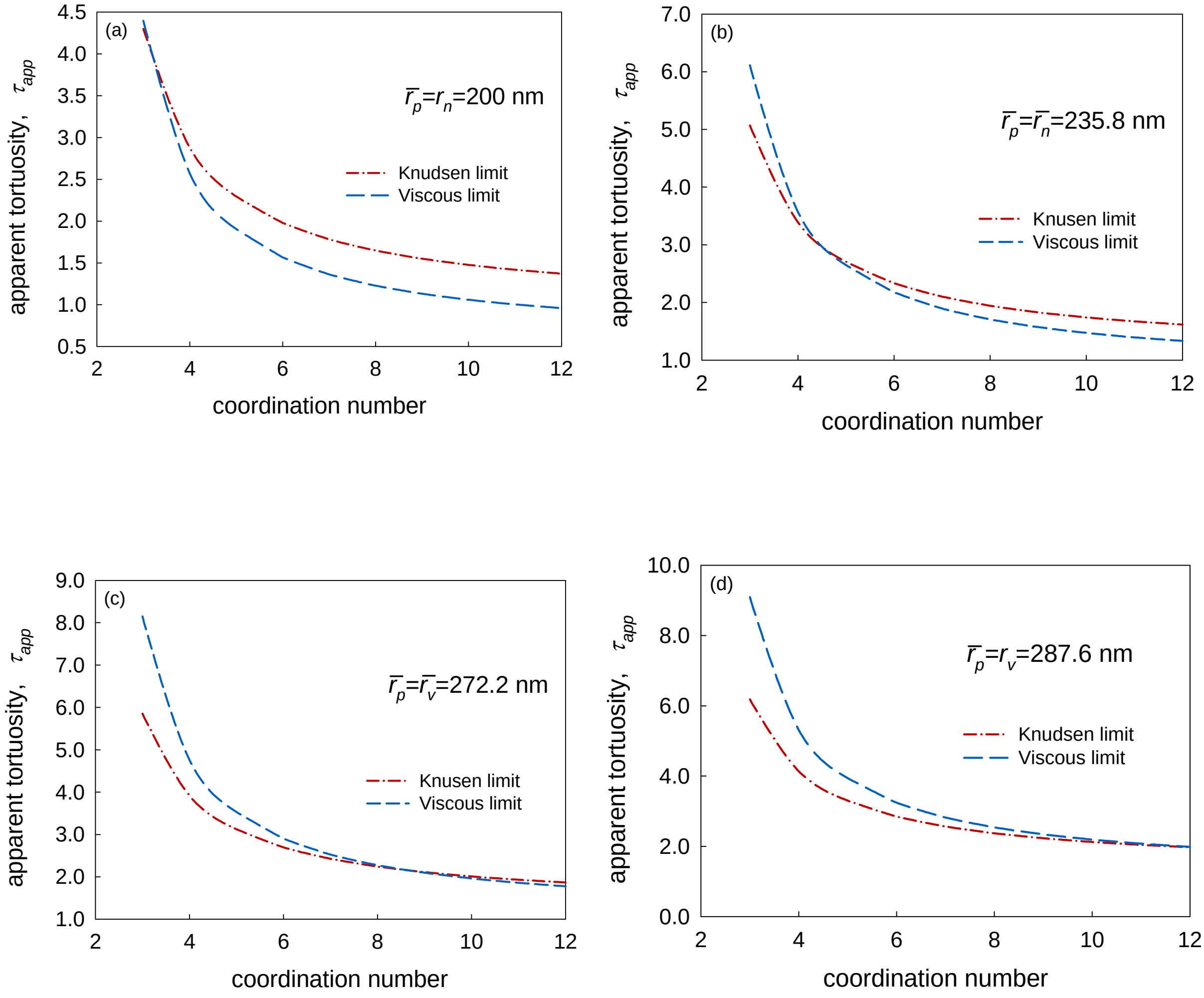

Figure 6.14 Variation of apparent tortuosity with coordination number in the Knudsen and viscous flow limits, for several representative pore radii, in an unconsolidated porous medium following a Rayleigh pore number distribution, with r_n = 200 nm, l = 800 nm, and s/r_n=0.50 at P=200 kPa for argon. (a) r_n, (b) $\bar{r}_n$, (c) $\bar{r}_v$ and (d) r_v.

As illustrated in Figure 6.15(a), the apparent tortuosities of all gases decrease with increase in temperature, following a systematic pattern: CO_2 > CH_4 > Ar > H_2, which is consistent with a decreasing order of relative importance of viscous flow. This order is reversed in Figure 6.15(b) when the smaller representative pore radius of 200 nm is used, due to the increased importance of Knudsen diffusion. Upon plotting the apparent tortuosity versus relative standard deviation based on r_v and r_n in Figures 6.15(c) and (d) respectively, the two different gas orders are again found, consistent with the conclusion derived in Figure 6.13 that the ordering of the tortuosity in the

Knudsen and viscous limits significantly depends on the representative pore radius, with the viscous limit higher for larger representative pore radius but lower for smaller representative pore radius.

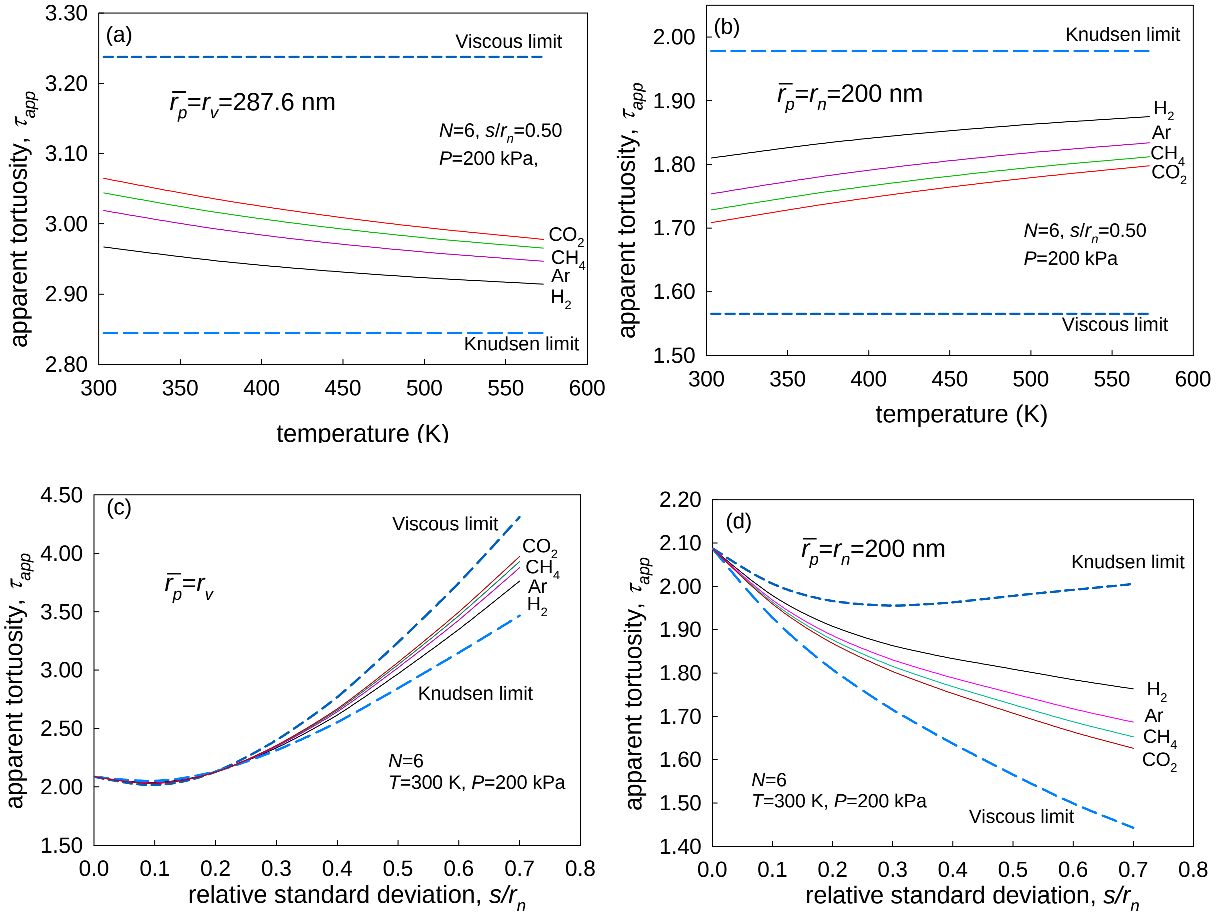

Figure 6.15 Variation of apparent tortuosity with temperature for different gases, using representative pore radius (a) r_v, and (b) r_n, at pressure P = 200 kPa, and variation of apparent tortuosity with relative standard deviation, for different gases using representative pore radius (c) r_v, and (d) r_n, at T=300 K and P=200 kPa. Based on slip flow in an unconsolidated porous medium following a Rayleigh pore number distribution, with N=6, r_n = 200 nm and l = 800 nm.

6.4.2.2 Mesoporous network

In mesoporous materials, the pores exist either as the spaces between precipitated small agglomerated crystal particles [28], or as spaces within the consolidated particles themselves, created by molecular imprinting or liquid crystal templating [1]. The pores of the first type have comparable pore radius and pore length, so that the aspect ratio effect must be appropriately considered (i.e. $x \neq 0$); while for the second type pores, the pore radius is far less than the pore length, and the aspect ratio effect is negligible (i.e. $x = 0$). One aim of the current work is to investigate the effect of network structure on the tortuosity trends for consolidated materials such as mesoporous silica, for which the aspect ratio effect is taken to be negligibly small, and the diffusivity is evaluated based on the Oscillator model with the parameters given above.

Figure 6.16 depicts the variation of tortuosity of several gases with temperature, using representative pore radii r_v and r_n, for different coordination numbers (N=3 and 6), based on the Oscillator model, in a mesoporous silica material having a Rayleigh pore number distribution with r_n=2 nm and s/r_n=0.50. Figure 6.16(a) shows that for low coordination number, the tortuosity-temperature trend based on r_v depends on the gas species - the tortuosity decreases (weakly) with increase in temperature for a non-adsorbed gas (He) but increases for the adsorbed gases (Xe, i-butane and CH_4). When the coordination number increases to 6 in Figure 6.16(b), the trend is similar; however, compared to the results in Figure 6.16(a), the tortuosity is roughly halved and the temperature dependence is weaker. This is due to the reduction in short circuiting effects with increase in connectivity. In Figure 6.16(c), for low coordination number and r_n as representative pore radius, weak tortuosity dependence on gas is also seen, in which the tortuosity is almost constant for He but increases with increase in temperature for Xe and CH_4.

On the other hand, the tortuosity of i-butane slightly decreases at first before increasing, with increase in temperature. When the coordination number increases to 6 in Figure 6.16(d), the tortuosity slightly increases with increase in temperature for He but decreases for Xe and CH_4, although the effects are not strong. It is of interest to note that the tortuosity of i-butane is substantially larger than the others at low temperature, and monotonically decreases with increase in temperature, approaching the tortuosity of the other gases at high temperature.

The diverse tortuosity behavior of the different gases can be understood from the variation of the conductance with the pore radius for the gases. As shown in Figure 6.17(a) and (b), the conductance increases monotonically with pore radius for He, CH_4 and Xe, however, the effect of temperature on conductance is weak for these gases at all pore sizes, so that there is little change in the short circuiting effect of the larger pores with temperature. Consequently the tortuosity is only weakly affected by temperature for these gases. For i-butane it is seen that the small pores have a high conductance at low temperature, consequently the short circuiting effect is lower at low temperature, leading to a significantly lower tortuosity, especially at low temperatures. With increase in temperature the conductance peak at small pore size is attenuated, leading to greater short circuiting by larger pores, and increase in tortuosity with increase in temperature. However, the opposite behavior is obtained for high connectivity (N=6) and $\overline{r}_p = r_n = 2\ \mathrm{nm}$, because the conductance reduces significantly with increase in temperature for this pore size, leading to a decrease in tortuosity with increase in temperature. Thus, it is clear that the dependence of tortuosity on coordination number and representative pore radius is caused by the difference in temperature dependence between $D_o(\bar{r}_p)K(\bar{r}_p)$ and effective conductance (λ_e).

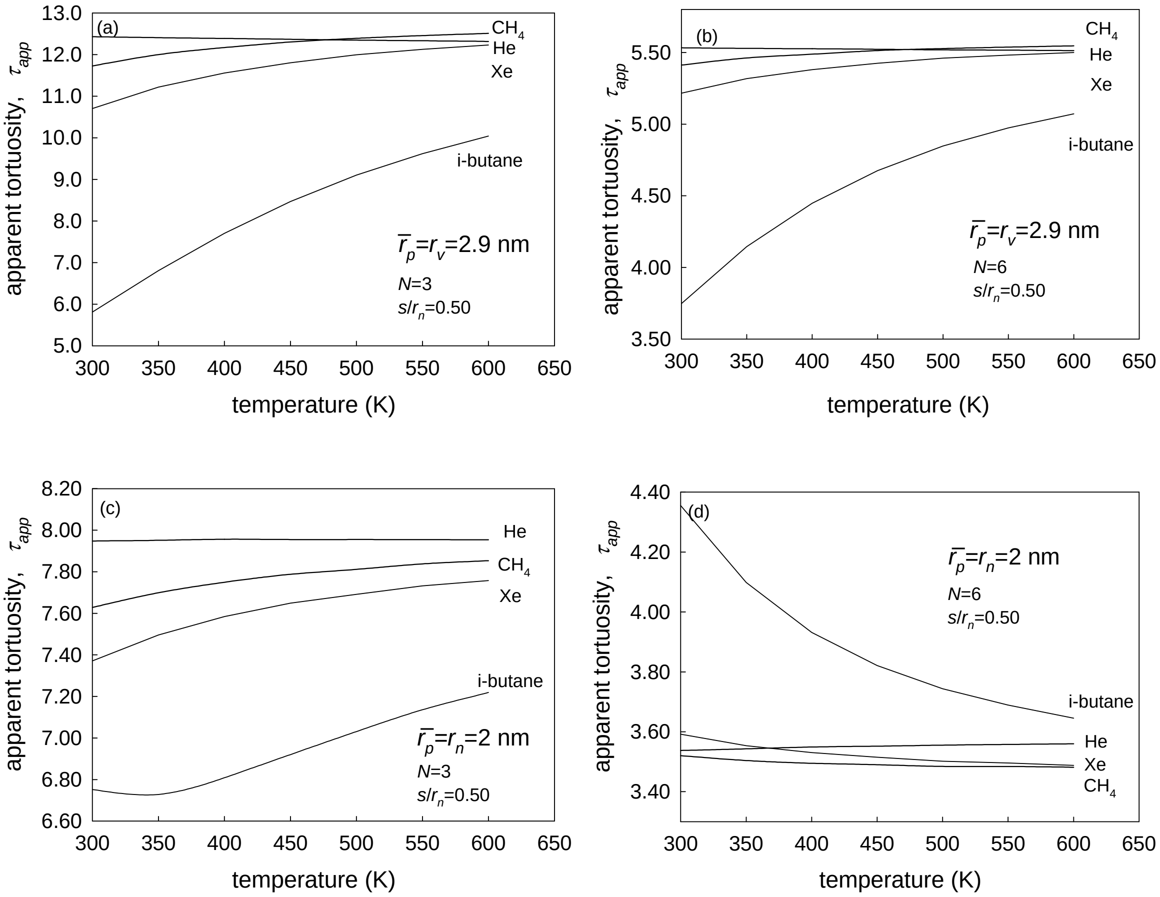

Figure 6.16 Variation of apparent tortuosity with temperature for different gases in the low-pressure region, using representative pore radius r_v and different coordination numbers, (a) N=3 and (b) N=6, and using representative pore radius r_n and different coordination numbers, (c) N=3 and (d) N=6. Based on the Oscillator model in a consolidated porous silica medium with infinite thick walls, following a Rayleigh pore number distribution, with r_n=2 nm and s/r_n=0.50.

Figure 6.18 depicts the variation of tortuosity with relative standard deviation, s/r_n, for several gases, in a mesoporous silica material having a Rayleigh pore number distribution, with r_n = 2 nm and T = 300 K.

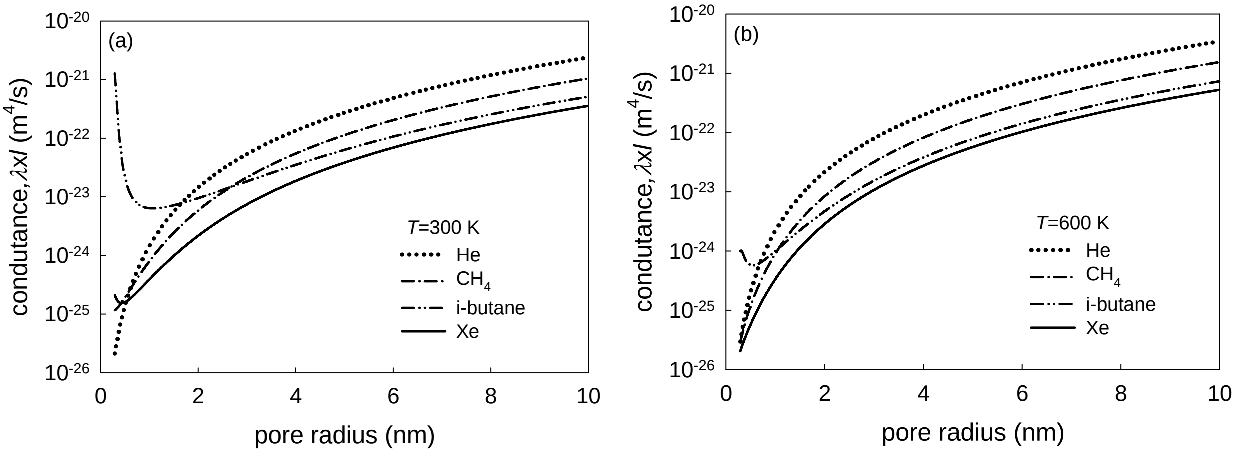

Figure 6.17 Variation in conductance (as λl) with pore radius for different gases, at (a) 300 K, and (b) 600 K.

As shown in Figures 6.18(a) and (b) at $N = 3$, the apparent tortuosity based on r_v increases significantly with increase in s/r_n for all gases except the most strongly adsorbing one (i-butane). The steep increase for the less adsorbing gases (He, CH_4 and Xe) is due to the increased short circuiting with increase in s/r_n, due to the increase in conductance with pore size for these gases (Figure 6.17(a)), combined with the increase in $D_o(\bar{r}_p)K(\bar{r}_p)$ resulting from increase in r_v with increase in s/r_n. However, for i-C_4H_{10} the short circuiting effect is weak due to the high conductance of small pores, evident from Figure 6.17(a), and as a result the tortuosity varies only slightly from the uniform network value of 5.4. Similar behaviour is observed when the representative pore radius is taken to be r_n (2 nm) and the coordination number is 3, as seen in Figure 6.18(c); however, in this case the tortuosity increase for the less adsorbing gases is smaller than in Figure 6.18(a), because $D_o(\bar{r}_p)K(\bar{r}_p)$ remains constant with increase in s/r_n. On the other hand the tortuosity shows a stronger increase for i-C_4H_{10}, because $D_o(\bar{r}_p)K(\bar{r}_p)$ remains constant while the short circuiting by larger pores increases (i.e. λ_e decreases) with increase in s/r_n. Figure 6.18(d) shows that for a larger connectivity of $N = 6$, for which the short circuiting effects are weaker, the value of λ_e initially increases, before decreasing as s/r_n increases. On the other hand for i-C_4H_{10} the short circuiting effect dominates and λ_e decreases, leading to increase in tortuosity with increase in s/r_n (albeit more weakly than for $N = 3$). As discussed above, such diverse tortuosity behaviors are mainly caused by the different dependence of $D_o(\bar{r}_p)K(\bar{r}_p)$ and effective conductance (λ_e) on coordination number.

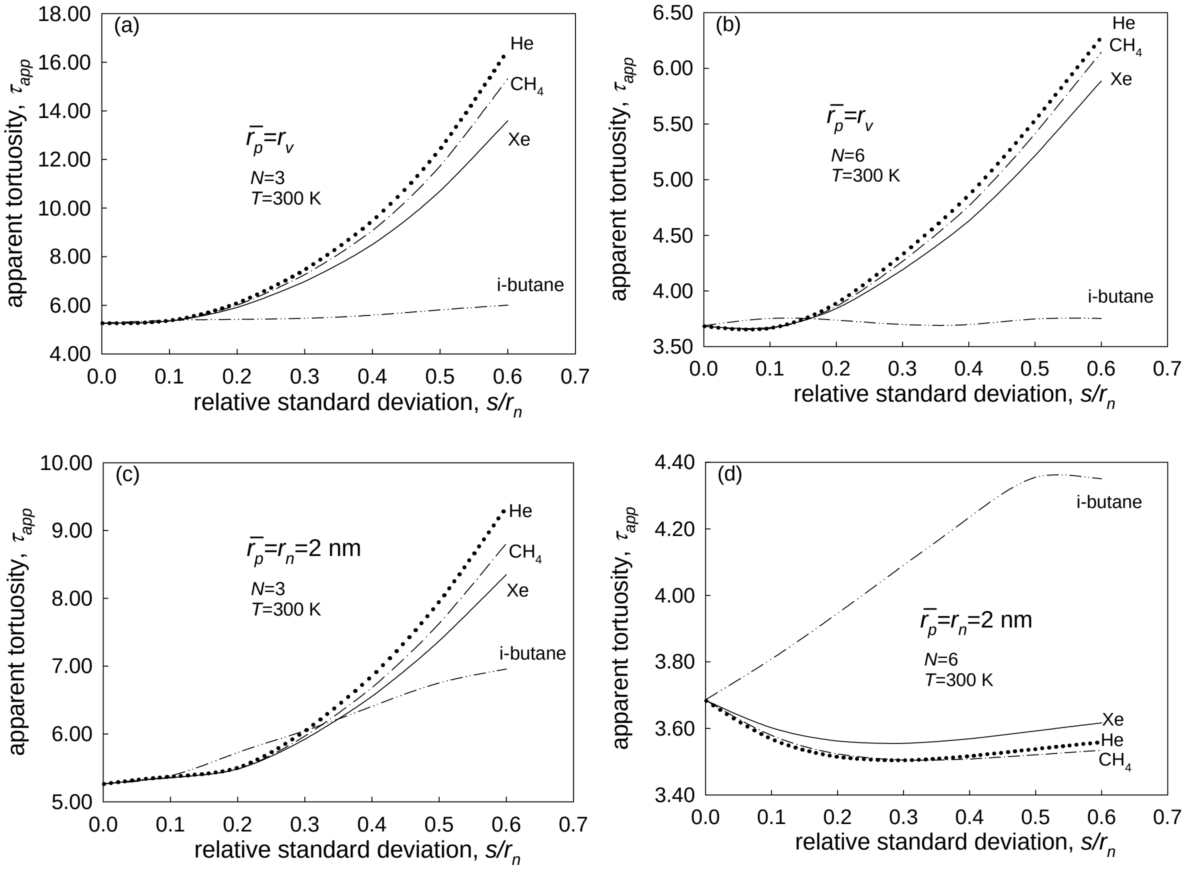

Figure 6.18 Variation of tortuosity with relative standard deviation for different gases in the low pressure region, using representative pore radius r_v, and coordination number (a) N=3 and (b) N=6, and using representative pore radius r_n, and coordination number (c) N=3 and (d) N=6. based on the Oscillator model in a consolidated porous silica material with infinite thick pore walls following a Rayleigh pore number distribution with r_n=2 nm.

In summary, the apparent tortuosity of a nonuniform mesoporous network is not only determined by the properties of porous medium but also significantly affected by the diffusing fluid and choice of representative pore radius.

6.5 Conclusion

We have demonstrated here that the tortuosity of a porous material, as obtained from experimental transport data, depends on the choice of the representative pore size at which the model-based diffusivity is evaluated. Interpretation of the data of Reyes et al. [35] for the diffusion of various gases in Shell silica spheres, using different representative pore sizes and models with EMT, indicates that the fitted coordination numbers obtained using EMT are relatively independent of the representative pore radius for all the models. This suggests that the coordination number in the EMT is a more robust parameter than the apparent tortuosity based on arbitrary representative pore size, in modelling of transport in disordered nanoporous materials. The coordination number obtained by the classical Knudsen model is 2.92, which is slightly low given the high porosity of this consolidated material (68 %). On the other hand, the coordination numbers fitted using the corrected Knudsen and Oscillator models are 3.24 and 4.00 respectively, of which the latter is more in line with expectation, suggesting that the transport mechanism is more accurately represented by the Oscillator model. However, at the large pore size of this silica (7.4 nm mean pore radius), the differences between the models are small.

The effective medium theory approach has been used to investigate the dependence of the apparent tortuosity on operating conditions and pore network characteristics for macroporous and mesoporous materials in different flow regimes. In the slip flow regime for a macroporous network, the apparent tortuosity is highly affected by the pore network structure and operating conditions (temperature, pressure and gas species), and displays different tortuosity limits for Knudsen diffusion and viscous flow in nonuniform networks. Besides, the dependence of tortuosity on temperature is also highly affected by the network coordination number and choice of representative pore radius at which the pore diffusivity is evaluated.

The tortuosity can increase, decrease or remain almost constant with change in temperature, due to the changes in short circuiting effects of the more conducting pores with changes in coordination number. In general, for large representative pore radius and low coordination number, the tortuosity tends to be higher in the viscous limit than in the Knudsen limit. Similar behaviour is found for mesoporous consolidated silica materials, where the tortuosity dependence on temperature is highly determined by the pore network, representative pore radius and gas species, and is governed by the different temperature dependence of $D_o(\overline{r}_p)K(\overline{r}_p))$ and the effective conductance (λ_e). In general more strongly adsorbed gases tend to show lower tortuosity at low coordination number and temperature. These complex effects are largely overlooked by experimentalists, as it is common to fit a temperature and species independent tortuosity. Nevertheless, while the effective medium theory approach is successful in interpreting the tortuosity, we note here that the assumption of cylindrical pore shape and a network of uniform connectivity are clearly idealistic, and deviations from the theory may be ascribed to the inaccuracies of such assumptions. It is pertinent here to recall Aris' observation that "when models are made of the configuration of the pore structure the tortuosity can be related to some other geometrical parameter but in general it is a fudge factor of greater or less sophistication" [53]. It may be argued that to some extent the effective medium approach reduces the level of “fudge”, as it incorporates the effect of process conditions not otherwise addressed by purely geometrical considerations in the case of pure component systems.

6.6 Nomenclature

D_a	apparent diffusivity in pore, based on a combination of Knudsen and viscous diffusivities, m^{-2} s^{-1}
D_a^c	apparent diffusivity in pore, based on a combination of corrected Knudsen and viscous diffusivities in a pore, m^{-2} s^{-1}
D_a^{osc}	apparent diffusivity in a pore based on the Oscillator model, m^{-2} s^{-1}
D_e	effective diffusivity, m^{-2} s^{-1}
D_{Kn}	Knudsen diffusivity, m^{-2} s^{-1}
D_{Kn}^c	corrected Knudsen diffusivity in pore, m^{-2} s^{-1}
D_o	diffusivity in pore, m^{-2} s^{-1}
D_{osc}	Oscillator model diffusivity pore, m^{-2} s^{-1}
D_{vis}	viscous contribution to diffusivity in pore, m^{-2} s^{-1}
D_{vis}^c	corrected viscous contribution to diffusivity in pore, m^{-2} s^{-1}
$\bar{D}_a$	apparent diffusivity based on mean pore radius, m^{-2} s^{-1}
f_{N}	pore number distribution, 1/nm
f_{V}	pore volume distribution, cm^{-3} nm^{-1} g^{-1}
$F_h(x,y,z;w)$	Hypergeometric function
$g(x)$	local diffusion factor
J	molar flux, mol^{-1}s m^{-2}
k_B	Boltzmann constant, J K^{-1}
K	equilibrium constant in a pore
l	pore length, nm
m	molecular mass, kg
M	molecular molar weight, g/mol
N	pore coordination number
p_r	radial momentum, kg.m/s
p_θ	angular momentum, kg.m^2/s
$\bar{P}$	mean pressure in the pore, Pa
r_s	geometrical pore radius, nm
r_c	corrected pore radius, nm
r_{cl}	upper radial position of the trajectory, nm
r_{co}	lower radial position of the trajectory, nm
r_o	minimum pore radius in the pore size distribution, nm

r_v	representative pore radius based on the peak of pore volume distribution, nm
r_n	representative pore radius based on peak of pore number distribution, nm
r_{osc}	pore radius for Oscillator model, nm
$\bar{r}_n$	representative pore radius based on number average, nm
$\bar{r}_p$	representative pore radius, nm
$\bar{r}_v$	$2V_p/S_g$, nm
R_g	ideal gas constant, J.K^{-1}.mol^{-1}
s	standard deviation of the pore size distribution, nm
S_g	pore surface area, m^2/g
T	temperature, K
V_p	pore volume, cm^3/g
x	aspect ratio, r_p/l
z	coordinate in the transport direction

Greek letters

β	$1/k_BT$, J^{-1}
ΔP	pressure difference, Pa
ε	porosity
ε_{ff}	LJ fluid-fluid potential well depth, J
ε_{fs}	LJ fluid-solid potential well depth, J
ε_{ss}	LJ solid-solid potential well depth, J
η	viscosity of the fluid, Pa.s
λ	conductance, m^3/s
λ_e	effective conductance, m^3/s
ρ	skeletal density, g/cm^3
ρ_v	atom volume density, 1/nm^3
σ_{ff}	LJ fluid-fluid collision diameter, nm
σ_{fs}	LJ fluid-solid collision diameter, nm
σ_{ss}	LJ solid-solid collision diameter, nm
τ_{app}	apparent tortuosity
ϕ_{fs}	LJ fluid-solid potential, J

6.7 References

[1] D. Zhao, J. Feng, Q. Huo, N. Melosh, G.H. Fredrickson, B.F. Chmelka, G.D. Stucky, Triblock copolymer syntheses of mesoporous silica with periodic 50 to 300 angstrom pores, Science, 279 (1998) 548-552.

[2] J.C. Diniz da Costa, G.Q. Lu, V. Rudolph, Y.S. Lin, Novel molecular sieve silica (MSS) membranes: characterisation and permeation of single-step and two-step sol-gel membranes, J. Membr. Sci., 198 (2002) 9-21.

[3] D. Grosso, F. Cagnol, G.J.A.A. Soler-Illia, E.L. Crepaldi, H. Amenitsch, A. Brunet-Bruneau, A. Bourgeois, C. Sanchez, Fundamentals of mesostructuring through evaporation induced self assembly, Adv. Funct. Mater., 14 (2004) 309-322.

[4] Y. Dai, J.R. Johnson, O. Karvan, D.S. Sholl, W.J. Koros, Ultem®/ZIF-8 mixed matrix hollow fiber membranes for CO_2/N_2 separations, J. Membr. Sci., 401-402 (2012) 76-82.

[5] M. Yoshimune, T. Yamamoto, M. Nakaiwa, K. Haraya, Preparation of highly mesoporous carbon membranes via a sol–gel process using resorcinol and formaldehyde, Carbon, 46 (2008) 1031-1036.

[6] T. Yoshioka, E. Nakanishi, T. Tsuru, M. Asaeda, Experimental studies of gas permeation through microporous silica membranes, AIChE J., 47 (2004) 2052-2063.

[7] S. Higgins, W. DeSisto, D.M. Ruthven, Diffusive transport through mesoporous silica membranes, Micropor. Mesopor. Mat., 117 (2009) 268-277.

[8] R. Krishna, J.M. van Baten, An investigation of the characteristics of Maxwell-Stefan diffusivities of binary mixtures in silica nanopores, Chem. Eng. Sci., 64 (2009) 870-882.

[9] S.K. Bhatia, Capillary network models for transport in packed beds: considerations of pore aspect ratio, Chem. Eng. Commun., 154 (1996) 183-202.

[10] S. Hwang, Fundamentals of membrane transport, Korean J. Chem. Eng., 28 (2011) 1-15.

[11] J. Xiao, J. Wei, Diffusion mechanism of hydrocarbons in zeolites-I. Theory, Chem. Eng. Sci., 47 (1992) 1123-1141.

[12] V.N. Burganos, S.V. Sotirchos, Diffusion in pore networks: effective medium theory and smooth field approximation, AIChE J., 33 (1987) 1678-1689.

[13] E.A. Mason, A.P. Malinauskas, R.B. Evans III, Flow and diffusion of gases in porous media, J. Chem. Phys., 46 (1967) 3199-3216.

[14] P.D. Deepak, S.K. Bhatia, Transport in capillary network models of porous media: theory and simulation, Chem. Eng. Sci., 49 (1994) 245-257.

[15] S.K. Bhatia, M.R. Bonilla, D. Nicholson, Molecular transport in nanopores: a theoretical perspective, Phys. Chem. Chem. Phys., 13 (2011) 15350-15383.

[16] S.K. Bhatia, Stochastic theory of transport in inhomogeneous media, Chem. Eng. Sci., 41 (1986) 1311-1324.

[17] X. Gao, M.R. Bonilla, J.C. Diniz da Costa, S.K. Bhatia, The transport of gases in a mesoporous γ-alumina supported membrane, J. Membr. Sci., 428 (2013) 357-370.

[18] S.K. Bhatia, D. Nicholson, Comments on" Diffusion in a mesoporous silica membrane: Validity of the Knudsen diffusion model" by Ruthven, D.M., et al., Chem. Eng. Sci. 64 (2009) 3201-3203, Chem. Eng. Sci., 65 (2010) 4519-4520.

[19] S.K. Bhatia, D. Nicholson, Some pitfalls in the use of the Knudsen equation in modelling diffusion in nanoporous materials, Chem. Eng. Sci., 66 (2010) 284-293.

[20] F.T. De Bruijn, L. Sun, Ž. Olujić, P.J. Jansens, F. Kapteijn, Influence of the support layer on the flux limitation in pervaporation, J. Membr. Sci., 223 (2003) 141-156.

[21] R. Krishna, J.A. Wesselingh, The Maxwell-Stefan approach to mass transfer, Chem. Eng. Sci., 52 (1997) 861-911.

[22] P.J.A.M. Kerkhof, M.A.M. Geboers, Analysis and extension of the theory of multicomponent fluid diffusion, Chem. Eng. Sci., 60 (2005) 3129-3167.

[23] H. Preising, D. Enke, Relations between texture and transport properties in the primary pore system of catalyst supports, Colloids Surface A, 300 (2007) 21-29.

[24] A. Markovic, D. Stoltenberg, D. Enke, E.U. Schlünder, A. Seidel-Morgenstern, Gas permeation through porous glass membranes: Part I. Mesoporous glasses-effect of pore diameter and surface properties, J. Membr. Sci., 336 (2009) 17-31.

[25] J. Kärger, F. Stallmach, S. Vasenkov, Structure-mobility relations of molecular diffusion in nanoporous materials, Magn. Reson. Imaging, 21 (2003) 185-191.

[26] P. Uchytil, O. Schramm, A. Seidel-Morgenstern, Influence of the transport direction on gas permeation in two-layer ceramic membranes, J. Membr. Sci., 170 (2000) 215-224.

[27] S.K. Bhatia, Modeling pure gas permeation in nanoporous materials and membranes, Langmuir, 26 (2010) 8373-8385.

[28] X. Gao, M.R. Bonilla, J.C. Diniz da Costa, S.K. Bhatia, The transport of gases in macroporous α-alumina supports, J. Membr. Sci., 409-410 (2012) 24-33.

[29] X. Gao, J.C. Diniz da Costa, S.K. Bhatia, The transport of gases in a supported mesoporous silica membrane, J. Membr. Sci., 438 (2013) 90-104.

[30] D.M. Ruthven, Response to comments from S.K. Bhatia and D. Nicholson, Chem. Eng. Sci., 65 (2010) 4521-4522.

[31] O.G. Jepps, S.K. Bhatia, D.J. Searles, Wall mediated transport in confined spaces: exact theory for low density, Phys. Rev. Lett., 91 (2003) 126102.

[32] J. Xiao, J. Wei, Diffusion mechanism of hydrocarbons in zeolites-II. Analysis of experimental observations, Chem. Eng. Sci., 47 (1992) 1143-1159.

[33] S.K. Bhatia, O. Jepps, D. Nicholson, Tractable molecular theory of transport of Lennard-Jones fluids in nanopores, J. Chem. Phys., 120 (2004) 4472-4485.

[34] M.R. Bonilla, S.K. Bhatia, The low-density diffusion coefficient of soft-sphere fluids in nanopores: accurate correlations from exact theory and criteria for applicability of the Knudsen model, J. Membr. Sci., 382 (2011) 339-349.

[35] S.C. Reyes, J.H. Sinfelt, G.J. DeMartin, R.H. Ernst, E. Iglesia, Frequency modulation methods for diffusion and adsorption measurements in porous solids, J. Phys. Chem. B, 101 (1997) 614-622.

[36] E. Iglesia, S.L. Soled, J.E. Baumgartner, S.C. Reyes, Synthesis and catalytic properties of eggshell cobalt catalysts for the Fischer-Tropsch synthesis, J. Catal., 153 (1995) 108-122.

[37] K. Vollmayr, W. Kob, K. Binder, Cooling-rate effects in amorphous silica: A computer-simulation study, Phys. Rev. B, 54 (1996) 15808-15827.

[38] W. Tsang, Chemical kinetic data base for combustion chemistry Part 4. Isobutane J. Phys. Chem. Ref. Data, 19 (1990) 1-68.

[39] D.A. McQuarrie, Statistical Mechanics, University Science Books, Sausalito, 2000.

[40] S.Z. Qiao, S.K. Bhatia, Diffusion of *n*-decane in mesoporous MCM-41 silicas, Micropor. Mesopor. Mat., 86 (2005) 112-123.

[41] C.N. Satterfield, Mass transfer in heterogeneous catalysis, MIT Press, Cambridge, 1970.

[42] S. Yashonath, P. Santikary, Diffusion of sorbates in zeolites Y and A: Novel dependence on sorbate size and strength of sorbate-zeolite interaction, J. Phys. Chem., 98 (1994) 6368-6376.

[43] P. Demontis, G.B. Suffritti, E.S. Fois, S. Quartieri, Molecular dynamics studies on zeolites. 6. Temperature dependence of diffusion of methane in silicalite, J. Phys. Chem., 96 (1992) 1482-1490.

[44] X. Zhang, W. Wang, G. Jiang, a potential model for interaction between the Lennard Jones cylindrical wall and fluid molecules, Fluid Phase Equilibr., 218 (2004) 239-246.

[45] A.V.A. Kumar, H. Jobic, S.K. Bhatia, Quantum effects on adsorption and diffusion of hydrogen and deuterium in microporous materials, J. Phys. Chem. B, 110 (2006) 16666-16671.

[46] S. Kirkpatrick, Classical transport in disordered media: Scaling and effective-medium theories, Phys. Rev. Lett., 27 (1971) 1722-1725.

[47] S. Ismadji, S.K. Bhatia, Investigation of network connectivity in activated carbons by liquid phase adsorption, Langmuir, 16 (2000) 9303-9313.

[48] N.A. Seaton, Determination of the connectivity of porous solids from nitrogen sorption measurements, Chem. Eng. Sci., 46 (1992) 1895-1909.

[49] S.P. Friedman, N.A. Seaton, A corrected tortuosity factor for the network calculation of diffusion coefficients, Chem. Eng. Sci., 50 (1995) 897-900.

[50] H. Liu, L. Zhang, N.A. Seaton, Determination of the connectivity of porous solids from nitrogen sorption measurements—II. Generalisation, Chem. Eng. Sci., 47 (1992) 4393-4404.

[51] L. Zhang, N.A. Seaton, Prediction of the effective diffusivity in pore networks close to a percolation threshold, AIChE J., 38 (1992) 1816-1824.

[52] A. Imhof, D.J. Pine, Ordered macroporous materials by emulsion templating, Nature, 389 (1997) 948-950.

[53] R. Aris, The mathematical theory of diffusion and reaction in permeable catalysts. Vol. I: The theory of the steady state, Clarendon, Oxford, (1975).

Chapter 7: Adsorption and transport of gases in a supported microporous silica membrane

In this chapter, we investigate gas adsorption and transport in a disordered microporous silica membrane having mean pore diameter 1.5 nm, coated on a porous tubular asymmetric support. The adsorption isotherms are found to be Langmuirian, with equilibrium constants that are accurately predicted for nonpolar gases, considering Lennard-Jones (LJ) interactions with a single layer of oxygen atoms on the pore surface. For the polar gas, CO_2, the hydroxyls groups on the pore walls strongly increase the affinity with the pore wall s, and a superposition of the LJ potential and an empirically represented electrostatic interaction is found to be adequate in correlating the Langmuirian equilibrium constant.

The gas transport in the microporous silica layer is investigated using effective medium theory, with single pore transport represented by combination of pore mouth and internal pore diffusion resistances. Good agreement is observed for all the gases using different coordination numbers, indicating that the essential features of the transport in the silica micropores are captured in the approach. It is found that the overall transport resistance is dominated by the pore mouth barrier; however, the internal diffusion resistance in the relatively smaller pores is significant, especially for weakly adsorbed gases at higher temperature. In addition, the dependence of the pore mouth barrier coefficient on temperature and diffusing species are in good agreement with predictions of transition-state theory, with larger more strongly adsorbed molecules having higher activation energy. The proposed methodology is validated against experiment by comparison of the predicted flux for different gases in the supported membrane at various feed pressures in the low pressure range of 2-4 bar, using the parameters obtained at 2 bar.

7.1 Introduction

The modeling of fluid transport in narrow pores and confined spaces has attracted considerable interest among scientists and engineers for over a century [1-3], due to its importance to a variety of conventional applications in adsorptive gas separation as well as in heterogeneous catalysis and electrochemical process. Interest in the subject has considerably increased in the last two decades, as a consequence of the development of a vast array of novel disordered and ordered nanoporous materials [4-9], having potential for use in these as well as in emerging applications such as in gas storage [10], molecular sieve membranes [11], drug delivery [12] and biosensors [13], all of which involve the movement of fluids through highly confined spaces. The established and most popular approach to modeling gas transport in narrow pores is that of Knudsen [1], dating back to the first decade of the 20th century, and neglects the effects of dispersive fluid-solid interactions on the diffusion. While this simplification is justified for the relatively large tubes of 33-145 µm used by

Knudsen in his original experimental verification [1], its applicability to nanoscale pores where the density profile is highly nonuniform has been questioned [2, 14-16]. However, due to its simplicity and ease of use, the Knudsen model and its analogues have been routinely applied to gas transport in narrow pore materials [17-20].

In actual practice, the intermolecular interaction is non-negligible, and must be considered when the mean free path in the pressure range of interest (generally in the region of a few bars) is not much larger than the pore size. In the case of macropores the effect of intermolecular interactions may be included by means of an additive viscous contribution [21-23]. The most popular method based on this principle is the Dusty Gas Model (DGM) of Mason and coworkers, which arbitrarily divides the total flux vector into a wall-affected diffusive and a hydrodynamic non-segregative contribution [24]. When adsorption is negligible, the pore wall-affected diffusion is often represented by the Knudsen model, which is supplemented by a surface diffusion contribution when adsorption is significant in mesopores [25]. Consequently, the intrinsic characteristics of the Knudsen model are inherited in this approach, and the confirmation of the diffusion model still largely relies on the correlation of diffusion data with $\sqrt{T/M}$, where M is molecular weight, as predicted by the Knudsen model [26].

Although it lacks a firm molecular basis, due to its simplicity the DGM approach is commonly employed to explore the diffusion mechanism in newly-synthesized materials; this is generally done by empirically correlating experimental data using a representative pore size, while determining a structure-related parameter such as tortuosity [27]. Use of a single pore size is a key deficiency of this method as the pore size distribution (PSD) has significant influence on the transport, especially for materials with several nanometers. Another weakness inherent to the Knudsen model is the disregard of the dispersive solid-fluid interaction arising from the presence of the wall; the dispersive van der Waals interaction, for example via the Lennard-Jones (LJ) interaction model, dramatically decreases the diffusivity by reducing the travel time between successive collisions [15]. As a result of the dispersive interaction, the fluid density in the pore is non-uniform, and significantly differs from that in the bulk, and is strongly dependent on the pore radius and gas species as well as temperature [2, 28].

Traditionally, the tortuosity factor is incorporated as an effective parameter and assumed to be exclusively determined by the properties of the porous medium. However, it has been theoretically and experimentally shown that in nanoscale pores the apparent tortuosity is influenced by operating conditions such as temperature, pressure and gas species [14, 15, 21, 29]. All errors arising from the neglect of such dependence are therefore lumped within the fitted tortuosity, masking errors related to the transport model itself [21]. Consequently, unambiguous confirmation of the validity of the Knudsen diffusion in nanosized pores, to which the Knudsen model is frequently employed, is not possible by simple correlation. Indeed, it has been extensively demonstrated that while the DGM can empirically correlate experimental data, extremely high tortuosities are often obtained for mesoporous materials when the Knudsen model is utilized [17, 30-32]. This is mainly due to the omission of adsorption effects and overprediction of the diffusivity by the Knudsen equation, and to a lesser extent due to the disregard of the pore size distribution when a single representative pore size is used [14, 15, 33].

For small pore sizes, approaching the micropore scale, it is frequently assumed that the gas molecules adsorb on the pore walls, and migrate on the pore surface as an adsorbed species. In this spirit, models comprising surface diffusion and Knudsen flow in parallel have been formulated in order to provide stronger temperature dependence and yield an acceptable tortuosity [18, 34]; however, such models often lead to tortuosities that increase greatly for weakly adsorbed gases [18]. Substantial work has been devoted to develop rigorous theories based on molecular principles to account for the effect of dispersive solid-fluid interaction on the transport [35-39], or otherwise indirectly consider the effect of interactions by using measured pure component diffusivities in mixture transport models [25]. However, most interpretations of experimental data largely rely on arbitrary modification of the Knudsen equation by introducing an Arrhenius-type factor to better capture the effect of temperature in micropores [17, 19, 35]. The most widely used model following this approach, originally used for hydrocarbons and known as the gas translation (GT) theory, is that of Xiao and Wei [35]. Later, the theory was extended to any adsorptive gases by Yoshioka et al [19] by considering the effective diffusion length instead of the actual pore size. However, the original derivation of the GT theory is semi-empirical, as the estimation of the activation energy based on the difference of LJ potential energy between the pore channel and intersection lacks a firm molecular basis [39]. For instance, in a silica pore of 3 nm, the diffusivity of CH_4 as modeled by the GT approach falls in the Knudsen regime due to the low apparent activation energy for such a small molecule [35], which is contradicted by molecular dynamics (MD) simulations [2, 35, 40].

Considerable success has been accomplished recently in this laboratory, through the development of a statistical mechanical theory of transport in nanopores, aided by the finding from MD simulations that the nonuniform equilibrium density profile of the fluid is essentially preserved during the transport [41]. The new model, termed as ‘Oscillator model’, considers the dispersive solid-fluid interaction before collision, and the adsorption effect is represented through the canonical energy distribution in the pore [36], overcoming the limitations of the Knudsen approach. Not only has the new theory been extensively validated against MD simulations [36, 39], but it has also been successfully used to interpret experimental data [14-16, 29]. Indeed, comparison of the Knudsen and Oscillator model diffusivities with those from MD simulations for silica pores shows that the Knudsen equation significantly overpredicts the diffusivity for methane at 450 K by 30% even for a pore diameter of 10 nm, indicating the importance of considering the effect of van der Waals forces on pore diffusion even when the molecule/channel size ratio is less than 5% [39].

However, in disordered materials narrow pore necks may affect the rate of entry of molecules in the pores, although this has little impact on the equilibrium constant, which principally depends on the size of the pore body. This effect may be considered by means of transition-state theory (TST) [37, 42-44], and the GT theory of Xiao and Wei [35] may be envisioned in this light. While the pore mouth resistance may be expected to control in materials with very narrow molecularly sized entries, in systems with transitional pores the internal pore diffusion may also have significant resistance. Membrane transport models involving such dual resistances have yet to be formulated, but may be derived by combining the Oscillator model with a TST-based pore mouth resistance model to investigate the transport in such disordered microporous materials.

Another significant impediment in the application of any diffusion theory to microporous or mesoporous materials is the complexity of the pore network, including the pore connectivity, and the presence of a pore size distribution as well as surface roughness. This is particularly challenging for the investigation of supported membranes, in which the system comprises a thin selective top layer and a mesoporous interlayer coated on a macroporous substrate. Not only must the pore size distribution of each layer be considered, but also the aspect ratio and pore shape are of importance. Effective medium theory (EMT) provides the necessary machinery for resolving such issues, and has been used to derive fundamental insights into transport in disordered nanoporous materials [14-16, 21, 29]. In this method, a nonuniform pore network with a distribution of conductance is replaced by a uniform one in which each conductance is assigned an effective value. This allows explicit modeling of network-related effects, thereby permitting more direct verification of transport models. In our previous work [16] employing this technique we have demonstrated that the transport in a mesoporous silica membrane having pores of mean size 3.7 nm is not well represented by the Knudsen model due to overestimation of the diffusivity and neglect of adsorption effects, and that the Oscillator model, which accounts for these factors provides a more accurate result. Following the line of our previous work [16], here we further develop this approach to include also a pore mouth resistance, and investigate the diffusion for a microporous supported silica membrane, having a mean pore diameter of 1.5 nm, coated on an asymmetric alumina support, while also considering the pore size distribution for each layer. The results permit an understanding of the mechanism of fluid transport in the microporous silica layer, and demonstrate the importance of considering both the dispersive interaction and pore mouth restriction effect in the silica micropores.

7.2 Materials characterization and experiments

7.2.1 Asymmetric support

As described in a recent publication from this laboratory [29], the asymmetric support was synthesized by dip-coating a diluted γ-alumina solution (2 wt.% from Sigma-Aldrich) on the outer surface of a tubular α-alumina substrate (Australia Chemtech Trading & Service Company), having an inner radius of 4.25 mm and an outer radius of 6.38 mm, and a length of 8.20 cm. Since the pores of the substrate and interlayer are mainly made of interstitial spaces between crystal particles by sintering at high temperature, the particle size has significant influence on the size of the pores. Therefore, before conducting any adsorption-based characterization, the pore network structure of the substrate and interlayer was investigated by Scanning Electron Microscopy (SEM), revealing the mean particle sizes to be 3 μm and 50 nm, respectively, with an interlayer thickness of around 2 μm. A more accurate pore size distribution of the substrate was determined by mercury porosimetry (Micromeritics, IV 9500), indicating a mean pore radius of 250 nm. The pore size distribution (PSD) of the interlayer was assumed to be represented by that of the agglomerated γ-alumina powder, which was analyzed by N_2 adsorption at 77 K, using a Micromeritics ASAP2020 volumetric analyser. The adsorption isotherm was interpreted by nonlinear density function theory (NLDFT) assuming cylindrical pore with an oxide surface, and the indicative pore radius was around 5.2 nm. The details of characterization of the pore network for the substrate and the interlayer can be found in our recent work [29].

7.2.2 Microporous silica preparation

The microporous silica membrane used in this work was prepared by the sol-gel process, which comprises two steps: (1) preparation of the colloidal sol, and (2) sol-coating on the pre-synthesized asymmetric support and firing [45, 46]. In the first step, the silica colloidal-sol solution was prepared by co-polymerization of methyltriethoxysilane (TEOS) and tetraethylorthosilane (MTES) using a two-step acid-catalyst process. A mixture of 13.50 mL MTES, 29.0 mL TEOS, 39.20 mL EtOH, 3.90 mL H_2O and 0.06 mL diluted HCl (2.30 mol/L) was refluxed at 333 K for 90 min with stirring at 200 rpm, then additional 4.54 mL water and 4.80 mL HCl were added to the solution, resulting in the final molar ratio of 0.35: 0.65: 3.8: 5.1: 0.056. In the second step, the asymmetric support was dipped into the solution, using a dip-coating apparatus, at a rate of 10 cm/min. The support was immersed for 1 min, and subsequently oven-dried at 333 K for 2 h. The membrane was then heated at 1 K/min to 673 K, and calcined at this temperature for 30 min. To ensure full coverage of the membrane, ten layers were coated on the asymmetric support, and each layer was processed under the same conditions as the first layer.

After completing the coating on the support, the remained sol was dried and ground using a mortar and pestle, then calcined under the same conditions as the membrane, and subsequently characterized for its pore size distribution using N_2 adsorption at 77 K, as above. This PSD was used to represent the pore network of the membrane layer. The calcination condition was designed based on the decomposition curve of the uncalcined xerogels by thermogravimetric analysis (TGA), which indicated that the selected temperature was sufficient to remove the nonhydrolyzed groups. As seen in Figure 7.1(a), at temperatures less than 373 K the weight loss was mainly caused by the vaporization of water; after 523 K, the nonhydrolyzed groups began to decompose and condensation reactions continued to occur in the silica matrix until 1073 K. The complete disappearance of the nonhydrolyzed groups in the membrane layer is further demonstrated by Fourier transform infrared spectroscopy (FTIR) for the calcined and uncalcined xerogels in Figure 7.1(b), in which the characteristic band of CH_3 and CH_2 in TEOS and MTES (around 2900 cm^{-1}) was completely eliminated after calcination, indicating the absence of any organic residuals in the silica sample [16].

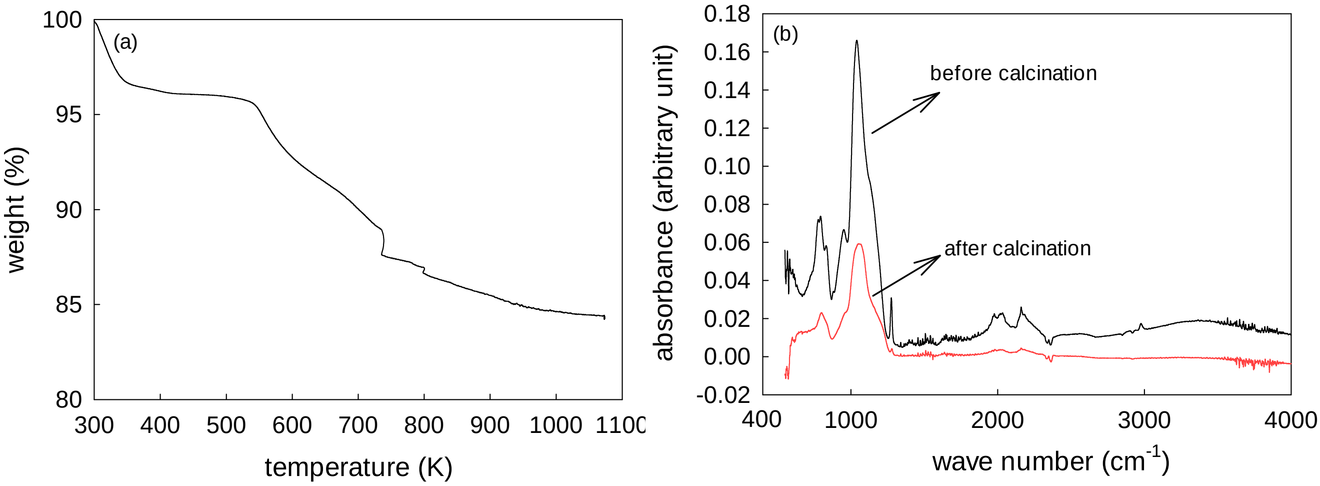

Figure 7.1 (a) Decomposition curve of the uncalcined silica xerogel by thermogravimetric analysis (TGA), and (b) Fourier transform infrared spectroscopy (FTIR) of the calcined and uncalcined silica xerogel.

7.2.3 Microporous silica characterization

7.2.3.1 Low temperature nitrogen adsorption

The pore size distribution of the calcined silica powder was obtained using density function theory (DFT) based interpretation of the N_2 isotherm at 77 K, assuming cylindrical pores with an oxide surface. As illustrated in Figure 7.2, the majority of the pores are within the micropore range, and the corresponding pore volume (V_p) and surface area (S_g) are 0.18 cm^3/g and 528.34 m^2/g, respectively. The pore structure of the silica powder was further examined by High Resolution Transmission Electron Microscopy (HRTEM) at 200kV (JEOL 2010). The TEM micrograph, shown in Figure 7.3, indicates a pore diameter of around 1.5 nm, in accord with the average pore diameter evaluated based on the pore volume to surface area ratio, given by $4V_p/S_g$. The skeletal density of the silica powder extracted from Helium pycnometry was 2.00 g/cm^3, which is slightly smaller than the theoretical density of around 2.30 g/cm^3 [47], suggesting the presence of pores inaccessible to He inside the amorphous silica. The accessible porosity of the powder can be determined by

$$\varepsilon = \frac{V_p \rho}{1 + V_p \rho} \tag{7.1}$$

in which ρ is the true density from Helium pycnometry. Following eqn. (7.1), the accessible porosity of the microporous silica is estimated to be 0.26.

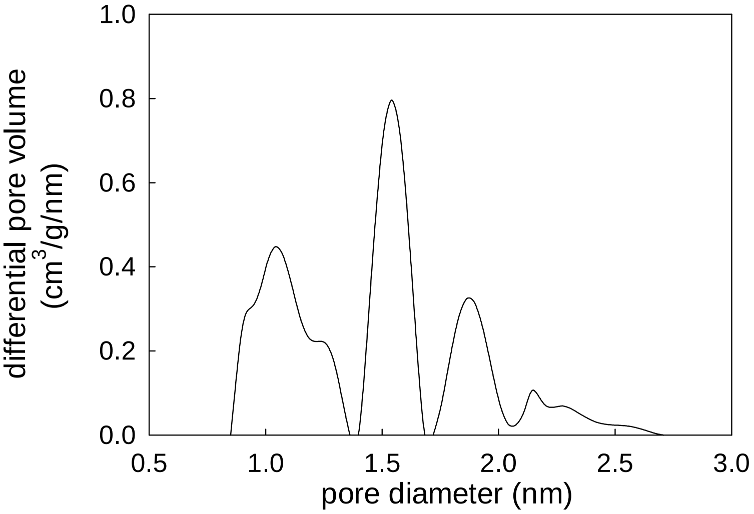

Figure 7.2 Pore size distribution of the calcined silica gel, obtained using nonlinear density function theory (NLDFT) interpretation of N_2 adsorption data at 77 K.

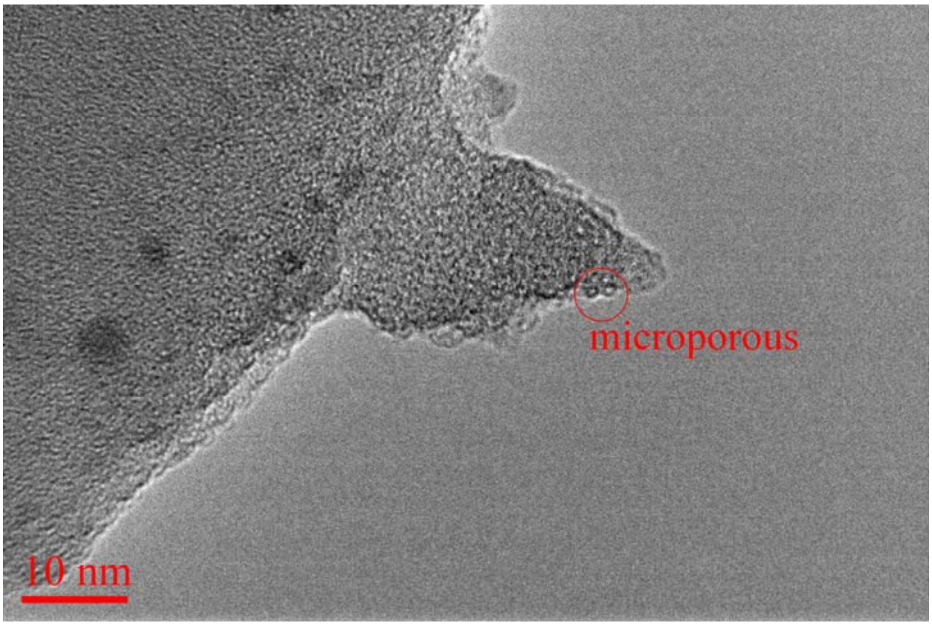

Figure 7.3 High Resolution Transmission electron microscopy (HRTEM) image of the microporous silica powder.

7.2.3.2 Thermogravimetry

Characterization of hydroxyl groups on the pore surface was performed on the calcined silica powder by thermogravimetry, following the method of Markovic et al [17]. The surface density of the hydroxyl groups can be estimated by

$$N_{OH} = \frac{2000\, w_m}{3 S_g} \tag{7.2}$$

in which w_m is the percentage weight loss and N_{OH} is the concentration of hydroxyl groups in nm^{-2}. By excluding the physically adsorbed water on the silica surface, the measured weight loss of the sample during temperature increase (473-1273 K) is 5.9%, which yields a surface density of the hydroxyl groups of approximately 7.5 nm^{-2}. This value is significantly larger than the density of hydroxyl groups in the silica glass membrane synthesised by Markovic [18], for which a low value of 3.8 nm^{-2} was obtained. More polar hydroxyl groups on the surface increase the adsorption affinity for polar gases due to the additional dipolar interactions besides the dispersive force [17].

7.2.3.3 Scanning electron microscopy

Knowledge of the dimension of each layer is crucial to modeling of the transport in the supported membrane, which requires consideration of the resistance for each layer. For the macroporous substrate, the measurement can be directly conducted; for the interlayer and membrane layer, the thicknesses are only several microns and have to be estimated by electron microscope imaging. Considering that the boundaries between the interlayer and membrane layer are ill-defined and irregular, the distance cannot be precisely evaluated. As illustrated in Figure 7.4, the average membrane thickness is about 5 μm after excluding the interlayer thickness; this thickness was used in the analysis of the diffusion in the silica layer.

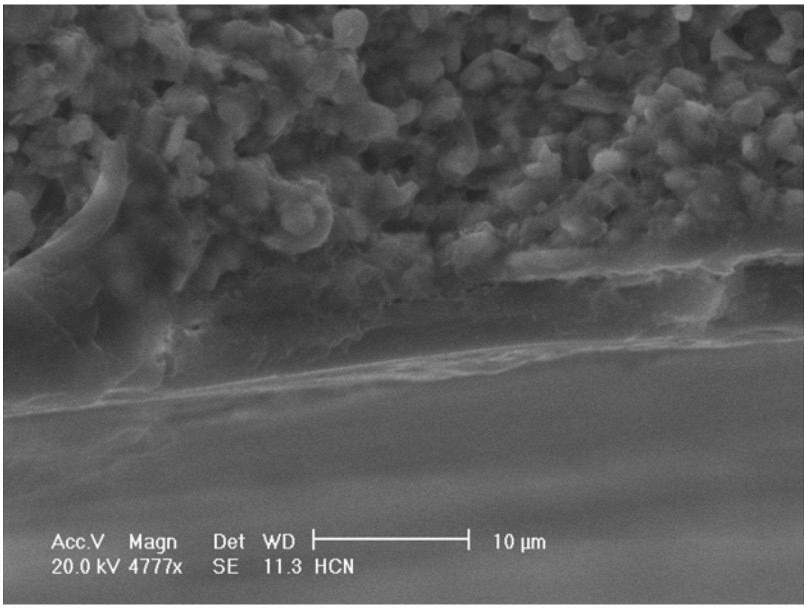

Figure 7.4 Scanning electron microscopy (SEM) image of the cross section of the supported microporous silica membrane.

7.2.4 Adsorption equilibria of single gases

Adsorption measurements were carried out using a high pressure volumetric analyzer (Micromeritics HPVA-100) based on a classical volumetric method operated in the static mode. Since the free space was measured by He, the isotherms of five other pure gases (H_2, CH_4, Ar, N_2 and CO_2) were examined for three different temperatures (303, 333 and 363 K). In the experiments, the silica powder was degassed at 573 K for several hours and subsequently exposed to the adsorptive gas at different pressures up to 30 bar, with temperature control provided by a circulating water bath. The classical Langmuir isotherm was applied to describe the equilibrium relationship between the adsorbed amount, *q*, and the pressure in the gas phase, *P*, following

$$q = q_{\max} \frac{K_l P}{1 + K_l P} \tag{7.3}$$

in which K_l (Pa^{-1}) is the Langmuir adsorption constant and $q_{\max}$ (mol/g) is the total saturation capacity of the adsorbate. In this model $q_{\max}$ is only determined by the gas species, while K_l is dependent on temperature and gas species, following the thermodynamic relation, $K_l = (e^{\Delta S^o / R_g})(e^{-\Delta H^o / R_g T}) / P^o$, where ΔH^o is the adsorption enthalpy change, ΔS^o is the entropy change relative to the standard pressure P^o (101325 Pa). The isosteric heat of adsorption, Q ($= -\Delta H^o$), can be readily evaluated from the slope of the linear correlation between ln K_l and $1/T$.

7.2.5 Single gas permeation measurements

The transport in the macroporous substrate and mesoporous interlayer has been independently examined in our previous work by conducting two sets of single gas (H_2, He, CH_4, N_2, Ar, and CO_2) permeation experiments [29]. It was confirmed that the transport in the macroporous substrate at low pressure can be adequately represented by a combination of Knudsen diffusion and viscous flow. The corresponding transport for the interlayer can be adequately modeled by any of three different diffusion models; these are the classical Knudsen model, a modified Knudsen model corrected for finite molecular size, and the Oscillator model. To explore the diffusion mechanism in the microporous silica layer, single gas permeation experiments were carried out at temperatures between 303 K and 573 K for several feed pressures (1.98, 2.98 and 3.98 bar). It is noted that the permeation experiments was carried out from high temperature (300 ºC) to low temperature (30 ºC) to avoid any water blockage effect. Details of the experimental setup and procedure can be found in our previous work [16].

In the analysis to follow, to distinguish the driving force for each layer, the outlet pressure (equal to the atmosphere pressure) is labeled as P_o, and the feed pressure is represented by P_F. Further, the interfacial pressure between the interlayer and substrate is given as P_1, while the interfacial pressure between the interlayer and membrane layer is represented by P_2. To distinguish the flow rates and structural parameters for the substrate, interlayer and membrane layers, the subscripts s, c and m are used for these layers, respectively.

7.3 Transport models

7.3.1 Transport in a single pore

The main aim of this work is to investigate the transport of gases in a disordered microporous silica membrane having nonuniform pore size, and to validate the use of Oscillator model at this scale. The diffusivity in a single pore is strongly related to its pore size, and therefore the pore size must be precisely defined. As described in Figure 7.5, there are several ways to determine a pore radius, depending on the diffusion model used.

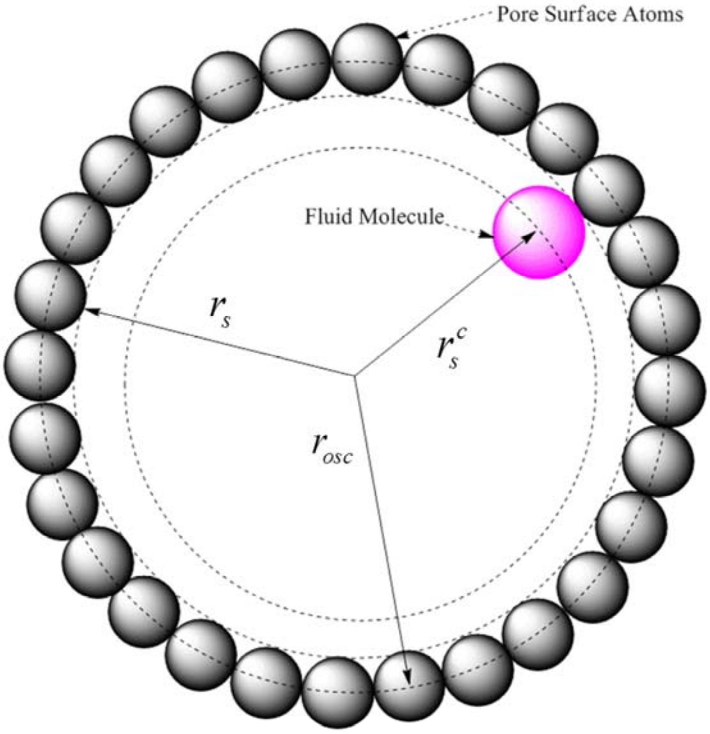

Figure 7.5 Illustration of different pore radii used in the classical Knudsen model (r_s), the corrected Knudsen model (r_s^c), and the Oscillator model (r_{osc}).

7.3.1.1 Classical slip flow model

In the classical slip flow model, the transport coefficient (also referred to as diffusivity) is evaluated based on the geometrical pore radius (r_s), defined as the distance between the centerline of the pore and the surface of the walls, with the fluid molecular size considered negligible in comparison. The slip diffusivity is a combination of Knudsen (D_{Kn}) and viscous contributions, which are respectively represented as

$$D_{Kn} = 97 r_s \sqrt{\frac{T}{M}} \tag{7.4}$$

$$D_{vis} = \frac{\bar{P} r_s^2}{8\eta} \tag{7.5}$$

in which T represents temperature in K, M is the fluid molecular weight (g/mol), $\bar{P}$ is the average pressure (Pa) and η is fluid viscosity (Pa.s). In the Knudsen and viscous flow models the density profile along the radial coordinate is considered uniform and identical to the bulk, thus the equilibrium constant is unity for slip flow (K=1). Since the pores in the alumina substrate are macroporous, the slip flow model with an apparent diffusivity $(D_o^a = D_{Kn} + D_{vis})$ can be safely used for the transport in the substrate, with exclusion effects due to finite fluid molecular size neglected [21]. Since the interlayer has a large mesopore size of about 11.5 nm diameter, while providing only about 10% of the transport resistance in the asymmetric support, the transport in this layer may also be satisfactorily represented by the classical slip flow model, as demonstrated in our recent work [29].

7.3.1.2 Oscillator model

In the microporous silica layer, the dispersive interaction between fluid and pore wall must be considered, and the Oscillator model is applied to evaluate the diffusivity and equilibrium constant. However, the pore radius used in the Oscillator model differs from the ones used in the Knudsen and viscous flow equations, and is taken as the half center-to-center pore diameter for the surface atoms on the walls, r_{osc}, following:

$$r_{osc} = r_s + \sigma_{ss}/2 \tag{7.6}$$

where σ_{ss} is the LJ solid-solid collision diameter of the atoms on the pore walls.

In the Oscillator model [36], the diffusivity of a LJ fluid under diffuse reflection in a cylindrical pore is given as

$$D_{osc}(r_{osc}) = \frac{2}{\pi m Q}\int_0^\infty e^{-\beta\varphi_{sf}(r)}dr\int_0^\infty e^{-\frac{\beta p_r^2}{2m}}dp_r\int_0^\infty e^{-\frac{\beta p_\theta^2}{2mr^2}}dp_\theta\int_{r_{co(r,p_r,p_\theta)}}^{r_{cl}(r,p_r,p_\theta)}\frac{dr'}{p_r(r',r,p_r,p_\theta)} \tag{7.7}$$

Here

$$p_r(r? r, p_r, p_\theta) = \left(2m\left[\varphi_{sf}(r) - \varphi_{sf}(r')\right] + \frac{p_\theta^2}{r^2}\left[1 - \left(\frac{r}{r'}\right)^2\right] + p_r^2(r)\right)^{1/2} \tag{7.8}$$

is the radial momentum when it is at radial position, r', given that it has radial momentum p_r at r, p_θ is the angular momentum, and r_{c1} and r_{c0} represent the radial bounds of the trajectory of the molecular particle between two continuous reflections, obtained from the solution of $p_r(r',r,p_r,p_\theta) = 0$. Further, m is the molecular mass, $\beta = (k_B T)^{-1}$ and $Q = \int_0^\infty re^{-\beta\varphi_{sf}(r)}dr$.

$\varphi_{sf}(r)$ is the one dimensional solid-fluid interaction potential profile, and strongly depends on the structure and composition of the pore wall. Here, we consider a smooth cylindrical pore composed of a single layer wall with randomly distributed Lennard Jones sites. Integration of the LJ solid-fluid interaction over the pore surface yields the hypergeometric potential [48],

$$\frac{\varphi_{sf}(r)}{k_B} = \frac{4\pi^2 \varepsilon_{sf} \rho_s \sigma_{sf}^2}{k_B} \left\{ \frac{63 F_h(-4.5,-4.5,1;(r/r_{osc})^2)}{128 (r_{osc}/\sigma_{sf})^{10} \left[1-(r/r_{osc})^2\right]^{10}} - \frac{3 F_h(-1.5,-1.5,1;(r/r_{osc})^2)}{4 (r_{osc}/\sigma_{sf})^{4} \left[1-(r/r_{osc})^2\right]^{4}} \right\} \tag{7.9}$$

Here σ_{sf} is the LJ solid-fluid collision diameter, ε_{sf} is the LJ potential well depth, ρ_s is the pore wall surface site density (atoms per unit area) and $F_h(x, y, z; w)$ is the Hypergeometric function. In silicas, the interaction between the fluid and pore walls is often considered to be dominated by a surface layer of oxygen ions, and the LJ parameters for the solid are evaluated based on the results from Neimark et al. [49] as $\varepsilon_{ss}/k_B = 492.7$ K, $\sigma_{ss} = 0.28$ nm, with $\rho_s = 10.47$ nm^{-2}. The Lorentz-Berthelot mixing rules are applied to estimate the solid-fluid LJ parameters ε_{sf}/k_B and σ_{sf}, using the LJ parameters of the gases listed in Table 7.1.

Table 7.1 Fluid-fluid Lennard-Jones parameters used in the Oscillator model

Parameters	H_2	He	CH_4	N_2	Ar	CO_2
σ_{ff} (nm)	0.2915	0.2551	0.381	0.3572	0.341	0.3472
ε_{ff}/k_B (K)	38.0	10.22	148.2	93.98	120.0	221.9

The low density equilibrium constant (K) for a given pore radius is readily obtained from

$$K(r_{osc}) = \frac{2}{r_{osc}^2} \int_0^{r_{osc}} e^{-\varphi_{sf}(r)/k_B T} r dr \tag{7.10}$$

7.3.1.3 Transition-State theory

The above diffusion models are developed for a long cylindrical pore with a uniform surface. However, in practice, pores in nanoporous materials are irregular, having constricted pore necks or mouths, which can significantly reduce the pore accessibility. As illustrated in Figure 7.6, although a nonuniform pore may be idealised as an equivalent perfect cylindrical pore with radius based on the pore volume to surface area ratio, this does not consider the presence of a pore mouth resistance effect in the irregular pore, arising from the narrow entry; thus the total transport resistance may be underpredicted in the model pore.

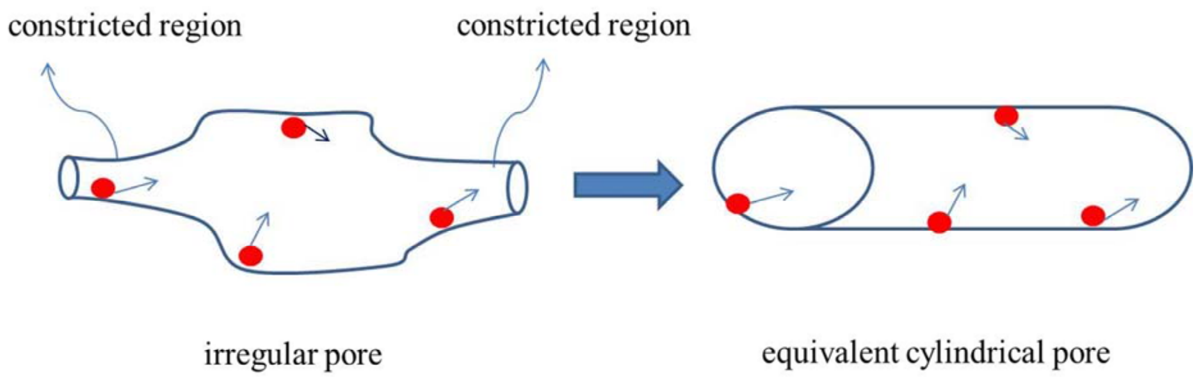

Figure 7.6 Schematic drawing of a representative irregular pore and its equivalent cylindrical pore representation.

To address this restriction effect in micropores, we employ the TST [37, 42-44] to estimate the crossing frequency for pore mouth penetration by adsorbate molecules. According to the TST, the hopping time, τ, from a pore body A to a neighboring pore body B is generally given as

$$\tau_{A\rightarrow B} = \frac{1}{k_{A\rightarrow B}} \tag{7.11}$$

where the crossing frequency $k_{A\rightarrow B}$ follows

$$k_{A\rightarrow B} = \kappa\sqrt{\frac{k_B T}{2\pi m}}\,\frac{\int_{DS} e^{-\beta\varphi(\mathbf{r})} d^2\mathbf{r}}{\int_{Pore\ A} e^{-\beta\varphi(\mathbf{r})} d^3\mathbf{r}} \tag{7.12}$$

Here κ is a transmission probability, m is the molecular mass, $\varphi(\mathbf{r})$ is the potential energy of the diffusing molecule, and the integral in the numerator is taken over the dividing surface (DS) between the two pores. The above integrals over the diving surface and the pore volume combine to provide the Gibbs free energy barrier (ΔG_c) of the hopping process through the pore mouth, and the above equation can be expressed as

$$k_{A\rightarrow B} = \kappa\sqrt{\frac{k_B T}{2\pi m}}\,\frac{e^{-\beta\Delta G_c} A_{DS}}{V_A} \tag{7.13}$$

in which A_{DS} is the area of the dividing surface and V_A is volume of pore body A, and ΔG_c is the free energy barrier for a molecule in pore body A to cross the dividing surface DS. Expressing the Gibbs free barrier in terms of the corresponding enthalpy and entropy changes, the crossing frequency $k_{A\to B}$ is readily obtained as

$$k_{A\to B} = \kappa\sqrt{\frac{k_B T}{2\pi m}}\frac{A_{DS}}{V_{DP}}e^{-\Delta H_c/R_g T}e^{\Delta S_c/R_g} \tag{7.14}$$

in which ΔH_c and $-\Delta S_c$ are the enthalpic and entropic barriers for a fluid molecule migrating from the pore body A through the pore mouth to pore body B. We note that ΔH_c is determined by the interaction between the fluid and pore walls, and ΔS_c is predominantly related to the difference in degree of confinement of the fluid molecules between the dividing surface and the pore body A.

A pore mouth restriction-related diffusivity (D_{TST}) may be obtained as $D_{TST} = k_{A\to B}\zeta^2 / 6$ [42], where ζ is the centre-to-centre distance between neighbouring pores, and following the arguments of Nguyen and Bhatia [37, 43] and Nguyen et al. [44] is approximated as

$$D_{TST} = A_o\sqrt{\frac{T}{M}}e^{-E_a/RT} \tag{7.15}$$

Here E_a is the activation energy, given by the enthalpy barrier in eqn. (7.14), and is affected by the interaction between the fluid and pore walls. A_o is a constant related to the pore length, fluid molecular size and pore shape. In general ΔS_c varies only weakly with gas species in eqn. (7.14), so that A_o is nearly constant (i.e. only weakly dependent on the diffusing species).

Since the transport through the pore mouth and internal diffusion in the pore body occur in series, the pore mouth resistance based on the above model can be combined with the Oscillator theory of pore diffusion to represent the overall transport resistance in a single pore of arbitrary size. Suitable averaging over the pore size distribution, such as by effective medium theory [14-16, 21, 29], then provides the effective diffusivity in the pore structure.

7.3.2. Transport in pore networks

As discussed above, the presence of nonuniformity in disordered nanoporous materials is a key factor complicating the direct application of any diffusion model to experimental data. This is the case for the supported silica membrane. For instance, the asymmetric support comprises a macroporous substrate and mesoporous interlayer, and in both layers the pores are mainly formed by the space between crystal particles of different size. Consequently, both the support and interlayer are unconsolidated, and have pore lengths comparable to diameter. Thus, not only must the pore size distribution and connectivity be considered, but also the effect of finite aspect ratio (pore radius to length ratio) should be suitably addressed [50], as pore network and tortuosity models commonly assume essentially zero aspect ratio. However, the amorphous silica membrane layer is generally consolidated, as the pores are synthesized by molecular imprinting, and so the aspect ratio is small. However, for microporous membranes the pore entry resistance due to pore mouth constrictions in the disordered silica may be important, and should be accurately incorporated in the transport model for the microporous silica layer.

Effective medium theory provides the tools for describing these complexities in disordered porous materials by replacing the nonuniform network with a uniform one in which all of the pores offer the same conductance to the flow. Following the line of our previous work, we extend this methodology to interpret the transport in the microporous silica layer deposited on an identical asymmetric support by considering the pore diffusion resistance and that of the pore mouth based on the combination of Oscillator model and transition-state theory. The application of effective medium theory for the macroporous substrate and the mesoporous interlayer, while using the classical slip flow model in each layer, has been demonstrated elsewhere [16], so only the derivation of EMT for the microporous silica layer is given in the current work.

For a cylindrical pore of radius r_p, the conductance, λ can be expressed in terms of the pore mouth and Oscillator model transport coefficients, following the series resistance model

$$\frac{1}{\lambda}=\frac{l}{\pi r_p^2 K_{osc}(r_p)}\left(\frac{1}{D_{osc}(r_p)}+\frac{1}{D_{TST}}\right) \tag{7.16}$$

It is assumed that local equilibrium prevails at the nanoscale so that the pseudo-pressure drop in the pores is independent of the size of the pores. The effective medium conductance, λ_e, is estimated by the solution to [51]

$$\left\langle \frac{(\lambda-\lambda_e)}{(\lambda+(N/2-1)\lambda_e)} \right\rangle = 0 \tag{7.17}$$

where N is the coordination number or pore connectivity, *i.e.*, the average number of pores meeting at each node, and $\langle\cdot\rangle$ represents a number average over the pores. For the effective medium, the pore flux is obtained as

$$j(r_p) = \frac{\lambda_e l}{\pi r_p^2 R_g T}\left(-\frac{dP}{dz}\right) \tag{7.18}$$

Considering that the pseudo-bulk pressure is uniform in the pores of the membrane, and the silica material is consolidated, the net flux in the equivalent uniform network is obtained by integration of eqn. (7.18) over the pore volume distribution, to yield [16, 52, 53]

$$J_m = \frac{\varepsilon_m \lambda_e < l_m^2 >}{3\pi < r_p^2 l_m > R_g T}\left(\frac{N_m - 1}{N_m + 1}\right)\left(-\frac{dP}{dz}\right) \tag{7.19}$$

At steady state, the flow rate (F) in the tubular supported membrane is constant, and integration of eqn. (7.19) over the radial coordinate of the silica membrane layer provides [16]

$$F_m = \frac{2\varepsilon_m R_o \lambda_e L < l_m^2 >}{3 z_m < r_p^2 l_m > R_g T}\left(\frac{N_m - 1}{N_m + 1}\right)(-\Delta P) \tag{7.20}$$

where R_o is the outer radius of the tube (R_o = 6.38 mm), and z_m is the membrane thickness and L is the tube length (L= 8.20 cm). It is to be noted that the predicted flow rate in the silica layer is independent of l, as the effective conductance, λ_e, is inversely proportional to l, so that the l factor cancels out in eqn. (7.20). The derivation of the EMT expressions for the flow rate for the substrate (F_s) and the interlayer (F_c) can be found elsewhere [29].

The estimation of the theoretical flow rate requires solving the flow rate relationships for the three layers:

$$F_s\left(P_F, P_1, N_s, l_s\right) = F_c\left(P_1, P_2, N_c, l_c\right) = F_m\left(P_2, P_o, N_m, E_a, l_m\right) \tag{7.21}$$

to determine the interfacial pressures, P_1 and P_2. For the asymmetric support used here the structural parameters of the unconsolidated structure of the support (N_s, l_s) and interlayer (N_c, l_c) have been determined in our prior study [29], and have the values $N_s = N_c = 12$, l_s = 300 nm, l_c = 5 nm. These values have been used in the present work in conjunction with effective medium theory to determine the pore structure and activation energy in the microporous silica layer.

7.4 Results and discussion

7.4.1 Adsorption isotherms

Figures 7.7 (a-e) depict the experimental isotherms (symbols) and the Langmuir model fittings (solid lines) for various adsorptive gases (H_2, CH_4, N_2, Ar and CO_2) in the microporous silica powder at temperatures of 303, 333 and 363 K, with the adsorption capacity $\overline{q}_{\max}$ assumed constant for each gas at the different temperatures.

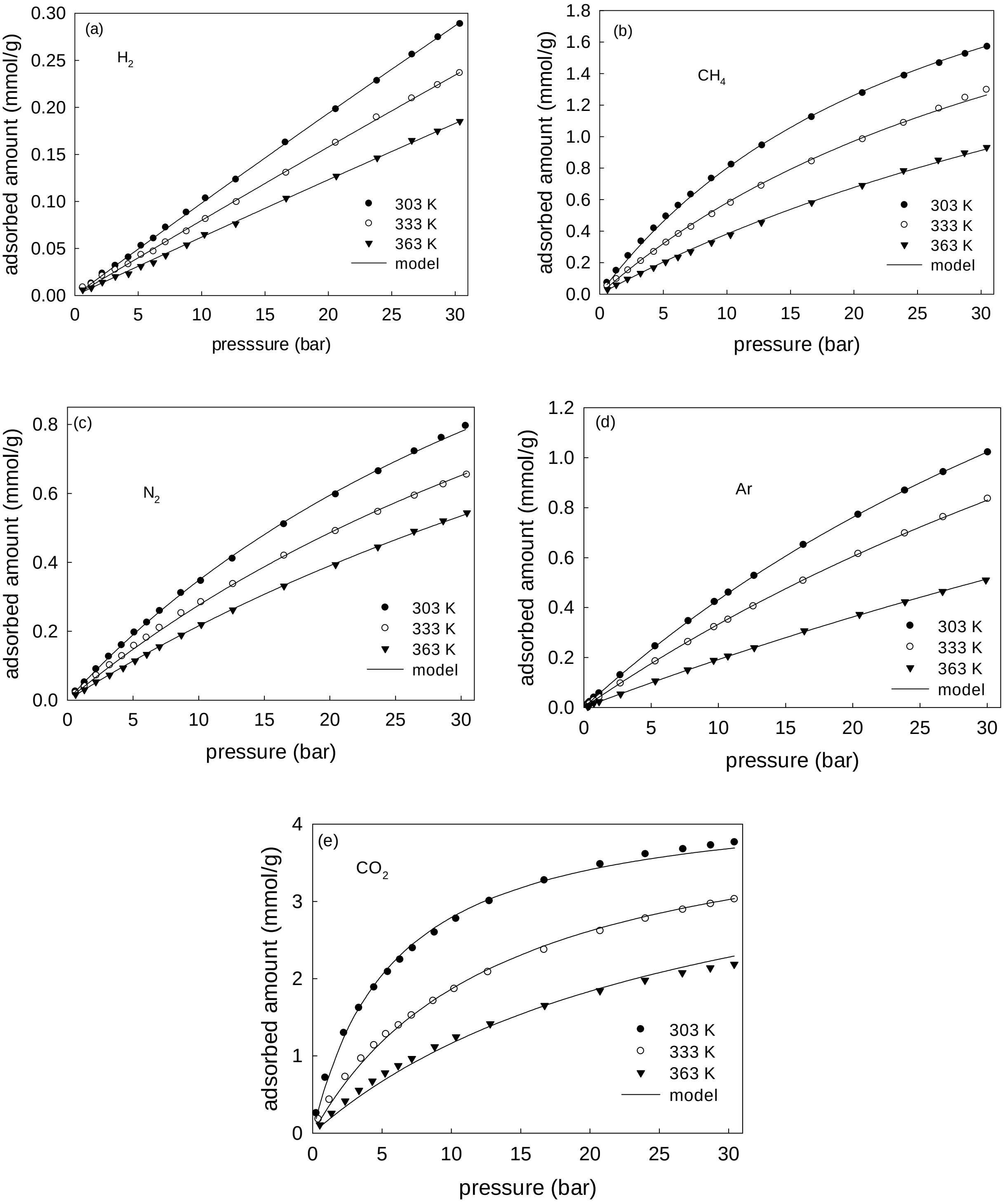

Figure 7.7 Measured adsorption equilibria of (a) H_2, (b) CH_4, (c) N_2, (d) Ar and (e) CO_2 at three temperatures (T =303, 333 and 363 K) fitted with Langmuir isotherm model (parameters given in Table 7.2). Fitted isotherms are represented by lines, and experimental data by symbols.

It is evident that CO_2 is the most strongly adsorbed molecule, followed by CH_4, while N_2 and Ar have comparatively weaker adsorption, and H_2 is the least-adsorbed gas. For H_2 the isotherms are nearly linear and show very small amount of adsorption in the given condition. It is also seen that the Langmuir model (solid lines) provides good agreement with the experimental data for all the gases, over the pressure range below 30 bar, suggesting that fluid-solid interaction dominates under these conditions. The fitted Langmuir parameters, obtained using eqn. (7.3) with a nonlinear fitting method, are listed in Table 7.2. We note that the obtained Langmuir parameters in eqn. (7.3) are only the 'apparent' values ($\overline{q}_{\max}$ and $\overline{K}_l$) for the silica material due to the nonuniformity of the pore structure. Since $\overline{K}_l$ is related to the adsorption affinity, it is meaningful to compare the values between the gases. It is evident that $\overline{K}_l$ tends to be lower at higher temperature for all the gases as is to be expected, and follows the pattern CO_2>CH_4>N_2>Ar>H_2, which is consistent with the ordering of the adsorption affinities based on the isotherms discussed above. Further, the adsorption isosteric heat (Q), based on the linear fitting of the correlation between $\ln(\overline{K}_l)$ and $1/T$, is also given in the Table 7.2, and will be subsequently compared with the activation energy for the silica membrane layer obtained by effective medium theory in the next.

The equilibrium constant in eqn. (7.10) represents the ratio between the pore density and the bulk gas density at low density in a pore of radius r_{osc}. Averaging over the pore volume yields the effective low density equilibrium constant of the silica micropores

$$\overline{K} = \frac{1}{\int_0^\infty f_v(r_p)dr_p} \int_0^\infty K_{osc}(r_p) f_v(r_p) dr_p \tag{7.22}$$

which is related to the Langmuir constant K_l in eqn. (7.3) by

$$\overline{K} = \frac{\overline{K}_l R_g T \overline{q}_{\max}}{V_p} \tag{7.23}$$

Here $f_v(r_p)$ is the pore volume distribution of the micropores, to which the pore volume V_p is related by $V_p = \int_0^\infty f_v(r_p)dr_p$.

As discussed above, the equilibrium constant in a pore is dependent on the potential field, and therefore strongly influenced by the model for the pore walls. We therefore compared the predictions of eqs. (7.10) and (7.22) for the effective equilibrium constant using the potential energy model in eqn. (7.9), with that from eqn. (7.23) using the Langmuir adsorption constant of our microporous silica.

Table 7.2 Adsorption equilibrium parameters and isosteric heat for the gases on calcined silica powder at three different temperatures based on fit of eqn. (7.3)

Parameters	H_2			CH_4			N_2			Ar			CO_2		
	303 K	333 K	363 K	303 K	333 K	363 K	303 K	333 K	363 K	303 K	333 K	363 K	303 K	333 K	363 K
q_{max} (mol/g)	2.92×10^{-3}			3.00×10^{-3}			2.06×10^{-3}			3.26×10^{-3}			4.38×10^{-3}		
K_l (Pa^{-1})	3.57×10^{-8}	2.87×10^{-8}	2.21×10^{-8}	3.64×10^{-7}	2.39×10^{-7}	1.46×10^{-7}	2.03×10^{-7}	1.54×10^{-7}	1.17×10^{-7}	1.52×10^{-7}	1.14×10^{-7}	6.25×10^{-8}	1.76×10^{-6}	7.43×10^{-7}	3.61×10^{-7}
Q (kJ/mol)	7.27			13.85			8.38			13.36			24.14		

Figure 7.8 depicts the variation of ln($\bar{K}$) with 1000/*T* for the results based on the adsorption data (symbols) and the model predictions (solid lines) for the single layer pore wall structure. It is found that that the obtained order of the equilibrium constants, $CO_2 > CH_4 > N_2 \approx Ar > H_2$, agrees with the observed result. Further, it is evident that the predictions for the single layer wall model are in good agreement with experimental values for most of the gases (H_2, CH_4, N_2 and Ar), indicating the potential field is accurately represented by this model for the nonpolar gases. The disagreement for CO_2 in Figure 7.8 is largely caused by the high density (7.5 nm^{-2}) of hydroxyl group on the pore surface, which significantly increases fluid-solid interaction strength due to the associated electrostatic interactions [17]. To allow for this effect, an additional term, intended to empirically represent the Coulombic interactions, is superimposed with the single layer LJ interaction potential so as to permit matching of the experimental equilibrium constants for CO_2. We empirically represent the electrostatic interaction potential, $\chi_e(r)$, as

$$\chi_e(r) = \frac{B}{(r_{osc} - r)^2} \tag{7.24}$$

in which *B* ($K.nm^2$) is a fitting constant.

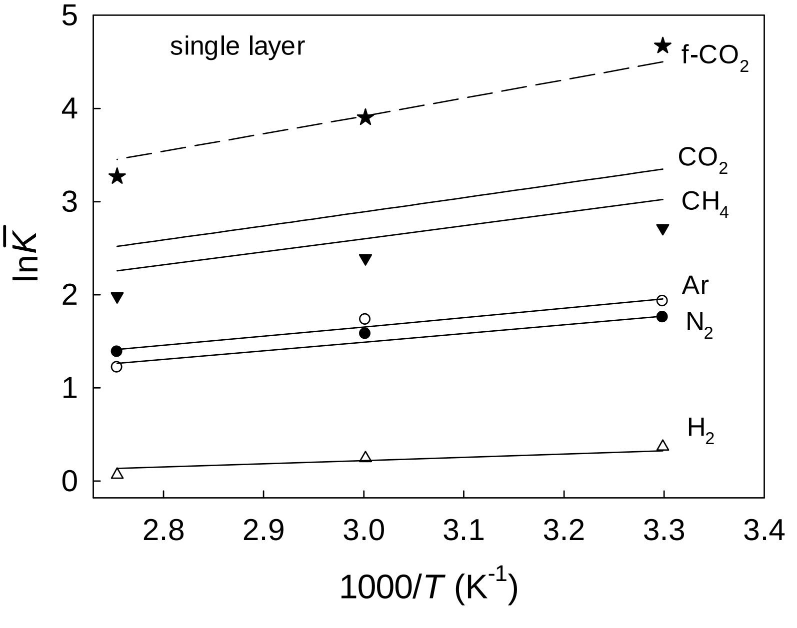

Figure 7.8 Comparison of the model prediction with experiment data for the variation of apparent equilibrium constant with temperature. The symbols represent the experimental apparent equilibrium constant from gas adsorption data, $\bar{K}$, based on eqn. (7.23), and the solid lines represent the predicted apparent equilibrium constant, $\bar{K}$, using eqn. (7.22). The dashed line is the fitted result of CO_2, after empirical addition of the electrostatic interaction with the wall following eqn. (7.22).

The above interaction term is additively combined with the right hand side of eqn. (7.9) to yield an effective fluid-solid interaction to predict the corresponding equilibrium constant and diffusivity for CO_2 in Oscillator model. As shown in Figure 7.8, the fitted result (dashed line) provides good agreement with the experimental data, and the obtained constant B has the value of -37.51 K.nm^2. The above results indicate that the gas species and temperature-dependent adsorption in the silica micropores is successfully captured by the canonical energy distribution in eqn. (7.10) and in the Oscillator model, while using the information on the pore size distribution.

In view of the above agreement, the standard silica LJ parameters of the single layer model given is Section 7.3.1.2 were employed in the Oscillator model to predict the diffusivity and adsorption effect for all the gases, with the added electrostatic interaction empirically modeled in eqn. (7.24) only used in the prediction for CO_2 in the silica membrane layer.

7.4.2 Application of effective medium theory

Given the complexity of the pore structure in each layer, we employed effective medium theory to investigate the transport in the supported microporous silica layer using the proposed theoretical description of gas diffusivity discussed above in eqn. (7.16). The advantage of this approach is that the entire pore size distribution for each layer is appropriately considered, rather using an arbitrary mean pore radius for empirical correlation. By utilizing the relationship between the macroscopic flow rate and the pore structure, following eqn. (7.20), the diffusion model can be directly validated, using the activation energy, E_a, and coefficient A_o in eqn. (7.15) as the only fitting parameters for any coordination number N_m.

With the classical slip flow applied in the macroporous substrate and the mesoporous interlayer, the above three-layer membrane model was fitted to the experimental flow rate data for various temperatures at a feed pressure at 1.98 bar using eqn. (7.21) to obtain the interfacial pressures between the layers, P_1 and P_2. Various coordination numbers lying between 3 and 6 were chosen, based on connectivity range for silica reported by Seaton [54]. All the coordination numbers work equally well in the fitting, and a relevant example of the obtained result is plotted in Figure 7.9(a) for N_m=6, with the experimental data representing by symbols and model results by solid lines. It is evident that the agreement between the experimental data and model results is excellent, suggesting that the transport in the silica micropores is adequately represented by the combination of Oscillator model and transition-state theory. The corresponding variation of interfacial pressure, P_1 and P_2, with temperature is depicted in Figures 7.9(b) and (c), respectively, showing strong gas dependence due to the adsorption effect as predicted in our earlier work [16].

It is seen that the interfacial pressures of the least adsorbed gases He and H_2, P_1 and P_2, decrease monotonically with increase in temperature, while for the intermediate adsorbed gases, N_2 and Ar, a milder decreasing tendency occurs. It is of interest that for the more strongly adsorbed gas (CH_4), the interfacial pressures increase up to about 350 K, and decrease mildly at higher temperature after passing through a weak maximum. However, for the strongest adsorbed gas, CO_2, the corresponding interfacial pressures monotonically increase over the given temperature range. Using these pressures, the pressure gradients for substrate, interlayer and membrane layers were examined for each gas at different temperature, and it was found that the pressure drop in both the substrate (P_F-P_1) and the interlayer (P_1-P_2) is very small, less than 5% of the total pressure difference, suggesting the resistance in the supported membrane is mainly provided by the silica membrane layer (> 95%)

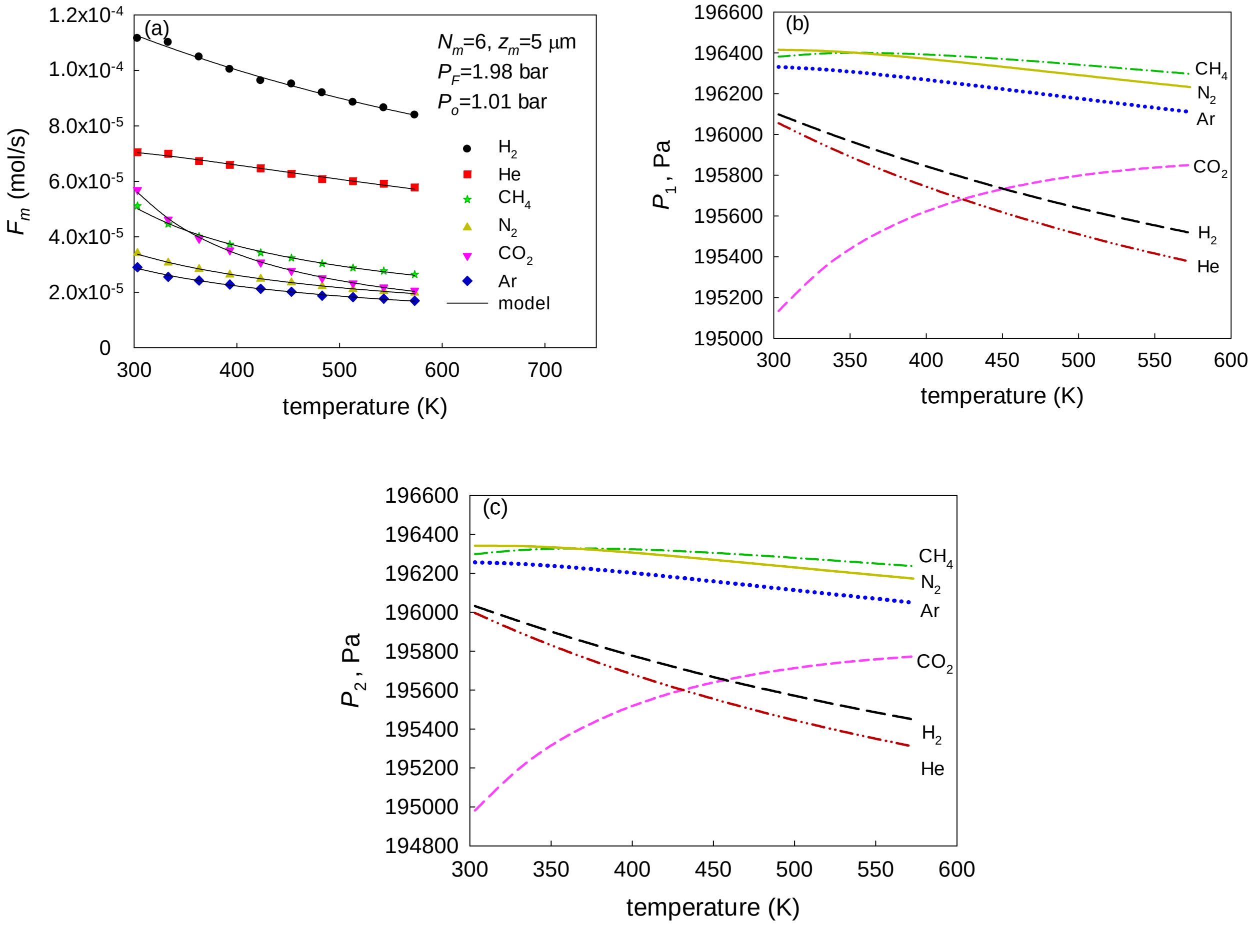

Figure 7.9 (a) Variation of flow rate, (b) interfacial pressure, P_1 and (c) P_2, with temperature at feed pressure P_F=1.98 bar based on eqn. (7.21), using the parameter values N_m=6, and z_m=5 μm. In (a) the symbols are the experimental data and the lines are the model results.

Following our earlier work [16], the relative importance of the individual diffusion resistance for each layer was also examined by comparison of the corresponding permeation data separately obtained for the substrate, the asymmetric support and the supported membrane, with the apparent permeance of each gas at different temperatures estimated using $\pi = J/(-\Delta P)$. Figures 7.10(a) and (b) depict the variation of the permeance with gas molecular size (taken as LJ size parameter), for the substrate and the asymmetric support based on the earlier experiments [16], and for the 3-layer composite membrane based on the data obtained here, for the lowest and highest experimental temperature (303 and 573 K), respectively. In estimating the flux based on the experimental flow rate the area is based on the outer surface of the macroporous substrate. It is evident that the difference of the apparent permeance between the substrate and asymmetric support is very small, around 5% in both cases, suggesting that the main resistance (95%) in the asymmetric support is experienced in the alumina substrate. In addition, the apparent permeance of the supported silica membrane is only 4% of the apparent permeance of the asymmetric support, indicating that the main transport resistance (> 95%) is provided by the microporous silica layer, in agreement with the analysis of the pressure drop in each layer based on the data in Figures 7.9(b) and (c). The similarity of the both methods suggests that the support resistance can be safely neglected in preliminary analyses of the transport in the supported microporous silica membrane layer.

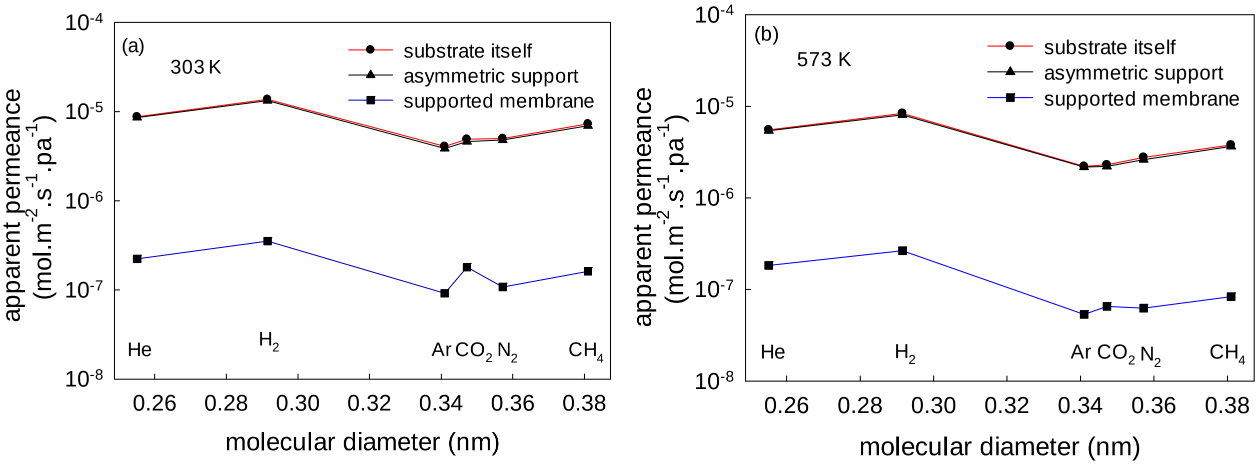

Figure 7.10 Variation of the apparent permeance with gas molecular size for the substrate, the asymmetric support and supported membrane, at (a) 303 K, and (b) 573 K, respectively.

Table 7.3 shows the effect of assumed pore coordination number, N_m, on the fitted pore mouth resistance-related parameters. It is noted that A_o deceases slightly with increase in assumed pore coordination number, to compensate for the reduced network tortuosity associated with larger N_m. Further, although all the values of A_o for the different gases are of similar magnitude, it is evident that a small variation occurs, with smaller molecule tending to have higher value for all the coordination numbers. This small variation is consistent with eqn. (7.14) as larger molecules will be subjected to greater degree of confinement at the narrow pore mouths, so that the entropy decrease ($-\Delta S_c$) increases with increase of diffusant molecular size. Further, the activation energy, E_a, while decreasing much more mildly for different coordination numbers, is strongly dependent on the molecular size and adsorption strength, and follows a systematic pattern, i.e., $CO_2 > CH_4 > Ar > N_2 > H_2 > He$, suggesting more strongly adsorbed molecules need to overcome higher activation energy to migrate through the same pore mouth. For instance, for N_m=6, the activation energy of Ar, with a LJ diameter 0.314 nm, is 7.39 kJ/mol, which is significantly higher than that for He (1.79 kJ/mol), with a much smaller LJ diameter of 0.2551 nm. On the other hand, CO_2 (11.93 kJ/mol) shows slightly higher activation energy than CH_4 (9.90 kJ/mol), despite its smaller LJ size parameter (c.f. Table 7.1). This is most likely related to the stronger interaction of CO_2, and to rotational restrictions faced by the real CO_2 at narrow pore entries, which is not explicitly considered through a LJ model based approach.

To explore the relationship between the temperature dependence of the pore diffusion resistances, we examine the apparent activation energy for the Oscillator model diffusivity, E_a^{osc}, given by [39]

$$E_a^{osc} = -\frac{d \ln D_{osc}}{d\beta} \tag{7.25}$$

It is noted that the above activation energy is only construed as an 'apparent' value based on the Arrhenius character of the temperature dependence for each pore radius, as there is no real activation barrier to the axial transport for the structureless cylindrical pore surface assumed here; this can only be considered as the 'energy' suitably averaged over the trajectories arising from diffuse reflection. Figure 7.11 depicts the variation in apparent activation energy of diffusion with pore radius for all the gases. It is evident that 'apparent activation energy' increases with pore radius, especially for stronger adsorbed gas species. Comparing this energy with the entry activation energy barrier (E_a) in Table 7.3, it is evident that although their ordering with respect to gas is similar, the value of the Oscillator model apparent energy E_a^{osc} is far less than that for the pore mouth (E_a), suggesting that the entry activation barrier is due to the repulsive effects associated with the steric hindrance in the narrow space of the pore mouth, rather than dispersive effects.

Table 7.3 Fitted parameters of the transition-state theory for different coordination numbers in the microporous silica membrane based on eqn. (7.16) at feed pressure 1.98 bar

gas species	N=3		N=4		N=5		N=6	
	A_o ($m^2 s^{-1} kg^{0.5} mol^{-0.5} K^{-0.5}$)	E_a (kJ/mol)	A_o ($m^2 s^{-1} kg^{0.5} mol^{-0.5} K^{-0.5}$)	E_a (kJ/mol)	A_o ($m^2 s^{-1} kg^{0.5} mol^{-0.5} K^{-0.5}$)	E_a (kJ/mol)	A_o ($m^2 s^{-1} kg^{0.5} mol^{-0.5} K^{-0.5}$)	E_a (kJ/mol)
H_2	3.07×10^{-8}	3.98	2.07×10^{-8}	3.66	1.68×10^{-8}	3.51	1.48×10^{-8}	3.42
He	2.54×10^{-8}	2.06	1.76×10^{-8}	1.91	1.44×10^{-8}	1.83	1.28×10^{-8}	1.79
CH_4	2.09×10^{-8}	10.17	1.63×10^{-8}	10.02	1.42×10^{-8}	9.95	1.30×10^{-8}	9.90
N_2	2.19×10^{-8}	7.23	1.62×10^{-8}	6.98	1.37×10^{-8}	6.84	1.23×10^{-8}	6.76
Ar	2.31×10^{-8}	7.85	1.72×10^{-8}	7.60	1.46×10^{-8}	7.47	1.32×10^{-8}	7.39
CO_2	1.92×10^{-8}	12.12	1.53×10^{-8}	12.02	1.35×10^{-8}	11.96	1.24×10^{-8}	11.93

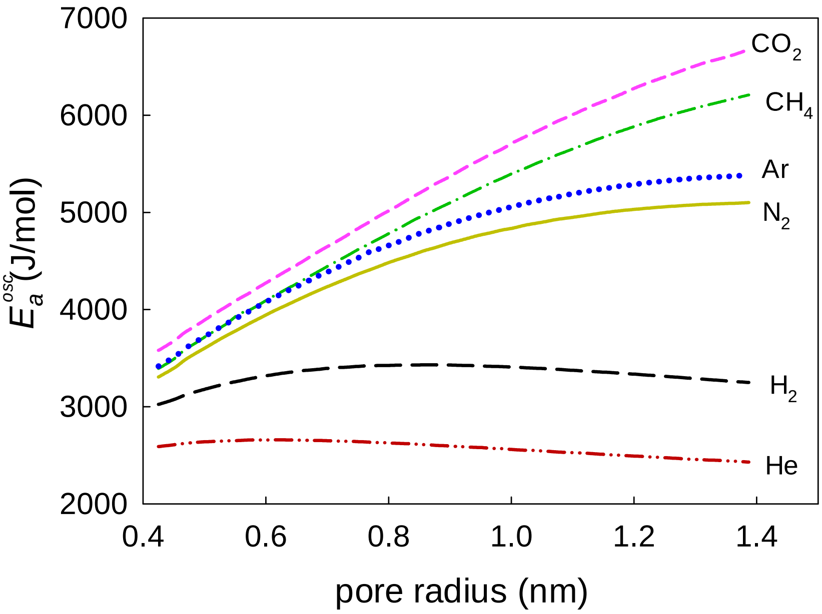

Figure 7.11 Variation of apparent activation energy of Oscillator model diffusivity with pore radius in the silica layer.

In microporous materials, the activation energy is frequently assumed to be linearly related to the adsorption enthalpy change or the isosteric heat following [55, 56]

$$E_a = -\alpha \Delta H^o \tag{7.26}$$

in which α is defined as the Brønsted–Evans–Polanyi (BEP) relation constant and commonly assumed to be 0.50 [57]. By comparing the obtained activation energy (E_a) in Table 7.3 with the fitted isosteric heat (Q) in Table 7.2, it is evident that the gas with higher isosteric heat encounters a larger pore mouth energy barrier, indicating the two parameters are correlated. On the other hand, although the activation energy is systematically smaller than the isosteric heat in the current work, the E_a/Q ratio is not uniform at 0.50, and is strongly dependent on the gas species, varying from 0.48 to 0.85. Similar results have been found by Trivedi and Axe [58], who measured the intraparticle diffusion of Cd and Zn in microporous oxides, over a wide range of ionic strength. Their data shows that the BEP relation constant strongly depends on the adsorbent and varies between 0.58 and 0.82.

Since the activated energy is determined by the enthalpic barrier ΔH_c, it may be expected that E_a is strongly dependent on the fluid-solid interactions in the pore body and at the pore neck. Figure 7.12 depicts the variation in apparent activation energy of each gas (E_a) with the interaction parameter ($\varepsilon_{fs}\sigma_{fs}^2/k_B$) for different coordination numbers. This correlation is suggested by the form of eqn. (7.9). It is evident that apparent activation energy correlates with the parameter $\varepsilon_{fs}\sigma_{fs}^2/k_B$, and stronger fluid-solid interaction does enhance the 'energy barrier' for the gas flowing through the pore mouth.

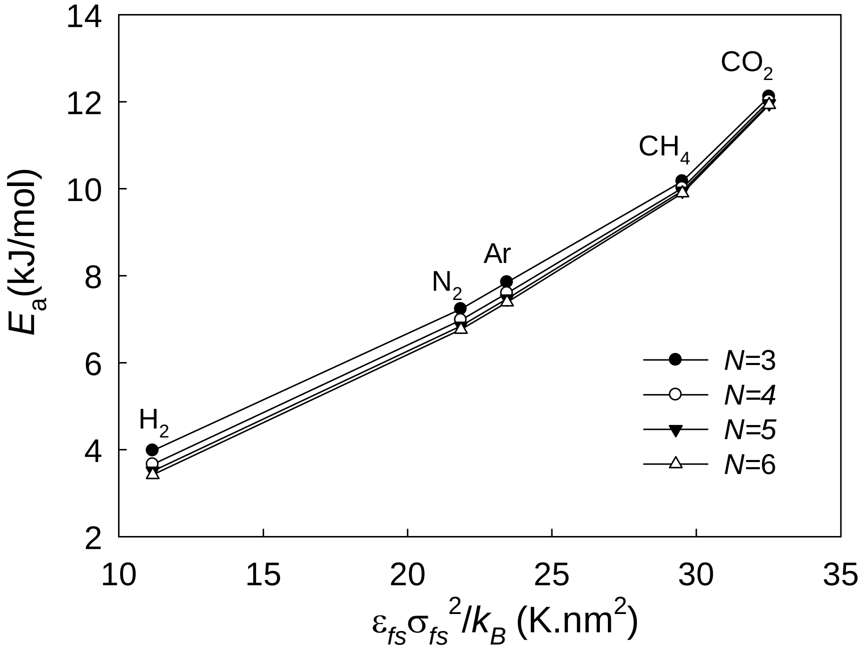

Figure 7.12 Variation of apparent activation energy of each gas with the parameter group $\varepsilon_{fs}\sigma_{fs}^2/k_B$, for different coordination numbers in the silica layer.

The above results indicated that the activation energy is indeed influenced by fluid-solid interaction, but the assumption of linearity between the activation energy and adsorption heat is largely empirical and arbitrary. One explanation for this artifact is that the activation energy E_a is determined by both the pore mouth and pore body structure, while the isosteric heat of the gas is mainly related to the adsorption in the pore body. Further, the linear empirical relation is based on fit of an overall diffusivity [55, 56], without the decomposition into the pore mouth and internal pore body diffusional resistances. Since the ratio of these resistances depends on the diffusing species, as will be subsequently shown, this linearity can only be expected to be a 'rough' guide.

It is noted that the pore mouth resistance and Oscillator resistance is not affected by hydroxyl groups for nonpolar gases, as their interaction sites are not ascribed partial charges. However, for polar gases such as CO_2, the hydroxyl group density may be expected to have significant influence on the parameters of the transition state theory and the Oscillator model due to electrostatic interactions. Thus, the magnitude of the constant B in eqn. (7.24) may be expected to increase with increase in the surface hydroxyl group density, and this will lead to an increase in the equilibrium constant and reduction in the Oscillator model pore diffusion coefficient. Further, as given in eqn.

(7.14), for the transition state theory, the activation energy (E_a) is determined by the enthalpy change (ΔH_c) of the migration from the pore body to the pore mouth, which is predominantly related to fluid-solid interactions; consequently, E_a may be expected to increase for polar gases when the hydroxyl group density increases.

Following the transition-state theory, the coefficient, A_0, should slightly depend only weakly on the gas species as the features captured in this coefficient are mainly related to the pore structure and the entropic barrier at the pore mouth [43]. This is indeed observed in Table 7.3, with A_0 varying only mildly between gases for a given coordination number. The least variation is obtained for N_m= 6, for which the average value of A_o is about 1.30×10^{-8} $m^2s^{-1}.kg^{0.5}.mol^{-0.5}.K^{-0.5}$. This value of A_0 may now be used to estimate the order of magnitude of the model pore length, l, following eqs. (7.14) and (7.15), while assuming the jump length ζ in $D_{TST} = k_{A\rightarrow B}\zeta^2/6$ to be equal to the mean pore length and neglecting the entropic barrier. Since the transmission probability κ, is generally close to unity [43], this yields $A_0 = (l/6b)\sqrt{1000R_g/2\pi}$, where b is the ratio of the pore cross-section to that of the dividing surface at the pore mouth, from which we obtain . While the precise value of the area ratio b is unknown, one may reasonably assume it to be in the region of 4-9 (i.e. a radius ratio of 2-3, given the mean pore body radius of 0.75 nm). Thus, an order of magnitude of the mean pore length is about 10 nm, which is a very reasonable value for the pore body radius of 0.75 nm.

To demonstrate the importance of internal diffusion resistance in the pore body during the transport, the Oscillator conductance is defined as

$$\lambda^{osc} = \frac{\pi r_p^2 D_{osc} K_{osc}(r_p)}{l} \tag{7.27}$$

By comparing the pore diffusion conductance, λ^{osc}, with the overall pore conductance, λ, in eqn. (7.16), the relative pore body resistance can be precisely investigated.

Figures 7.13(a-f) depict the variation of the ratio between the Oscillator and pore conductance (λ^{osc}/λ), for pore radius in the range of 0.4 to 1.4 nm for each gas, and coordination number N_m=6. It is evident that strong temperature dependence occurs for each gas. It is noted that the conductance ratio decreases with increase in temperature for all the gases, suggesting the importance of the pore body resistance is enhanced at high temperature. In addition, by comparing the value of λ^{osc}/λ between the gases, it is evident that stronger adsorbed gas tends to have relatively higher conductance ratio, suggesting the pore body resistance becomes relatively lower. For instance, at the same temperature, the conductance ratio for CO_2 is much larger than that for

H_2, so the restriction effect of pore mouth is far more influential on the more strongly adsorbed molecule, which is consistent with the trend based on the activation energy, E_a. Thus, for example, for H_2 the relative pore body resistance (λ/λ^{osc}) lies in the range of 0.08-0.25, and is significant, while that for CO_2 at 423 K and 573 K it is in the range of about 0.025-0.1, and is essentially negligible.

On the other hand, it is of interest to see that the conductance ratio increases with increase in pore radius, so that the internal pore diffusion resistance is more significant and non-negligible for smaller pores. However, this may be an artefact as we have not considered any correlation between pore body and pore mouth size. In practice smaller pores may also have a narrower more constricted entry. While we have considered the superposition of pore mouth and pore body resistance here, the most common method arbitrarily neglects diffusion resistance in the pore body for the transport, and assumes that the total resistance is governed by the narrow pore mouth, thus the overall conductance is exclusively determined by the transition-state theory [8, 59], with

$$\lambda^{TST} = \frac{\pi r_p^2 D_{TST} K_{osc}(r_p)}{l} \tag{7.28}$$

By applying eqn. (7.28) in the effective medium theory, the approach could be equally well fitted to the experimental data, and the obtained values of $A_0^{'}$ and $E_a^{'}$ for each gas are given in Table 7.4. It is evident that although the newly-fitted values of $E_a^{'}$ are slightly smaller than previous ones in Table 7.3 for all the coordination numbers, the ordering of the activation energies remains similar. In addition, in comparison with the fitted results in Table 7.3, the new results for $A_0^{'}$ become significantly smaller and still vary with gas species for all the coordination numbers. This decrease is due to a compensation effect, arising from neglect of the internal diffusion resistance in the pore body.

The above result demonstrates a key advantage of the combination of transition-state theory and the Oscillator model over the traditional method of using a single resistance, in that the effect of underlying factors, including pore and fluid properties and temperature, are correctly resolved, and the internal diffusion resistance in the pore body is properly considered. However, it is important to note that this does not necessarily suggest failure of the traditional method using a single resistance based on the use of TST, given the similarity in the fittings. A factor to be considered is that the Oscillator model diffusivity is obtained based on infinite-long pores, while imposing diffuse reflection at a uniform structureless pore wall. Since the real pores in the silica membrane have finite pore length and an atomistic surface with non-diffuse reflection, the diffusional

Table 7.4 Fitted parameters of the transition-state theory approach for different coordination numbers in the microporous silica membrane based on eqn. (7.28) at feed pressure 1.98 bar

gas species	*N*=3		*N*=4		*N*=5		*N*=6	
	$A_0^{'}$ (m^2 s^{-1}kg$^{0.5}$ mol$^{-0.5}$ K$^{-0.5}$)	$E_a^{'}$ (kJ/mol)	$A_0^{'}$ (m^2 s^{-1}kg$^{0.5}$ mol$^{-0.5}$ K$^{-0.5}$)	$E_a^{'}$ (kJ/mol)	$A_0^{'}$ (m^2 s^{-1}kg$^{0.5}$ mol$^{-0.5}$ K$^{-0.5}$)	$E_a^{'}$ (kJ/mol)	$A_0^{'}$ (m^2 s^{-1}kg$^{0.5}$ mol$^{-0.5}$ K$^{-0.5}$)	$E_a^{'}$ (kJ/mol)
H_2	1.71×10^{-8}	3.26	1.36×10^{-8}	3.18	1.19×10^{-8}	3.14	1.09×10^{-8}	3.10
He	1.56×10^{-8}	1.72	1.25×10^{-8}	1.69	1.08×10^{-8}	1.66	0.99×10^{-8}	1.65
CH_4	1.59×10^{-8}	9.55	1.31×10^{-8}	9.52	1.17×10^{-8}	9.51	1.09×10^{-8}	9.50
N_2	1.48×10^{-8}	6.49	1.20×10^{-8}	6.41	1.06×10^{-8}	6.36	0.97×10^{-8}	6.33
Ar	1.57×10^{-8}	7.08	1.27×10^{-8}	7.01	1.13×10^{-8}	6.96	1.04×10^{-8}	6.93
CO_2	1.55×10^{-8}	11.61	1.28×10^{-8}	11.59	1.15×10^{-8}	11.59	1.07×10^{-8}	11.58

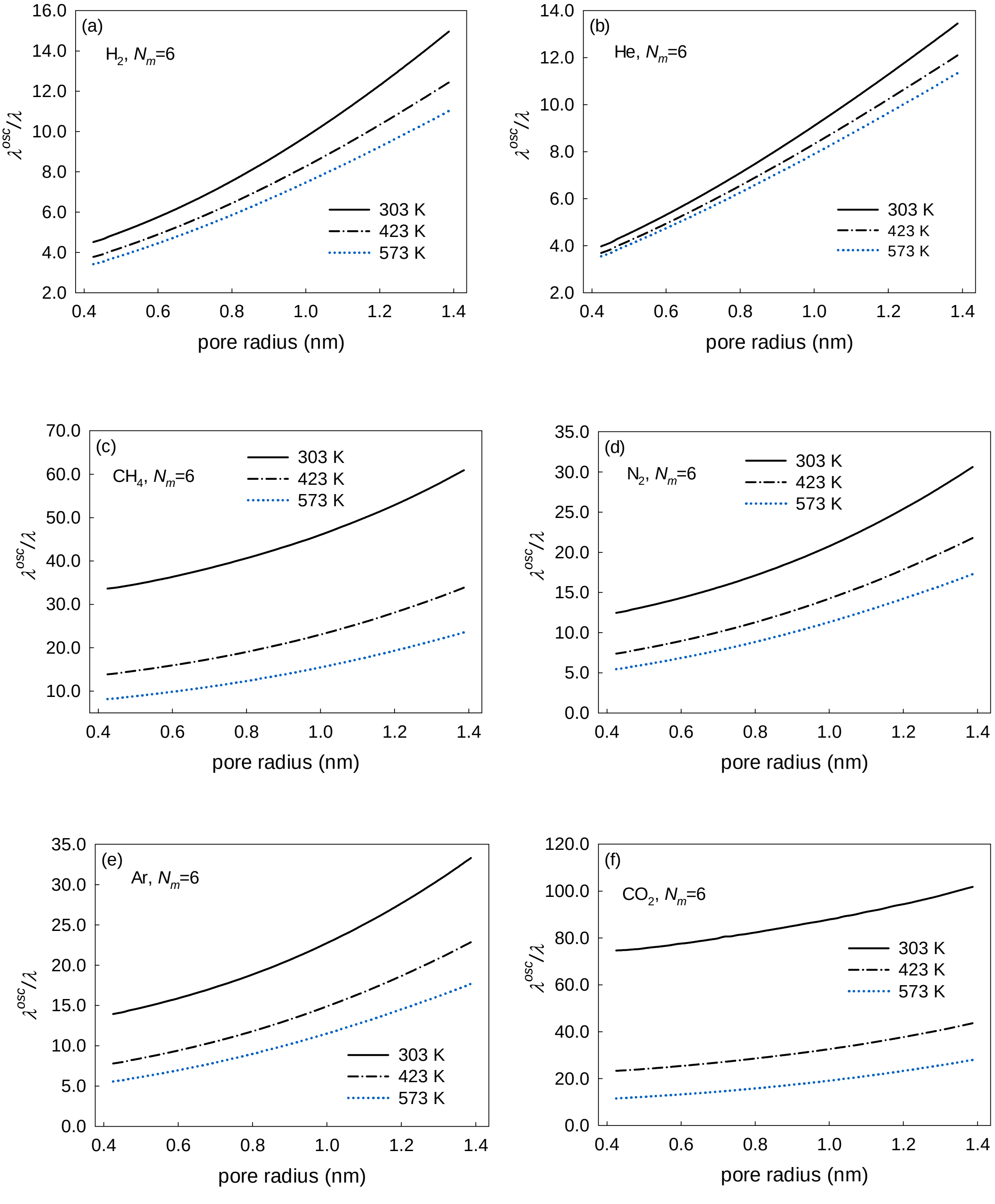

Figure 7.13 Variation of the conductance ratio (λ^{osc}/λ) with pore radius in the silica layer, for the lowest (303 K), intermediate (423 K) and highest temperature (573 K) for each gas, based on the parameters obtained at low feed pressure (1.98 bar), using coordination number N_m=6. (a) H_2, (b) He, (c) CH_4, (d) N_2, (e) Ar and (f) CO_2.

resistance in the silica pores may be less than that predicted by the Oscillator model, and may then be negligible in such pores. Further, the pores in which the internal diffusion resistance is relatively significant only constitute a small portion of the pore size distribution in Figure 7.2, leading to the transport of the microporous silica membrane lying in the transition region between the two methods.

Since the internal diffusion resistance in the pore body should be appropriately taken into account for the smaller pores in the silica membrane layer, the transport in the silica layer is more accurately represented by the combination of transition-state theory and the Oscillator model. This is subsequently used below to predict the flux in the supported membrane at different pressures.

7.4.3 Prediction of flux at different pressures

The above results indicate the success of effective medium theory using the combination of transition-state theory and Oscillator model to evaluate the pore conductance. Since the best fitting is obtained for coordination number $N_m = 6$, it is meaningful to apply the corresponding parameters in Table 7.1 to validate the proposed approach for other feed pressures. Figure 7.14(a) depicts the variation of flow rate with temperature for the different gases at the feed pressure 2.98 bar in the supported microporous silica membrane, using the fitted values of A_o and E_a for N_m=6 based on the 1.98 bar data (Figure 7.9a). The symbols correspond to the experimental points, and lines to the model results. It is evident that the model prediction matches the experimental data accurately for all the gases, indicating that the fitted parameters are independent of pressure, in this low-pressure range region. The variation of extracted interfacial pressures P_1 and P_2 with temperature is plotted in Figures 7.14 (b) and (c) respectively, having similar trends to the results obtained at lower pressure, i.e., the interfacial pressures for the least adsorbed gases (He and H_2) decrease more sharply with increase in temperature than that for the intermediate adsorbed gases (N_2 and Ar), and the interfacial pressure for CO_2 still mildly increases with increases in temperature due to the strong adsorption effect. However, the interfacial pressure for CH_4 monotonically decreases with increase in temperature, slightly different from the observation in Figures 7.9(b) and (c), which show a maximum before monotonically decreasing with temperature. The difference is largely caused by the decrease of the resistance in the macroporous substrate at higher pressure, arising from the increase of the viscous contribution.

Figures 7.15 (a-c) depict the predictions for the supported membrane at a feed pressure of 3.98 bar, using the previous fitted value of A_o and E_a for N_m=6. It is evident that the model prediction (lines) is in a good agreement with the experimental points (symbols) for all the gases in Figure 7.15(a), and the interfacial pressure trends with temperature in Figures 7.15(b) and (c) are similar to the results in Figures 7.14(b) and (c) respectively, with the main pressure drop experienced in the membrane layer. It is evident that the resistance of the supported membrane is still dominated by the microporous membrane layer (>95%) and the resistance in the asymmetric support is negligible, in accord with our previous conclusion based on Figures 7.9(b) and (c). The above results indicate that the applicability of the combination of Oscillator model and transition-state theory to the microporous silica layer is effective over a wide low pressure region. In addition, the above methodology, based on the hybrid effective medium-correlated random walk theory [53], can be extended to multicomponent systems to predict the Onsager coefficient for each gas, demonstrated in a general manner by Bonilla and Bhatia [60].

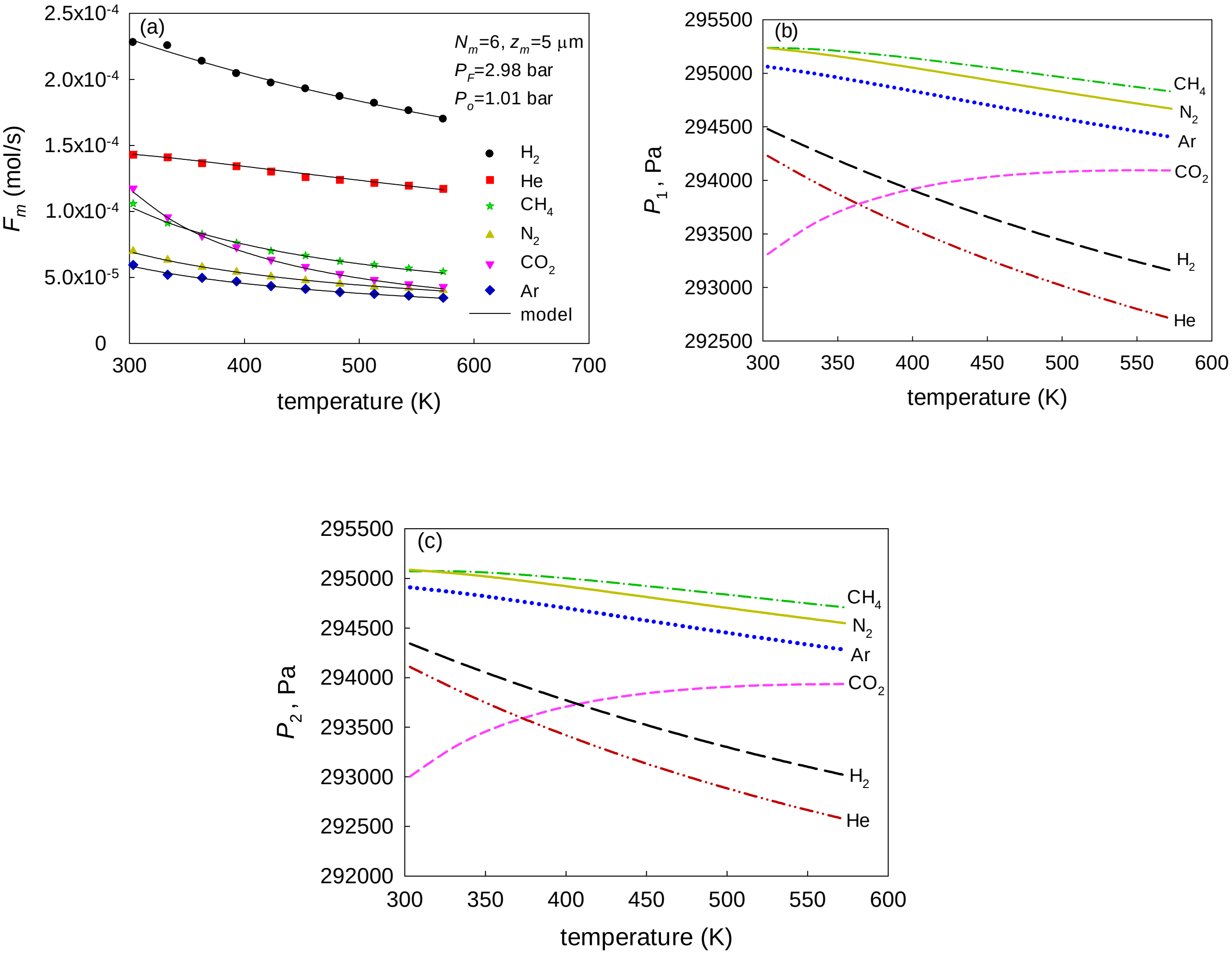

Figure 7.14 (a) Variation of flow rate, (b) interfacial pressure, P_1 and (c) P_2, with temperature at feed pressure P_F=2.98 bar based on eqn. (7.21), using parameter values N_m=6 and z_m=5 μm. In (a) the symbols are the experimental data and the lines are the model results.

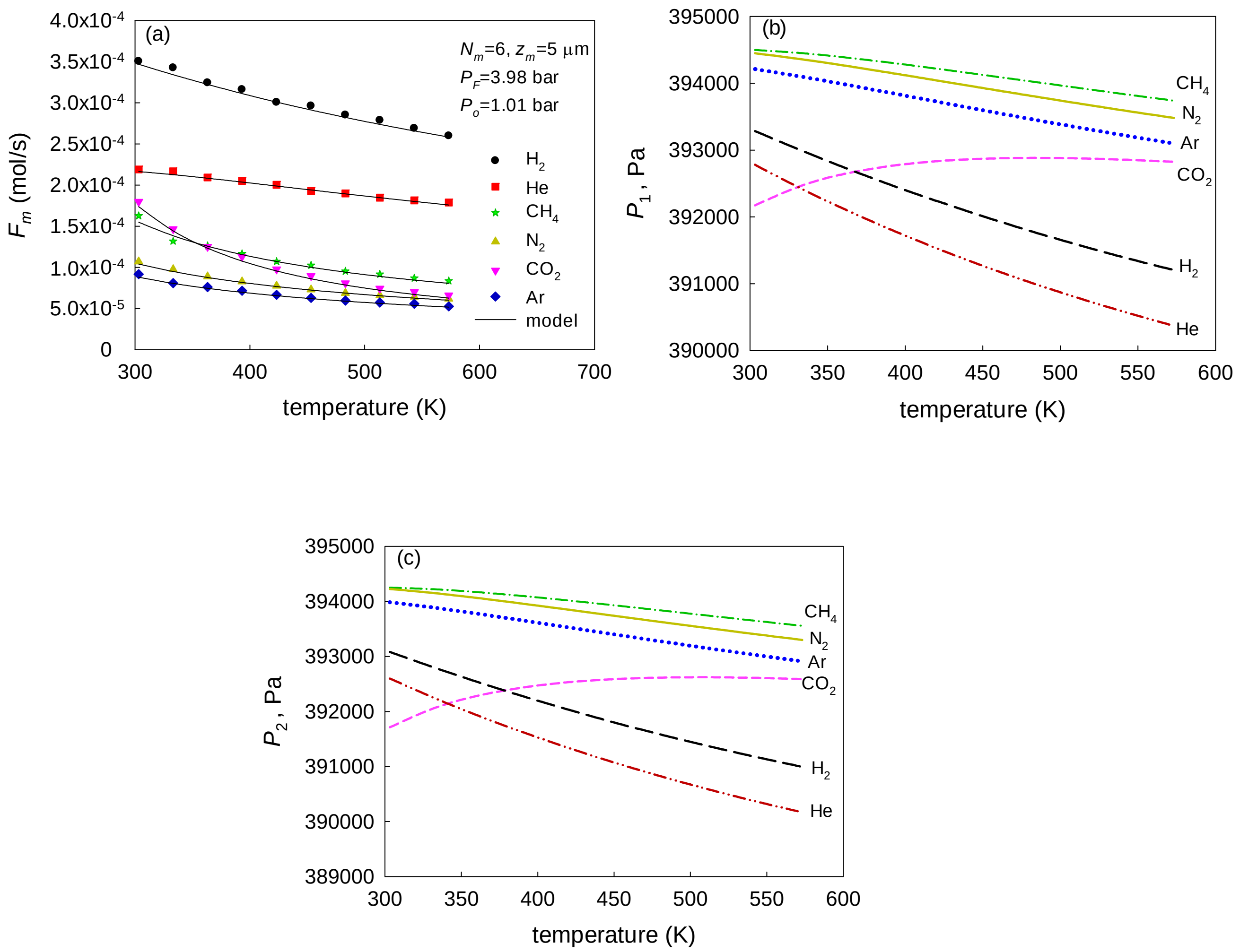

Figure 7.15 (a) Variation of flow rate, (b) interfacial pressure, P_1 and (c) P_2, with temperature at feed pressure P_F=3.98 bar based on eqn. (7.21), using parameter values N_m=6 and z_m=5 μm. In (a) the symbols are the experimental data and the lines are the model results.

7.5 Summary and conclusions

Single gas adsorption experiments with five gases (H_2, CH_4, N_2, Ar and CO_2) have been carried out at three temperatures (303, 333 and 363 K) in a microporous silica powder, and the corresponding adsorption equilibrium isotherms fitted by the conventional Langmuir adsorption model. Excellent agreement of the equilibrium constant for nonpolar gases (H_2, CH_4, N_2 and Ar) with that based on the canonical energy distribution using known LJ interaction parameters of silica is observed. However, significant underestimation occurs to CO_2 due to the additional electrostatic interaction of the polar molecule with pore walls, which strongly increases the adsorption. The disagreement for CO_2 was resolved by empirically modelling this interaction additively with the van der Waals interaction. The relatively high value of equilibrium constant for CO_2 in experiment was explained by the high density (7.5 nm^{-2}) of hydroxyl groups on the pore surface.

Single gas permeation experiments with six gases (H_2, He, CH_4, N_2, Ar and CO_2) have been conducted over a wide range of temperatures from 303 to 573 K in the supported microporous silica membrane, and the transport in the silica membrane layer is examined using effective medium theory based on a superposition of the Oscillator model and transition-state theory for predicting the macroscopic flow rate. Excellent agreement between the model and experimental data is obtained, and the results indicate that the pore mouth restriction provides the dominant resistance of each gas; however, the internal resistance in the pore body is still significant for relatively small pores, especially for less adsorbed gases at high temperature. The high values of pore mouth activation energy are considered to be caused by constrictions at the narrow pore mouths, not readily characterized independently.

The results show that larger molecules need higher energy to migrate through the pore mouth, and the obtained activation energy of the pore mouth restriction effect systematically follows the pattern, CO_2>CH_4>Ar>N_2>H_2>He. The larger value of CO_2 compared to CH_4 is most likely due to the stronger adsorption in the pore body, although there may also be some effect of rotational restriction at pore mouths. The interfacial pressure analysis shows that the main pressure drop along the supported membrane is caused by the microporous silica layer and the resistance in the asymmetric support is negligible. The relationship of the interfacial pressure to temperature depends on gas species. For less adsorbed gas, the interfacial pressure tends to decrease with increase in temperature, contrary to the behaviour for CO_2 which monotonically increases with temperature. The above approach has been used to describe the transport in the supported membrane at higher feed pressure, and the prediction is found to be in good agreement with experimental data, suggesting that the application of the superposition of the Oscillator model and transition-state theory in the microporous silica membrane is effective over the low pressure region.

7.6 References

[1] M. Knudsen, W.J. Fisher, The molecular and the frictional flow of gases in tubes, Phys. Rev., 31 (1910) 586-588.

[2] S.K. Bhatia, M.R. Bonilla, D. Nicholson, Molecular transport in nanopores: a theoretical perspective, Phys. Chem. Chem. Phys., 13 (2011) 15350-15383.

[3] M.R. Bonilla, S.K. Bhatia, The low-density diffusion coefficient of soft-sphere fluids in nanopores: accurate correlations from exact theory and criteria for applicability of the Knudsen model, J. Membr. Sci., 382 (2011) 339-349.

[4] C.T. Kresge, M.E. Leonowicz, W.J. Roth, J.C. Vartuli, J.S. Beck, Ordered mesoporous molecular sieves synthesized by a liquid-crystal template mechanism, Nature, 359 (1992) 710-712.

[5] D. Zhao, J. Feng, Q. Huo, N. Melosh, G.H. Fredrickson, B.F. Chmelka, G.D. Stucky, Triblock copolymer syntheses of mesoporous silica with periodic 50 to 300 angstrom pores, Science, 279 (1998) 548-552.

[6] S. Lijima, Helical microtubules of graphitic carbon, Nature, 354 (1991) 56-58.

[7] A.K. Cheetham, G. Férey, T. Loiseau, Open framework inorganic materials, Angew. Chem. Int. Edit, 38 (1999) 3268-3292.

[8] J.C. Diniz da Costa, G.Q. Lu, V. Rudolph, Y.S. Lin, Novel molecular sieve silica (MSS) membranes: characterisation and permeation of single-step and two-step sol-gel membranes, J. Membr. Sci., 198 (2002) 9-21.

[9] Y. Wan, D. Zhao, On the controllable soft-templating approach to mesoporous silicates, Chem. Rev., 107 (2007) 2821-2860.

[10] S.K. Bhatia, A.L. Myers, Optimum conditions for adsorptive storage, Langmuir, 22 (2006) 1688-1700.

[11] M.C. Duke, J.C. Diniz da Costa, G.Q. Lu, M. Petch, P. Gray, Carbonised template molecular sieve silica membranes in fuel processing systems: permeation, hydrostability and regeneration, J. Membr. Sci., 241 (2004) 325-333.

[12] F. Ye, H. Guo, H. Zhang, X. He, Polymeric micelle-templated synthesis of hydroxyapatite hollow nanoparticles for a drug delivery system, Acta. Biomater., 6 (2010) 2212-2218.

[13] M.J. Thust, M. Schöning, S. Frohnhoff, R. Arens-Fischer, P. Kordos, H. Lüth, Porous silicon as a substrate material for potentiometric biosensors, Meas. Sci. Technol., 7 (1996) 26-29.

[14] S.K. Bhatia, D. Nicholson, Some pitfalls in the use of the Knudsen equation in modelling diffusion in nanoporous materials, Chem. Eng. Sci., 66 (2010) 284-293.

[15] S.K. Bhatia, Modeling pure gas permeation in nanoporous materials and membranes, Langmuir, 26 (2010) 8373-8385.

[16] X. Gao, J.C. Diniz da Costa, S.K. Bhatia, The transport of gases in a supported mesoporous silica membrane, J. Membr. Sci., 438 (2013) 90-104.

[17] A. Markovic, D. Stoltenberg, D. Enke, E.U. Schlünder, A. Seidel-Morgenstern, Gas permeation through porous glass membranes: Part I. Mesoporous glasses-effect of pore diameter and surface properties, J. Membr. Sci., 336 (2009) 17-31.

[18] A. Marković, D. Stoltenberg, D. Enke, E.-U. Schlünder, A. Seidel-Morgenstern, Gas permeation through porous glass membranes: Part II: transition regime between Knudsen and configurational diffusion, J. Membr. Sci., 336 (2009) 32-41.

[19] T. Yoshioka, M. Kanezashi, T. Tsuru, Micropore size estimation on gas separation membranes: a study in experimental and molecular dynamics, AIChE J., 59 (2012) 2179-2194.

[20] T. Yoshioka, E. Nakanishi, T. Tsuru, M. Asaeda, Experimental studies of gas permeation through microporous silica membranes, AIChE J., 47 (2004) 2052-2063.

[21] X. Gao, M.R. Bonilla, J.C. Diniz da Costa, S.K. Bhatia, The transport of gases in macroporous α-alumina supports, J. Membr. Sci., 409-410 (2012) 24-33.

[22] F. Jareman, J. Hedlund, D. Creaser, J. Sterte, Modelling of single gas permeation in real MFI membranes, J. Membr. Sci., 236 (2004) 81-89.

[23] W. Jin, S. Li, P. Huang, N. Xu, J. Shi, Preparation of an asymmetric perovskite-type membrane and its oxygen permeability, J. Membr. Sci., 185 (2001) 237-243.

[24] E.A. Mason, A.P. Malinauskas, R.B. Evans III, Flow and diffusion of gases in porous media, J. Chem. Phys., 46 (1967) 3199-3216.

[25] R. Krishna, J.A. Wesselingh, The Maxwell-Stefan approach to mass transfer, Chem. Eng. Sci., 52 (1997) 861-911.

[26] C. Brazinha, A.P. Fonseca, H. Pereira, O.M.N.D. Teodoro, J.G. Crespo, Gas transport through cork: modelling gas permeation based on the morphology of a natural polymer material, J. Membr. Sci., 428 (2012) 52-62.

[27] D.M. Ruthven, W. DeSisto, S. Higgins, Diffusion in a mesoporous silica membrane: validity of the Knudsen diffusion model, Chem. Eng. Sci., 64 (2009) 3201-3203.

[28] S.K. Bhatia, D. Nicholson, Friction based modeling of multicomponent transport at the nanoscale, J. Chem. Phys., 129 (2008) 164709.

[29] X. Gao, M.R. Bonilla, J.C. Diniz da Costa, S.K. Bhatia, The transport of gases in a mesoporous γ-alumina supported membrane, J. Membr. Sci., 428 (2013) 357-370.

[30] H. Preising, D. Enke, Relations between texture and transport properties in the primary pore system of catalyst supports, Colloids Surf. A, 300 (2007) 21-29.

[31] J. Kärger, F. Stallmach, S. Vasenkov, Structure-mobility relations of molecular diffusion in nanoporous materials, Magn. Reson. Imaging, 21 (2003) 185-191.

[32] P. Uchytil, O. Schramm, A. Seidel-Morgenstern, Influence of the transport direction on gas permeation in two-layer ceramic membranes, J. Membr. Sci., 170 (2000) 215-224.

[33] X. Gao, J.C. Diniz da Costa, S.K. Bhatia, Understanding the diffusional tortuosity of porous materials: an effective medium theory perspective, Chem. Eng. Sci. (In Press), (2013).

[34] S. Hwang, Fundamentals of membrane transport, Korean J. Chem. Eng., 28 (2011) 1-15.

[35] J. Xiao, J. Wei, Diffusion mechanism of hydrocarbons in zeolites-I. Theory, Chem. Eng. Sci., 47 (1992) 1123-1141.

[36] O.G. Jepps, S.K. Bhatia, D.J. Searles, Wall mediated transport in confined spaces: exact theory for low density, Phys. Rev. Lett., 91 (2003) 126102.

[37] T.X. Nguyen, S.K. Bhatia, Kinetic restriction of simple gases in porous carbons: transition-state theory study, Langmuir, 24 (2008) 146-154.

[38] J. van den Bergh, S. Ban, T.J.H. Vlugt, F. Kapteijn, Modeling the loading dependency of diffusion in zeolites: the relevant site model, J. Phys. Chem. C, 113 (2009) 17840-17850.

[39] S.K. Bhatia, O. Jepps, D. Nicholson, Tractable molecular theory of transport of Lennard-Jones fluids in nanopores, J. Chem. Phys., 120 (2004) 4472-4485.

[40] R. Krishna, J.M. van Baten, An investigation of the characteristics of Maxwell-Stefan diffusivities of binary mixtures in silica nanopores, Chem. Eng. Sci., 64 (2009) 870-882.

[41] S.K. Bhatia, D. Nicholson, Hydrodynamic origin of diffusion in nanopores, Phys. Rev. Lett., 90 (2003) 016105.

[42] E. Beerdsen, B. Smit, D. Dubbeldam, Molecular simulation of loading dependent slow diffusion in confined systems, Phys. Rev. Lett., 93 (2004) 248301.

[43] T.X. Nguyen, S.K. Bhatia, Determination of pore accessibility in disordered nanoporous materials, J. Phys. Chem. C, 111 (2007) 2212-2222.

[44] T.X. Nguyen, H. Jobic, S.K. Bhatia, Microscopic observation of kinetic molecular sieving of hydrogen isotopes in a nanoporous material, Phys. Rev. Lett., 105 (2010) 085901.

[45] C.J. Brinker, G.W. Scherer, Sol-Gel Science: The Physics and Chemistry of Sol-Gel Processing, Academic Pr., San Diego, CA, 1990.

[46] N.K. Raman, C.J. Brinker, Organic "template" approach to molecular sieving silica membranes, J. Membr. Sci., 105 (1995) 273-279.

[47] K. Vollmayr, W. Kob, K. Binder, Cooling-rate effects in amorphous silica: A computer-simulation study, Phys. Rev. B, 54 (1996) 15808-15827.

[48] W.A. Steele, M.J. Bojan, Simulation studies of sorption in model cylindrical micropores, Adv. Colloid Interfac., 76 (1998) 153-178.

[49] A.V. Neimark, P.I. Ravikovitch, M. Grün, F. Schüth, K.K. Unger, Pore size analysis of MCM-41 type adsorbents by means of nitrogen and argon adsorption, J. Colloid. Interf. Sci., 207 (1998) 159-169.

[50] S.K. Bhatia, Capillary network models for transport in packed beds: considerations of pore aspect ratio, Chem. Eng. Commun., 154 (1996) 183-202.

[51] S. Kirkpatrick, Percolation and conduction, Rev. Mod. Phys., 45 (1973) 574-588.

[52] S.K. Bhatia, Stochastic theory of transport in inhomogeneous media, Chem. Eng. Sci., 41 (1986) 1311-1324.

[53] P.D. Deepak, S.K. Bhatia, Transport in capillary network models of porous media: theory and simulation, Chem. Eng. Sci., 49 (1994) 245-257.

[54] N.A. Seaton, Determination of the connectivity of porous solids from nitrogen sorption measurements, Chem. Eng. Sci., 46 (1992) 1895-1909.

[55] V.J. Inglezakis, A.A. Zorpas, Heat of adsorption, adsorption energy and activation energy in adsorption and ion exchange systems, Desalination and Water Treat., 39 (2012) 149-157.

[56] M. Suzuki, Adsorption Engineering, Co-published by Kodansha Ltd., Tokyo and Elsevier Science Publishers B.V., Amsterdam, 1990.

[57] A. Michaelides, Z. Liu, C. Zhang, A. Alavi, D.A. King, P. Hu, Identification of general linear relationships between activation energies and enthalpy changes for dissociation reactions at surfaces, J. Am Chem. Soc., 125 (2003) 3704-3705.

[58] P. Trivedi, L. Axe, Modeling Cd and Zn sorption to hydrous metal oxides, Environ. Sci. & Technol., 34 (2000) 2215-2223.

[59] A.J. Burggraaf, Single gas permeation of thin zeolite (MFI) membranes: theory and analysis of experimental observations, J. Membr. Sci., 155 (1999) 45-65.

[60] M.R. Bonilla, S.K. Bhatia, Multicomponent effective medium-correlated random walk theory for the diffusion of fluid mixtures through porous media, Langmuir, 28 (2011) 517-533.

Chapter 8: Conclusions and Recommendations

8.1 Conclusions

The focus of this thesis was on the investigation of transport mechanism in supported silica membranes at low pressure (below 4 bar) limits in the temperature between 30 and 300 ^{o}C by flowing gas from high temperature to low temperature. A key aim of this work was to develop a novel approach to include the important parameters of the pore network of each layer for the transport to explore the diffusion mechanism for the pores in the mesoporous and microporous silica membrane, using the well-established diffusion models in the literature. Table 8.1 summaries the main discoveries performed in current project, and the details of the novel findings are discussed below in details.

Table 8.1 The summarized discoveries for the supported silica membranes in the thesis

Materials	Known permeation mechanism	New findings
Macroporous substrate (500 nm)	Slip flow and constant tortuosity	Slip flow, but with tortuosity weakly varying with operating conditions.
Mesoporous interlayer (10.4 nm)	Knudsen diffusion mechanism and constant tortuosity	Both the Knudsen based and Oscillator models are applicable, but with weakly fluid and temperature dependent tortuosity
Mesoporous silica layer (3.8 nm)	Knudsen diffusion mechanism and negligible adsorption effect, with constant tortuosity	The Oscillator model diffusion applies, and Knudsen model fails. The adsorption effect is significant, and tortuosity varies strongly with gases and temperature
Microporous silica layer (1.5 nm)	Knudsen diffusion or surface diffusion mechanism	Transport mechanism in the transition region between mesopores and micropores, and the adsorption effect is strong. Effect of pore mouth resistance dominates.

The first contribution of this thesis is related to the modification of effective medium theory (EMT) utilizing the entire pore size distribution and including the aspect ratio effect for the unconsolidated porous media in which pore lengths are comparable to diameters. By the choice of a representative pore radius, the approach is employed to predict the apparent tortuosity to estimate the infiltration of single gases in macroporous substrates whose mean pore sizes are above 500 nm, under low pressure limits. The analytical results indicate that both the Knudsen diffusion and viscous diffusion are of importance in the macropores at given conditions, and the flow contributions is consistent with the theoretical estimation from the diffusion model, thus the arbitrary assumption in the literature that a viscous flow dominates the resistance of the substrate in the supported membrane is incorrect. In addition, it is found that the apparent tortuosity is not exclusively determined by the pore topology, but varies with temperature and operating conditions in the slip flow regime due to the difference of the tortuosity limits for the pure Knudsen and viscous flow. The theoretical results of EMT demonstrates an advancement on existing models (Dusty Gas Model (DGM)) that the apparent tortuosity can be explicitly resolved in terms of the pore network structure and fluid species as well as operating conditions rather than empirically obtained through the fitting based on the assumption of a constant value.

The second contribution of this thesis is related to the investigation of transport mechanism of single gases in the mesoporous γ-alumina interlayer coated on the macroporous substrate based on the extension of EMT approach to predict the macroscopic flow rate rather than apparent tortuosity, without any assumption regarding the dominant resistance in substrate and arbitrary choice of the mean pore radius. The analysis results indicate that the diffusion in the interlayer having a mean pore size of 10.4 nm can be independently represented by the Knudsen model, and a correction for the finite molecular size, and the Oscillator model, and the interfacial pressure is correctly resolved, which monotonically decreases with increase in temperature without anomalies observed with the approach based on a single pore size. In addition, the results demonstrate the importance of the pressure difference for different gas species and temperature in each layer, which should be correctly taken into account in any investigation for a multi-layered supported membrane. Similar results are also obtained for a mesoporous silica spheres (S980B) having a mean pore size of around 14 nm that both the Knudsen model and Oscillator model adequately interpret the data in conjunction with effective medium theory (EMT) by fitting a network coordination number. This insensitivity to model is due to the large mesopore radius for this silica; however, the Oscillator model is found to predict a value of the coordination number closer to the range of values expected for this material based on percolation theory.

The third contribution of this thesis is related to the investigation of transport mechanism of single gases in the mesoporous silica membrane layer of mean pore diameter 3.7 nm, coated on the asymmetric support. It is discovered that both the classical and corrected Knudsen models yield extreme high apparent tortuosity which varies with temperature and gas species, and the result are unexpected in the Knudsen models. This is largely caused by the overestimation of the diffusivity and neglect of adsorption effect. The most satisfactory results are obtained with the Oscillator model, in which variation of apparent tortuosity and adsorption is correctly considered. The results indicate that the Knudsen model fails to represent the diffusivity for the mesopores of mean size of 3.7 nm in silica, and that the Oscillator model provides a more accurate diffusivity and equilibrium constant which accounts for the effects of dispersive interaction between the fluid and walls.

The fourth contribution of this thesis is related to the investigation the influence of different representative pore radius of disordered porous materials on apparent tortuosity to explore its gas and temperature dependence. Using the EMT we demonstrate that the apparent tortuosity varies with operating conditions and diffusion mechanism due to the differences in temperature dependence between the conductance at the representative pore radius and the effective conductance which depends on the pore connectivity and PSD. In the slip flow regime for unconsolidated macroporous media, it is discovered the combination of Knudsen and viscous mechanisms leads to temperature and species dependence of tortuosity, because of the different pore size dependence of the two contributions. This leads to different limiting tortuosities and PSD dependence in the Knudsen and viscous flow regimes. For consolidated mesoporous media, the tortuosity variation of temperature and gas dependence is associated with the shortcut effect in pores having higher conductance, which can be attributed to either diffusivity or adsorption effect.

The fifth contribution of this thesis is related to the evaluation of adsorption and transport mechanism of single gases in the microporous silica membrane layer of the mean pore diameter 1.5 nm, deposited on the asymmetric support. The adsorption isotherms are found to be Langmuirian, and the equilibrium constants can be accurately predicted for nonpolar gases in Oscillator model by considering Lennard-Jones (LJ) interactions. For the polar gas, CO_2, the hydroxyls groups on the pore walls strongly enhance the gas affinity with the pore walls, and an empirically additive electrostatic interaction is employed to predict the Langmuirian equilibrium constant. The EMT analysis results indicates that the pore transport can be adequately represented by combination of pore mouth and internal pore diffusion resistances based on the Oscillator model and Transition-state theory, respectively, and the overall transport resistance is governed by the pore mouth barrier.

In summary, this work highlights the importance of considering the fluid-solid interaction in the pores of several nanometers to predict the fluid transport and equilibrium constant. In addition, the analytical results essentially suggest the entire pore size distribution should be taken into account in any approach to investigate the apparent tortuosity and macroscopic transport. Furthermore, based on our discoveries, it is fairly safe to conclude that the Knudsen model is satisfactory in pores lager than 20 nm for light gases, and the Oscillator model is useful in the pore range below that.

8.2 Recommendations

Although a significant progress of modeling the transport of single gases in disordered mesoporous and microporous silica materials has been made to understand the influence of the fluid-solid interaction on the diffusivity and adsorption effect, the complex nature of nanoporous silicas that dominates the physical behaviors of diffusant in narrow pores requires further intensive studies which is beyond the scope of the thesis. Indeed, this is an enormous subject and plenty of work can be done in the further. Based on this work, I list some potential work that could be derived from the present work.

1. To enhance the hydrothermal stability of the amorphous silica, metal oxides are often doped in the silicas to prevent any further condensation of hydroxyl groups on the pore surface, which may block the passage of pores, thus further investigations can be made to investigate the adsorption and transport mechanism of gases in metal or metal oxides doped silica membranes to provide the location and nature of the interaction between the gases and metal oxide phases, which is little known in the literatures. Such a study will be beneficial to understanding the formation mechanism of oxidant, which is instructive to the experimental work.

2. The work in this project is mostly associated with light gases for which the dispersive interaction is normally weak, thus the experimental conclusion cannot be directly extended to the heavier gases whose dispersive interaction is much stronger. It is of interest to experimentally test several other gases to investigate the adsorption and transport mechanism in the mesoporous and microporous silica pores in different range. Finally it will be great to experimental produce a diagram for different gases, showing the conditions where the Knudsen model start to fails for these gases.

3. The gases used in this work are mostly pure gases under low density limits, and the intermolecular interaction is negligible. However, in the most industrial application, the gas sources consists of mixtures; thus, the interaction between different species may hold importance at low temperature, which should be taken into account in the defined conductance for effective medium theory approach. To achieve this purpose, the Maxwell-Stefan intermolecular diffusivity ($Đ_{ij}(i \neq j)$) should be well understood to combine with the Knudsen model and Oscillator model in the future work.

4. The silica membranes used in this work have relatively large pores, and it cannot be employed to conduct gas separation process. The pores in molecular sieve membrane (MSM) are only several angstroms, exerting extremely high energy barrier to the gas molecules larger than the pores, thus the MSM is extensively synthesized to separate gas mixtures. However, the fundamental adsorption and diffusion mechanism of gases in this type membrane is poorly understood, and most of the work is largely based on empirical activation energy correlations. The Oscillator model and transition-state theory can be applied to provide more details on this subject.

5. Beside silica membranes, other novel mesoporous and microporous membranes are also developed rapidly, such as titanium oxides membranes, carbon nanotubes (CNT) and metal organic frames (MOF), but the transport process remains elusive. To well predict the adsorption and transport of gases in these materials, the LJ parameters should be provided in advance to evaluate the dispersive fluid-solid interaction to determine the pores where the Knudsen model prevails or fails by effective medium theory.